Title

Computational Framework for the Ab Initio Description of Noncollinear Magnetism

Author

Moore, Guy Carleton

Publication Date

2024

Peer reviewed|Thesis/dissertation

Computational Framework for the Ab Initio Description of Noncollinear Magnetism

By

Guy Carleton Moore

A dissertation submitted in partial satisfaction of the

requirements for the degree of

Doctor of Philosophy

in

Engineering Science - Materials Science and Engineering

in the

Graduate Division

of the

University of California, Berkeley

Committee in charge:

Professor Kristin A. Persson, Chair
Dr. Sinéad M. Griffin
Professor Jeffrey B. Neaton
Professor Daryl Chrzan

Summer 2024

Computational Framework for the Ab Initio Description of Noncollinear Magnetism

Abstract

Computational Framework for the Ab Initio Description of Noncollinear Magnetism

By

Guy Carleton Moore

Doctor of Philosophy in Engineering Science - Materials Science and Engineering

University of California, Berkeley

Professor Kristin A. Persson, Chair

The accurate description of correlated electronic states in magnetic strongly correlated systems, e.g. many transition metal oxides (TMOs), presents a significant challenge in density functional theory (DFT), especially when dealing with noncollinear magnetism. Identifying noncollinear ground states is inherently complex and computationally demanding due to the high-dimensional landscape of spin configurations and the critical role of spin-orbit coupling. This dissertation addresses these challenges through a sequential and integrated computational approach, encompassing the development of workflows, implementation of new exchange-correlation (XC) functionals, and the introduction of a novel optimization algorithm for identifying noncollinear magnetic ground states.

First, we present a high-throughput computational study using the DFT+U method to correct self-interaction errors (SIE) in the description of correlated electronic states. This study focuses on the accurate determination of Hubbard U and Hund J parameters using the linear response (LR) methodology. We compute the U and J values for transition metal d-electron states in over 1000 TMOs, providing a valuable reference for researchers. An automated workflow developed within the `atomate` framework enables these calculations on massively parallel supercomputing architectures. The applicability of this workflow is demonstrated through the calculation of spin-canting magnetic structures and unit cell parameters of the multiferroic olivine $LiNiPO_4$, showing strong effects of Ni-d U and J corrections and significant improvements in computed lattice parameters when including an O-p U value.

Building on this foundation, we expand the source-free (SF) exchange-correlation (XC) functional developed by Sangeeta Sharma and co-workers to plane-wave DFT based on the projector augmented wave (PAW) method. This implementation, integrated within the VASP source code, leverages parallel three-dimensional fast Fourier transforms (FFTs) for improved computational efficiency. We explore the enhanced convergence behavior and the impact on non-collinear magnetic ground states when applying the SF constraint to the GGA-PBE+U+J functional. Our findings show significantly improved agreement with ex-

perimentally measured magnetic structures. Additionally, we analyze the importance of probability current densities and XC torque in spin-polarized systems, highlighting connections to spin-current density functional theory (SCDFT) and paving the way for future extensions of the SF corrected XC functional.

Finally, we propose and implement a novel hybrid meta-heuristic optimization algorithm, SpinPSO, designed to identify noncollinear global ground states in magnetic systems. This algorithm combines particle swarm optimization (PSO) with atomistic spin dynamics, allowing for the accurate determination of magnetic ground states using inputs directly from non-collinear DFT calculations. The workflow, implemented in `atomate`, is optimized for high-performance computing environments. SpinPSO successfully converges to experimentally resolved magnetic ground states for diverse test materials exhibiting exotic spin textures.

This dissertation demonstrates a comprehensive and integrative approach to tackling the complexities of correlated electronic states and magnetic ordering in TMOs, contributing useful computational tools and methodologies to the field of condensed matter physics. Sections, figures, and tables are included, with permission, from: Ref. [1] (Copywrite 2024 American Physical Society), Ref. [2] (Copywrite 2024 Springer Nature), Ref. [3] (Copywrite 2023 arXiv), and Ref. [4] (Copywrite 2023 arXiv).

To Grandpa Jay, and his memory

To dream the impossible dream
To fight the unbeatable foe
To bear with unbearable sorrow
To run where the brave dare not go
...

- Written and composed by
Joe Darion and Mitch Leigh
in "Man of La Mancha"

...
"Beware the Jabberwock, my son!
The jaws that bite, the claws that catch!
Beware the Jubjub bird, and shun
The frumious Bandersnatch!"
...
And, as in uffish thought he stood,
The Jabberwock, with eyes of flame,
Came whiffling through the tulgey wood,
And burbled as it came!
...

- Lewis Carroll

Contents

List of Figures

List of Tables

Acknowledgments

I am deeply grateful to my advisor, Professor Kristin Persson, for her continued support and belief in me. As someone who is interested in many topics, often leading me to work on several projects "in parallel," I have greatly benefited from her mentoring style. She strikes a careful balance between encouragement and guidance, keeping me on track and focused within the greater goal of my research. Each graduate student requires a different mentoring style, and I flourished under her trusting leeway paired with constructive critical analysis of my approach. Furthermore, she always motivated me to seek out additional expertise and collaborations, which has led to several fruitful and productive projects with experimentalists and theorists alike. I am forever inspired by Kristin's ability to effectively manage a large computational group with expertise ranging from machine learning and data management to battery anode materials discovery and solid-electrolyte-interface (SEI) formation, not to mention my studies in magnetism and phase transformations, in which she also maintains academic authority. Her scientific knowledge, innovative spirit, mentorship style, and kind personality are reflected in the highly inquisitive researchers she attracts to her research group. She has always sought to maintain a collaborative, friendly, and engaged working atmosphere. I have always felt her support, both directly and through the support network offered by the Persson Group.

Kristin's ability to provide a cohesive support structure for her graduate students is exemplified by her choice of my co-mentor in research, Dr. Matt Horton. I am inspired by Matt's kindness, generosity, and scientific integrity. In addition to Matt's abilities as a scientist, he is an incredible coder. I have Matt to thank for my ability to create halfway decent Python code and figures. I aspire to one day be a research mentor like Matt. He was never overbearing, while always being there for assistance. To exemplify how lucky I am to be his mentee, he asked me what mentorship style I most preferred to help me achieve my goals. He was our research group's point person for all things relating to software infrastructure and magnetism, in addition to the numerous other projects he was involved in. Despite that, he always was able to make time for me and provide invaluable feedback and advice.

Matt introduced me to Dr. Sinéad Griffin, my future PI. My collaborations with Sinéad have spanned over a year so far and have resulted in some of the most productive work of my PhD, both with experimentalists and on a theoretical level. One of the greatest validating moments of my academic career was Sinéad's approval of my multi-scale modeling framework developed during my PhD. I've benefited immensely from her knowledge of quantum mechanics and field theory, to name a couple areas of her expertise. I'm looking forward to future collaborations and scientific endeavors in partnership with Sinéad and other members of her group, who have already welcomed me as one of their own.

This research would not be possible without the funding and academic freedom provided by the Department of Energy Computational Science Graduate Fellowship (DOE CSGF) under grant DE-SC0020347. I thank my undergrad mentors at LBNL, including Dr. Andy Nonaka, Dr. Changho Kim, Dr. Ann Almgren, Dr. John Bell, and Dr. Dan Martin, for their support, encouraging me to apply, and guiding me through the application process.

This includes my undergraduate professors who gently directed me towards graduate school and to apply for fellowships, which includes Dr. Elizabeth Basha, Dr. Aleksei Beltukov, Dr. Kieran Holland, and Dr. Rahim Khoie at the University of the Pacific. In addition to the generous public funds, the academic community of DOE CSGF is truly welcoming, astounding, and wide-reaching. I've felt continuous support and engagement from my friends in the program. I look forward to providing the same mentorship and comradeship to others in current and future classes of the program. I am eternally grateful for public funding in science such as DOE CSGF and the opportunities it provides to students to flourish in academia and the national lab environment.

I would like to thank my family next for their continuous and unwavering care for my education. I firmly believe that I would not be where I am now if it wasn't for my mom's decision to homeschool me until college and enroll me in community college courses starting at the age of thirteen. While I don't consider myself very bright, I'm curious to an extent that is hard to sequester. My mom's guidance and teaching allowed me to follow my academic interests without getting burnt out or losing the love of the subject. My dad has always supported my dreams and ambitions in a loving and gentle way. He is my role model in terms of both work ethic and how not to take myself too seriously. I'm certain that most parents of PhD students do not read their child's papers; mine listened to them using a text-to-speech app! Rachel, my sister, is one of my best friends. She has always been there for me through it all, and she has become so interested in my work that she is letting me give her Python coding lessons on weekends.

Next, I would like to thank my Grandma Karin and Grandpa Jay, to whom this dissertation is dedicated. I would not have found my love for math and science if it wasn't for my grandpa. As a set designer for Broadway and film during his professional career, he always found a way to weave together art and mathematics. My sister and I spent countless hours in "math camp," which would span several days at a time at my grandparents house. I was only able to enjoy it and avoid burnout because Grandma knew when we were approaching saturation and when it was time for a walk outside. I only wish you were here to chat physics now, Grandpa.

If I were to thank all of my friends who showed their support for me during my PhD, it would take many more pages. I'll start from oldest to newest. My friends Gustavo Bartolo and Kyle Poe from undergrad were always willing to share in the struggles of grad school, even though they were across the country, in completely different research fields. Somehow we are still able to have fascinating and in-depth conversations about math and physics. Next, I'd like to thank my good friend and colleague Dr. Shivani Srivastava, for her incredible friendship, support, and mentorship (even though she is only one year my senior). Having a friend close by to have a quick coffee and confide in was invaluable. I look forward to many more years of friendship and collaboration. Lastly, to Bo Lotti, my neighbor turned friend: I'm so happy that I get to experience this potent and exciting part of our life together. He keeps me inspired on a creative level and also reminds me not to take myself too seriously.

And of course, to Shelly, my love and best friend. I could not have made it this far if it wasn't for your reminders to take a breath of fresh air and smell the wild roses. This

isn't to mention the countless existential crises and feelings of self-doubt that you helped me navigate. You remained supportive of my academic career through it all, despite the challenges it has presented for us. To say that I lucked out meeting you would be an enormous understatement.

In conclusion, I extend my deepest gratitude to all who have supported me throughout my tilting at windmills. Your guidance, support, and encouragement have been invaluable, and I am forever grateful.

Chapter 1

Introduction

1.1 In search of the magnetic ground-state, an alleged ground-truth

Beyond the horizon of the place
we lived when we were young
In a world of magnets and
miracles
Our thoughts strayed constantly
and without boundary
The ringing of the division bell
had begun
...
Leaving the myriad small
creatures trying to tie us to the
ground
To a life consumed by slow
decay

Pink Floyd

The arts magnetic
The flow athletic
Dimensions is effected whether
static or kinetic
And power blast pressure amass
beyond measure

---

dj honda feat. Mos Def

The magnetic state of materials couples directly to their functional performance in applications including quantum computers, spintronics, multiferroics, magnetic refrigeration, and alternatives to rare-earth permanent magnets [5]. In order to design materials for improved functionality, it is necessary to correctly identify the magnetic ground state and its correlation with other properties. While the collinear magnetic ground states have been addressed successfully using density-functional-theory (DFT) automatic workflows [6], non-collinear magnetic ground-states - attributable to a variety of different phenomena such as spin-orbit coupling (SOC) [7], to magnetic frustration, both geometric and other [8, 9], are inherently more challenging.

1.2 Theoretical Approach and Background

In this section, we will briefly layout the theoretical background for the computational and theoretical approaches of this study, which will include density functional theory (DFT) in Section 1.2.1, as well as atomistic spin dynamics (ASD) in Section 1.2.2.1 and particle swarm optimization (PSO) in Section 1.2.2.2. The latter two methods will set the stage for the hybrid physics informed meta-heuristic optimization algorithm, `SpinPSO`, and accompanying workflow for optimizing to the global noncollinear magnetic ground-state.

1.2.1 Ab initio foundations

1.2.1.1 From the Many-Body Schrödinger Equation to Density Functional Theory

The foundation of quantum mechanics is the Schrödinger equation, which describes how the quantum state of a physical system changes over time. For a system of N interacting electrons, the many-body time-independent Schrödinger equation is:

$$\hat{H}\Psi(\mathbf{r}_1, \mathbf{r}_2, \ldots, \mathbf{r}_N) = E\Psi(\mathbf{r}_1, \mathbf{r}_2, \ldots, \mathbf{r}_N), \tag{1.1}$$

where $\hat{H}$ is the Hamiltonian operator, given by

$$\hat{H} = -\sum_{i=1}^{N} \frac{\hbar^2}{2m}\nabla_i^2 + \sum_{i<j} \frac{e^2}{|\mathbf{r}_i - \mathbf{r}_j|} + \sum_{i=1}^{N} v_{\text{ext}}(\mathbf{r}_i). \tag{1.2}$$

Solving this equation exactly for many-electron systems is computationally infeasible due to the exponential growth of complexity with N.

1.2.1.2 Hartree-Fock Theory

To make the problem tractable, approximations are introduced. The Hartree-Fock (HF) method is an important approximation that simplifies the many-body problem by considering

a single Slater determinant as an approximate wavefunction:

$$\Psi(\mathbf{r}_1, \mathbf{r}_2, \ldots, \mathbf{r}_N) = \frac{1}{\sqrt{N!}} \det[\psi_i(\mathbf{r}_j)], \tag{1.3}$$

where ψ_i are the single-electron orbitals.

Following from the statement made in Ref. [10], the HF energy can be stated in the convenient form

$$E_{HF} = \frac{1}{2} \sum_{\sigma\sigma'} \int d\boldsymbol{r} \int d\boldsymbol{r'}\, u_{\sigma\sigma'}(\boldsymbol{\Delta r}) \left[\rho_\sigma(\boldsymbol{r})\rho_{\sigma'}(\boldsymbol{r'}) - \zeta_{\sigma\sigma'}(\boldsymbol{r}, \boldsymbol{r'})\zeta_{\sigma'\sigma}(\boldsymbol{r'}, \boldsymbol{r})\right], \tag{1.4}$$

where $\boldsymbol{\Delta r} = \boldsymbol{r} - \boldsymbol{r'}$, and $u_{\sigma\sigma'}(\boldsymbol{\Delta r}) = e^2/|\boldsymbol{\Delta r}|$ is the Coulomb kernel. The electron densities, ρ_σ, and $\zeta_{\sigma\sigma'}$ can be defined in terms of single-electron wave functions as

$$\rho_\sigma(\boldsymbol{r}) = \sum_i \psi^*_{\sigma,i}(\boldsymbol{r})\psi_{\sigma,i}(\boldsymbol{r}) \tag{1.5}$$

$$\zeta_{\sigma\sigma'}(\boldsymbol{r}, \boldsymbol{r'}) = \sum_i \psi^*_{\sigma,i}(\boldsymbol{r})\psi_{\sigma',i}(\boldsymbol{r'}). \tag{1.6}$$

The non-spin-polarized exchange contribution to the energy is given by [11]:

$$E_x = -\frac{e^2}{2} \sum_{i,j} \int\int\ d\mathbf{r}\ d\mathbf{r}'\ \frac{\psi^*_i(\mathbf{r})\psi_i(\mathbf{r}')\psi^*_j(\mathbf{r}')\psi_j(\mathbf{r})}{|\mathbf{r} - \mathbf{r}'|}, \tag{1.7}$$

which cannot be stated in terms of the electron density $\rho(\mathbf{r})$ alone. While HF theory captures exchange effects exactly, it does not fully account for electron correlation, which is crucial for an accurate description of many-body systems. This approximation comes from the assumption of the single Slater determinant used in HF theory, in Equation 1.3.

1.2.1.3 The Exchange Hole

Along these lines, in HF theory, the exchange interaction is introduced through the concept of the exchange hole, which represents the reduction in the probability of finding two electrons with the same spin close to each other. The Hartree-Fock energy can then be conveniently expressed as the following pairwise potential,

$$E_{HF} = \frac{1}{2} \sum_{\sigma\sigma'} \int d\boldsymbol{r} \int d\boldsymbol{r'}\, \tilde{u}_{\sigma\sigma'}(\boldsymbol{\Delta r})\rho_\sigma(\boldsymbol{r})\rho_{\sigma'}(\boldsymbol{r'}), \tag{1.8}$$

with

$$\tilde{u}_{\sigma\sigma'}(\boldsymbol{r}, \boldsymbol{r'}) = u_{\sigma\sigma'}(\boldsymbol{\Delta r}) \left(1 - \frac{\zeta_{\sigma\sigma'}(\boldsymbol{r}, \boldsymbol{r'})\zeta_{\sigma'\sigma}(\boldsymbol{r'}, \boldsymbol{r})}{\rho_\sigma(\boldsymbol{r})\rho_{\sigma'}(\boldsymbol{r'})}\delta_{\sigma\sigma'}\right). \tag{1.9}$$

It is interesting to note the links between $\tilde{u}_{\sigma\sigma'}(\boldsymbol{r}, \boldsymbol{r'})/u_{\sigma\sigma'}(\boldsymbol{\Delta r})$ and the pairwise correlation functions between electron densities of spin σ and σ' [10, 11]. This expression provides an interdependence between the pairwise potential between electrons and their pair correlation function, which in principle should be calculated self-consistently, in addition to the electron density.

1.2.1.4 Kohn-Sham Equations and Density Functional Theory

DFT addresses the limitations of HF theory by introducing the electron density $\rho(\mathbf{r})$ as the central variable. The Hohenberg-Kohn theorems [12] provide the foundation of DFT, stating that the ground-state properties of a system are uniquely determined by its electron density. The Kohn-Sham (KS) approach [13] reformulates the problem in terms of electrons interacting in an effective potential:

$$\left(-\frac{\hbar^2}{2m}\nabla^2 + v_{\mathrm{KS}}(\mathbf{r})\right)\psi_i(\mathbf{r}) = \epsilon_i\psi_i(\mathbf{r}), \tag{1.10}$$

where the KS potential v_{KS} is given by:

$$v_{\mathrm{KS}}(\mathbf{r}) = v_{\mathrm{ext}}(\mathbf{r}) + e^2\int\frac{\rho(\mathbf{r}')}{|\mathbf{r}-\mathbf{r}'|}d\mathbf{r}' + v_{\mathrm{xc}}(\mathbf{r}). \tag{1.11}$$

Here, $v_{\mathrm{xc}}(\mathbf{r})$ is the exchange-correlation potential, which, in principle should incorporate all many-body effects.

1.2.1.5 Exchange-Correlation Functionals

The exchange-correlation energy $E_{\mathrm{xc}}[\rho]$ is a functional of the electron density and is crucial for the accuracy of DFT. However, an exact mathematically tractable form of $E_{\mathrm{xc}}[\rho]$ is not known, so several assumptions are needed [11]. Several approximations exist for E_{xc}, including [11, 14]:

- Local Density Approximation (LDA): Assumes E_{xc} depends only on the local density $\rho(\mathbf{r})$.
- Generalized Gradient Approximation (GGA): Includes the gradient of the density $\nabla\rho(\mathbf{r})$ to account for inhomogeneities.
- Hybrid Functionals: Combine exact exchange from HF theory with GGA.

1.2.1.6 The Hubbard functional

DFT is a workhorse of computational materials science. However, the proper treatment of electronic exchange and correlation within the framework of DFT is a long-standing challenge [15]. Local density approximation (LDA) and generalized gradient (GGA) [14] functionals were developed to add exchange-correlation (XC) contributions to the energy functional within the Kohn–Sham (KS) formalism [13]. However, numerous studies have shown that these XC functionals have an associated self-interaction error (SIE) [15–17]. This shortcoming ultimately derives from the difficulty in quantifying exact exchange and correlation effects, without solving the many-body Schrödinger equation, using only density-based approximations.

The Hubbard functional is a corrective functional, in the sense that it involves adding a corrective term $E_{\text{Hub}} - E_{\text{dc}}$ on top of some base functional E_{DFT} (typically a local or semi-local functional), resulting in a total energy functional

$$\begin{aligned} E_{\text{DFT}+U+J}&\left[\rho, \left\{\boldsymbol{n}_\gamma^\sigma\right\}\right] \\ &= E_{\text{DFT}}\left[\rho\right] \\ &\quad + E_{\text{Hub}}\left[\left\{\boldsymbol{n}_\gamma^\sigma\right\}\right] - E_{\text{dc}}\left[\left\{n_\gamma^\sigma\right\}\right] \\ &= E_{\text{DFT}}\left[\rho\right] + E_{U/J}\left[\left\{\boldsymbol{n}_\gamma^\sigma\right\}\right] \end{aligned} \tag{1.12}$$

where E_{Hub} and E_{dc} are defined and discussed below. The $(\boldsymbol{n}_\gamma^\sigma)_{mm'} = \langle\varphi_{\gamma m}|\,\hat{\rho}^\sigma\,|\varphi_{\gamma m'}\rangle$ are matrices that represent the projection of the (spin-dependent) density operator onto Hubbard subspaces (indexed γ) defined by some set of orbitals $|\varphi_{\gamma m}\rangle$. These orbitals are typically atom-centred, fixed, spin-independent, localised, and orthonormal, often corresponding to the $3d$ or $4f$ subshell of a transition metal or lanthanide. The n_γ^σ occupation numbers are the corresponding traces of $\boldsymbol{n}_\gamma^\sigma$ matrices.

In the following paragraphs, we will provide a summary of some of the most well known formulations of DFT+U(+J). We note that because we are interested in the fully localized limit (FLL), we will not discuss extensions of DFT+U+J to metallic systems, where an "around mean field" (AFM) double-counting correction may be more appropriate [18].

Starting from DFT+U+J implementations of the highest complexity, and moving forward through increasing levels of simplification, we introduce the rotationally invariant implementation proposed by Liechtenstein et al. [19]. Within this flavor of DFT+U+J, E_{Hub} and E_{dc} take the following form

$$\begin{aligned} E_{\text{Hub}} = &\frac{1}{2}\sum_{\{m\},\gamma,\sigma}\langle m,m''|V_{ee}|m',m'''\rangle(n_\gamma^\sigma)_{mm'}(n_\gamma^{-\sigma})_{m''m'''} \\ &+\frac{1}{2}\sum_{\{m\},\gamma,\sigma}\left\{\langle m,m''|V_{ee}|m',m'''\rangle - \langle m,m''|V_{ee}|m''',m'\rangle\right\}(n_\gamma^\sigma)_{mm'}(n_\gamma^\sigma)_{m''m'''} \end{aligned} \tag{1.13}$$

$$E_{\text{dc}} = \sum_\gamma \frac{U_\gamma}{2} n_\gamma\left(n_\gamma - 1\right) + \sum_{\gamma,\sigma}\frac{J_\gamma}{2} n_\gamma^\sigma\left(n_\gamma^\sigma - 1\right), \tag{1.14}$$

where $\langle\cdot|V_{ee}|\cdot\rangle$ are the Coulomb integrals projected on the orbital basis, indicated by the associated $\{m\}$ set of quantum numbers [18–20]. This correction is parameterized by both Hubbard U_γ and Hund J_γ coupling constants through the double-counting energy contribution, E_{dc}.

As an aside, we note that it is possible to extend this formalism to non-collinear magnetism, which is essential for the inclusion of spin-orbit coupling (SOC). In this case the on-site occupation matrix acquires off-diagonal elements $(n_\gamma^{\sigma,\sigma'})_{mm'}$, in accordance with the

spinor extension of DFT, and DFT+U+J by extension [21–24]. Within this formalism, the notion of "up" and "down" spin electron densities is tied to the eigenvalues of the $n^{\sigma,\sigma'}$, and become $n^{\uparrow} = \frac{1}{2}\left(n + |\boldsymbol{m}|\right)$ and $n^{\downarrow} = \frac{1}{2}\left(n - |\boldsymbol{m}|\right)$, where $\boldsymbol{m} = [m_x\ m_y\ m_z]^T$ is the magnetization, on-site or otherwise [25]. Equations 1.13 and 1.14 still apply to the non-collinear case, provided $(n^{\sigma}_{\gamma})_{mm'}$ are obtained from a spin-diagonalization of $(n^{\sigma,\sigma'}_{\gamma})_{mm'}$.

Simplified versions of Equations 1.13 & 1.14 were proposed by Dudarev et al. [26], and later by Himmetoglu and coworkers [27], which approximate $\langle\cdot|V_{ee}|\cdot\rangle$ using Slater integrals, which can be parameterized through U and J values. There are many helpful explanations for this approximation, such as those summarized in Refs. [18, 20].

In the spirit of following increasing levels of simplification, we will start with the Himmetoglu implementation [27], inspired by the work of Solovyev et al. [28]. Using the Slater integral parameterization of U and J, it is possible to approximate and simplify $E_{U/J}$ from Equations 1.13 & 1.14 into the following

$$E_{U/J} = E_{\text{Hub}} - E_{\text{dc}} = \sum_{\gamma\sigma} \frac{U_\gamma - J_\gamma}{2} \text{Tr}\left[\boldsymbol{n}^{\sigma}_{\gamma}(1 - \boldsymbol{n}^{\sigma}_{\gamma})\right] + \sum_{\gamma\sigma} \frac{J_\gamma}{2} \text{Tr}\left[\boldsymbol{n}^{\sigma}_{\gamma}\boldsymbol{n}^{-\sigma}_{\gamma}\right]. \tag{1.15}$$

A well known further simplification of Equation 1.15, notwithstanding that it substantially pre-dated the latter, is the formulation of DFT+U_{eff} put forth by Dudarev et al. [26] and given by

$$E_U = E_{\text{Hub}} - E_{\text{dc}} = \sum_{\gamma\sigma} \frac{U^{\text{eff}}_{\gamma}}{2} \text{Tr}\left[\boldsymbol{n}^{\sigma}_{\gamma}(1 - \boldsymbol{n}^{\sigma}_{\gamma})\right]. \tag{1.16}$$

This approximation arises by assuming spherical symmetry of the Coulomb interactions, $\langle\cdot|V_{ee}|\cdot\rangle$ [18, 20, 27]. Within the simplified Dudarev DFT+U_{eff} of Equation 1.16, the effective Hubbard U becomes $U^{\text{eff}}_{\gamma} = U_\gamma - J_\gamma$ [18, 20, 26].

1.2.1.7 Hubbard U and Hund J spin polarized linear response

The DFT+U_{eff} correction of Equation 1.16 adds a convex energy penalty to fractional occupations of the orbitals that diagonalize $\mathbf{n}^{\sigma}_{\gamma}$, which can (in principle) counterbalance the SIE present in these Hubbard subspaces. In the linear-response approach, one measures the curvature in the total energy as a function of the subspace occupancy, and then chooses a value U to match the observed curvature. Naïvely computing this energy curvature as a function of the subspace occupancy would require a constrained DFT calculation, but one can recast the problem and instead measure the energy curvature with respect to the magnitude v_γ of an on-site perturbing potential $\hat{v}_\gamma = \sum_{mm'} v_\gamma \left|\varphi_{\gamma m}\right\rangle \left\langle\varphi_{\gamma m'}\right|$. The energy functional is then given by

$$E[\{v_\gamma\}] = \min_{\rho(\boldsymbol{r})} \left\{ E[\rho(\boldsymbol{r})] + \sum_{\gamma} v_\gamma n_\gamma \right\} \tag{1.17}$$

from which one computes the response matrices

$$\chi_{\gamma\gamma'} = \frac{\partial n_\gamma}{\partial v_{\gamma'}}. \tag{1.18}$$

Thus far we have used a general index "γ" to represent each site. Conventionally, this index refers purely to the atom γ on which the Hubbard site is centered. In this case, the Hubbard parameter for that subspace is given by

$$U_\gamma = \left(\chi_0^{-1} - \chi^{-1}\right)_{\gamma\gamma} \tag{1.19}$$

where χ and χ_0 are the interacting, (or self-consistent) and non-interacting (or non-self consistent) response matrices [16, 18]. We note that the sign of the response matrices in Equation 1.19 is consistent with the foundational linear response body of literature, such as in Ref. [16], however, they are defined as having opposite sign within VASP (Vienna ab initio Simulation Package) [29], which is used throughout this thesis.

The above strategy does not delineate between spin channels: during the linear-response calculations the spin-up and spin-down channels are perturbed simultaneously by the same amount, i.e., $v_\gamma^\uparrow = v_\gamma^\downarrow$ and we only observe the change in total occupancy $n_\gamma = n_\gamma^\uparrow + n_\gamma^\downarrow$. If we want to calculate J, one must instead consider the spin-dependent perturbation

$$\hat{v}_\gamma^\sigma = \begin{cases} +\sum_{mm'} v_\gamma \left|\varphi_{\gamma m}\right\rangle \left\langle\varphi_{\gamma m'}\right| & \sigma = \uparrow \\ -\sum_{mm'} v_\gamma \left|\varphi_{\gamma m}\right\rangle \left\langle\varphi_{\gamma m'}\right| & \sigma = \downarrow \end{cases} \tag{1.20}$$

and then construct a second set of response matrices which then relate to J in a completely parallel approach [30] to the calculation of U in Equation 1.19.

A separate but ultimately equivalent strategy is to treat the spin channels separately [17]. In this case a general index runs over both the atom index $\gamma = \{1, ..., N\}$ and also the two spin channels $\sigma = \{\uparrow, \downarrow\}$. In this case the response matrices of Equation 1.18 become rank-four tensors, i.e.,

$$\chi_{\gamma\gamma'}^{\sigma\sigma'} = \frac{\partial n_\gamma^\sigma}{\partial v_{\gamma'}^{\sigma'}}. \tag{1.21}$$

and now the equivalent of Equation 1.19 is

$$f_{\gamma\gamma}^{\sigma\sigma'} = \left(\chi_0^{-1} - \chi^{-1}\right)_{\gamma\gamma}^{\sigma\sigma'} \tag{1.22}$$

where now we must now prescribe how to map the 2×2 matrix $f_{\gamma\gamma}^{\sigma\sigma'}$ to the scalar parameters $U_\gamma = G_U(f_{\gamma\gamma}^{\sigma\sigma'})$ and $J_\gamma = G_J(f_{\gamma\gamma}^{\sigma\sigma'})$. Possible definitions for these mappings G_U and G_J are motivated and explored in detail in Ref. [17], but the end result is the following: there are two possible approaches. In the first approach one can define this mapping in order to recover the U_γ and J_γ that one would obtain using the conventional spin-agnostic approach

of Equations 1.19 and 1.20. In this approach, the spin moment is permitted to vary during a charge perturbation, and vice versa. We will hereafter refer to this as the "conventional" strategy (in the language of Ref. [17] this is the "scaled" approach). Throughout this work, unless otherwise stated, we will use the conventional strategy, which as the name suggests is the one that has been in almost universal use to date.

In the second approach, one defines the mapping to impose the condition that the local magnetic moment (local occupation) is held fixed during the perturbation while calculating the Hubbard (Hund) parameter, specifically by means of the equations rather than in the explicit sense of fixing these quantities using constrained DFT. We will refer to this as the "constrained" approach (the "simple" approach in Ref. [17]). This approach has recently been demonstrated to be the correct one for use with a DFT+U type functional "BLOR" explicitly designed to impose the flat-plane condition upon subspaces [31]. The spin-polarized linear response formalism permits us to compute the "constrained" approach U and J values simultaneously, at no additional cost.

1.2.1.8 Link Between Exchange Integral and Heisenberg Exchange Constants

The exchange integral in HF theory has a direct connection to the Heisenberg exchange constants J_{ij} used to describe magnetic interactions in the Heisenberg model. In both the quantum and classical Heisenberg models, the Hamiltonian for a system of spins is given by:

$$\mathcal{H} = -\sum_{\langle i,j \rangle} J_{ij} \mathbf{S}_i \cdot \mathbf{S}_j, \tag{1.23}$$

where J_{ij} represents the exchange interaction between spins at sites i and j.

The HF exchange integral can be related to J_{ij} by considering the energy contributions from spin-spin interactions [32]. Specifically, the exchange integral measures the energy gain due to the parallel alignment of electron spins, analogous to the exchange term in the Heisenberg Hamiltonian. Thus, J_{ij} can be interpreted as an effective exchange parameter derived from the HF exchange integrals, capturing the interaction strength between localized magnetic moments.

Furthermore, through the intuition of the Hubbard model and its extensions, the exchange constants can be directly related to Hubbard U and Hund J values [33]. However, we will not dive too deeply into these relationships here, because the meaning of $+U$ within DFT+U is distinct from its definition within the Hubbard model, as well as from hopping integrals [1].

1.2.1.9 Spin-Current Density Functional Theory

There are two primary approaches for incorporating magnetism in DFT. The first approach is spin density functional theory (SDFT), in which a functional is defined with respect to spin-up and spin-down electron densities, $\rho_\uparrow(\boldsymbol{r})$ and $\rho_\downarrow(\boldsymbol{r})$, respectively. The extension of SDFT to non-collinear magnetism motivates a spinor representation of the functional,

inspired by the Pauli matrix spin-1/2 formalism. Under this reformulation, functionals of $\rho_\uparrow(\boldsymbol{r})$ and $\rho_\downarrow(\boldsymbol{r})$ can be expressed in terms of total electron density $\rho(\boldsymbol{r}) = \rho_\uparrow(\boldsymbol{r}) + \rho_\downarrow(\boldsymbol{r})$, and magnetization, which in both collinear and non-collinear formulations obeys the relationship $|\boldsymbol{m}(\boldsymbol{r})| = |\rho_\uparrow(\boldsymbol{r}) - \rho_\downarrow(\boldsymbol{r})|$, under a local diagonalization of the spinor 2×2 representation [34]. Details on the connection between the spinor and density/magnetization formulation of non-collinear DFT is touched on in Equation 2.52, Equation 2.54, and Equation 2.55 in Section 2.2.2.4.

The second DFT formulation that incorporates non-collinear magnetism is current density functional theory (CDFT). This methodology is commonly used to incorporate electrodynamic effects in time-dependent density functional theory (TDDFT) [35, 36]. The "current" in CDFT conveys the reformulation of the functional of the ground state energy to be minimized with respect to the spin current density $\boldsymbol{j}_s(\boldsymbol{r}) \propto \nabla \times \boldsymbol{m}(\boldsymbol{r})$, rather than $\boldsymbol{m}(\boldsymbol{r})$, the magnetization field itself [37].

Several works have explored the theoretical justification for reformulating SDFT functionals within the CDFT setting [37–39]. In particular, Sharma and coauthors show through variational calculus that applying a divergence-free constraint to $\boldsymbol{B}_{xc}$ is equivalent to redefining the exchange correlation energy functional $E_{xc}[\rho, \boldsymbol{m}]$ in terms of $\nabla \times \boldsymbol{m}(\boldsymbol{r})$, $E_{xc}[\rho, \nabla \times \boldsymbol{m}]$, which is consistent with CDFT methodology [38].

In conventional SDFT, the exchange correlation local potential fields can be expressed as follows

$$\begin{aligned} v_{xc}(\boldsymbol{r}) &= \frac{1}{2}\left(v_{xc}^{\uparrow}(\boldsymbol{r}) + v_{xc}^{\downarrow}(\boldsymbol{r})\right) \\ \boldsymbol{B}_{xc}(\boldsymbol{r}) &= \frac{1}{2}\left(v_{xc}^{\uparrow}(\boldsymbol{r}) - v_{xc}^{\downarrow}(\boldsymbol{r})\right)\hat{\boldsymbol{m}}(\boldsymbol{r}), \end{aligned} \tag{1.24}$$

which are the complementary local potential fields for total electron density, ρ, and magnetization density, $\boldsymbol{m}$, respectively, and $\hat{\boldsymbol{m}}(\boldsymbol{r})$ is the unit vector in the direction of the magnetization.

Spin-current density functional theory (SCDFT) generalizes DFT to account for spin-dependent phenomena and spin currents [40, 41]. The basic variable in SCDFT are spin and probability currents, which we will explore in more detail in the Methods chapter. The Kohn-Sham equations in SCDFT are modified to include spin and current-dependent potentials:

$$\sum_\beta \left\{ \frac{1}{2m}\left(-i\hbar\nabla + \frac{e}{c}\boldsymbol{A}_{\text{eff}}(\boldsymbol{r})\right)^2 + V_{\text{eff}}(\boldsymbol{r}) \right\}_{\alpha\beta} \psi_\beta(\boldsymbol{r}) = \epsilon\psi_\alpha(\boldsymbol{r}) \tag{1.25}$$

where $\mathbf{A}_{\text{eff}}$ and V_{eff} are the effective magnetic vector and scalar potentials, respectively.

1.2.2 Physics-informed optimization

This section provides the theoretical background that inspired our algorithm `SpinPSO` for identifying noncollinear magnetic ground-states, with input from noncollinear DFT data.

1.2.2.1 Atomistic Spin Dynamics

Atomistic spin dynamics [42] is a theoretical framework applied towards modeling the time evolution of magnetic moments at the atomic scale. This method is particularly useful for studying the dynamic properties of magnetic materials, including their response to external fields, thermal fluctuations, and the effects of spin currents [42]. One of the key equations governing the dynamics of magnetic moments is the Landau-Lifshitz-Gilbert (LLG) equation, which can be extended to include stochastic terms to account for thermal fluctuations.

The LLG equation describes the precession and damping of a magnetic moment $\mathbf{S}_i$ under the influence of an effective magnetic field $\mathbf{B}_{\text{eff},i}$. The equation is given by [42, 43]:

$$\frac{d\mathbf{S}_i}{dt} = -\gamma \mathbf{S}_i \times \mathbf{B}_{\text{eff},i} - \frac{\gamma\lambda}{S}\mathbf{S}_i \times \left\{\mathbf{S}_i \times \mathbf{B}_{\text{eff},i}\right\}, \tag{1.26}$$

where γ is the gyromagnetic ratio, $\gamma\frac{\lambda}{S}$ is the Gilbert damping parameter, and S_i is the magnitude of the spin moment at site "i." The first term on the right-hand side represents the precession of the magnetic moment around the effective field, while the second term accounts for the damping that aligns the magnetic moment with the effective field.

To model the effects of thermal fluctuations, the LLG equation is extended to include a stochastic term, resulting in the stochastic Landau-Lifshitz-Gilbert (SLLG) equation. This term introduces random thermal fields that mimic the effect of temperature on the magnetic moments. The SLLG equation is written as [42, 43]:

$$\frac{d\mathbf{S}_i}{dt} = -\gamma \mathbf{S}_i \times \left(\mathbf{B}_{\text{eff},i} + \mathbf{B}_{\text{th},i}\right) - \frac{\gamma\lambda}{S}\mathbf{S}_i \times \left\{\mathbf{S}_i \times \left(\mathbf{B}_{\text{eff},i} + \mathbf{B}_{\text{th},i}\right)\right\}, \tag{1.27}$$

where $\mathbf{B}_{\text{th},i}$ is the thermal magnetic field, which is typically modeled as a Gaussian white noise with the following properties:

$$\langle \mathbf{B}_{\text{th},i}(t) \rangle = 0, \tag{1.28}$$

$$\langle B^{\mu}_{\text{th},i}(t) B^{\nu}_{\text{th},j}(t') \rangle = 2D\delta_{ij}\delta_{\mu\nu}\delta(t-t'), \tag{1.29}$$

$$D = \frac{\lambda}{1+\lambda^2}\frac{k_B T}{\gamma S} \tag{1.30}$$

where μ and ν denote the Cartesian components, k_B is the Boltzmann constant, T is the temperature, and δ represents the Dirac delta function.

1.2.2.2 Standard & Guaranteed Convergence PSO

The particle swarm optimization (PSO) method [44] is a multi-agent method where agents optimize a fitness function by moving based on their own knowledge (moving towards the best point that they have reached before) and the knowledge of the other agents in the "swarm" (moving towards some local or global optimum point). For the application of finding a ground-state by optimizing over structural and magnetic degrees of freedom, for

example, the fitness function is the potential energy function defining the potential energy surface (PES). Traditional PSO algorithms are gradient-free, which can result in a reduced cost compared to traditional optimization methods.

To identify local minima on the PES, we have employed a particle swarm optimization (PSO) algorithm. The general PSO algorithm can be described by the following dynamical relations:

$$v_{p,i}^{n+1} = av_{p,i}^{n} + a_{\text{cognition}} r_c \cdot (x_{p,i}^{n} - y_{p,i}) + a_{\text{social}} r_s \cdot (x_{p,i}^{n} - \hat{y}_i)$$
$$x_{p,i}^{n+1} = x_{p,i}^{n} + v_{p,i}^{n+1}$$

where $x_{p,i}^{n+1}$ and $v_{p,i}^{n+1}$ are the position and velocity of an agent p in dimension i, at the subsequent time-step. The first contribution to the velocity update includes an inertial term based on the velocity at the previous time-step (with $a < 1$ for stability). The second term includes a "cognition" term based on the previous "personal best" location of the agent $y_{p,i}$. The last addition to the velocity updates includes a "social" term that governs each agent's attraction to the best position of the swarm, $\hat{y}_{p,i}$. The cognitive and social terms are both weighted with uniformly distributed random numbers r_c and r_c between 0 and 1. These random numbers perturb the relative attraction between each contribution to the velocity, allowing each agent to sufficiently explore the possible pathways to a global optimum.

In order to increase the convergence capabilities of the minima finder, we have modified the conventional PSO algorithm to the guaranteed convergence particle swarm optimization (GCPSO) developed by Brits and Engelbrecht [45]. This algorithm can ensure convergence by introducing a random perturbation to the velocity of the agent in the subswarm that has the "best fitness" (with particle index = $*$):

$$v_{*,i}^{n+1} = -x_{*,i}^{n} + \hat{y}_i + av_{*,i}^{n} + \rho^{n+1} r_\rho, \quad \rho^{n+1} = \begin{cases} c\rho^n & \#\text{ of successes} > l_s \\ \frac{1}{c}\rho^n & \#\text{ of failures } > l_f \end{cases}$$
$$x_{*,i}^{n+1} = x_{*,i}^{n} + v_{*,i}^{n+1}$$

where r_ρ is a uniformly distributed random number between -1 and 1, and $c < 1$.

1.3 Brief outline of subsequent chapter

In the following Methods chapter, we will expand and develop upon the theory introduced in this chapter, towards the application of identifying the magnetic ground-state of magnetic materials using density functional theory. A brief outline is as follows:

- We discuss the implementation and benchmarking of a high-throughput algorithm for calculating Hubbard U and Hund J values using linear response.
- Next, we will delve into an exploration to a divergence-free constraint on the $\boldsymbol{B}_{xc}$, and the connections it lends between spin DFT and current DFT.

- Lastly, a custom physics-informed optimization algorithm, `SpinPSO`, is discussed, including its theoretical foundations and implementation as a workflow in `atomate` [46]. This algorithm uses energy and local field values from DFT, the results of which will strongly depend on the treatment of the first two initiatives.

Chapter 2

Methods

2.1 Density Functional Theory: DFT+U+J and Linear Response

Over the past couple of decades, DFT+U has found favor as a method that strikes a reasonable balance between accuracy and computational cost, making it particularly suitable for high-throughput computation [18, 47–50]. DFT+U functionals add a correction to the conventional XC functional to account for the Coulombic interaction between localized electrons [16, 51]. In more recent studies, various researchers have explored extensions of DFT+U with the goal of further correcting for static correlation effects and delocalization errors [20, 52, 53].

One drawback to DFT+U type functionals is that one must first determine its associated parameters, the Hubbard U and Hund J, and possibly also inter-site electronic interactions denoted as "+V" [54–56]. The results of a DFT+U calculation can quantitatively and even qualitatively change depending on these parameters, and so obtaining reliable values is of paramount importance. This is as true for the Hund J as it is for the Hubbard U, even in the simplified rotationally invariant DFT+U_{eff} functional [26]. In this particular functional, the Hubbard U and Hund J are grouped in single effective Hubbard parameter U_{eff}, defined as $U_{\text{eff}} = U - J$. This formalism assumes spherically symmetric on-site interactions, and results in a corrective term that only couples electrons of the same spin [18, 23, 26]. Nevertheless, the reduction in the effective parameter by J can be significant.

While the aforementioned approximation may seem more justifiable for systems with no magnetic order, in the case of magnetic systems it results in a lost opportunity to use the Hund J to beneficially enhance the spin moments in simulated broken-symmetry ground states. Moreover, when we move to non-collinear magnetism, the spin texture of materials is particularly sensitive to screening interactions between spin channels [21, 23, 24]. In fact, magnetic exchange constants can be derived from the extended Hubbard model, from which it is possible to relate exchange constants to ratios between U and J values [33]. The famous Hubbard model provides a simplified framework on which to explain the rich

physics of correlated transition metal compounds [33]. Additionally, it has been shown that the Hund J term is important for describing important physical phenomena, such as Jahn-Teller distortions [33, 57], emergent intra-atomic exchange, and the Kondo effect [58, 59]. Therefore, the introduction of explicit unlike-spin exchange corrections beyond simplified rotationally invariant DFT+U_{eff} is clearly of interest, and this requires the treatment of the Hund J on the same footing as the Hubbard U.

2.1.1 Strategies for determining Hubbard parameters

A common approach for determining Hubbard U values is to tune them such that some desired property — for example, the DFT+U_{eff} band gap, or a formation energy — matches its experimental value, or a value obtained via more accurate and computationally expensive beyond-DFT methods [60, 61]. There are several problems with this strategy. Firstly, it is not systematic: just because one result (e.g., the band gap) now matches experiment, this does not guarantee the same will be true for other observables (e.g., local magnetic moments). Indeed, there are a multitude of reasons why DFT may not match experiment, and can be problematic to rely on Hubbard corrections to correct for errors that do not arise from self-interaction [62]. Secondly, this strategy is not predictive: it relies on the existence of experimental/beyond-DFT data. This makes it particularly ill-suited to the prediction of novel materials and high-throughput studies.

Yet another difficulty that arises is the lack of transferability of Hubbard and Hund parameters. It has been repeatedly shown that these parameters are in fact very sensitive to the local chemical environment [63]. Even the specific pseudopotentials [17] or the specific site occupation projection scheme [64] have a significant effect on the computed Hubbard U values. The end result is that U values (and by extension Hund J values, which are albeit normally less environment-sensitive) are not transferable: they cannot be tabulated, and must always be determined on a case-by-case basis.

These issues can be overcome by calculating the Hubbard and Hund parameters from first principles. The two primary methods for doing so are the constrained random phase approximation (cRPA) [65, 66] and the linear response (LR) methods [16, 18]. In this study, we focus on the LR method due to its lower computational cost compared to existing cRPA methods, which are not yet appropriate for high-throughput applications.

The linear response method, as introduced by Cococcioni and coworkers [16], is founded on the idea that SIE can be related to the behaviour of the total energy as a function of the total occupation [67]. It is known that the total energy ought to be piece-wise linear with respect to total site occupation numbers in the dissociated limit [31], but in fact for semi-local DFT XC functionals, the energy is erroneously convex at fractional electron numbers. Cococcioni and co-workers illustrated that the $+U$ correction counteracts this erroneous curvature within local subspaces (the hope being that correcting local curvature will help address the erroneous global curvature [68]). Crucially, the magnitude of this curvature can be directly measured by a DFT linear response calculation, allowing the value of U to be determined accordingly. Unlike empirical fitting, this approach is (a) systematic, because

the value of U is derived directly as a measure of the underlying SIE present in the DFT calculation, and (b) it is predictive, because it only requires DFT calculations to extract the Hubbard parameters, and not experimental or beyond-DFT results.

2.1.2 Implementation of linear response within a high-throughput workflow

In this study, we implemented the linear response method as a workflow within the high-throughput `atomate` framework [46]. The workflow allows the user to compute Hubbard U and Hund J values using either a spin-polarized or a non-spin-polarized response. In addition to screening between spin channels, the implementation provides the straightforward extension to multiple levels of screening, including inter-site and inter-spin-channel responses [17]. A more detailed explanation of how these screening matrices are computed is provided in Section 2.1.3.

All of the individual DFT calculations within this workflow were performed with VASP (Vienna ab initio Simulation Package) [29], a plane-wave DFT code. The PBE exchange-correlation functional was used throughout as the base functional [69]. Unless otherwise stated we use PAW PBE pseudopotentials, which are the default pseudopotentials for the `pymatgen` input sets for VASP [70]. In this regard, our work supplements the high-throughput work of Bennett et al. [71] where ultrasoft pseudopotentials were used to reduce computational cost in high-throughput computations [71], mirroring early foundational studies on the linear response method [16, 54].

We have used an automatic k-point generation scheme that uses 50 k-points per reciprocal angstrom, and a cutoff energy of 520 eV. The full set of input parameters can be found in the `HubbardHundLinRespSet` in the `atomate` repository [72], and the derived VASP input sets in the `pymatgen` repository [70]. For the linear response analysis, the on-site applied potential $v_{I\sigma}$ range was from -0.2 eV to $+0.2$ eV (-0.05 eV to $+0.05$ eV for the periodic table data set) sampled at nine points at uniform intervals. In Section 2.1.5, we address the sensitivity of the linear response analysis to the truncated precision in VASP's occupation number I/O, which we observed for some TMO systems.

2.1.3 Screening matrix inversions

Below are the matrix representations of the response matrices at each level of response matrix inversion outlined by Linscott and others for a system with two Hubbard sites [17].

Point-wise 1×1 inversion:

$$\chi^{-1} = \begin{pmatrix} 1/\chi_{11} & 0 \\ 0 & 1/\chi_{22} \end{pmatrix} \tag{2.1}$$

Atom-wise (conventional) 2×2 inversion:

$$\chi^{-1} = \begin{pmatrix} \chi_{11} & \chi_{12} \\ \chi_{21} & \chi_{22} \end{pmatrix}^{-1} \tag{2.2}$$

We can extend this formalism to the multiple site (multi-site) responses by considering the response matrix for two sites, χ_{ij}, where i and j are the site indices.
Point-wise inversion:

$$\chi^{-1} = \begin{pmatrix} \begin{pmatrix} 1/\chi_{11}^{\uparrow\uparrow} & 0 \\ 0 & 1/\chi_{11}^{\downarrow\downarrow} \end{pmatrix} & 0 \\ 0 & \begin{pmatrix} 1/\chi_{22}^{\uparrow\uparrow} & 0 \\ 0 & 1/\chi_{22}^{\downarrow\downarrow} \end{pmatrix} \end{pmatrix} \tag{2.3}$$

Atom-wise (conventional) inversion:

$$\chi^{-1} = \begin{pmatrix} \begin{pmatrix} \chi_{11}^{\uparrow\uparrow} & \chi_{11}^{\uparrow\downarrow} \\ \chi_{11}^{\downarrow\uparrow} & \chi_{11}^{\downarrow\downarrow} \end{pmatrix}^{-1} & 0 \\ 0 & \begin{pmatrix} \chi_{22}^{\uparrow\uparrow} & \chi_{22}^{\uparrow\downarrow} \\ \chi_{22}^{\downarrow\uparrow} & \chi_{22}^{\downarrow\downarrow} \end{pmatrix}^{-1} \end{pmatrix} \tag{2.4}$$

Full inversion:

$$\chi^{-1} = \begin{pmatrix} \chi_{11}^{\uparrow\uparrow} & \chi_{11}^{\uparrow\downarrow} & \chi_{12}^{\uparrow\uparrow} & \chi_{12}^{\uparrow\downarrow} \\ \chi_{11}^{\downarrow\uparrow} & \chi_{11}^{\downarrow\downarrow} & \chi_{12}^{\downarrow\uparrow} & \chi_{12}^{\downarrow\downarrow} \\ \chi_{21}^{\uparrow\uparrow} & \chi_{21}^{\uparrow\downarrow} & \chi_{22}^{\uparrow\uparrow} & \chi_{22}^{\uparrow\downarrow} \\ \chi_{21}^{\downarrow\uparrow} & \chi_{21}^{\downarrow\downarrow} & \chi_{22}^{\downarrow\uparrow} & \chi_{22}^{\downarrow\downarrow} \end{pmatrix}^{-1} \tag{2.5}$$

We note that in the latter case, when performing a spin-polarize linear response calculation, one constructs a $2N \times 2N$ response matrix where N is the number of Hubbard sites (or $N \times N$ in the case of non-spin-polarized linear response). For bulk systems often several Hubbard sites will be equivalent, and one can save computational time by performing linear response calculations for the set of inequivalent sites, and then populating the response matrix for all equivalent Hubbard-site pairs.

2.1.4 Post-processing & uncertainty quantification

In order to extract the response matrices from the raw DFT data, curve fitting was performed using a least-squares polynomial fit implemented in `numpy` [73]. The uncertainty associated with each computed slope was obtained from the covariance matrix produced as a result of

the least-squares fit. These uncertainty values were then utilized to determine the errors associated with the Hubbard U and Hund J values. The error quantification was performed by computing the propagation of uncertainty based on the Jacobian of each scaling formula for Hubbard U and Hund J. This method for error propagation is general to multiple levels of screening between spin, site, and orbital responses.

We begin by considering the following screening matrix introduced in Equation 1.22, from which Hubbard U and Hund J values are derived [17]

$$f_{ij} = \left(\chi_0^{-1} - \chi^{-1}\right)_{ij}$$

Derivatives of the χ^{-1} matrix with respect to individual χ_{kl} can be obtained by the following relation:

$$\begin{aligned}
\frac{\partial}{\partial \chi_{kl}}\left(\chi^{-1}\right) &= -\chi^{-1}\left(\frac{\partial}{\partial \chi_{kl}}\chi\right)\chi^{-1} \\
&\text{where } \frac{\partial}{\partial \chi_{kl}}\left\{\chi\right\}_{ij} = \begin{cases} 1 & \text{if } kl = ij \\ 0 & \text{otherwise} \end{cases} \\
\frac{\partial}{\partial \chi_{kl}}\left\{\chi^{-1}\right\}_{ij} &= -\left\{\chi^{-1}\right\}_{ik}\left\{\chi^{-1}\right\}_{lj}
\end{aligned} \tag{2.6}$$

Using this fact, it is possible to obtain the full Jacobian of f with respect to response χ matrices which can be used to obtain the covariance uncertainty matrix associated with the elements of f_{ij}, to a first-order expansion of f_{ij} [74]

$$\boldsymbol{\Sigma}_f = \boldsymbol{J}_{\chi_0}\boldsymbol{\Sigma}_{\chi_0}\boldsymbol{J}_{\chi_0}^T + \boldsymbol{J}_{\chi}\boldsymbol{\Sigma}_{\chi}\boldsymbol{J}_{\chi}^T \tag{2.7}$$

where $\boldsymbol{\Sigma}_f$ is a $N^2 \times N^2$ matrix (f is $N \times N$). Each element of $\boldsymbol{\Sigma}_f$, $\left\{\Sigma_f\right\}_{ij,kl}$, corresponds to the covariance between f_{ij} and f_{kl} matrix elements. $\boldsymbol{\Sigma}_{\chi}$ and $\boldsymbol{\Sigma}_{\chi_0}$ are the covariance matrices for each $\{\chi\}_{kl}$ and $\{\chi_0\}_{kl}$, and the diagonal elements are populated using the squared uncertainty values associated with the slopes fit to the response data. In addition, $\boldsymbol{J}_{\chi}$ and $\boldsymbol{J}_{\chi_0}$ are the symbolically derived Jacobians corresponding to each response value, as proposed in Equation 2.6. Assuming that the individual elements of χ and χ_0 are independent, we can assume that $\boldsymbol{\Sigma}$ covariance matrices are diagonal in order to make the following simplification:

$$\begin{aligned}
\sigma^2(f_{ij}) = &\sum_{kl}\left(\frac{\partial}{\partial\left\{\chi_0\right\}_{kl}}f_{ij}\right)^2\sigma^2(\{\chi_0\}_{kl}) \\
&+\sum_{kl}\left(\frac{\partial}{\partial\left\{\chi\right\}_{kl}}f_{ij}\right)^2\sigma^2(\{\chi\}_{kl}),
\end{aligned} \tag{2.8}$$

where $\sigma^2(f_{ij})$, $\sigma^2(\{\chi_0\}_{ij})$, and $\sigma^2(\{\chi\}_{ij})$ correspond to the diagonal elements of $\boldsymbol{\Sigma}_f$, $\boldsymbol{\Sigma}_{\chi_0}$, and $\boldsymbol{\Sigma}_{\chi}$, respectively.

With the established expression for the uncertainty values of f in Equation 2.8, we can express the squared uncertainty of U, for an atomic site γ, in the next level of uncertainty propagation,

$$\sigma^2(U^\gamma) = \sum_{\sigma,\sigma'} \left(\frac{\partial}{\partial f_{\gamma\gamma}^{\sigma\sigma'}} G_U(f_{\gamma\gamma}) \right)^2 \sigma^2(f_{\gamma\gamma}^{\sigma\sigma'}). \tag{2.9}$$

Equation 2.9 can be extended to an expression of the squared uncertainty of Hund J, where G_U and G_J are functions of 2×2 sub-matrices along the diagonal of f, as introduced in Equation 1.22, and depend on the different scaling schemes introduced in Ref. [17]. The results of this error analysis are shown in Table 3.2.

2.1.5 VASP precision issue

We found that for some closed-shell systems, such as those containing Zn, the I/O precision of the occupation numbers in VASP had a significant effect on the resulting linear response analysis. This is because the change in occupation number on Zn-d states induced by the on-site potential was on the same order of magnitude as the precision cutoff itself. For this reason, we created a very basic patch to the VASP version 6.2.1 source code to increase the precision of occupation numbers and site magnetization written in the VASP `OUTCAR` file.

Using this higher precision, we found that the U and J calculated using linear response for Zn-d were 2.3±0.1 eV and 1.7±0.0 eV, respectively. This is in stark contrast to the original VASP code I/O precision, which wrongly produced U, $J = 0.0$ eV.

2.1.6 An exploration of inter-site Hubbard forces due to both $+U$ and $+V$ contributions

2.1.6.1 Including on-site forces due to $+V$, in addition to $+U$

The following is based on Section 4.1 of Chapter 4, by Matteo Cococcioni, of [15], "The LDA+U Approach: A Simple Hubbard Correction for Correlated Ground States." Our goal is to expand on Section 4.1 to include the $+V$ contributions to the Hubbard forces, in addition to $+U$, with the goal of providing a footing on which to compare the force contributions from $+U$ versus $+V$. The force acting on site α in spatial direction i due to the $+U+V$ correction can be expressed as

$$F_{\alpha,i}^{UV} = -\frac{\partial E_{UV}}{\partial \tau_{\alpha i}} = -\left(\frac{\partial E_U}{\partial \tau_{\alpha i}} + \frac{\partial E_V}{\partial \tau_{\alpha i}} \right), \tag{2.10}$$

where $\tau_{\alpha i}$ is the i^{th} component of the position vector corresponding to a site indexed by α. The partial derivatives can be expressed using the chain rule, following from Equation (20)

in [15]:

$$\frac{\partial E_U}{\partial \tau_{\alpha i}} = \sum_{\gamma,m,m',\sigma} \frac{\partial E_U}{\partial n^{\gamma\gamma\sigma}_{mm'}} \frac{\partial n^{\gamma\gamma\sigma}_{mm'}}{\partial \tau_{\alpha i}} \quad \text{and} \tag{2.11}$$

$$\frac{\partial E_V}{\partial \tau_{\alpha i}} = \sum_{\substack{\gamma,\gamma',m,m',\sigma \\ \gamma\neq\gamma'}} \frac{\partial E_V}{\partial n^{\gamma\gamma'\sigma}_{mm'}} \frac{\partial n^{\gamma\gamma'\sigma}_{mm'}}{\partial \tau_{\alpha i}}, \tag{2.12}$$

where the sum is over site indices γ & γ', m & m' quantum numbers, and σ spin channels. From the definition of E_{UV}, Equation (54) in [15], we can write derivatives of the $+U+V$ energy with respect to occupancy numbers

$$\frac{\partial E_U}{\partial n^{\gamma\gamma\sigma}_{mm'}} = u^{\gamma\gamma\sigma}_{mm'} = -\frac{U^\gamma}{2}\left(2n^{\gamma\gamma\sigma}_{m'm} - \delta_{m'm}\right) \quad \text{and} \tag{2.13}$$

$$\frac{\partial E_V}{\partial n^{\gamma\gamma'\sigma}_{mm'}} = v^{\gamma\gamma'\sigma}_{mm'} = -V^{\gamma'\gamma} n^{\gamma'\gamma\sigma}_{m'm}. \tag{2.14}$$

The occupancy numbers are defined as

$$n^{\gamma\gamma'\sigma}_{mm'} = \sum_{k,v} f^\sigma_{kv} \left\langle \psi^\sigma_{kv} | \phi^{\gamma'}_{m'} \right\rangle \left\langle \phi^\gamma_m | \psi^\sigma_{kv} \right\rangle . \tag{2.15}$$

in Equation (51) in [15]. The derivatives of occupancy numbers w.r.t. positions $\tau_{\alpha i}$, can be expressed as

$$\begin{aligned}
\frac{\partial n^{\gamma\gamma'\sigma}_{mm'}}{\partial \tau_{\alpha i}} &= \sum_{k,v} f^\sigma_{kv} \left[\frac{\partial}{\partial \tau_{\alpha i}} \left(\left\langle \psi^\sigma_{kv} | \phi^{\gamma'}_{m'} \right\rangle \right) \left\langle \phi^\gamma_m | \psi^\sigma_{kv} \right\rangle + \left\langle \psi^\sigma_{kv} | \phi^{\gamma'}_{m'} \right\rangle \frac{\partial}{\partial \tau_{\alpha i}} \left(\left\langle \phi^\gamma_m | \psi^\sigma_{kv} \right\rangle \right) \right] \\
&= \sum_{k,v} f^\sigma_{kv} \left[\delta_{\alpha\gamma'} \left\langle \psi^\sigma_{kv} | \phi^\gamma_m \right\rangle^* \frac{\partial}{\partial \tau_{\gamma' i}} \left(\left\langle \phi^{\gamma'}_{m'} | \psi^\sigma_{kv} \right\rangle^* \right) + \delta_{\alpha\gamma} \left\langle \psi^\sigma_{kv} | \phi^{\gamma'}_{m'} \right\rangle \frac{\partial}{\partial \tau_{\gamma i}} \left(\left\langle \phi^\gamma_m | \psi^\sigma_{kv} \right\rangle \right) \right] \\
&= \delta_{\alpha\gamma'} \left(\tilde{n}^{\gamma'\gamma\sigma}_{m'm} \right)^*_i + \delta_{\alpha\gamma} \left(\tilde{n}^{\gamma\gamma'\sigma}_{mm'} \right)_i .
\end{aligned} \tag{2.16}$$

Note the short-hands that we have defined so far for energy and occupancy partial derivatives in Eqns. 2.13, 2.14, and 2.16: $u^{\gamma\gamma\sigma}_{mm'}$, $v^{\gamma\gamma'\sigma}_{mm'}$, and $\left(\tilde{n}^{\gamma\gamma'\sigma}_{mm'}\right)_i$, respectively. The Kronecker deltas in front of each term is discussed following Equation (26) in [15], which also provides the relevant insight

> *"[T]he derivative of the atomic wave function is different from zero only in the case it is centered on the atom which is being displaced. Thus, the derivative in Eq.(23) only contributes to forces on atoms subject to the Hubbard correction. Finite off-site terms in the expression of the forces arise when using ultrasoft pseudopotentials."*

2.1.6.2 Bond forces for the one-dimensional binary lattice

Next, let us consider a simplified Hubbard chain of alternating α and β species, as illustrated in Figure 2.1. For the sake of simplicity, we are only considering next-nearest $V^{\alpha\beta}$ inter-site terms, but the following derivation can be easily extended to systems of higher complexity. For the force acting on an α-β bond, and therefore along the inter-site vector $\boldsymbol{\tau}_{\alpha\beta} = \boldsymbol{\tau}_\alpha - \boldsymbol{\tau}_\beta$,

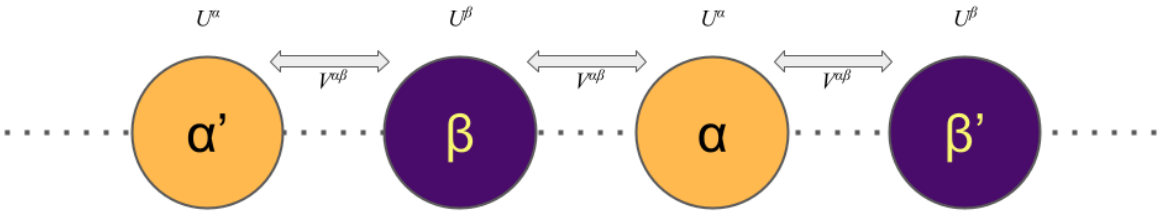

Figure 2.1: One-dimensional Hubbard chain of alternating α and β species. Only NN $V^{\alpha\beta}$ inter-site terms are considered for simplicity. The goal here is to provide a simplified picture of a binary TM-O system.

where $F_i\left(\boldsymbol{\tau}_\alpha - \boldsymbol{\tau}_\beta\right)$ corresponds to the i direction of the inter-site bond force between α and β, we have [1]

$$\begin{aligned} F_i^{UV}\left(\boldsymbol{\tau}_\alpha - \boldsymbol{\tau}_\beta\right) = -\frac{\partial E_{UV}}{\partial\left(\tau_{\alpha i} - \tau_{\beta i}\right)} &= -\frac{\partial E_{UV}}{\partial \tau_{\alpha i}} + \frac{\partial E_{UV}}{\partial \tau_{\beta i}} = F_{\alpha,i}^{UV} - F_{\beta,i}^{UV} \\ &= -\frac{\partial E_U}{\partial \tau_{\alpha i}} + \frac{\partial E_U}{\partial \tau_{\beta i}} - \frac{\partial E_V}{\partial \tau_{\alpha i}} + \frac{\partial E_V}{\partial \tau_{\beta i}}. \end{aligned} \tag{2.17}$$

[1] Here, we use $\nabla_{\boldsymbol{u}} f = \nabla f \cdot \boldsymbol{u}$, the expression of the directional gradient of a multivariate function f in the direction of $\boldsymbol{u}$, in terms of the gradient ∇f.

The individual contributions to these forces can be expressed as follows, calling on the derivatives that we have expressed in Eqn.'s 2.13, 2.14, and 2.16:

$$F^U_{\alpha,i} = -\sum_{m,m',\sigma} 2\Re\left\{u^{\alpha\alpha\sigma}_{mm'}\left(\tilde{n}^{\alpha\alpha\sigma}_{mm'}\right)_i\right\} \quad \text{and} \tag{2.18}$$

$$\begin{aligned} F^V_{\alpha,i} &= -\sum_{m,m',\sigma}\left[v^{\alpha\beta\sigma}_{mm'}\left(\tilde{n}^{\alpha\beta\sigma}_{mm'}\right)_i + v^{\beta\alpha\sigma}_{mm'}\left(\tilde{n}^{\alpha\beta\sigma}_{mm'}\right)^*_i\right] \\ &= -\sum_{m,m',\sigma} v^{\alpha\beta\sigma}_{mm'}\left[\left(\tilde{n}^{\alpha\beta\sigma}_{mm'}\right)_i + \left(\tilde{n}^{\alpha\beta\sigma}_{mm'}\right)^*_i\right] \\ &= -\sum_{m,m',\sigma} 2\Re\left\{v^{\alpha\beta\sigma}_{mm'}\left(\tilde{n}^{\alpha\beta\sigma}_{mm'}\right)_i\right\}. \end{aligned} \tag{2.19}$$

We have used the symmetry of the occupation numbers that can be shown following from Equation 2.15,

$$\begin{aligned} n^{\gamma\gamma'\sigma}_{mm'} &= \sum_{k,v} f^\sigma_{kv}\left\langle\psi^\sigma_{kv}|\phi^{\gamma'}_{m'}\right\rangle\left\langle\phi^\gamma_m|\psi^\sigma_{kv}\right\rangle = \sum_{k,v} f^\sigma_{kv}\left\langle\psi^\sigma_{kv}|\phi^\gamma_m\right\rangle^*\left\langle\phi^{\gamma'}_{m'}|\psi^\sigma_{kv}\right\rangle^* \\ &= \left\{\sum_{k,v} f^\sigma_{kv}\left\langle\psi^\sigma_{kv}|\phi^\gamma_m\right\rangle\left\langle\phi^{\gamma'}_{m'}|\psi^\sigma_{kv}\right\rangle\right\}^* = \left\{n^{\gamma'\gamma\sigma}_{m'm}\right\}^* = n^{\gamma'\gamma\sigma}_{m'm}, \end{aligned} \tag{2.20}$$

where the last step was justified on the grounds that occupation numbers must be real. This symmetry holds for $v^{\gamma\gamma'\sigma}_{mm'}$, in accordance with Equation 2.14, which permits the factorization in Equations 2.19 & 2.22.

Next, we can write the bond force terms as follows[2]:

$$F^U_i\left(\boldsymbol{\tau}_\alpha - \boldsymbol{\tau}_\beta\right) = F^U_{\alpha,i} - F^U_{\beta,i} = -2\Re\left\{\sum_{m,m',\sigma}\left[u^{\alpha\alpha\sigma}_{mm'}\left(\tilde{n}^{\alpha\alpha\sigma}_{mm'}\right)_i - u^{\beta\beta\sigma}_{mm'}\left(\tilde{n}^{\beta\beta\sigma}_{mm'}\right)_i\right]\right\}. \tag{2.21}$$

$$\begin{aligned} F^V_i\left(\boldsymbol{\tau}_\alpha - \boldsymbol{\tau}_\beta\right) = F^V_{\alpha,i} - F^V_{\beta,i} &= -2\Re\left\{\sum_{m,m',\sigma}\left[v^{\alpha\beta\sigma}_{mm'}\left(\tilde{n}^{\alpha\beta\sigma}_{mm'}\right)_i - v^{\beta\alpha\sigma}_{mm'}\left(\tilde{n}^{\beta\alpha\sigma}_{mm'}\right)_i\right]\right\} \\ &= -2\Re\left\{\sum_{m,m',\sigma} v^{\alpha\beta\sigma}_{mm'}\left[\left(\tilde{n}^{\alpha\beta\sigma}_{mm'}\right)_i - \left(\tilde{n}^{\beta\alpha\sigma}_{mm'}\right)_i\right]\right\}. \end{aligned} \tag{2.22}$$

At this point, it is helpful to keep in mind that $u^{\alpha\alpha\sigma}_{mm'} \propto U^\alpha$, $u^{\beta\beta\sigma}_{mm'} \propto U^\beta$, and $v^{\alpha\beta\sigma}_{mm'} \propto V^{\alpha\beta}$ from Eqs. 2.13 & 2.14. We see that while the contribution to the force from $V^{\alpha\beta}$ is only

[2]The reader may notice that in F^V_i terms, the contributions from α' and β' sites are neglected, as shown in Figure 2.1. These would intuitively "tug on" the corresponding β and α sites in the opposite direction.

dependent on the difference between $\tilde{n}$ occupation number derivatives, the contribution from U values depends additionally on the relative magnitude of U^{α} and U^{β}.

This is not to say that the former is insignificant, but rather that both $+U$ (to both species) and $+V$ contributions should be accounted for if one is interested in correcting for α-β bond length. It is common practice to add a correction to d and f-block species alone ("α" sites). Adding a U value to O-p sites ("β"), if large enough, could possibly reverse the sign of $F_i^U\left(\boldsymbol{\tau}_{\alpha} - \boldsymbol{\tau}_{\beta}\right)$. This could explain the improved bond lengths after adding $+U$ corrections to O-p sites, and not solely to TM-d and f sites.

Based on TMO test cases in this study, and the results of other studies [17, 54], it appears that applying a U to TM sites only overestimates the TM-O bond-length. Furthermore, both (a) adding a +U to the O-p manifold [17] and (b) +V between TM and O sites [54] appears to reduce the severity of this overestimation. This leads us to assume that starting from the DFT (no $+U/J/V$) optimized structure, $F_{\alpha}^U < 0$ (tensile) and $F_{\beta}^U < 0$ (compressive), where it's still the case that $|F_{\alpha}^U| > |F_{\beta}^U|$ (tensile), because the bond lengths are still overestimated with +U(O-p). Finally, we may asssume that $F_{\alpha}^V - F_{\beta}^V > 0$ (compressive), on the basis that Campo et al. appear have found that $+V$ helped correct for TM-O bond length in NiO [54].

2.2 Spin-Current DFT (SCDFT) and the Source-Free (SF) Exchange Correlation (XC) Functional

It is a well-known physical fact that Maxwell's equations preclude the existence of unphysical magnetic monopoles. It is less conventional to apply this divergence-free constraint to density functional theory functionals for *ab initio* calculations. It has recently been a topic of exploration to apply this constraint to the exchange correlation component of the effective internal magnetic field, $\boldsymbol{B}_{xc}$ [37, 75]. Previous studies have shown that applying this physically inspired constraint to $\boldsymbol{B}_{xc}$ results in improved agreement with the majority of a small test set of over twenty experimentally measured magnetic structures, both in terms of magnetic moment magnitudes [37] and non-collinear ground states [75], which can be challenging to accurately match experiment with conventional DFT approaches.

The source-free constraint is applied by projecting the original exchange-correlation magnetic field onto a divergence-free field. Consistent with the work of Sharma and others, we use the fundamental theorem of vector calculus, the Helmholtz identity, to reformulate our equations in terms of vector and scalar fields. This theorem states that any once differentiable, $\mathcal{C}^1$, vector field can be decomposed into a divergence free and a curl free component,

$$\boldsymbol{B}(\boldsymbol{r}) = -\nabla\phi(\boldsymbol{r}) + \nabla \times \boldsymbol{A}(\boldsymbol{r}) + \overline{\boldsymbol{B}} \tag{2.23}$$

where ϕ is a scalar field, and $\boldsymbol{A}$ is a vector potential field. The identity is conveniently written in this way due to two important mathematical properties: the curl of a gradient is zero everywhere in the domain $\nabla \times \nabla\phi = 0$ and likewise for the divergence of the curl of a vector field $\nabla \cdot (\nabla \times \boldsymbol{A}) = 0$. For a magnetic field $\boldsymbol{B}$, such that $\nabla \cdot \boldsymbol{B} = 0$, we can define $\boldsymbol{B} = \nabla \times \boldsymbol{A}$, where $\boldsymbol{A}$ is the well-known magnetic vector potential.

One may ask why we include a constant $\overline{\boldsymbol{B}}$, which is not included in most statements of the Helmholtz identity. This comes down to the fact that under periodic boundary conditions,

$$\int_\Omega d\boldsymbol{r}\ \nabla\phi(\boldsymbol{r}) = \boldsymbol{0} \tag{2.24}$$

$$\int_\Omega d\boldsymbol{r}\ \nabla \times \boldsymbol{A}(\boldsymbol{r}) = \boldsymbol{0} \tag{2.25}$$

by Equations 2.43 & 2.44 in Section 2.2.2.2. Therefore, we must include a constant term, such that $\int_\Omega d\boldsymbol{r}\ \boldsymbol{B}(\boldsymbol{r})$ need not be the zero vector.

By taking the divergence of both sides of Equation (2.23), we see that, for the exchange-correlation magnetic field,

$$\nabla \cdot \boldsymbol{B}_{xc} = -\nabla \cdot (\nabla\phi) = -\nabla^2\phi. \tag{2.26}$$

Therefore, solving for ϕ requires the solution to the Poisson equation above, which is the method suggested by Sharma et al. for applying the source-free constraint [37]. It is interesting to note that $\boldsymbol{B}'_{xc}(\boldsymbol{r})$ must be non-collinear, as we show in Section 2.2.3.2.

Equation (2.23) can be employed rigorously, because while the Helmholtz decomposition is not unique, it can be under the correct constraints. The uniqueness of the gradient of the solution to the Poisson equation (e.g. $\nabla\phi$) can be used to prove this. In summary, each field in Equation (2.23) can be uniquely solved for under periodic boundary conditions (PBCs), as follows

1. The curl-free term:

$$\nabla^2\phi = -\nabla \cdot \boldsymbol{B}_{xc}. \tag{2.27}$$

   Therefore, $\nabla\phi$ is unique under PBCs.

2. The divergence-free term:

$$\nabla^2\boldsymbol{A}_{xc} = -\nabla \times \boldsymbol{B}_{xc}, \tag{2.28}$$

   subject to the Coulomb gauge constraint, $\nabla \cdot \boldsymbol{A}_{xc} = 0$ (see Appendix 2.2.2.5). Under this constraint, $\nabla A_{xc,i}$ are unique under PBCs.

3. The constant term:

$$\overline{\boldsymbol{B}}_{xc} = \frac{1}{V_\Omega}\int_\Omega d\boldsymbol{r}\ \boldsymbol{B}_{xc}(\boldsymbol{r}). \tag{2.29}$$

Therefore, in order to compute $\boldsymbol{B}'_{xc}$, the source-free projection of $\boldsymbol{B}_{xc}$, one simply needs to compute $\nabla\phi$

$$\begin{aligned}\boldsymbol{B}'_{xc}(\boldsymbol{r}) &= \boldsymbol{B}_{xc}(\boldsymbol{r}) + \nabla\phi(\boldsymbol{r}) \\ &= \boldsymbol{B}_{xc}(\boldsymbol{r}) + \boldsymbol{H}_{xc}(\boldsymbol{r}) \\ &= \nabla \times \boldsymbol{A}_{xc}(\boldsymbol{r}) + \overline{\boldsymbol{B}}_{xc}\end{aligned} \tag{2.30}$$

In other words, we leave $\overline{\boldsymbol{B}}_{xc}$ untouched from SDFT, to be consistent with Ref. [37]. In Sections 4.2.6 & 2.2.1, we explore the justifications and implications of this, and lay some potential groundwork for future studies to employ in a more careful treatment of the constant term, $\overline{\boldsymbol{B}'}_{xc}$. In a concrete sense, we explore the role of $\overline{\boldsymbol{B}'}_{xc}$ on the converged magnetic ground states in Section 4.2.6.

2.2.1 Source-free implementation

In Section 2.2.1.1, we provide the details of the source-free $\boldsymbol{B}_{xc}$ implementation in VASP [29], which, generally speaking, should be consistent with both References [37] & [76]. As stated in Equation (2.37), we do not modify the $\boldsymbol{q} = \boldsymbol{0}$ component of $\boldsymbol{B}'_{xc}$. In other words, we set $\widehat{\boldsymbol{B}'}_{xc}(\boldsymbol{q} = \boldsymbol{0}) = \widehat{\boldsymbol{B}}_{xc}(\boldsymbol{q} = \boldsymbol{0})$, which still satisfies the divergence-free constraint. Our choice appears to be consistent with the implementation of Ref. [37] in the `Elk` source code [77, 78].

Our justification for leaving $\overline{\boldsymbol{B}'}_{xc} = \overline{\boldsymbol{B}}_{xc}$ is the arbitrary choice of $\widehat{\boldsymbol{B}'}_{xc}(\boldsymbol{q})$, which is apparent from the singularity with respect to $|\boldsymbol{q}|^2$ in Equation (2.37). However, one can entertain possible physically motivated constraints on $\overline{\boldsymbol{B}'}_{xc}$. For example, $\overline{\boldsymbol{B}'}_{xc}$ will enter into the net torque expression, Equation (2.74). Therefore, one may consider a least-squares constraint on $\overline{\boldsymbol{B}'}_{xc}$, based on the ZTT, as well as a possible term that preserves the net XC energy expression from SDFT. An in-depth and rigorous treatment of $\overline{\boldsymbol{B}'}_{xc}$, the real-space integral of $\boldsymbol{B}'_{xc}$, will be left to future studies.

2.2.1.1 Numerical details of source-free constraint

Because plane-wave DFT is defined on periodic boundary conditions, we can start with the definition of the inverse discrete Fourier transform, because the density fields lie in regular three-dimensional grids,

$$\begin{aligned} \phi_{\boldsymbol{n}} &= \frac{1}{M} \sum_{\boldsymbol{k}} \widehat{\phi}_{\boldsymbol{k}} \exp\left(i 2\pi \boldsymbol{k}^T D^{-1} \boldsymbol{n} \right) \\ &= \mathcal{F}^{-1} \widehat{\phi} \end{aligned} \tag{2.31}$$

$$\text{where } D = \begin{pmatrix} N_x & 0 & 0 \\ 0 & N_y & 0 \\ 0 & 0 & N_z \end{pmatrix}, \text{ and } M = N_x N_y N_z$$

where $n_i, k_i \in [0, 1, ..., N_i]$, and N_x, N_y, N_z are the dimensions of the 3D grid. If we define the real-space position vector as $\boldsymbol{r} = LD^{-1}\boldsymbol{n}$, where L has columns as lattice vectors $L = [\boldsymbol{a}\ \boldsymbol{b}\ \boldsymbol{c}]$. Therefore, $\boldsymbol{k}^T D^{-1} \boldsymbol{n} = \boldsymbol{k}^T D^{-1} D L^{-1} \boldsymbol{r} = \boldsymbol{k}^T L^{-1} \boldsymbol{r}$. From here, we can apply the convenient "scaling" property describing how differential operators commute with the inverse discrete

Fourier transform, where $l = x, y, z$ is the dimension of the partial derivative,

$$\frac{\partial}{\partial r_l}\phi(\boldsymbol{r}) \approx i2\pi \cdot \mathcal{F}^{-1}\left(q_l \widehat{\phi}\right) \tag{2.32}$$
$$\text{where } q_l = \sum_j L^{-1}_{jl} k_j, \quad \boldsymbol{q} = L^{-T}\boldsymbol{k}$$

To obtain the (discrete) spectral approximation of the divergence of the $\boldsymbol{B}$ field:

$$\begin{aligned}\nabla \cdot \boldsymbol{B}_{xc} &= \frac{\partial B_x}{\partial x} + \frac{\partial B_y}{\partial y} + \frac{\partial B_z}{\partial z} \\ &\approx i2\pi \cdot \mathcal{F}^{-1}\left(q_x \widehat{B}_x + q_y \widehat{B}_y + q_z \widehat{B}_z\right) \\ &\approx i2\pi \cdot \mathcal{F}^{-1}\left(\boldsymbol{q}^T \widehat{\boldsymbol{B}}_{xc}\right)\end{aligned} \tag{2.33}$$

In order to solve the Poisson equation, as posed in Equation (2.26), we apply a similar reasoning as before, and see that

$$\begin{aligned}\nabla^2\phi &= \frac{\partial^2\phi}{\partial x^2} + \frac{\partial^2\phi}{\partial y^2} + \frac{\partial^2\phi}{\partial z^2} \\ &\approx -(2\pi)^2 \cdot \mathcal{F}^{-1}\left((q_x^2 + q_y^2 + q_z^2)\widehat{\phi}\right) \\ &\approx -(2\pi)^2 \cdot \mathcal{F}^{-1}\left(|\boldsymbol{q}|^2 \widehat{\phi}\right)\end{aligned} \tag{2.34}$$

Therefore, combining Equations (2.26), (2.33) and (2.34), we find that the discrete Fourier transform of ϕ can be expressed as

$$\widehat{\phi}(\boldsymbol{q}) = \begin{cases} \frac{i}{2\pi}\frac{\boldsymbol{q}\cdot\widehat{\boldsymbol{B}}_{xc}(\boldsymbol{q})}{|\boldsymbol{q}|^2}, & |\boldsymbol{q}| \neq 0 \\ 0, & |\boldsymbol{q}| = 0 \end{cases} \tag{2.35}$$

We are interested in $\nabla\phi$. Which we can approximate as

$$-\nabla\phi \approx \mathcal{F}^{-1}\left(\frac{\boldsymbol{q}^T \widehat{\boldsymbol{B}}_{xc}(\boldsymbol{q})}{|\boldsymbol{q}|^2}\boldsymbol{q}\right) \tag{2.36}$$

Therefore, the source-free correction is achieved by performing the following

$$\widehat{\boldsymbol{B}'}_{xc}(\boldsymbol{q}) = \widehat{\boldsymbol{B}}_{xc}(\boldsymbol{q}) - \begin{cases} \frac{\boldsymbol{q}\cdot\widehat{\boldsymbol{B}}_{xc}(\boldsymbol{q})}{|\boldsymbol{q}|^2}\boldsymbol{q}, & |\boldsymbol{q}| \neq 0 \\ 0, & |\boldsymbol{q}| = 0 \end{cases} \tag{2.37}$$

and as a result, $\nabla \cdot \boldsymbol{B}_{xc}{}' = 0$ is obtained in the discrete numerical sense.

2.2.1.2 Hubbard U, Hund J and neglect of the exchange splitting parameter

In our implementation of the source-free correction [79], we leave out the exchange-splitting scaling parameter s included in the study of Sharma and coworkers. In other words, $s = 1$ in our implementation. There are two primary reasons that we neglected this scaling parameters. The first reason for not including this parameter, is that while s is not material-specific in theory, it requires fitting to the magnetic structure of a finite set of material systems. In addition to this ambiguity, it has been shown that Hubbard U and Hund J values have a significant effect on the magnitude of magnetic moments, as well as non-collinear magnetic structure [75]. For this reason, we utilize pre-computed, and/or custom-computed, U and J values for the magnetic systems that we explore in this study.

That is not to say that the inclusion of s is unjustified – its inclusion maintains the variational nature of the XC functional with respect to the magnetization field, $\boldsymbol{m}$ [37]. However, we choose to not include this feature, due to its ambiguous nature, and the fact that it has nothing to do with the source-free constraint itself [3]. In our implementation and test cases, we did not find a need for $s \neq 1$.

2.2.2 Leveraging connections between SF XC functional and SCDFT

2.2.2.1 The comparative degeneracies of E_{xc} for SDFT versus CDFT with respect to $\boldsymbol{m}$

Capelle and Gross (CG) show that within SDFT, the exchange-correlation energy, E_{xc} only depends on the magnetization via the "spin vorticity" [38]

$$\boldsymbol{\nu}_s(\boldsymbol{r}) = \nabla \times \left(\frac{\boldsymbol{j}_s(\boldsymbol{r})}{\rho} \right) = \frac{c}{q} \nabla \times \left(\frac{\nabla \times \boldsymbol{m}(\boldsymbol{r})}{\rho(\boldsymbol{r})} \right), \tag{2.38}$$

where c and q are the speed of light and elementary charge, respectively. Therefore, transformations of the magnetization density, $\boldsymbol{m}(\boldsymbol{r}) \mapsto \boldsymbol{m}'(\boldsymbol{r})$, of the form

$$\begin{aligned} \boldsymbol{m}'(\boldsymbol{r}) &= \boldsymbol{m}(\boldsymbol{r}) + \nabla\alpha(\boldsymbol{r}) + \boldsymbol{\Gamma}(\boldsymbol{r}) \\ \text{where } \nabla \times \boldsymbol{\Gamma}(\boldsymbol{r}) &= \rho(\boldsymbol{r}) \nabla\gamma(\boldsymbol{r}) \end{aligned} \tag{2.39}$$

will have no effect on XC contributions to the SDFT functional, E_{xc}^S, i.e. $E_{xc}^S[\rho, \boldsymbol{m}'] = E_{xc}^S[\rho, \boldsymbol{m}]$. $\alpha(\boldsymbol{r})$ and $\boldsymbol{\Gamma}(\boldsymbol{r})$ are arbitrary functions, which are only subject to the relevant aforementioned constraints.

By comparison, in CDFT, E_{xc}^C depends on $\boldsymbol{m}$ via the spin current, $\boldsymbol{j}_s = \frac{c}{q} \nabla \times \boldsymbol{m}$ [37, 38]. Therefore, E_{xc}^C is invariant to transformations of the form, $\boldsymbol{m}(\boldsymbol{r}) \mapsto \boldsymbol{m}'(\boldsymbol{r})$,

$$\boldsymbol{m}'(\boldsymbol{r}) = \boldsymbol{m}(\boldsymbol{r}) + \nabla\alpha(\boldsymbol{r}), \tag{2.40}$$

[3] After all, Sharma et al. describe the s scaling as an "additional modification" to the XC functional [37]. This was further confirmed in conversation with S. Sharma and J. K. Dewhurst.

for arbitrary $\nabla\alpha(\boldsymbol{r})$. Therefore, $\boldsymbol{\Gamma}(\boldsymbol{r})$ of the form in Equation (2.39) provides the additional degree of freedom that introduces ambiguity into the non-collinear magnetic ground state obtained using SDFT compared with CDFT.

Again, we emphasize that the functions α, $\boldsymbol{\Gamma}$, and γ are all completely arbitrary, and have been introduced to illustrate the gauge invariance of non-collinear SDFT [38]. The high number of degrees of freedom associated with $\boldsymbol{\Gamma}(\boldsymbol{r})$ provides an explanation for the highly degenerate energy landscape in non-collinear SDFT. The additional gauge invariance explains why the site-projected magnetic moments – related to $\boldsymbol{m}$ – rotate very little during convergence, compared with the source-free functional, which is in fact a current density functional, to reiterate [37, 38]. This is the core computational exploration of the present study.

2.2.2.2 Vanishing integrals under periodic boundary conditions

We can see by the fundamental theorem of calculus, that the following integral is zero under periodic boundary conditions (PBCs) on a grid of dimensions $L_x \times L_y \times L_z$

$$\begin{aligned}\int_\Omega \frac{\partial\phi}{\partial x_i}\, d\boldsymbol{r} &= \int_0^{L_j} \prod_{j\neq i} dx_j \int_0^{L_i} dx_i \, \frac{\partial\phi}{\partial x_i} \\ &= \int_0^{L_j} \prod_{j\neq i} dx_j \, \left[\phi(x_i = L_i, ..., x_{j\neq i}) - \phi(x_i = 0, ..., x_{j\neq i})\right] \\ &= 0, \end{aligned} \tag{2.41}$$

because $\phi(x_i = L_i, ..., x_{j\neq i}) = \phi(x_i = 0, ..., x_{j\neq i})$ by the definition of PBCs. From Equation 2.41, it is straightforward to show that the following integrals are also zero under PBCs:

$$\int_\Omega \nabla \cdot \boldsymbol{L}\, d\boldsymbol{r} = 0 \tag{2.42}$$

$$\int_\Omega \nabla\phi\, d\boldsymbol{r} = \boldsymbol{0} \tag{2.43}$$

$$\int_\Omega \nabla \times \boldsymbol{L}\, d\boldsymbol{r} = \boldsymbol{0}. \tag{2.44}$$

2.2.2.3 Consideration of additional currents arising in CDFT

Within the framework of current density functional theory (CDFT), we can introduce the probability (denoted with subscript p) current density [38, 41]. The classical field of the probability current, (also known as the "paramagnetic current") can be expressed as the

expectation of the quantum mechanical operator

$$\begin{aligned}\boldsymbol{j}_p(\boldsymbol{r}) &= \left\langle \hat{\boldsymbol{j}}_p(\boldsymbol{r}) \right\rangle \\ &= \frac{\hbar}{2mi}\left\langle \hat{\Psi}(\boldsymbol{r})^\dagger \nabla \hat{\Psi}(\boldsymbol{r}) - \nabla \hat{\Psi}(\boldsymbol{r})^\dagger \hat{\Psi}(\boldsymbol{r}) \right\rangle \\ &= \frac{\hbar}{2m}\left\langle \Im\left(\hat{\Psi}(\boldsymbol{r})^\dagger \nabla \hat{\Psi}(\boldsymbol{r}) \right) \right\rangle . \end{aligned} \tag{2.45}$$

The probability current can be motivated by expressing the Schrödinger equation as a conservation law, $\partial\rho/\partial t = \nabla \cdot \boldsymbol{j}_p$ [80]. Therefore, $\boldsymbol{j}_p$ is directly related to the probability flux of an electron in real space. It is also known as the "paramagnetic current," because $\boldsymbol{j}_p$ couples in a Zeeman-like manner to the external vector potential in a similar fashion to Equation (2.50). Therefore, the magnetization induced by $\boldsymbol{j}_p$ will preferentially align with the external magnetic field.

Capelle and Gross explore the form of $\boldsymbol{j}_p$ within Kohn-Sham (KS) SDFT [38],

$$\boldsymbol{j}_p^{KS} = \frac{i\hbar}{2m}\sum_{k=1}^{N}\left(\phi_k \nabla \phi_k^* - \phi_k^* \nabla \phi_k\right), \tag{2.46}$$

where ϕ_k are Kohn-Sham orbitals, and the sum is over the N lowest-energy bands. $\hbar$ is the familiar reduced Planck constant, and m is the electron mass. Any complex function, and therefore ϕ_k, can be expressed as $\phi_k(\boldsymbol{r}) = |\phi_k(\boldsymbol{r})|e^{iS_k'(\boldsymbol{r})}$. Letting $S_k(\boldsymbol{r}) = \hbar S_k'(\boldsymbol{r})$, it is possible to show that [80]

$$\boldsymbol{j}_p^{KS}(\boldsymbol{r}) = \sum_{k}^{N}\frac{1}{m}\left|\phi_k(\boldsymbol{r})\right|^2 \nabla S_k(\boldsymbol{r}). \tag{2.47}$$

Next, we consider the case in which all ∇S_k are equal to the same function, ∇S. In this case, the following simplification can be made

$$\widetilde{\boldsymbol{j}}_p^{KS}(\boldsymbol{r}) = \frac{1}{m}\rho(\boldsymbol{r})\nabla S(\boldsymbol{r}). \tag{2.48}$$

We have drawn on the fact that $\rho(\boldsymbol{r}) = \sum_k^N \left|\phi_k(\boldsymbol{r})\right|^2$, and are reminded that ∇S is linked to classical momentum [80]. Therefore, $\boldsymbol{j}_p^{KS}(\boldsymbol{r}) = \widetilde{\boldsymbol{j}}_p^{KS}(\boldsymbol{r})$ only in the case when these ∇S_k momenta are equal across all ground state KS orbitals, $\phi_k(\boldsymbol{r})$.

In their original seminal work, Vignale and Rasolt (VR) consider the physical constraint that the current density functional should be invariant to gauge transformations of the external magnetic vector potential $\boldsymbol{A}' \mapsto \boldsymbol{A} + \nabla\Lambda$, where $\Lambda(\boldsymbol{r})$ is an arbitrary function [81]. Under this gauge invariance constraint, VR demonstrate that E_{xc} depends on $\boldsymbol{j}_p$ through the probability/paramagnetic current vorticity alone, which is defined as such [81]

$$\boldsymbol{\nu}_p(\boldsymbol{r}) = \nabla \times \left[\frac{\boldsymbol{j}_p(\boldsymbol{r})}{\rho(\boldsymbol{r})}\right]. \tag{2.49}$$

This result is a foundational pillar of CDFT, and provides a basis for useful results in other key works, such as Ref. [38].

Interestingly, in the hypothetical case in which $\boldsymbol{j}_p^{KS}(\boldsymbol{r}) = \widetilde{\boldsymbol{j}}_p^{KS}(\boldsymbol{r})$ (Equation (2.48)) we see that $\boldsymbol{\nu}_p(\boldsymbol{r}) = \boldsymbol{0}$ everywhere, and therefore we may neglect any $\boldsymbol{j}_p$ contributions to E_{xc} entirely. However, this is not the case for differing ∇S_k. We presume that, among other effects, the inhomogeneity across ground state ∇S_k is accentuated by spin-orbit coupling (SOC) [82], which will introduce an angular-momentum dependence on ϕ_k. This hypothesis can most likely be further explored by the machinery proposed in Ref. [83], which provides a framework for rigorously incorporating SOC within SCDFT. However, on a more elementary level, even a non-interacting homogeneous electron gas will obey Fermi statistics. Therefore the electron gas will possess a distribution of momenta, which can be directly related to single-electron ∇S_k [80, 84].

Under no external magnetic field, i.e. a curl-free $\boldsymbol{A}$, $\boldsymbol{j}_p$ enters into the exchange-correlation component of the CDFT functional in the following form [38, 41, 81],

$$E_p \equiv -\int_\Omega \boldsymbol{j}_p(\boldsymbol{r}) \cdot \boldsymbol{A}_{xc}(\boldsymbol{r})\, d\boldsymbol{r}. \tag{2.50}$$

In VR's extension of SCDFT to non-collinear magnetism, a set of spin-projected currents, $\boldsymbol{j}_{p,\lambda}$, and their associated $\boldsymbol{A}_{xc,\lambda}$ are introduced as additional quantities. As we will see later, $\boldsymbol{j}_{p,\lambda}$ play a crucial role in the extension of the zero torque theorem, Equation (2.78). Furthermore, in Ref. [83], Bencheikh demonstrates that $\boldsymbol{A}_{xc,\lambda}$ become essential in the inclusion of SOC effects in SCDFT. However, because SOC is treated differently in VASP [82], we will not explore this further here.

The probability current, $\boldsymbol{j}_p$, has been introduced as the gauge-invariant kinetic energy density in the metaGGA extension of SCDFT [35, 85]. Following from Ref. [85],

$$\tilde{\tau}_\sigma = \tau_\sigma - m\frac{\left|\boldsymbol{j}_{p,\sigma}\right|^2}{\rho_\sigma} \tag{2.51}$$

where σ denotes the different spin channels, $\sigma \in \{\uparrow, \downarrow\}$. Starting from the definitions of VR [86], it is straightforward to show that the squared magnitude of the spin probability currents $\left|\boldsymbol{j}_{p,\sigma}\right|^2$ in Equation (2.51) can be related to $\left|\boldsymbol{j}_{p,\lambda}\right|^2$, which we explore in Section 2.2.2.4. Therefore, we hope it to be the subject of future studies to explore the extensions of this work to metaGGA functionals.

Furthermore, in Appendix 2.2.2.7, we abstract from the definition in Equation (2.45), and consider a separation of $\boldsymbol{j}_{p,\lambda}$ into divergence and curl-free contributions. We provide these small derivations to the reader in the hope that may be useful for the reformulation of SDFT metaGGA functionals to their SCDFT counterparts.

2.2.2.4 Expressing kinetic energy contributions in terms of projected spin currents

It has been established in Ref. [86] that the density and spin current matrices within SCDFT are related via the following relations

$$\rho_{\alpha\beta}(\boldsymbol{r}) = \rho(\boldsymbol{r})\delta_{\alpha\beta} + \sum_{\lambda=1}^{3} s_\lambda(\boldsymbol{r})\sigma^\lambda_{\alpha\beta} \tag{2.52}$$

$$\boldsymbol{j}_{p,\alpha\beta}(\boldsymbol{r}) = \boldsymbol{j}_p(\boldsymbol{r})\delta_{\alpha\beta} + \sum_{\lambda=1}^{3} \boldsymbol{j}_{p,\lambda}(\boldsymbol{r})\sigma^\lambda_{\alpha\beta}. \tag{2.53}$$

From Ref. [41], $\hat{s}$ denotes the "direction of the local spin polarization," from which it is possible to define a set of variables projected along spin orientation

$$|\boldsymbol{s}(\boldsymbol{r})| = \left(\sum_\lambda s_\lambda(\boldsymbol{r})^2\right)^{1/2} \tag{2.54}$$

$$\rho_{\pm\hat{\boldsymbol{s}}}(\boldsymbol{r}) = \frac{1}{2}\left(\rho(\boldsymbol{r}) \pm |\boldsymbol{s}(\boldsymbol{r})|\right) \tag{2.55}$$

$$\boldsymbol{j}_{p\pm\hat{\boldsymbol{s}}}(\boldsymbol{r}) = \frac{1}{2}\left(\boldsymbol{j}_p(\boldsymbol{r}) \pm \boldsymbol{j}_{p\|}(\boldsymbol{r})\right) \tag{2.56}$$

$$\boldsymbol{j}_{p\|}(\boldsymbol{r}) = \sum_{\lambda=1}^{3} \boldsymbol{j}_{p\lambda}(\boldsymbol{r}) s_\lambda(\boldsymbol{r})/|\boldsymbol{s}(\boldsymbol{r})| \tag{2.57}$$

where $\boldsymbol{j}_{p\|}(\boldsymbol{r})$ is the "longitudinal (in spin-space) current." Armed with these definitions, it is straightforward to show that

$$\left|\boldsymbol{j}_{p,\uparrow}\right|^2 + \left|\boldsymbol{j}_{p,\downarrow}\right|^2 = \frac{1}{2}\left|\boldsymbol{j}_p\right|^2 + \frac{1}{2}\sum_\lambda \left|\boldsymbol{j}_{p,\lambda}\right|^2 \tag{2.58}$$

Therefore, we can express the relationship between current contributions to kinetic energy densities (Equation 2.51) as

$$\frac{\rho_\uparrow}{\rho}\overline{\tau}_\uparrow + \frac{\rho_\downarrow}{\rho}\overline{\tau}_\downarrow = \frac{1}{2}\left\{\overline{\tau} + \sum_\lambda \frac{\rho_\lambda}{\rho}\overline{\tau}_\lambda\right\}, \tag{2.59}$$

where $\overline{\tau}_\mu = -m\left|\boldsymbol{j}_{p,\mu}\right|^2/\rho_\mu$.

2.2.2.5 Choice of $\boldsymbol{A}_{xc}$ gauge

It is worth noting that two gauge choices of $\boldsymbol{A}_{xc}$ have been presented in the literature. Within the original works of Vignale and Rasolt [41, 81, 86], the $\nabla\cdot(\rho\boldsymbol{A}_{xc}) = 0$ arises naturally.

However, by comparison, in [38], the Coulomb gauge $\nabla \cdot \boldsymbol{A}_{xc} = 0$ is implied by the Helmholtz decomposition.

Under the $\nabla \cdot \boldsymbol{A}_{xc} = 0$ gauge, it is possible to solve for $\boldsymbol{A}_{xc}$ using the following Poisson equation,

$$\begin{aligned} \nabla \times (\nabla \times \boldsymbol{A}_{xc}) &= \nabla \times \boldsymbol{B}_{xc} \\ -\nabla^2 \boldsymbol{A}_{xc} + \nabla (\nabla \cdot \boldsymbol{A}_{xc}) &= \nabla \times \boldsymbol{B}_{xc} \\ \nabla^2 \boldsymbol{A}_{xc} &= -\nabla \times \boldsymbol{B}_{xc} \end{aligned} \tag{2.60}$$

In order to solve for $\boldsymbol{A}_{xc}$ subject to $\nabla \cdot (\rho \boldsymbol{A}_{xc}) = 0$, we can employ another Helmholtz decomposition

$$\boldsymbol{A}_{xc} = \boldsymbol{A}'_{xc} + \nabla \xi \tag{2.61}$$

where $\nabla \cdot \boldsymbol{A}'_{xc} = 0$ and is solved using Equation (2.60), and ξ is determined from the following elliptical equation

$$\nabla \cdot (\rho \nabla \xi) = -\nabla \cdot \left(\rho \boldsymbol{A}'_{xc}\right). \tag{2.62}$$

However, the spatial dependence of ρ in Equation (2.62) makes the equation more difficult to solve using a single spectral solve step. Instead, an iterative spectral solver could be used to solve this elliptical equation, using the subtractive solver presented in Ref. [87], for example.

2.2.2.6 Considerations for $\boldsymbol{j}_p \cdot \boldsymbol{A}_{xc}$ energy contributions under periodic boundary conditions

We will use the following result, Equation (2.63), to draw a few conclusions. Let's start by considering two differentiable functions $\alpha(\boldsymbol{r}) \in \mathbb{R}$ and $\boldsymbol{L}(\boldsymbol{r}) \in \mathbb{R}^3$. The following integral can be expressed as

$$\begin{aligned} &\int_\Omega \nabla \alpha(\boldsymbol{r}) \cdot \boldsymbol{L}(\boldsymbol{r}) \, d\boldsymbol{r} \\ &= \int_\Omega \left\{ \nabla \cdot \left[\alpha(\boldsymbol{r}) \boldsymbol{L}(\boldsymbol{r})\right] - \alpha(\boldsymbol{r}) \left[\nabla \cdot \boldsymbol{L}(\boldsymbol{r})\right] \right\} \, d\boldsymbol{r} \\ &= \oint_{\partial\Omega} \left[\alpha(\boldsymbol{r}) \boldsymbol{L}(\boldsymbol{r})\right] \cdot d\boldsymbol{S} - \int_\Omega \alpha(\boldsymbol{r}) \left[\nabla \cdot \boldsymbol{L}(\boldsymbol{r})\right] \, d\boldsymbol{r} \end{aligned} \tag{2.63}$$

If Ω obeys periodic boundary conditions, then $\oint_{\partial\Omega} \left[\alpha(\boldsymbol{r}) \boldsymbol{L}(\boldsymbol{r})\right] \cdot d\boldsymbol{S} = 0$.

We can start by considering the Coulomb gauge $\nabla \cdot \boldsymbol{A}_{xc} = 0$. If this gauge is chosen, charge conservation should still be obeyed through the following

$$\nabla \cdot \left(\boldsymbol{j}_p + \rho \boldsymbol{A}_{xc}\right) = 0 \tag{2.64}$$

By the Helmholtz identity, we can decompose $\boldsymbol{j}_p$ into the following

$$\boldsymbol{j}_p = \nabla\eta + \nabla \times \boldsymbol{\Gamma}. \tag{2.65}$$

Therefore, we may rewrite Equation (2.64) as

$$\nabla^2\eta = -\nabla \cdot (\rho \boldsymbol{A}_{xc}) \tag{2.66}$$

Here, it is interesting to note that while η can satisfy charge conservation, by Equation (2.63), under periodic boundary conditions and the $\nabla \cdot \boldsymbol{A}_{xc} = 0$ gauge, the following is true

$$\int_\Omega \nabla\eta \cdot \boldsymbol{A}_{xc}\, d\boldsymbol{r} = 0. \tag{2.67}$$

Therefore, η will not enter into the energy term, Equation (2.50), allowing us to conclude that

$$E_p\big|_{\nabla\cdot\boldsymbol{A}_{xc}=0} = \int_\Omega (\nabla \times \boldsymbol{\Gamma}) \cdot \boldsymbol{A}_{xc}\, d\boldsymbol{r} \quad \forall \left\{\boldsymbol{j}_p,\ \boldsymbol{A}_{xc}|_{\nabla\cdot\boldsymbol{A}_{xc}=0}\right\}. \tag{2.68}$$

Equation (2.68) states that while the curl-free projection of $\boldsymbol{j}_p$, $\nabla\eta$, maintains local charge conservation, only the divergence-free projection, $\nabla \times \boldsymbol{\Gamma}$, enters into the expression for E_p.

2.2.2.7 Considerations for $\boldsymbol{j}_{p,\lambda}$

Starting from a Helmholtz decomposition of the probability current density

$$\boldsymbol{j}_{p,\lambda} = \nabla\eta_\lambda + \nabla \times \boldsymbol{\Gamma}_\lambda \tag{2.69}$$

We see that the following conservation law

$$\nabla \cdot \left[\boldsymbol{j}_{p,\lambda} + m_\lambda \boldsymbol{A}_{xc}\right] = (\boldsymbol{m} \times \boldsymbol{B}_{xc})_\lambda \tag{2.70}$$

only places a constraint on the curl-free contribution to $\boldsymbol{j}_{p,\lambda}$, similarly to Equation (2.66),

$$\nabla^2\eta_\lambda = -\nabla \cdot [m_\lambda \boldsymbol{A}_{xc}] + (\boldsymbol{m} \times \boldsymbol{B}_{xc})_\lambda. \tag{2.71}$$

Therefore, only the divergence-free component, $\nabla\times\boldsymbol{\Gamma}_\lambda$, is independent from this conservation law, and will contribute to the energy in an analogous form of Equation (2.68).

2.2.2.8 Orbital magnetic moments

Having explored the connections to CDFT, we will now turn our attention to the orbital magnetic moments, which are a measurable link to the orbital current density, $\boldsymbol{j}_{\text{orb}}$. The orbital character of the magnetic moment can be teased out using x-ray magnetic circular dichroism (XMCD) [88, 89], and sometimes in combination with other x-ray spectroscopy techniques, such as Resonant Inelastic X-ray Scattering (RIXS) [89].

It is possible to express the orbital magnetic moment in terms of the orbital current [90]

$$\boldsymbol{m}_i^{\text{orb}} = \int_{\Omega_i} \boldsymbol{r}_i \times \boldsymbol{j}_{\text{orb}}(\boldsymbol{r}_i)\ d\boldsymbol{r}_i, \tag{2.72}$$

where Ω_i is a region surrounding the magnetic site i, such as a PAW sphere, and $\boldsymbol{r}_i$ is the position vector relative to the center of the sphere. The orbital magnetic moment is directly associated with the expectation value of the orbital angular momentum at an atomic site. Consequently, the magnitude and direction of the orbital moment relative to the spin moment can be influenced by factors such as Hund's rules, crystal field splitting (CFS), and spin-orbit coupling (SOC) [84]. SOC primarily determines the orientation of the orbital moment, while CFS can significantly reduce or quench the orbital moment, a phenomenon particularly notable in $3d$ transition metal species [84]. In contrast, CFS has a lesser impact on the orbital moments in uranium and other f-block elements, as the partially filled f-states are more effectively shielded from crystal fields by outermost electrons [84]. We will explore the effect of the source-free constraint on the ground state orbital moments in the UO_2 test case explored in Section 4.2.4.

2.2.3 Zero torque theorem and $\boldsymbol{\tau}_{xc}$

Within full magnetostatic spin-current DFT (SCDFT), additional spin currents arise subject to the following continuity equation

$$\nabla \cdot \left[\boldsymbol{j}_{p,\lambda} + m_\lambda \boldsymbol{A}_{xc}\right] = \left(\boldsymbol{m} \times \boldsymbol{B}_{xc}\right)_\lambda \tag{2.73}$$

where $\lambda = 1, 2, 3$ and corresponds to the three components of the non-collinear magnetic fields. Some SCDFT formulations include additional $\boldsymbol{A}_{xc,\lambda}$ fields as well [86]. Equation (2.73) is an extension of the zero torque theorem (ZTT), in which local torques may arise without violating conservation laws.

The magnetic torque due to the XC component of the functional can be expressed as $\boldsymbol{\tau}_{xc} = \boldsymbol{m} \times \boldsymbol{B}_{xc}$ [91]. We call on the definition of $\boldsymbol{B}_{xc}$ in Equation (1.24), as defined in conventional SDFT, to show that $\boldsymbol{\tau}_{xc} = \boldsymbol{m} \times \boldsymbol{B}_{xc} = \boldsymbol{0}$. This is simply due to the fact that $\boldsymbol{B}_{xc} \parallel \boldsymbol{m}$ everywhere in Ω (the periodic domain) at every self-consistency step. The zero magnetic torque theorem [91],

$$\int_\Omega \boldsymbol{\tau}_{xc}\ d\boldsymbol{r} = \int_\Omega \boldsymbol{m} \times \boldsymbol{B}_{xc}\ d\boldsymbol{r} = \boldsymbol{0} \tag{2.74}$$

states that "a system cannot exert a net torque on itself." Since $\boldsymbol{\tau}_{xc} = \boldsymbol{m} \times \boldsymbol{B}_{xc} = \boldsymbol{0}$ then Equation (2.74) is trivially satisfied at every step of the DFT minimization algorithm.

By comparison, within the source-free implementation, local torques may arise [37], in which case, from Equation (2.30) we see that

$$\begin{aligned}\boldsymbol{\tau}'_{xc} &= \boldsymbol{m} \times \boldsymbol{B}'_{xc} \\ &= \boldsymbol{m} \times \boldsymbol{B}_{xc} + \boldsymbol{m} \times \boldsymbol{H}_{xc} \\ &= \boldsymbol{m} \times \nabla\phi \\ &= \phi(\nabla \times \boldsymbol{m}) - \nabla \times (\phi\boldsymbol{m}).\end{aligned} \tag{2.75}$$

Under periodic boundary conditions on Ω, we may show that

$$\begin{aligned}\int_\Omega \boldsymbol{\tau}'_{xc}\, d\boldsymbol{r} &= \int_\Omega \boldsymbol{\tau}_{xc}\, d\boldsymbol{r} + \int_\Omega \boldsymbol{m} \times \boldsymbol{\nabla}\phi\, d\boldsymbol{r} \\ &= \int_\Omega \phi\,(\nabla \times \boldsymbol{m})\; d\boldsymbol{r}.\end{aligned} \tag{2.76}$$

Again, we have used the property that the surface integral vanishes under periodic boundary conditions, $\int_\Omega d\boldsymbol{r}\ \nabla \times (\phi\boldsymbol{m}) = \boldsymbol{0}$, via Equation 2.44 provided in Section 2.2.2.2. It is not apparent why Equation (2.76) should be zero, and therefore why ZTT should be obeyed for the source-free functional. From Equation (2.76), it is clear that the net XC torque possesses the same gauge invariance of E_{xc}^C (Equation (2.40)), and therefore it cannot be eliminated via the addition of a gradient field to $\boldsymbol{m}$. In Section 4.2.5, we explore the adherence to the ZTT computationally, and possible ways to maintain the zero torque condition in Appendix 2.2.3.1.

Several previous studies have sought to address adherence to the ZTT with various proposed XC non-collinear functionals. For example, in Ref. [92], the authors rigorously explore the dependence of $\boldsymbol{B}_{xc}$ on $\boldsymbol{m}$ that would result in satisfying the ZTT for all $\boldsymbol{m}$. Additionally, Ref. [91] proposed a way to maintain the zero global torque constraint in Section III of their Supplemental Material. While their approach is promising, the method that we propose in Appendix 2.2.3.1 leverages the convenient property that volume integrals of derivatives disappear under PBCs. Therefore, in comparison to Ref. [91], we are able to ensure that

1. The resultant $\boldsymbol{B'}_{xc}$ is indeed source-free, i.e. $\nabla \cdot \boldsymbol{B'}_{xc} = 0$, by solving for the auxiliary vector potential, $\boldsymbol{A'}$, rather than the magnetic field itself.

2. Our least-squares solution only requires solving 3 linear equations, whereas Ref. [91] requires solving $3P - 3$ linear equations, where P is the size of the real-space grid [91].

3. We treat all points on the real-space grid on the same footing. In other words, we do not solve for the field to maintain ZTT on "boundary" grid points separately from the bulk, as proposed in Ref. [91]. In our setting of PBCs, there is no notion of "edge" versus "bulk" to begin with.

We emphasize again that our proposal to maintain the ZTT in Appendix 2.2.3.1 is not currently implemented in our VASP code patch. We hope that this will be the subject of subsequent studies.

All this being said, ZTT may not be a strict constraint on the spin-current density functional. We see this by starting from Equation 33 of Ref. [83], which is also Equation 6.10b of Ref. [86],

$$\begin{aligned}\nabla \cdot \boldsymbol{j}_{p,\lambda} + \frac{2}{\hbar}\nabla \cdot (m_\lambda \boldsymbol{A}_{xc}) + \frac{q}{mc}\nabla \cdot \left(\rho \boldsymbol{A}_{xc,\lambda}\right) \\ = -\frac{2}{\hbar}\left[\boldsymbol{m} \times \boldsymbol{B}_{xc}\right]_\lambda + \frac{2q}{\hbar c}\sum_{\mu,\nu}\epsilon_{\lambda\mu\nu}\boldsymbol{j}_{p,\nu} \cdot \boldsymbol{A}_{xc,\mu}.\end{aligned} \tag{2.77}$$

where $\boldsymbol{j}_{p,\lambda}$ are defined in Section 2.2.2.4, and $\frac{q}{c}\boldsymbol{A}_{xc,\lambda} = \delta E_{xc}/\delta \boldsymbol{j}_{p,\lambda}$. Additionally, $\epsilon_{\lambda\mu\nu}$ is the Levi-Civita symbol. In the spirit of Ref. [92], we see that by taking the integral of both sides, and imposing periodic boundary conditions on the region of integration Ω, we arrive at

$$\int_\Omega d\boldsymbol{r}\ \left[\boldsymbol{m} \times \boldsymbol{B}_{xc}\right]_\lambda = \frac{q}{c}\int_\Omega d\boldsymbol{r}\ \sum_{\mu,\nu}\epsilon_{\lambda\mu\nu}\ \boldsymbol{j}_{p,\nu} \cdot \boldsymbol{A}_{xc,\mu}. \tag{2.78}$$

There is no reason for the right hand side of this equation to be zero. Therefore, the above continuity equation provides an extension of the "zero torque theorem." In other words, in order to satisfy the steady state conservation law, it is no longer necessary for the net torque to be zero, i.e. $\int_\Omega d\boldsymbol{r}\ \boldsymbol{m} \times \boldsymbol{B}_{xc} = \boldsymbol{0}$ need not be obeyed.

2.2.3.1 A general approach to satisfy the zero torque theorem

Our goal is to solve for an auxillary field $\boldsymbol{A}'$ such that the zero torque condition is obeyed

$$\int_\Omega d\boldsymbol{r}\ \boldsymbol{m} \times \boldsymbol{B} = \int_\Omega d\boldsymbol{r}\ \boldsymbol{m} \times (\nabla\phi + \nabla \times \boldsymbol{A}') = \boldsymbol{0}. \tag{2.79}$$

The trivial solution, $\nabla \times \boldsymbol{A}' = -\nabla\phi$, can only hold if $\nabla\phi = \boldsymbol{0}$. Therefore, we recast the problem as such

$$\int_\Omega d\boldsymbol{r}\ \boldsymbol{m} \times (\nabla \times \boldsymbol{A}') = -\int_\Omega d\boldsymbol{r}\ \boldsymbol{m} \times \nabla\phi = -\boldsymbol{\tau}'. \tag{2.80}$$

By expanding the triple product, we see that

$$\begin{aligned}\boldsymbol{m} \times (\nabla \times \boldsymbol{A}') &= \left[m_j\partial_i {A'}_j - m_j\partial_j {A'}_i\right]\hat{\boldsymbol{e}}_i \\ &= \nabla_{\boldsymbol{A}'}(\boldsymbol{m} \cdot \boldsymbol{A}') - (\boldsymbol{m} \cdot \nabla)\boldsymbol{A}'.\end{aligned} \tag{2.81}$$

At this step, we can apply the product rule, $u\partial_x v = \partial_x(uv) - v\partial_x u$, to show that integrals of the form $\int d\boldsymbol{r}\ \partial_x(uv)$ vanish under periodic boundary conditions (PBCs) by Equation 2.43.

Having leveraged this convenient property of the PBCs, it is possible to transfer the derivatives from $\boldsymbol{A}'$ to $\boldsymbol{m}$ such that we can restate Equation (2.80) as

$$\begin{aligned}&\int d\boldsymbol{r}\ \boldsymbol{m} \times (\nabla \times \boldsymbol{A}') \\ &\quad = \int d\boldsymbol{r}\ \left[A'_i \partial_j m_j - A'_j \partial_i m_j\right] \hat{\boldsymbol{e}}_i = -\boldsymbol{\tau}'\end{aligned} \tag{2.82}$$

Now, we will introduce the following discretized approximation for the L^2 inner product on regular grids

$$\langle u, v \rangle = \int_\Omega d\boldsymbol{r}\ u(\boldsymbol{r}) v(\boldsymbol{r}) \approx \frac{1}{\Delta V} \boldsymbol{u}^T \boldsymbol{v}, \tag{2.83}$$

where $\Delta V = \Delta x \Delta y \Delta z$. We introduce this shorthand for the purposes of this study, however, it is just as applicable to continuous functions. With this definition, we can recast the problem in Equation (2.82) as a matrix-vector system

$$M\boldsymbol{a} = -\boldsymbol{\tau}', \tag{2.84}$$

where $\boldsymbol{a} = \left[\boldsymbol{A}'^T_x\ \boldsymbol{A}'^T_y\ \boldsymbol{A}'^T_z\right]^T$, and the matrix M is defined as

$$M = \frac{1}{\Delta V} \begin{bmatrix} \boldsymbol{m}^T_{y,y} + \boldsymbol{m}^T_{z,z} & -\boldsymbol{m}^T_{y,x} & -\boldsymbol{m}^T_{z,x} \\ -\boldsymbol{m}^T_{x,y} & \boldsymbol{m}^T_{z,z} + \boldsymbol{m}^T_{x,x} & -\boldsymbol{m}^T_{z,y} \\ -\boldsymbol{m}^T_{x,z} & -\boldsymbol{m}^T_{y,z} & \boldsymbol{m}^T_{x,x} + \boldsymbol{m}^T_{y,y} \end{bmatrix}, \tag{2.85}$$

in which case $\boldsymbol{m}_{i,j} = \frac{\partial \boldsymbol{m}_i}{\partial x_j}$. Because the system of equations is underdetermined (i.e. M is "short and fat"), we can can solve for $\boldsymbol{a}$ using a least-squares approach,

$$\boldsymbol{a} = -M^+ \boldsymbol{\tau}', \tag{2.86}$$

which solves for the solution $\boldsymbol{a}$ with minimal L^2 norm,

$$||\boldsymbol{a}||_2 = \left\{ \sum_{i=x,y,z} \int_\Omega d\boldsymbol{r}\ |\boldsymbol{A}'_i(\boldsymbol{r})|^2 \right\}^{1/2}. \tag{2.87}$$

M^+ is the correspanding Moore-Penrose right-hand pseudoinverse $M^+ = M^T \left(MM^T\right)^{-1}$ such that $MM^+ = I$, as long as the rows of M are linearly independent. We note that MM^T is diagonally dominant, because it contains L^2 norms (which are guaranteed to be positive) of the spatial partial derivatives of $\boldsymbol{m}$ along the diagonal. Therefore, MM^T should be invertible, so long as the magnetization varies in all spatial directions over the domain, which it should for spin-polarized systems.

In conclusion, by applying both source-free and ZTT corrections to the exchange-correlation magnetic field, $\boldsymbol{B}_{xc}$,

$$\begin{aligned} \boldsymbol{B}_{xc} &\mapsto \boldsymbol{B}'_{xc} \\ \boldsymbol{B}'_{xc} &= \boldsymbol{B}_{xc} + \nabla\phi + \nabla \times \boldsymbol{A}' \end{aligned} \tag{2.88}$$

we can simultaneously satisfy

I. The source free constraint:

$$\nabla \cdot \boldsymbol{B}'_{xc} = 0$$

II. The zero torque theorem:

$$\int_{\Omega} d\boldsymbol{r}\ \boldsymbol{m} \times \boldsymbol{B}'_{xc} = \boldsymbol{0}.$$

However, we should stress that the second ZTT constraint is not implemented in the code at present. In other words, we set $\boldsymbol{A}'(\boldsymbol{r}) = \boldsymbol{0}$ in the context of this study.

2.2.3.2 Noncollinear nature of $\boldsymbol{B}_{xc}$

The source-free constraint forces the resultant $\boldsymbol{B}_{xc}$ to be noncollinear, and therefore this constrained functional is not applicable to collinear magnetic functionals. To illustrate this, consider the example where we define the magnetic field vector field $\boldsymbol{B}_{xc}(\boldsymbol{r})$ over $\mathbb{R}^3$. If we only allow one component of this three-dimensional vector field to be non-zero (in the z-direction for instance, where $\boldsymbol{B}_{xc}(\boldsymbol{r}) = B^z_{xc}\hat{\boldsymbol{z}}$) we can rewrite the divergence-free constraint of $\boldsymbol{B}_{xc}(\boldsymbol{r})$ as

$$\nabla \cdot \boldsymbol{B}_{xc}(\boldsymbol{r}) = \frac{\partial}{\partial z} B^z_{xc} = 0 \tag{2.89}$$

Therefore, B^z_{xc} must be constant with respect to z, where $\boldsymbol{B}_{xc}(\boldsymbol{r}) = B^z_{xc}(x, y)\hat{\boldsymbol{z}}$. In general, we would expect the ground-state magnetization field $\boldsymbol{m}(\boldsymbol{r})$ to align parallel to the corresponding $\boldsymbol{B}_{xc}(\boldsymbol{r})$, and therefore this constraint on $\boldsymbol{B}_{xc}(\boldsymbol{r})$ severely limits the possible $\boldsymbol{m}(\boldsymbol{r})$ in ways that are unphysical.

As we will demonstrate in the subsequent results chapters, we find improved local convergence to the magnetic ground-state, and better global convergence using a novel hybrid metaheuristic optimization algorithm, `SpinPSO`, which we introduce in the following sections.

2.3 SpinPSO Algorithm and Workflow: Noncollinear Ground-States

Previous computational and theoretical studies have had success in predicting non-collinear magnetic orderings using advanced symmetry-based models informed by first-principles for

collinear [93, 94] and noncollinear [95, 96] magnetic systems. The incorporation of symmetry has benefits from the standpoint of reduced computational cost [95, 96]. However, these approaches will not be suitable for systems of lower or broken crystal symmetry, such as in systems with interfaces or other defects, or amorphous magnets. Although we do not study these systems here, our methodology could be applicable in these instances, which we hope is a topic of future exploration.

In our algorithm, denoted `SpinPSO`, we modify the guaranteed convergence particle swarm optimization (GCPSO) algorithm developed by Ref. [45] & [97] by incorporating a variation of the well-known atomistic Landau Lifshitz Gilbert (LLG) equation [42, 98] into the PSO methodology.The LLG formalism is known to describe magnetization dynamics at multiple length scales [42, 99, 100] which makes it suitable for our purpose. Comparing to the inspirational work of Payne et al [101], in which the authors necessitate the definition of a distance metric between spins, our modification allows the facile extension to dynamics on $\mathcal{S}^2$.

Agent-based meta-heuristic schemes often have improved global convergence [45], in the sense that a large initial scattering of agents on the potential energy landscape reduces the possiblility of being trapped in a local minimum, compared to gradient descent based optimization schemes. Indeed, Payne et al [101] used a firefly optimization algorithm - the algorithmic cousin of PSO - towards optimizing noncollinear magnetic orderings. Notably, firefly has been shown to outperform PSO for noisy objective functions [102], however, DFT calculations, derived from variational principles, should exhibit noise on the order of the energy convergence tolerance, wherefore, in this study, we propose a PSO-based algorithm for convergence efficiency [103, 104].

In the formulation that we found to be the most successful, `SpinPSO` is further distinct from conventional GCPSO in the sense that we have included gradient information in the optimization scheme. While not conventionally included in most implementations of PSO,[45, 97] GCPSO does not explicitly preclude gradient information. After all, GCPSO was motivated on the grounds that PSO-type optimization schemes perform well when identifying global valleys of the potential energy surface (PES) [45]. However, the order of convergence can become sluggish - and even unsuccessful in some instances - within the same convex hull of the global minimum [45, 97]. Therefore, within the GCPSO formalism, a random noise term is added to the velocity of the agent with the "best" position on the PES [45], allowing for more thorough exploration of the local energy landscape.

Therefore, inspired by gradient-descent type optimization strategies, we inform the "best agent" dynamics with gradient information, as opposed to a fluctuating noise term. While this doesn't appear to be common knowledge within the non-collinear DFT community, information on the gradient, or a local effective magnetic fields, can be obtained from constraints on local magnetic moments, as implemented in VASP [1, 105]. The details of how we compute these local effective fields, and incorporate them into the workflow, are included in Section 2.3.1.2. We also explore how including gradient information improves convergence speed by orders of magnitude. This possibly explains why we are able to achieve much higher rates of convergence compared with other agent-based optimization strategies for computing

the noncollinear magnetic ground-states [101].

2.3.1 SpinPSO methodology

2.3.1.1 Physical inspiration for `SpinPSO`

This optimization strategy is comprised of a swarm of agents, in which each agent, or particle, corresponds to a different magnetic configuration. Each agent's position on the potential energy landscape is evolved in a fictitious "time" τ according to the atomistic LLG equation

$$\begin{aligned}\frac{\Delta \boldsymbol{s}_{i,j}}{\Delta \tau} &= \frac{\boldsymbol{s}_{i,j}^{n+1} - \boldsymbol{s}_{i,j}^{n}}{\Delta \tau} \\ &= -\gamma \boldsymbol{s}_{i,j}^{n} \times \boldsymbol{h}_{i,j}^{n} - \alpha \boldsymbol{s}_{i,j}^{n} \times \left(\boldsymbol{s}_{i,j}^{n} \times \boldsymbol{h}_{i,j}^{n} \right)\end{aligned} \tag{2.90}$$

Each "agent" i corresponds to a spin configuration $\left\{ \boldsymbol{s}_{i,1}, ..., \boldsymbol{s}_{i,n} \right\}$, where each atomic moment is normalized within $\mathbb{R}^3$, s.t. $s_{i,j} \in \mathcal{S}^2$. Each spin is evolved in τ according to a forward-difference Landau Lifshitz Gilbert (LLG) equation at interval $\Delta\tau$ indexed by time-step n. To ensure that the norms of the spins remain constant ($|\boldsymbol{s}| = 1$), we perform a simple re-scaling of the individual spins after each time step. We do not employ a more advanced time-stepping routine (e.g. mid-point method), because we are currently more concerned with convergence to the minimum energy ground-state than accurately describing the kinetics of the spins themselves.

The two terms on the right-hand side of the LLG equation can be intuited as follows. The single cross product term induces a precession of the moments about the effective field; e.g. about the best state in the pure particle swarm optimization scheme. This allows for slight curvature in the path towards convergence, which should in practice increase exploration of the potential energy landscape near to the identified lower energy state. Notably, in other particle swarm optimization dynamical schemes inertial terms are included in the optimization; here we opt for this precession term instead. The second term, the triple product, promotes a damping motion of the moments, resulting in a tendency to align with the on-site effective field, $\boldsymbol{h}$. These terms have physical meaning as the LLG equation can be derived from the quantum mechanical Heisenberg time evolution equation for spin operators [42] – at least without damping ($\alpha = 0$). As noted previously, the LLG equation has demonstrated effectiveness at describing magnetization dynamics at multiple length scales [99], and its use is often motivated on phenomenological grounds for this reason [100]. In the context of our algorithm, the damping term is the most important, because at convergence/equilibrium the spins should eventually align with the effective field, which contains information on the swarm's best position in the configuration space. For stability and convergence, we choose the coefficient of the second, α, to be significantly higher than the first, γ. We found a good rule of thumb to be at least a factor of three difference.

2.3.1.2 Swarm and gradient informed local fields

The effective field on individual moments, $\boldsymbol{h}_{i,j}^{n}$, is informed by particle swarm optimization input quantities from the swarm of agents,

$$\begin{aligned} \boldsymbol{l}_{i,j}^{n} &= a_c \sigma_c \tilde{\boldsymbol{s}}_{i,j}^{n} + a_s \sigma_s \hat{\boldsymbol{s}}_{j}^{n} \\ \boldsymbol{h}_{i,j}^{n} &= \frac{\boldsymbol{l}_{i,j}^{n}}{|\boldsymbol{l}_{i,j}^{n}|} \end{aligned} \tag{2.91}$$

where $(1-\sigma_c) \sim \mathcal{U}(0,1)$ and $(1-\sigma_s) \sim \mathcal{U}(0,1)$. The local fields are normalized stochastic linear combination of $\tilde{\boldsymbol{s}}_{i,j}^{n}$ and $\hat{\boldsymbol{s}}_{j}^{n}$, which are the "personal best" and "swarm best" spin configurations, respectfully, consistent with the PSO formalism. Particle swarm optimization algorithms are inherently stochastic, so in an analogy to their Cartesian counterparts, we introduced these random uniform weighting of the cognition term, which corresponds to the historical best position of the corresponding agent over its trajectory directory. In addition, we include the social term characteristic of particle swarm optimization schemes, which stores the best position compared to each time step of all agents over time.

To remain consistent with the guaranteed convergence particle swarm optimization (GCPSO) scheme developed by van den Bergh and Engelbrecht [45], we define an alternative time evolution equation to the "best" agent at any particular time. We replace the random perturbations of the "best" agent evolution in the guaranteed convergence PSO (GCPSO) [45] with gradient information from local moment constraints implemented in VASP, indicated by $(\boldsymbol{h}_{\text{eff}})_{i,j}^{n}$.

$$\begin{aligned} (\boldsymbol{h}_{\text{eff}})_{i,j}^{n} &= -\frac{\partial E}{\partial \boldsymbol{s}_{i,j}^{n}} \\ \hat{\boldsymbol{l}}_{i,j}^{n} &= \rho \frac{(\boldsymbol{h}_{\text{eff}})_{i,j}^{n}}{|\boldsymbol{s}_{i,j}^{n}|} + \frac{\boldsymbol{l}_{i,j}^{n}}{|\boldsymbol{l}_{i,j}^{n}|} \\ \hat{\boldsymbol{h}}_{i,j}^{n} &= \frac{\hat{\boldsymbol{l}}_{i,j}^{n}}{|\hat{\boldsymbol{l}}_{i,j}^{n}|} \end{aligned} \tag{2.92}$$

Therefore, this approach can be intuited as an extension of swarm optimization algorithms inspired by stochastic dynamics of variables belonging to sub-domains of $\mathbb{R}^n$ to the dynamics of a collection of spins that respectively belong to $\mathcal{S}^2$. A noted, prior work has applied a firefly optimization strategy to identifying noncollinear ground-states [101]. However, one comparative benefit of the LLG approach, is that it precludes the need to explicitly define a distance metric between spin configurations, in addition to the fact that the LLG equation, and its variants, emerges in magnetic systems at multiple length-scales [99].

It is through this effective field that we may also introduce gradient information in order to improve convergence near the local minima. The constraining effective site magnetic field,

$\boldsymbol{H}_i^{\text{eff}}$, can be described as the following [105]

$$\boldsymbol{H}_i^{\text{eff}} = 2\lambda \left[\boldsymbol{M}_i - \hat{\boldsymbol{M}}_i^0 \left(\hat{\boldsymbol{M}}_i^0 \cdot \boldsymbol{M_i} \right) \right] \tag{2.93}$$

where $\boldsymbol{M}_i$ are the integrated magnetic moments at site i, and $\hat{\boldsymbol{M}}_i^0$ are the unit vectors pointing in the individual site constraining directions [105].

Chapter 3

Linear response calculation of U and J values

We call upon the people
People have this power
The numbers don't decide

Radiohead

In this chapter, we discuss the calculation of Hubbard U and Hund J values using linear response, based on the methods and theory introduced in Sections 2.1, 1.2.1.6, and 1.2.1.7. Furthermore, we perform a more in-depth study of $BiFeO_3$, $LiNiPO_4$, and NiO as material test cases, highlighting the importance of accurately obtained U and J corrections to describe the magnetic properties of correlated electronic systems.

3.1 Results

We calculated Hubbard U and Hund J for over one thousand transition metal oxides using the linear response workflow that we implemented in `atomate`, as introduced in Chapter 2. The majority of the calculations corresponded to materials containing Mn-d, Fe-d, and/or Ni-d species. All the systems studied were previously predicted by Ref. [6] to have a collinear magnetic ground-state using a separate high-throughput workflow. That work used the empirical Hubbard U values reported on the Materials Project.

In addition, a representative set of O-p responses were calculated and analyzed. It is less common to include Hubbard corrections to oxygen $2p$ states. However, an appreciable number of studies have shown how O-p on-site corrections have improved the agreement with experimentally measured bond lengths between oxygen and transition metal species [17, 30, 106–109]. It is perhaps less intuitive to apply spin-polarized Hund J parameters to oxygen sites, because O-p states are conventionally not included in effective models for magnetism. However, while oxygen atoms do not develop magnetic moments, early studies

have demonstrated theoretically and computationally that O-p states mediate the antiferromagnetic superexchange interaction in transition metal oxides, such as MnO [33, 110, 111].

Table 3.1: Comparison of computed U_{eff} in the present work with values used by the Materials Project [63, 113]. Copyright (2024) by the American Physical Society. Reproduced from Ref. [1] with permission.

element	mean U_{eff} (eV)	$U_{\text{eff}}^{\text{MP}}$ (eV)	diff. (eV)
Co	4.430 ± 1.474	3.32	1.110
Cr	2.425 ± 0.472	3.7	-1.275
Fe	4.108 ± 1.322	5.3	-1.192
Mn	4.135 ± 0.724	3.9	0.235
Mo	1.911 ± 0.318	4.38	-2.469
Ni	5.258 ± 0.773	6.2	-0.942
V	3.060 ± 0.673	3.25	-0.190
W	1.461 ± 0.218	6.2	-4.739

3.1.1 Periodic table sample set

Figure 3.1 displays two periodic tables containing the distributions of computed Hubbard U_{eff} and Hund J values for each transition metal element (and oxygen) computed for different structures within the database. In Table 3.1, values obtained in this study are listed alongside the standard U_{eff} values employed by the Materials Project [63, 113]. Those values were determined using the procedure outlined by Wang et al. [114] which finds a U_{eff} value that minimizes the error in formation energy for several representative redox couples. Due to the limited amount of experimental data available, these U_{eff} values are determined with only experimental data from a single redox couple (Co, Cr, Mo, Ni, and W) or two redox couples (Fe, Mn, and V). Therefore, it is possible or likely that these U_{eff} values are not appropriate for a more general system containing these elements. Nevertheless, the MP U_{eff} values are found to be the same as the U_{eff} values in the present work within the standard deviation for most elements (Co, Fe, Mn, and V) or slightly outside the value in the present work (Ni). Exceptions are Cr, Mo, and W, with the largest, notable discrepancy of 4.739 eV for W.

To evaluate the impact of these discrepancies, compounds containing W from a dataset of experimental formation energies [115] used by the Materials Project were taken and relaxed using the new U_{eff} value for W from the present work but with all other calculation settings kept consistent with standard Materials Project settings, to obtain a new set of computed energies. These energies substantially lowered the correction introduced in Ref. [115] for W from -4.437 eV/atom to 0.12 eV/atom, suggesting that the newer U_{eff} is indeed more appropriate for the calculation of formation energies.

element	U			J		
	mean	σ	N	mean	σ	N
V	4.123	0.471	84	0.599	0.162	84
Mn	4.792	0.830	63	0.740	0.246	63
Cu	7.773	1.251	61	1.366	0.932	61
Fe	4.659	0.826	55	0.279	0.378	55
Ti	4.907	0.481	53	0.635	0.185	53
Cr	2.906	0.471	46	0.611	0.135	46
Nb	0.536	0.157	43	0.241	0.082	43
W	1.844	0.252	42	0.423	0.043	42
Zn	1.917	0.564	40	1.790	0.456	40
Co	5.159	0.608	31	0.560	0.292	31
Ni	5.849	0.797	31	0.682	0.186	31
Ta	3.733	0.164	30	0.668	0.041	30
Zr	4.199	0.244	28	0.907	0.091	28
Ag	2.254	0.852	25	1.236	0.256	25
Mo	2.561	0.321	23	0.483	0.062	23
Hg	0.521	0.142	20	0.429	0.032	20
Re	0.620	0.233	19	0.269	0.103	19
Cd	0.238	0.469	19	0.632	0.097	19
Sc	1.921	0.352	17	1.169	0.396	17
Y	4.302	0.343	17	1.694	0.361	17
Hf	3.515	0.229	13	1.085	0.167	13
Ru	3.000	0.371	11	0.506	0.146	11
Pt	1.554	0.315	10	0.447	0.041	10
Os	1.911	0.440	8	0.392	0.078	8
Pd	3.757	0.899	7	0.691	0.063	7
Au	1.120	0.248	6	0.495	0.034	6
Rh	1.528	0.196	5	0.457	0.056	5
Ir	1.902	0.095	4	0.315	0.324	4
Tc	2.946	0.012	3	0.580	0.004	3
Total			814			814

Table 3.2: The mean and standard deviation (σ) in the U and J parameters used in the periodic tables of Figure 3.1, alongside the number of samples N.

We stress that these values are not transferable to studies that use DFT+U+J implementations in other codes. Quantum ESPRESSO and Abinit use localized projections that are separately different from that in the projector augmented wave (PAW) method implemented in VASP [64], for different reasons.

The trends across these periodic tables — and in particular, the increasing U across

the $3d$ transition metals — are reminiscent of results from early studies that related the Hubbard and Hund parameters to Slater integrals over the Coulomb operator [18, 26, 116, 117]. For example, Ref. [116] proposes a linear relationship between the atomic number Z and the Hubbard and Hund parameters, based on both Hartree-Fock calculations and empirical observations. Note, however, that this is only valid for unscreened Coulomb kernels [18], and the Slater integrals are in fact highly dependent on the screening of Coulomb exchange between electrons (and hence the chemical environment) [18, 66]. We also do not want to overstate this comparison, which mixes older definitions of the Hubbard and Hund parameters (i.e. as derived from Slater integrals) with those used in this work (i.e. as measures of the deviation of the DFT functional from piecewise linearity).

Table 3.3: Computed range of U, J, and U_{eff} values compared with reported U_{eff} on the Materials Project (MP) [113], as well as the MP literature [63]. Each mean value has an associated standard deviation indicated after the "±." Copyright (2024) by the American Physical Society. Reproduced from Ref. [1] with permission.

Species	mean computed U (eV)	mean computed J (eV)	mean computed $U_{\text{eff}} = U - J$ (eV)	reported MP [113] U_{eff} (eV)	reported range [63] U_{eff} (eV)
Mn-d	4.953 ± 0.635	0.520 ± 0.156	4.433 ± 0.654	3.9	3.60 – 5.09
Fe-d	4.936 ± 0.700	0.177 ± 0.367	4.759 ± 0.790	5.3	3.71 – 4.90
Ni-d	5.622 ± 1.221	0.399 ± 0.434	5.223 ± 1.296	6.2	5.10 – 6.93
O-p	10.241 ± 0.910	1.447 ± 0.171	8.794 ± 0.926	N/A	N/A

3.1.2 Focused study on Mn-d, Fe-d, Ni-d, and O-p, including the reason for large O-p Hubbard U values

We now present a more detailed study on materials containing Mn-d, Fe-d, Ni-d, and O-p Hubbard sites. For these systems, the distributions of the computed Hubbard U and Hund J values are provided in Figure 3.2. The variations in U and J values calculated for these three species is immediately apparent, with a range on the order of approximately 1 to 2 eV. These distributions reflect the intrinsic screening environment dependence of the calculated value for a given element. At this point, we note only their apparently universal unimodality (single peak) and the near-general decrease in U with chemical period within a given group, however we will return presently to a more physically and chemically motivated observation. In Table 3.3 we list for comparison the U values currently used in Materials Project (fitted empirically) as well as a range of U values found for a set of spinels and olivines by Zhou and co-workers (calculated via self-consistent linear response) [63].

We find that O-p exhibits the largest associated Hubbard U value of approximately 10 eV, which agrees with the linear response results from a previous study using a different

code and somewhat different linear-response formalism [17]. While large oxygen Hubbard U values may seem surprising within a strongly correlated materials context, it has become more accepted in recent years within first-principles solid-state chemistry that oxygen $2p$ orbitals can warrant, both by direct calculation and by necessity (when resorting to fitting), a remarkably high U value in DFT+U.

3.1.2.1 Interpretation of Hubbard U in terms of the subspace chemical hardness

We will now attempt to motivate and explain the phenomenon of comparatively larger O-p U values. We note from the outset that the element projector orbital profile plays a complicating role in the following analysis. Over a sample of materials, we observe that the 2×2 averaged diagonal elements of the χ_0^{-1} non-interacting response are of approximately the same magnitude for both TM-d and O-p site matrix elements, with a mean difference close to zero. The non-self-consistent response can be interpreted as the response due to non-interacting response effects at a site due to its surroundings [18], and thus it can be understood as a property primarily of the environment of the atom under scrutiny. Then, unless screening is very short ranged (as it may be in a very wide-gap insulator), this quantity may be said to be somewhat similar, on average, for metal and oxygen ions in an oxide. Thereby, the chemical trends in the Hubbard U arise mostly in the interacting response, instead.

Next, for this same sample of materials, we note that the magnitude of the O-p interacting response χ tends to be significantly less than the interacting TM-d response. This indicates that $-\chi^{-1} = d^2E/dn_\gamma^2$, the curvature of the total energy versus occupation, n_γ, is greater for O-p states. This greater curvature versus occupation can be explained in terms of known trends in the chemical hardness, i.e., the second chemical potential, i.e., the derivative of the chemical potential with respect to total charge at fixed external potential. (We note in passing that some authors choose to include a factor of one half in the definition of the chemical hardness for historical reasons, but we suppress that discussion here.) Specifically, we can focus on the finite difference (three-point) approximation to the global chemical hardness [118], namely in terms of the following energy differences

$$\begin{aligned}\nu \equiv d^2E/dN^2 &\approx E\left(N-1\right) - 2E\left(N\right) + E\left(N+1\right) \\ &= \left[E\left(N+1\right) - E\left(N\right)\right] - \left[E\left(N\right) - E\left(N-1\right)\right] \\ &\equiv E_i - E_a \equiv E_g,\end{aligned} \tag{3.1}$$

which is nothing but the fundamental band-gap. This is a quantity that has been tabulated many times. Using the results of Ref. [119], we find that for atomic oxygen its value is 11.2 eV, compared to that of the transition metal atoms, where it ranges from 5.8 eV (Ti & Zr) to 8.0 eV (Mn) if we exclude the often problematic zinc group, where it reaches 11.6 eV. This mirrors and explains the observed relatively large first-principles Hubbard U value for oxygen $2p$ states predicted in this and several previous studies.

Ultimately, we conclude that the Hubbard U may be interpreted as the subspace-projected, environment-screened chemical hardness. More precisely, U can be intuited as contributions to the hardness due to interactions such as Hartree, exchange, correlation, and perhaps other terms like implicit solvent and PAW potential. After all, it is from these interactions that most chemical trends appear to arise in practice. For subspaces that project heavily at both band-edges, as in normal DFT+U_{eff} practice, the U inherits chemical trends from the chemical hardness (fundamental gap) of the atom that it resides upon. This is higher for a greater atomic ionization energy E_i (that of oxygen is generally around twice that of transition metals) and higher also for a more negative electron affinity E_a (that of oxygen is more negative than that of most but not all transition metals). By and large, both quantities are well known to increase in magnitude as we move 'up and right' in the periodic table, and this same broad trend is reflected in our periodic table of Hubbard U values.

When a DFT+U_{eff} subspace projects only onto one band edge, as is the case for charge-tranfer insulators, then only the trend in either the ionization energy or electron affinity will be very relevant to the trends in U. Due to the relatively large electronegativity of oxygen, typically there will be little weight at the conduction band edge for oxygen $2p$ orbitals projectors. Therefore, the particularly clear trend in ionization energy drives the relatively large U value for oxygen. Indeed, if this argument holds, then one would guess that the oxygen $2p$ U value is roughly twice that of an average transition-metal d-subspace, which turns out to be the case from first principles linear response.

Within the present formalism, the Hund J may be interpreted as an analog for the spin degree of freedom, and specifically as minus (by a convention thought to originate with Ising) the interaction part of the subspace-projected, environment screened spin-hardness, where the spin-hardness is a quantity discussed for example in Ref. [120].

3.1.2.2 Trends in U and J values

In order to explore trends in the distribution of U and J values, we have plotted these on-site corrections in scatter plots within Figure 3.2. These plots illustrate the relationship between U and J values with respect to site occupations. For transition metal species, we plot U and J versus the "d" component of the projected moment m, denoted as "$m_{l=2}$." These moment values are those output by VASP as the difference between up and down spin site occupancy numbers computed using PAW core-region operators. Because the oxygen atoms do not have an associated magnetic moment, we plot O-p Hubbard U and Hund J versus $n_{l=1}$ occupations on oxygen sites.

We should stress that the values of "m_l" and "n_l" are only computed from the calculation without the $+U/J$ correction. One reason for using the bare PBE computed m_l and n_l is that these occupations should be independent from the applied Hubbard U or Hund J values. This would offer the "bare" m, as well as n, as a possible predictors of U and J values. However, it is important to note that these occupations could change significantly with applied U and J values [17, 121, 122].

There is an apparent clustering of datapoints at different on-site m_l magnetizations in Figures 3.2a, 3.2b, and 3.2c. This grouping at different on-site magnetization values is most likely due to different spin and charge states dependent on the underlying chemistry. We also observe a larger range of U and J values for higher values of m_l, which is due to the coupling between highly spin-polarized states to on-site Coulomb screening for TM species. As would be expected, we see similar trends for J, a measure of the screened interaction between spin channels.

The clusters that lie at the associated maximum computed m_l fall off and exhibit a negative slope trend with the magnitude of the site moment. This is likely due to the fact that m_l is highly dependent on the local chemical environment, which will govern the interacting and non-interacting energy curvatures with respect to spin-occupations, which are related to U and J within linear response [16]. The clear trend for the manganese may be due to the strong tri-modal distribution of Mn magnetic moments seen in Figure 1 of Ref. [6]. The "stable" magnetic configurations from this study were used in the LR analysis, therefore a similar statistical distribution should hold for the subset of structures used in this LR analysis.

The trends of the datapoints for Hubbard U and Hund J values in Figure 3.2d appear to show a downward trend for U versus p-occupation numbers, $n_{l=1}$, and a slower, upward trend for J values versus $n_{l=1}$. We expect that the $n_{l=1}$ occupations will be strongly dependent on the oxidation/reduction state of oxygen atoms. Due to the nature of TM-O bonding in these oxides, and their generally greater electronegativity, the oxygen atoms will tend to maximize their valence. Therefore, building on the previous explanation of the magnitude of O-p U values based on chemical hardness and specifically the more relevant ionization potential component of that, the higher electron count for oxygen corresponds to a lower ionization potential, and therefore to a reduced Hubbard U, as observed.

3.1.2.3 Occupations calculated from DFT (no on-site corrections) versus guessed oxidation state

In Figures 3.4a-3.4c we provide scatter plots of the locally projected d ($l = 2$) component of the magnetic moments, $|m\text{-}d|$, versus oxidation state guessed using the bond valence method (BVM) [123] for a set of Mn, Fe, and Ni containing structures. Analogous plots versus total d occupations, n-d, are provided in Figures 3.4d-3.4f. We emphasize again that these local projections are obtained from VASP DFT calculations, without any on-site corrections applied. We use the BVM implemented in `pymatgen` [70].

As expected from chemical intuition, there are clear trends of $|m\text{-}d|$ and n-d versus guessed oxidation. However, in a few cases, namely the trends of $|m\text{-}d|$ versus Mn oxidation state in Figure 3.4a, the trends of $|m\text{-}d|$ is clearer than that of n-d. For this reason, we provide plots of the calculated U and J values versus $|m\text{-}d|$ in the manuscript. One of the goals of this study is to lay the groundwork for a future study to explore the chemical and/or physical justification for these trends.

3.1.2.4 Multiplet theory and U and J

The correlation between on-site corrections and projected site moments is not surprising. After all, Hund's rules introduce a link between the magnetic spin moment of an atom and its charge state [84, 116, 124]. This has been widely observed in DFT studies [125–127], and it has even been argued that DFT magnetic moments are often the most convenient and reliable indicator of charge states [125].

A model of multiplet splitting Next, we will summarize the theoretical basis for the comparison between our computed on-site corrections and multiplet theory, which we explore in Section 3.1.2.4. This theoretical foundation is based on the book by John C. Slater [124], in which the author presents the following energy expression

$$E = \sum_{i} I(nl) + \sum_{ii'} E(nl, n'l'). \tag{3.2}$$

The first sum runs over each single electron contribution to the multiplet state, and the second double sum runs over pairs of electrons, interacting via Coulomb exchange, which can be described in terms of Slater integrals [124]. The first two quantum numbers of electrons in states i and i' are indicated by nl and $n'l'$, respectively. While simple in its elocution, this energy expression has the power to describe the ground-states multiplets of transition metal and lanthanide charge states [116, 124], and therefore a quantitative explanation of Hund's rules.

Van der Marel and Sawatzky implement this theory in their paper, Ref. [116], in order to express the multiplet exchange energy in terms U_{eff} and J. Therefore, we directly use the mathematical expressions from their study in our analysis. Starting from the simple Hamiltonian in Equation 3.2, Van der Marel and Sawatzky arrive at the energy expression

$$E = \alpha_I I + \alpha_{F^0} F^0 + \alpha_J J + \alpha_C C, \tag{3.3}$$

where the α_μ coefficients are integer values that depend on the ground-state multiplet state, and C is the "angular part of the multiplet splitting" [116, 124]. From Equation 3.3, the authors obtain an expression for U_{eff} [116] using a finite difference scheme identical to Equation 3.1.

It is worth reemphasizing that the Slater integrals (F^0, F^2, F^4, and F^6) themselves are highly dependent on the screening of Coulomb exchange between electrons, and therefore the chemical environment [18, 66]. Therefore, the Slater integrals themselves are *not* an intrinsic property of the elemental species. Furthermore, the relationship of U and J to Slater integrals is valid only for "unscreened Coulomb kernels" [18]. Specifically, within the rotationally invariant formalism [19], the unscreened Coulomb integrals result in the well-known expressions for U and J, for d-states:

$$U = F^0 \tag{3.4}$$

$$J = \frac{F^2 + F^4}{14}. \tag{3.5}$$

In fact, these expressions are termed the "multiplet-averaged" Coulombic exchange corrections [18, 116, 124].

Despite the caveats outlined in the previous paragraph, Equation 3.2 is derived from first-principles [116, 124], and is therefore generalizable. Additional mechanisms for multiplet splitting, such as the hyperfine structure, are explored in Volume II of Ref. [124]. However, we do not explore these effects here, because the splitting of energy levels will be of smaller magnitude compared to the first-order mechanisms for splitting via the electrostatic and spin-spin interactions [124].

As we touched on in Section 1.2.1.7, it is possible to express the effective U as $U_{\text{eff}} = U - J$. Therefore, as a shorthand, we define J_h as $J_h = F^0 - U_{\text{eff}}$, where F^0 is the Slater integral commonly associated with the conventional Hubbard U. Therefore, based on Ref. [116], this effective J_h incorporates "angular part of the multiplet splitting," C [116], such that J_h is a function of J and C. While the expression for U_{eff} is multiplet-specific, the unscreened, multiplet-averaged U of Equation 3.4 is not. Therefore, we can think of J_h as an approximate quantity, dependent on the ground-state multiplet of a given charge state. We conclude that this simple model (Equation 3.3) can account for the oxidation-state dependence of the on-site corrections via the ground-state multiplet. This permits us to explore a simplified picture in which the influence of the chemical environment enters through the ground-state charge state of the cation. The quantitative behavior of J_h is explored in Section 3.1.2.4, and compared to our Hund J values calculated from linear response.

For illustration, in Ref. [66], the authors calculate the screened versus bare F^0 for a selected number of $3d$ species in $SrMO_3$ (M = V, Cr, Mn) [128]. For example, for $SrVO_3$, the authors find $F^0_{\text{screened}} = 3.2$ eV versus $F^0_{\text{bare}} = 19.5$ eV for V-d states, and observe a similar relative magnitude for the other $3d$ species. Therefore, this lower value is likely due to Coulombic screening from the oxygen octahedral environment of B-sites in the perovskite $SrMO_3$.

While this connection is physically motivated, localized states do not encompass all of the levels of correlation effects that are neglected by the specific DFT functional [52]. This perspective of U and J values as functional-specific, and not universal quantities, expands the definition of U and J from their initial inspiration from the Hubbard model, which treats U and J as intrinsic atomic properties.

To provide some theoretical background for the trends across these periodic tables, we turn our attention to Ref. [116]. In this study, van der Marel and Sawatzky apply Slater's multiplet energy splitting theory [124], in order to express U_{eff} in terms of Coulomb exchange and pair-hopping integrals, as well as the "angular part of the multiplet splitting" [116, 124]. This paper provides a convenient toy model for exploring the dependence of U_{eff} on ground-state multiplets for different cation charge states (e.g. Fe^{2+} versus Fe^{3+}). The authors obtain an expression for U_{eff} [116] using a finite difference scheme reminiscent to Equation 3.1.

In this paper, the authors assume a linear increasing relationship between F^0 and the atomic number, Z. As we cover in Section 2.1.1 with several caveats, the unscreened U value is equal to F^0. Therefore, the overall increasing trend of U across the $3d$ row in Figure 3.1a can be explained by this increasing Coulomb interaction with periodic table group index.

Furthermore, the multiplet splitting analysis in Ref. [116] may help to explain the dipping of Fe^{3+} spin-flip Hund J values into negative numbers. We leave an in-depth theoretical study of negative J values (consistent with the linear response methodology) to future studies.

Comparison with multiplet theory In this section, we compare the computed U_{eff} and J with their theoretical "unscreened" counterparts from the effective model for multiplet exchange, Equation 3.2, as discussed in Section 3.1.2.4. In Figure 3.5a, we plot a comparison of U_{eff} across $3d$ species. The "mean theoretical" values are obtained from an equally weighted average over the common oxidation states for each element. This mean is not appropriately weighted for the TMO dataset used in this paper. Therefore, the mean theoretical values are intended for visual comparison, and not as a direct comparison.

The expression for the F^0 Slater integral was adjusted heuristically to fit the computational trends. Specifically, we use the following approximate linear expression: $F^0 = 3.0 + 0.5(Z - 21)$, reported in electron volts. This expression differs from the linear expression used in Ref. [116]: $F^0 = 15.31 + 1.50(Z - 21)$ eV. This modified expression for F^0 can be justified from the more recent cRPA calculations presented in Ref. [66], in which the authors calculate the screened versus bare F^0 for a selected number of $3d$ species in $SrMO_3$ (M = V, Cr, Mn) using the `WIEN2k` code framework [128]. For example, for $SrVO_3$, the authors calculate $F^0_{\text{screened}} = 3.2$ eV versus $F^0_{\text{bare}} = 19.5$ eV for V-d states, and observe a similar relative magnitude for the other $3d$ species. Therefore, this lower value is likely due to Coulombic screening from the oxygen octahedral environment of B-sites in the perovskite $SrMO_3$. Furthermore, the atomic number scaling relationship that we use for $F^0(Z)$ across the $3d$ row brings the expression into closer agreement (on order of magnitude) with the values fit to empirical data, as reported in Ref. [116]. A complimentary comparison to the mean conventionally screened Hund J values is included in Figure 3.5b. The linear scaling relationship of Hartree-Fock unscreened J values versus atomic number Z is plotted as well, as reported in Ref. [116]. For most species, the mean conventionally screened J values calculated from linear response fall within the range of theoretical J_h values predicted for different oxidation states.

Generally speaking, the parameters from Hartree-Fock [1], have provided a theoretical basis on which to explain some trends that we observe across the $3d$ row elements. Namely, one observes the presence of strongly negative Fe-d Hund J values for Fe^{3+}, which agrees with the computational trends shown in Figure 3.2b. Fe^{3+} has a higher spin moment than Fe^{2+} [84], so the downward trend of J values with the magnetic moment can be explained on this basis. For U_{eff} in Figure 3.5a, we observe a general upward trend of values with atomic number, from Cr on, which is in agreement with the the average theoretical trends. This trend arises from the increasing behavior of F^0 versus Z. For most elements, there are theoretical values that fall within the computational error bars, with the exception of titanium. It is apparent that while this simple analysis from multiplet energies [116, 124] helps us provide quantum chemistry insight into some general trends, it is by no means a

[1] As tabulated from Ref. [116], which is fit to data from Ref. [129]

predictive technique. By the distributions of the U and J values alone, it is clear that other modes of Coulombic screening from the local environment play a key role in determining the final value of the on-site corrections.

3.1.2.5 Exploration using random forest regression

To more robustly tease apart these observed trends, we performed a rudimentary random forest regression test on the dataset, ultimately in an attempt to predict the on-site corrections U and J from the input crystal structures and site properties. We used the random forest regression algorithm as implemented in `scikit-learn`. The input quantities supplied to the random forest regression routine consisted of the corresponding PBE-computed m_l and n_l (i.e. without on-site corrections), as well as the oxidation state estimated using the bond-valence method [123], and finally a selection of relevant site featurizers provided by the `matminer` Python package [130]. Unsurprisingly the U and J values appeared to be the most sensitive to the magnetic moment magnitude, $m = n_\uparrow - n_\downarrow$, and site occupation, $n = n_\uparrow + n_\downarrow$. This is in accordance with what would be expected from the dependence on the Hubbard U values on spin and charge state [121, 122]. However, these features proved to be insufficient to accurately predict U and J.

Most of the `matminer` site featurizers were tested as input to the random forest regression model. Additionally, the oxidation states calculated using the bond valence method (BVM) [123] were also included as input to the model. For learning trends across different atomic species, the atomic number of the associated element was also supplied. Additionally, we tested the orbital field matrix (OFM) features as formulated by [131, 132]. The OFM encodes the orbital character of the surrounding chemical environment. For more information on this method please refer to Ref. [131]. The OFM functionality is not implemented in `matminer` or `pymatgen`. We were motivated to test the vectorized OFM by the chemical intuition that on-site Hubbard U and Hund J values are very sensitive to the local chemical environment. Additionally, the OFM has demonstrated success in predicting DFT-computed magnetic moments in the past [131]. Furthermore, the OFM nearest-neighbor contributions are weighted according to the geometry of the Voronoi cell, which could possibly provide information beyond the relative importance of the Voronoi `matminer` featurizer. Of the `matminer` featurizers, Ewald energy and Voronoi site featurizers had the greatest associated importance metric [130], second only to the on-site magnetization m_l. The on-site magnetization for Mn, Fe, and Ni, respectively, had an importance of at least ten percent more than any of the other local chemical environment descriptors.

From Hund's rules, it is possible to derive magnetochemistry rules governing the coupling between the magnetic spin-moment and associated charge state, dictated by the associated multiplet ground-state [84, 116, 124]. Therefore, the correlation between on-site corrections and projected site moments is not surprising. After all, previous studies have explored the connection between charge states of transition metal species and the integrated net spin calculated from DFT [125–127]. In fact, recent studies show that the magnetic moment is often the most convenient and reliable indicator of charge states [125].

3.1.2.6 Conventional vs. constrained linear response

In introducing the linear response theory in Section 1.2.1.7, we mentioned that there are two possible schemes for computing U and J: "conventional" and "constrained" linear response, where in the latter case the linear response is performed in such a way that the magnetic moment (occupation) is held fixed while measuring the curvature with respect to the occupation (magnetic moment). While arguments can be made as to theoretically which approach is the most valid for a given corrective functional (a topic which is the subject of ongoing research [31]), this dataset presents an opportunity to evaluate how much this choice will practically affect the resulting Hubbard and Hund parameters.

For the majority of the computed U and J values using these two methods, the difference between the two strategies fell within their computed uncertainty. However, we observed a significant deviation from $y = x$ behavior for the computed U and J values for iron Hubbard U and Hund J values shown in Figure 3.3. The width of this deviation from equality is greater than 1 eV for U in some regions, which is enough to affect computed physical properties [16, 121].

3.1.2.7 Dependence on structure and magnetic state

For some input magnetic structures, the magnetic configuration changed while applying the on-site potentials during the linear response analysis. Our hypothesis is that the input magnetic structure corresponds to a local minimum configuration, or possibly a metastable state. Therefore, in our analysis, we screen out these structures with the intent that these systems will be studied in the future using a self-consistent approach to calculating on-site corrections.

In order to test the sensitivity of U and J values to the input structure specifically, we perform a geometry-self-consistent linear response study of antiferromagnetic NiO in Section 3.1.5.3. Each iteration consists of a step which includes geometry optimization of cell shape, followed by a linear response calculation of the PBE-based U and J values at the DFT+U+J geometry (so as to isolate the impact of the geometry from the matter of parameter self-consistency). These on-site correction values are then used in the next subsequent geometry optimization step. Self-consistency is achieved once the U and J values fall within their corresponding uncertainty values. Starting from the input structure — which was optimized using the current default Materials Project U values [113] — convergence was achieved after only two iterations.

It has been well established in previous studies that U values should be computed self-consistently with geometry optimization [121, 133]. As demonstrated from the experiments with antiferromagnetic NiO in Section 3.1.5.3, both the Hubbard U and Hund J values should be calculated self-consistently. In this self-consistency study, J had the largest relative convergence, and therefore appeared to be most susceptible to geometric self-consistency. Due to the coupling between Hund J and magnetic exchange [33], it is possible that both magnetic and structural features should be included in the self-consistency cycle. Within

the `atomate` framework, it would be possible to incorporate an iterative workflow that wraps the workflow developed in this study, in order to alternate linear response calculations with geometry relaxation until self-consistency is achieved.

3.1.3 Case study: $BiFeO_3$

The following excerpts and figures are included, with permission, from Ref. [2].

3.1.3.1 Introduction

Multiferroic $BiFeO_3$ (BFO) exhibits both a large, room-temperature ferroelectric polarization and canted antiferromagnetism with deterministic coupling between these order parameters [134–139]. Thus, the magnetic nature of BFO can be controlled with electric fields, potentially paving the way for ultra-energy-efficient magnetic and spintronic devices with more favorable scaling [139–143]. Indeed, electric-field control of magnetism in coupled ferromagnetic layers using BFO been the subject of considerable attention [137, 144–146], and while this functionality has long excited researchers, understanding of the process has generally relied on mesoscale imaging and transport measurements to infer the structure and behavior of the BFO. This has left gaps in our understanding of the microscopic mechanism and details of this process.

In the bulk, BFO exhibits an antiferromagnetic (AFM) spin cycloid that exists in the plane defined by $\boldsymbol{P}$ and the propagation direction, $\boldsymbol{k}$, which points along a $\langle 1\,1\,0\rangle$ that is orthogonal to $\boldsymbol{P}$ [147–151]. This vector connects second-nearest neighbor iron sites which, in an unperturbed G-type AFM, would be ferromagnetically coupled within $\{1\,1\,1\}$ [151–153]. The spin cycloid itself has been modeled as a Néel-type, rotating uncompensated magnetization, $M(\boldsymbol{r})$, that exists in the plane defined by $\boldsymbol{k}$ and $\boldsymbol{P}$ (i.e., the $(1\,1\,\overline{2})$, where $\boldsymbol{P}$ is along the $[1\,1\,1]$ and $\boldsymbol{k}$ along the $[\overline{1}\,1\,0]$, unless otherwise noted) with a period of ~ 65 nm (Figure 3.6d). This has been described as

$$M(\boldsymbol{r}) = m\left[\cos(\boldsymbol{k}\cdot\boldsymbol{r})\boldsymbol{e_k} + \sin(\boldsymbol{k}\cdot\boldsymbol{r})\boldsymbol{e_p}\right]$$

where m is the volume-averaged magnetization, $|\boldsymbol{k}| = 2\pi/\lambda, \boldsymbol{r}$ is a coordinate in real space, and $\boldsymbol{e_k}$ and $\boldsymbol{e_P}$ are the unit vectors in the directions of $\boldsymbol{k}$ and $\boldsymbol{P}$, respectively [154]. A second-order canting also exists due to the Dzyaloshinskii-Moriya interaction (DMI) arising from the antiferrodistortive octahedral rotations [152, 155–157], causing the magnetization to buckle slightly out of the $\boldsymbol{k}-\boldsymbol{P}$ plane (Figure 3.6e). This second-order spin-density wave, noted here as M_{SDW}, can be described [158] by

$$M_{SDW}(\boldsymbol{r}) = m_{DM}\cos(\boldsymbol{k}\cdot\boldsymbol{r})\left(\boldsymbol{e_k}\times\boldsymbol{e_p}\right). \tag{3.6}$$

	$K_{\text{eff}}\left(\mu\text{eVf.u.}^{-1}\right)$	$U_{MS}\left(\mu\text{eVf.u.}^{-1}\right)$	θ_n
Unstrained	19.655	-	-
Strained	-3.011×10^{-1}	-20.125	56.57°

Table 3.4: Fitted coefficients of Equation 3.7. Copyright (2024) Springer Nature. Reproduced from Ref. [2] with permission.

3.1.3.2 Computational results

While DFT simulations can provide powerful insight into the local atomic structure, predicting the ground-state magnetic order of BFO is computationally intractable using plane-wave DFT due to the long period of the cycloid ($\sim$ 65 nm) and the corresponding large system size required to fully simulate it [160]. A practical alternative is to use the generalized Bloch condition for $\boldsymbol{q}$-spirals which can account for rotations in the cycloidal plane, but this cannot predict moments that are canted out of this plane due to boundary conditions. To then help understand the ground-state magnetization of the system, here we discretize the magnetic structure into subsections manageable by first principles. Starting from a $2 \times 2 \times 2$ unit cell with G-type antiferromagnetism, where anti-aligned iron moments point along the vector $\pm\boldsymbol{L}$, we systematically rotate the initial $\boldsymbol{L}$ within a fixed plane (given by the angle ϕ, Figure 3.7a) to simulate the cycloid and resolve the canted magnetism. In this case, ϕ is in the $(1\,1\,\overline{2})$, defined by $\boldsymbol{P}$ and $\boldsymbol{k}$, which hosts the cycloid. Additionally, calculations are performed applying on-site Hubbard U and Hund J corrections to the O-p manifold, in addition to the Fe-d and Bi-p, with further detail in Methods. We first demonstrate the validity of our approximations and methodology by reproducing the established spin texture, $\boldsymbol{L}$, as reported in the literature. Specifically, we rotate $\boldsymbol{L}$ within an orthogonal plane, $(1\,1\,1)$ which leads to an approximately two-times greater energy cost than $\boldsymbol{L}$ in $(1\,1\,\overline{2})$, relative to the reference minimum energy spin quantization axis (Figure 3.7b).

Initializing the iron moments along the rotation angle ϕ in the $(1\,1\,\overline{2})$, the canted M_{SDW} component of magnetization along the $[1\,1\,\overline{2}]$ spontaneously arises when the structure is relaxed (Figure 3.8). In these simulations, M_{SDW} is the net moment that comes from the canting of the atomic moments away from the initialization direction $\boldsymbol{L}$ and is reported as the vector sum of the iron spins. From our simulations, M_{SDW} follows the same period as the cycloid and reaches a maximum value when $\boldsymbol{L}$ is parallel to $[\overline{1}\,1\,0]$. This is consistent with the expectation from symmetry that M_{SDW} emerges due to the DMI from octahedral rotations with their axis along the polarization direction [152, 156, 157], where $\boldsymbol{D}_{ij} \cdot \left(\boldsymbol{S_i} \times \boldsymbol{S_j}\right)$ is maximized when $\boldsymbol{D_{ij}}$ and $\boldsymbol{S}_{ij}$ are orthogonal, in this case $\boldsymbol{S}_{i,j} \| \boldsymbol{k}$. The value of M_{SDW} reaches a maximum of 0.02 μ_B, which is consistent with previous predictions [160, 161] and is of the order of previous experimental results [148, 154, 156, 158]. Discretizing the magnetic cycloid in this way then produces results that agree exactly with previous experimental and theoretical interpretations of the canted M_{SDW} component of the cycloid [155–157], as well

as quantitative analysis of the data presented here (Figure 3.10).

With the magnetic structure reproduced using DFT, we next consider how anisotropy is introduced into the system through epitaxial constraints. Fixing the unit cell to the in-plane lattice constants of DSO, a calculation is performed where the iron moments are rotated in the planes defined by $\boldsymbol{P}$ and the three possible $\boldsymbol{k}$ directions (i.e., $[\bar{1}\,1\,0]$, $[\bar{1}\,0\,1]$, and $[0\,\bar{1}\,1]$). From these data, there is a clear anisotropy favoring the $\boldsymbol{k} \parallel [\bar{1}\,1\,0]$, approximately four-times lower than the original degenerate $\boldsymbol{k}$. The preference for the $\boldsymbol{k} \parallel [\bar{1}\,1\,0]$ is consistent with experimental observations (Figure 2 of Ref. [2]). This is in contrast to the bulk, zero strain state, where all possible directions of $\boldsymbol{k}$ are symmetry-wise and energetically equivalent. Understanding, then, that substrate constraints intrinsically break the degeneracy of the allowed $\boldsymbol{k}$ directions, one can then ask whether the state of the cycloid can be deterministically changed with an electric field and whether this anisotropy is strong enough to persist in the switched state.

Electronic structure calculation details DFT calculations were carried out in VASP. Hubbard U and Hund J corrections for the valence states of all species were calculated using collinear DFT using a linear response (LR) workflow developed in the atomate code framework [1]. Linear response analysis was performed without the inclusion of SOC to reduce computational cost, and because SOC has been found in other systems to have a relatively small effect on the on-site corrections from LR [1]. These values were calculated to be U, J = 5.2, 0.4 eV for Fe-d, U, J = 0.8, 0.8 eV for Bi-p, and U, J = 9.7 , 1.9 eV for O-p. Because MAE is on the order of μeV, geometry relaxation, spin-orbit coupling (SOC), and on-site Hubbard U and Hund J corrections are all accounted for in a holistic manner to address their interdependence. In all calculations, Hubbard and Hund corrections are applied to all outer shell manifolds (Fe-d, Bi-p, and O-p). These structures were calculated for the structure endpoint reported in Ref. [159]. Using these calculated on-site Hubbard corrections, full geometry relaxation of the structure was performed with SOC included until self-consistency was reached for an electronic energy tolerance of 10^{-6} eV. All calculations were performed for the $2 \times 2 \times 2$ supercell (eight times the formula unit) to accommodate the G-type antiferromagnetic structure. These computational subtleties are addressed in greater depth in the Figure 3.9 and Section 3.1.3.2.

In the unstrained calculation, the on-site Hubbard U and Hund J parameters on O-p, in addition to Fe-d, are primarily responsible for the minimum in the anisotropy energy along [1 1 1], instead of the intersections with the (1 1 1) as previously reported [160]. For the U/J parameters listed above, we observe that using U/J applied to Fe-d states alone, the [1 1 1] corresponds to a local maximum in energy. Conversely, [1 1 1] is a local minimum if we apply on-site corrections to the O-p manifold. This result appears to be agnostic to the flavor of on-site correction used, i.e. DFT+U+J [162] versus DFT + U_{eff} [26] with $U_{\text{eff}} = U - J$. This use of O-p Hubbard corrections could help to explain the differences between local minima on the MCAE energy landscape compared to previous DFT studies.

Additionally, when comparing DFT + U + J to DFT + U_{eff}, both an effective reduction

of antiferrodistortive rotations of oxygen polyhedra, as well as a reduction of ferroelectric distortions of Fe atoms are observed. Conventionally, the inclusion of the Liechtenstein DFT+$U+J$ formalism is known to amplify oxygen polyhedral distortions [33, 57] compared to the Dudarev DFT+U_{eff} counterpart. This can be explained on the basis that, in order to motivate $U_{\text{eff},}$ a spherical symmetry of the Coulomb exchange integrals is assumed [18] which is rarely the most accurate assumption, especially for transition metal oxide systems with symmetry broken by crystal field splitting [33, 57]. In this case, however, the possible conflict between SOC and the Hund J antisymmetric intra-orbital exchange is also considered, as explored in reference [163] and [164].

Discussion of the magnetoelastic anisotropy From the calculations presented here, the effective anisotropy is greatly reduced for the strained unit cell. This can be reconciled from the insight of previous DFT studies, which computationally confirmed that the single ion anisotropy is most strongly affected by ferroelectric distortions, while the net DMI vector is most sensitive to the magnitude of antiferrodistortive rotations of oxygen octahedra [161]. From Figure 3.9, strain induces a dominant cooperative distortion of oxygen, relative to iron and bismuth ions, which reduces the magnitude of the effective anisotropy. We observe the quantitative outcome of these distortions in the reduction of $|K_{\text{eff}}|$ in Table 3.4. This helps to rationalize, if the strained cell is not allowed to relax individual atomic positions, the experimentally observed behavior for the cycloid $\boldsymbol{k}$ vector to orient along $[\bar{1}\,1\,0]$, compared to $[\bar{1}\,0\,1]$ and $[0\,\bar{1}\,1]$, is not reproduced.

In order to provide further evidence for the magnetoelastic anisotropy induced by epitaxial strain, the data here are also fit to the analytical expression for the energy versus rotation angle for BFO, derived in the SI of Ref. [165]. These results in Figure 3.9 showcase an almost perfect agreement between the analytical expression and the data.

The anisotropy energy is defined in terms of the antiferromagnetic order parameter, oriented along the z-direction, which is parallel to $[1\,1\,1]$. K_{eff} includes both uniaxial magnetocrystalline anisotropy (MAE), as well as DMI energy contributions [165]. The magnetostrictive term accounts for plane strain in $(0\,0\,1)$, where the unit vector defines the direction normal to the film plane with $\boldsymbol{P} \parallel [1\,1\,1]$ under no applied stress. This energy can be expressed as:

$$F' = F_{\text{anis}} + F_{MS} = -K_{\text{eff}} L_Z^2 - U(\boldsymbol{L} \cdot \hat{n}) \tag{3.7}$$

where F' contains the effective anisotropy (F_{anis}) and plane-strain magnetostrictive (F_{MS}) contributions to the free energy and $\hat{n}$ is the unit vector that is normal to the thin film plane. Employing spherical coordinates, with the polar axis oriented along $\boldsymbol{P} \parallel [1\,1\,1]$ and the azimuthal axis along $[1\,1\,\bar{2}]$, we can express the AFM order parameter as $\boldsymbol{L} = |\boldsymbol{L}|[\sin\theta\cos\phi, \sin\theta\sin\phi, \cos\theta]$. Both energy contributions can then be expressed in terms of the polar and azimuthal angles θ and ϕ:

$$F_{\text{anis}} = -K_{\text{eff}} \cos^2\theta F_{MS} = -U\left(\sin\theta_n \sin\theta\cos\phi + \cos\theta_n\cos\theta\right)^2 \tag{3.8}$$

where θ_n defines the orientation of $\hat{n}$ within the polar reference frame. In the case of $\phi = \pi/2$, which corresponds to a $(1\,1\,\bar{2})$ rotation plane,

$$F'_{11\bar{2}} = -\left(K_{\text{eff}} + U_{MS}\cos^2\theta_n\right)\cos^2\theta \tag{3.9}$$

If $K_{\text{eff}} + U_{MS}\cos^2\theta_n < 0$, the [111] axis is favored. If $K_{\text{eff}} + U_{MS}\cos^2\theta_n > 0$, however, intersections between the $(1\,1\,\bar{2})$ and $(1\,1\,1)$ planes (i.e. $[\bar{1}\,1\,0]$ and $[1\,\bar{1}\,0]$) are preferred over the $[1\,1\,1]$ axis. This agrees with the energy versus rotation angle provided in Figure 2 of Ref. [2].

In Table 3.4, we report the fitted coefficients of the energy terms in Equation 3.7 for both the unstrained, relaxed structure, as well as the unit cell constrained to the $DyScO_3$ lattice parameters, $a \cong b \cong 0.394$ nm. The uncertainties of these obtained values from `scipy.optimize.curve_fit`, are less than 10^{-14} eV for all K_{eff} and U_{MS} values, and 0.003° for θ_n. By comparison, for the unstrained structure, $\theta_n = 54.7°$. The coefficient of the magnetostrictive term is negative, $U_S < 0$, which is expected under compressive epitaxial strain, based on the intuition provided by Ref. [165]. According to the calculation presented here, $|U_{MS}| > |K_{\text{eff}}|$, which further supports the claim that in $BiFeO_3$, strain strongly affects the easy axis/plane preference and orientation.

3.1.4 Case study: $LiNiPO_4$

We now present a detailed study on the olivine $LiNiPO_4$, designed to test the results produced by the linear response workflow. Previous GGA+U and GGA+U+J studies have attempted to reproduce the experimentally-observed spin-canting structure and unit cell shape as shown in Figure 3.11 [23, 63, 166].

We calculated U and J for this system via spin-polarized linear response. The spin-polarized linear response method introduced in Section 1.2.1.7 can be generalized to non-collinear DFT using the relationship between spin-density occupations and the magnitude of the magnetic moment: $n_\uparrow = \frac{1}{2}\left(n + |\vec{m}|\right)$ and $n_\uparrow = \frac{1}{2}\left(n - |\vec{m}|\right)$ [24]. Within the context of linear response, this simplification is akin to assuming that E_{Hub} and E_{dc} can be stated as functionals of n and $|\vec{m}|$ alone. As we discussed in Section 1.2.1.6, this assumption is justified in both collinear and non-collinear (with spin-orbit coupling) DFT+U+J, as stated in Equations 1.13 and 1.14. Reassuringly, $|\vec{m}|$ and m hold similar meanings in both non-collinear and collinear DFT, respectively.

For comparison to the "non-collinear" results, we also performed a collinear calculation, where the magnetic configuration for $LiNiPO_4$ was obtained by projecting the canted non-collinear structure shown in Figure 3.11 along the z-direction. In addition to one unit cell of the the collinear antiferromangetic (AFM) configuration, a linear response analysis was performed on a 1×2×2 supercell. Table 3.5 summarizes the results of the computed Hubbard U and Hund J values. From this table, it is evident that the U value is significantly smaller in magnitude with the inclusion of spin-orbit coupling. A possible justification for this behavior is the introduction of orbital contributions to the total localized magnetic moments with the inclusion of spin-orbit coupling [33, 168].

Table 3.5: Hubbard and Hund results for Ni-d in $LiNiPO_4$ (Atom-wise screening). Copyright (2024) by the American Physical Society. Reproduced from Ref. [1] with permission.

cell	magnetism	U (eV)	J (eV)
$1 \times 1 \times 1$	collinear	5.43 ± 0.16	0.38 ± 0.07
$1 \times 2 \times 2$	collinear	5.44 ± 0.24	0.54 ± 0.07
$1 \times 1 \times 1$	non-collinear	5.09 ± 0.15	0.42 ± 0.05

3.1.4.1 Canting angle exploration

In order to explore the effects of Hubbard and Hund parameters on the energetics of non-collinear magnetic structure, we calculated the energy as a function of constrained canting angle, which has been experimentally measured for $LiNiPO_4$ [166]. The non-collinear magnetic constraints were performed in VASP in accordance with the method developed by Ma and Dudarev [169]. We used the experimentally derived spin canted structure as a reference provided by the Bilbao Crystallographic Server, as shown in Figure 3.11 [166, 167]. The energy versus canting angle curve is shown in Figure 3.12a. We found that the stable canting direction is in the opposite direction to the experimentally measured canting angle. However, this discrepancy with experiment was limited to the canting direction; the computed stable magnetic structure still obeyed the symmetry of the $Pnm'a$ magnetic space group.

Similarly to the work by Bousquet and Spaldin [23], we observe an increasing canting angle with Hund J value. Interestingly, adding a U and J correction to O-p results in a slightly decreased stable canting angle. However, we find that in all cases, the computed stable canting angle is significantly less than the experimentally measured canting angle of 7.8 degrees [166].

The constraining effective site magnetic field, $\vec{H}_i^{\text{eff}}$, can be described as the following

$$\vec{H}_i^{\text{eff}} = 2\lambda \left[\vec{M}_i - \hat{M}_i^0 \left(\hat{M}_i^0 \cdot \vec{M}_i \right) \right], \tag{3.10}$$

where $\vec{M}_i$ are the integrated magnetic moments at site i, and $\hat{M}_i^0$ are the unit vectors pointing in the individual site constraining directions [169]. The x component of the constraining field (in the direction of canting), $H_{i,x}^{\text{eff}}$, is plotted versus the constraining angle in Figure 3.12b. We see that where $H_{i,x}^{\text{eff}}$ changes sign corresponds to the minimum of Figure 3.12a.

3.1.4.2 $LiNiPO_4$ response plots

The 2×2 spin-polarized response for Ni-d states is shown in Figure 3.13. In this figure, each subplot corresponds to a different component to the spin-channel response tensor, $\chi^{\sigma\sigma'}$, where $\sigma, \sigma' = \uparrow$ or $\downarrow$.

3.1.4.3 Effect of U and J values on geometry optimization

While the addition of Hubbard and Hund parameters go some way to addressing the canting angle of $LiNiPO_4$, introducing these terms can also alter the geometry of the system. To explore this effect, we performed structural relaxations of the system with various combinations of Hubbard and Hund corrections. In each of the structural relaxation calculations, a maximum force tolerance of 10 meV/Å was used. The Hubbard U and Hund J values used include those calculated using linear response, which are approximations of the values that are reported in Table 3.5. Additionally, we tested the Ni-d U and J values used in Ref. [23]. All calculations included spin-orbit coupling, and were constrained to the experimentally observed canting angle (7.8 degrees).

Table 3.6 lists the optimized unit cell parameters and volume, compared with the experimentally measured geometry [166]. For both the PBE+U_{eff} and PBE+U+J schemes, adding corrections to the Ni-d space worsens the geometry relative to the uncorrected PBE geometry (as earlier observed by Zhou and co-workers [63]). However, the further addition of corrections to the O-p subspace reduces the errors by three-fold, resulting in geometries that are closest to experiment. This is similar to observations in other studies when applying corrections to O-p subspaces [17, 30]. We note that applying a $+J$ correction to non-magnetic O-p states may seem unconventional. However, it should be stressed that this correction is for localized static correlation error effects that do not vanish at zero magnetization. Nor, indeed, does the introduction of $+J$ necessarily induce magnetization, and the projected magnetic moments on $LiNiPO_4$ remain just below 0.01 μ_B, with and without on-site corrections to O-2p states. Meanwhile, we can see that adding a $+J$ parameter does not significantly alter the cell parameters.

3.1.4.4 Discussion on TM-O bond length versus U, J, and V corrections

Table 3.6 also presents the change in mean Ni-O bond length between nearest-neighbor pairs for various on-site corrections. For the Ni-O bond length it is the same story as for the cell parameters: applying U and J to the Ni-d sites worsens the results relative to the PBE result, but by applying corrections to the O-p channels we obtain bond lengths that are in closer agreement with experiment. In Ref. [17], some of us attempted to rationalize this trend in the computed bond length between transition metal species and oxygen anions and how it improves with the introduction of corrections to the O-p subspace. We suggested that when $+U$ is added to the Ni-d subspace the resulting shift in the potential disrupts hybridization between the Ni-d and O-p orbitals, weakening the bonding between these two elements (and thus leading to bond lengthening). Applying corrections to the O-p re-aligns these two subspaces and allows them to "re-hybridize." The DMFT community has sought to address these issues with other approaches, including by tweaking the double-counting term or by using results from GW [170, 171].

In an attempt to more thoroughly explore this reasoning, Figure 3.14 provides a comparison for the projected density of states (DOS) of $LiNiPO_4$ for PBE and PBE+U+J (with

and without corrections to O-p). It is difficult to discern re-hybridization from these DOS plots alone.

Without an explicit quantification of hybridization effects, we have added a derivation in Section 3.1.4.4, that presents a mathematical expression of the forces acting on ions due to $+U+V$ corrections. This result is an extension of the theory put forth by Matteo Cococcioni in Section 4.1 of Ref. [18]. We argue that in quantifying the forces on TM-O bond lengths due to on-site corrections, it is possible to show that the force contributions due to both $+U^{\gamma}$ and $+V^{\gamma\gamma'}$ can, and should, be treated on the same footing, where γ and γ' correspond to atomic sites. It isn't possible to definitively state the comparative magnitude, or sign, of these force contributions without additional calculations or simplifications based on physical intuition. However, the result suggests that the forces on TM-O bond-length due to O-p U values will have a comparative magnitude to the forces due to inter-site Coulomb corrections from $+V$.

In Section 3.1.4.4, we further hypothesized the sign of these force contributions, starting from a DFT geometry-optimized structure without on-site corrections. Using these assumptions, which are based on computational trends in bulk TMOs, we conclude that either applying a $+U$ correction to the O-p manifold or a $+V$ between TM and O states mitigates the overestimation of TM-O bond lengths that arise when applying $+U$ to localized states around the TM species.

3.1.5 Case study: NiO

3.1.5.1 Supercell scaling test & Pseudopotential comparison

In this preliminary test, we perform a supercell scaling study for NiO using the antiferromagnetic (AFM) primitive cell, with lattice vectors $\boldsymbol{a} = [-2.02, +0.00, +2.02]$ Å, $\boldsymbol{b} = [-2.02, +2.02, +0.00]$ Å, and $\boldsymbol{c} = [-4.04, -2.02, -2.02]$ Å. In all calculations, we test the PBE GGA functional, and compare the various PAW PBE 52 pseudopotentials for nickel and oxygen, namely: `Ni_pv`, `Ni`, & `Ni_GW`, as well as `O` & `O_GW`, respectively. While we found that supercell size did not change the U values outside of uncertainty, the type of pseudopotential (PP) used had a very significant effect on the U/J values that resulted. While this isn't all together surprising, this demonstration should serve to underscore the lack of transferability of on-site corrections, which are calculated using the same DFT functional, but a different PP.

3.1.5.2 Full matrix inversion

In this short scaling study on NiO, we perform the full inversion on the primitive cell, and a supercell with twice as many atoms, as shown in Table 3.10. These values are calculated with the screening between all atoms included in the matrix inversion, i.e., 8×8 matrix in the $1 \times 1 \times 1$ cell ($2 \times$ spin-channels $\times$ ($2 \times$ Ni atoms + $2 \times$ O atoms) = 8 sites), and 16×16 matrix in the $2 \times 1 \times 1$ cell.

It is evident that these values change significantly between the two cell sizes - by nearly 1 eV. Therefore, we can conclude that for the full inversion, it is clear that more rigorous supercell scaling must be performed. This is a question that we hope will be addressed in future studies, which are interested in using this framework for obtaining $V^{\gamma\gamma'}$ inter-site exchange values relevant for DFT+U+V.

3.1.5.3 Experiment in self-consistent geometry with applied U & J

In this section, we performed a manual geometry "self-consistency" cycle for the NiO test case. The first iteration uses the relaxed primitive cell from using the MP default U_{eff} for Ni-d of 6.2 eV. For each geometric optimization step, we use an SCF energy convergence of 1.0^{-4} eV (`EDIFF`), which corresponds to a ionic relaxation tolerance of 1.0^{-3} eV (`EDIFFG`). As is evident from the table below, these tolerances were sufficient in order to achieve self-consistent U and J values for Ni-d and O-p, within their corresponding uncertainties. The smaller uncertainty values are due to the fact that we use seventeen evaluations for the linear response analysis, instead of nine in the previous section. The parameters are computed based on the PBE linear response, for the given Lichtenstein DFT+U+J geometry, so this test does not concern corrective parameter self-consistency per se. For this system, it is apparent that geometry-self-consistent on-site corrections are achieved within the first iteration. However, this may not be true for more complex oxides, in which the rotation of oxygen polyhedra play a more crucial role.

3.1.5.4 Electron localization function

In our study of NiO, we apply the electron localization function (ELF) to the system, as defined by Silvi et al. [172] and implemented in VASP, which is written to the ELFCAR output file. Other studies have shown that the ELF provides insight into locations of high self-interaction error (SIE) [173]. In Figures 3.15a - 3.15c, we provide a comparison over the visualized isosurfaces of the ELF for various levels of on-site corrections. We continue to focus on the antiferromagnetic primitive cell of NiO studied in Section 3.1.5.1. Applying the $+U+J$ to all sites in this case appears to have the strongest effect on the localization around the O-p states. It is interesting to note that it appears that in Figure 3.15b, applying on-site corrections to Ni-d sites appears to have a stronger effect on the localization function surrounding the oxygen atoms than the nickel atoms. While these visualizations are interesting to observe, it is difficult to conclude on this basis why a larger U value is needed for O-p sites.

(a) Periodic Table of Hubbard U values computed from first principles.

(b) Periodic Table of Hund J values computed from first principles.

Figure 3.1: Periodic table of Hubbard U and Hund J values computed for representative set of transition metal oxides. The color map indicates the mean value computed for each element over each material. The materials used in the creation of these periodic tabled were selectively chosen: noting that many databases, including the ICSD, contain a growing number of hypothetical materials which may or may not be realizable, we selected materials that are well-studied and exhibit more than two ICSD IDs each. Furthermore, to remove cross-correlations between magnetic elements, we also require that these compounds only contain a single d-block element (occupying a single symmetrically-equivalent site) with no f-block species. Ultimately, these data correspond to the U and J values for over 800 materials, and are distributed over the transition metal species. A more detailed table containing data on the distribution of values is included in Table 3.2 in the Appendix. The plotted distributions of U/J values are generated using a Gaussian kernel-density estimator implemented in `scipy` [112].

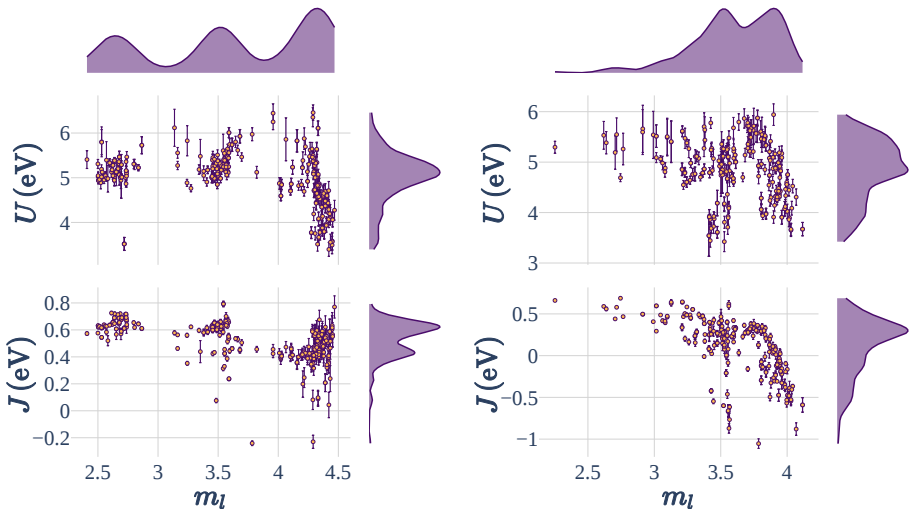

Figure 3.2: Distributions of Hubbard U and Hund J values computed using the linear response method; For the sub-figures (a), (b), and (c) that correspond to d-electron TM site corrections, the U and J values are plotted against the DFT (no $+U+J$ correction) computed site magnetic m_l, where $m_{l=2}$ corresponds to the d-character of the local moment, which has an $l = 2$ angular momentum quantum number. The O-p U and J values in sub-figure (d) are plotted against n_l (the p-occupation in the case of O-2p) total site occupations. The number of samples for on-site correction values for Mn-d, Fe-d, Ni-d, and O-p are 285, 248, 149, and 206, respectively. Copyright (2024) by the American Physical Society. Reproduced from Ref. [1] with permission.

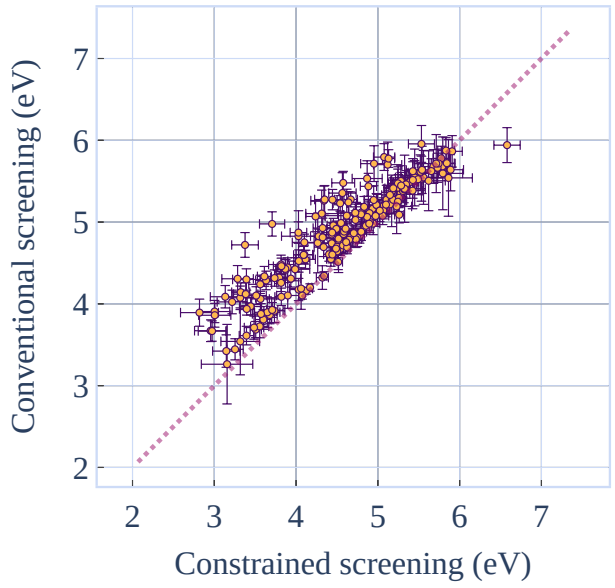

(a) Hubbard U (Fe-d)

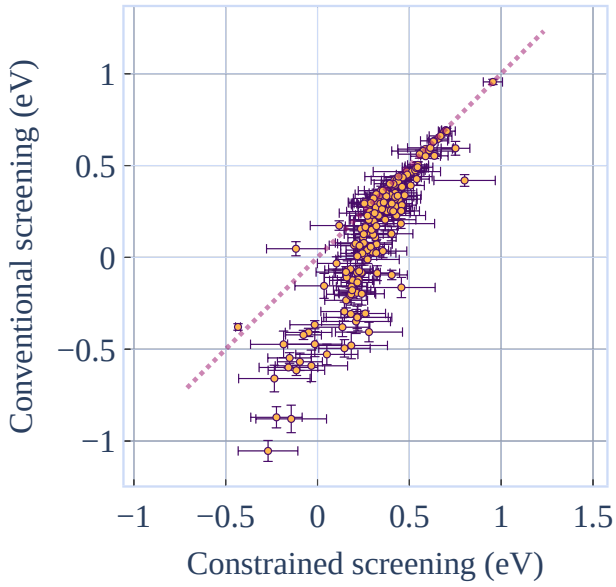

(b) Hund J (Fe-d)

Figure 3.3: Comparison between the conventional and constrained approaches for calculating (a) Hubbard U and (b) Hund J values for Fe-d Hubbard sites. Copyright (2024) by the American Physical Society. Reproduced from Ref. [1] with permission.

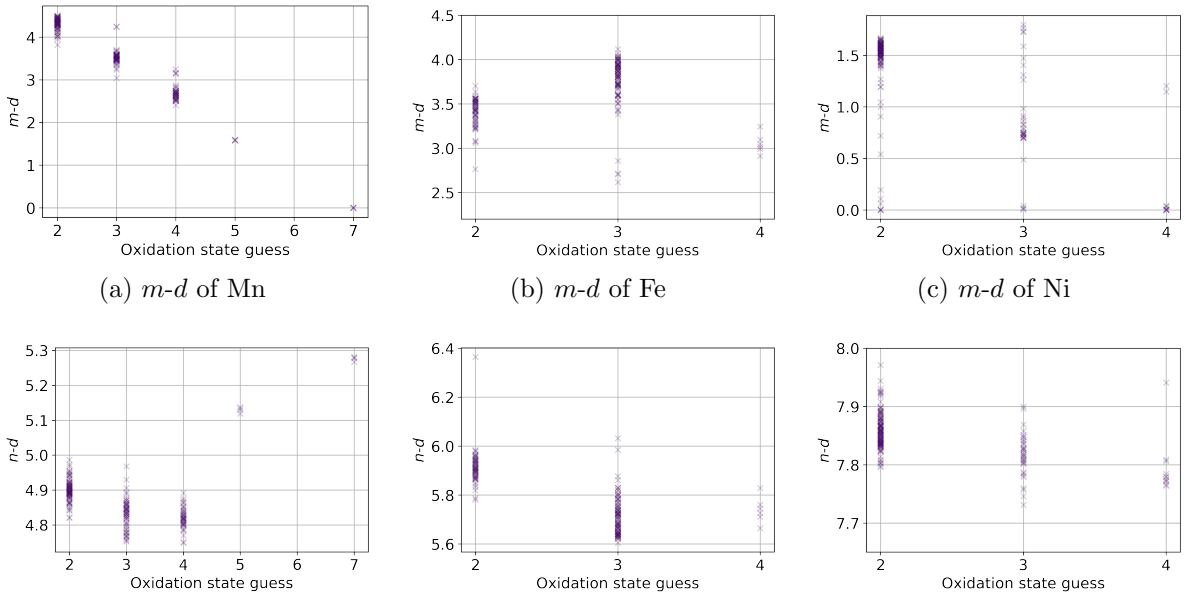

(a) m-d of Mn (b) m-d of Fe (c) m-d of Ni

(d) n-d of Mn (e) n-d of Fe (f) n-d of Ni

Figure 3.4: Each sub-figure provides a scatter plot of the computed m-d and n-d site occupations for Mn, Fe, and Ni, obtained from DFT calculations (without $+U/J$). These values are plotted against the "guessed" oxidation states using the bond valence method (BVM), as implemented in [70]. Copyright (2024) by the American Physical Society. Reproduced from Ref. [1] with permission.

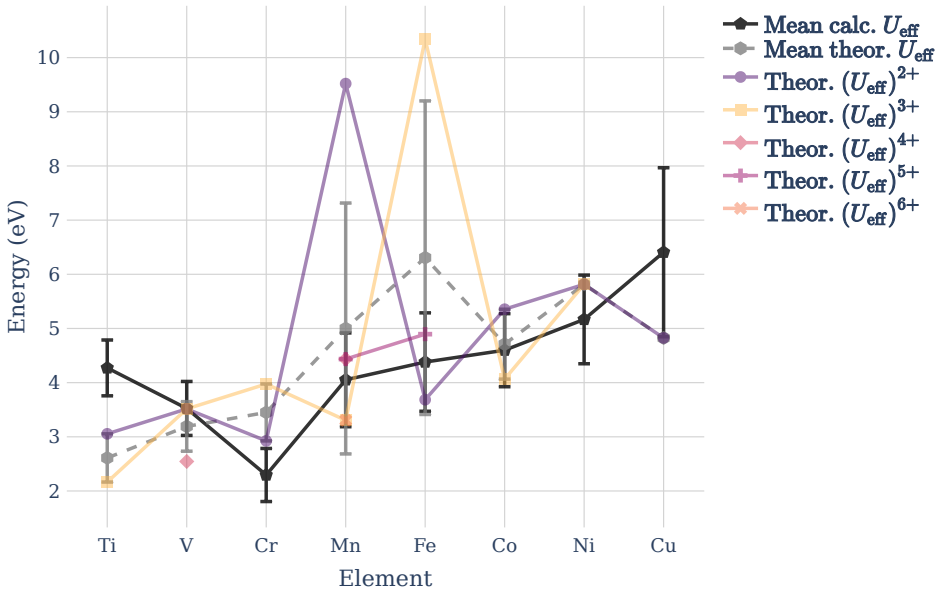

(a) Calculated Hubbard U_{eff} versus theoretical counterpart.

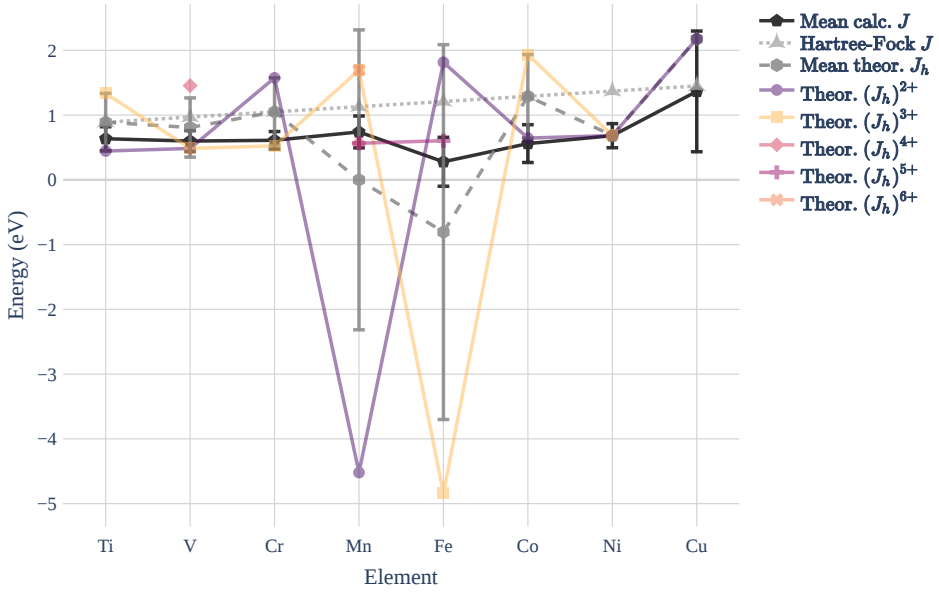

(b) Calculated Hund J versus theoretical unscreened J and $J_h = F^0 - U_{\text{eff}}$.

Figure 3.5: Mean computed (a) U_{eff} and (b) J for $3d$ block elements versus the theoretical counterparts from multiplet theory, as covered in Section 3.1.2.4. The error-bars indicate the corresponding standard deviation. The linear scaling relationship of C and J versus atomic number, Z, are from those reported in Ref. [116]. The scaling that we employ for F^0 is $F^0 = 3.0 + 0.5(Z - 21)$ eV, which we justify in the main text. In addition to the Hartree-Fock J (linear scaling) [116], we plot $J_h = F^0 - U_{\text{eff}}$.

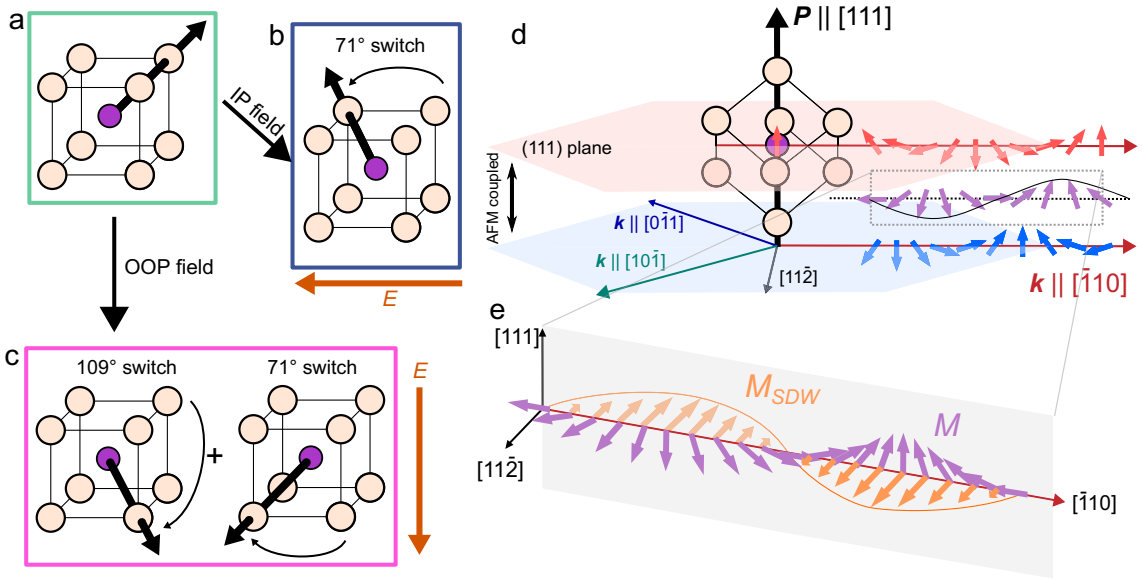

Figure 3.6: Complex structure of $BiFeO_3$. ***a*** Schematic unit cell of BFO with P along $[1\,1\,1]$. In thin films, an electric field applied in-plane, ***b*** switches the polarization by 71° to $[\bar{1}\,1\,1]$. In contrast, a field applied in the out-of-plane direction, ***c*** will drive successive 71° and 109° switches, resulting in a 180° final polarization along $[\bar{1}\,\bar{1}\,\bar{1}]$. ***d*** Iron moments in BFO are antiferromagnetically aligned along the $[1\,1\,1]$, modulated by the cycloid propagation along $\boldsymbol{k}$, $[\bar{1}\,1\,0]$. Other allowed directions of $\boldsymbol{k}$ also lie within this $(1\,1\,1)$. The canting of the AFM alignment gives rise to an uncompensated magnetization, $M(\boldsymbol{r})$, which rotates primarily in the $\boldsymbol{k}$-$\boldsymbol{P}$ plane with the same period as the antiferromagnetic moments, $\sim$ 65 nm. ***e*** M is further frustrated by DMI associated with the octahedral rotations, giving rise to a modulation $M_{SDW}(\boldsymbol{r})$ out of the $\boldsymbol{k}$-$\boldsymbol{P}$, $(1\,1\,\bar{2})$ plane. The $(1\,1\,\bar{2})$ plane is shown by the shaded plane and M_{SDW} points along the $[1\,1\,\bar{2}]$ direction. Copyright (2024) Springer Nature. Reproduced from Ref. [2] with permission.

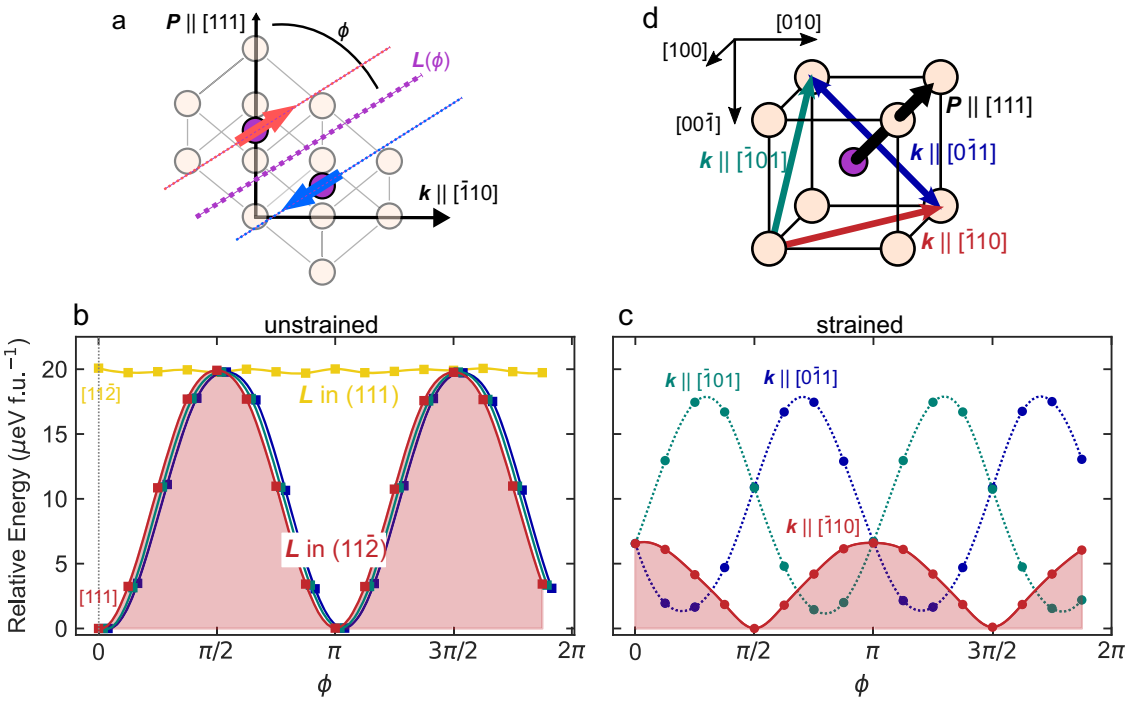

Figure 3.7: Resolution of $\mathbf{M}_{\mathrm{SDW}}$ from first principles. ***a*** Schematic showing the initialization angle θ within the cycloid plane for the antiferromagnetically aligned Fe spins. ***b*** Comparison of the magnetocrystalline anisotropy of the bulk unit cell when the Fe spins are rotated in the $(1\,1\,1)$ and $(1\,1\,\bar{2})$. This agrees with the expectation that the cycloid rotates within $(1\,1\,\bar{2})$, as the mean value of the energy is $2\times$ higher when moving the rotation to the $(1\,1\,1)$ plane. ***c*** Relative energy along the three possible $\boldsymbol{k}$ directions when the unit cell is epitaxially strained to DSO. The mean energy is $2\times$ lower when the cycloid propagates along the in-plane $[\bar{1}\,1\,0]$ direction, agreeing with our experimental observation. The dotted lines show the mean energy values. ***d*** Schematic of the three $\boldsymbol{k}$ directions in ***c***. Copyright (2024) Springer Nature. Reproduced from Ref. [2] with permission.

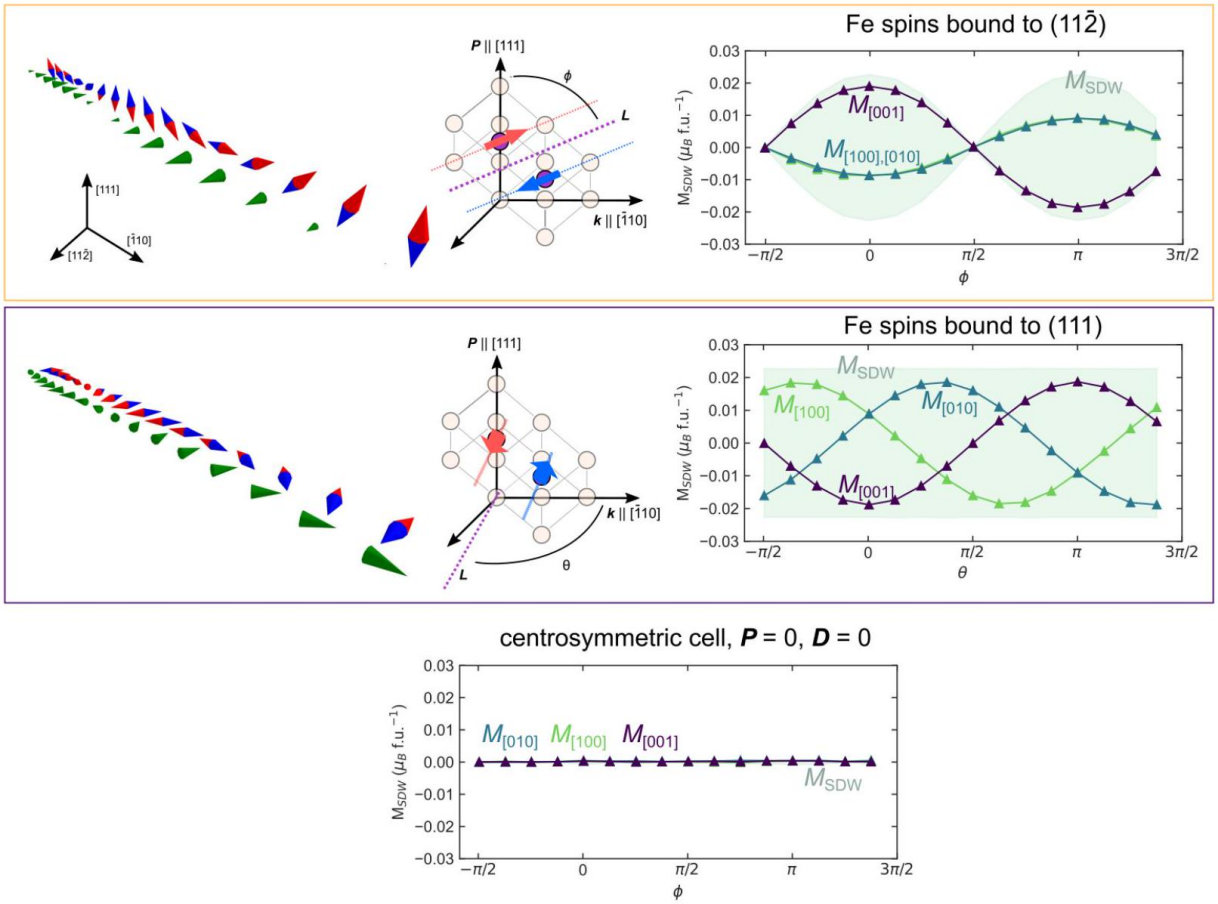

Figure 3.8: Modulation of M_{SDW} due to the cycloid. ***a*** In the discretized DFT calculations, when the Fe spins are rotated in the $(1\,1\,\bar{2})$, we observe the emergence of M_{SDW} in the $[1\,1\,\bar{2}]$ direction due to the interaction with the DMI caused by the antiferrodistortive rotations of the FeO_6 octahedra, pointing along the direction of $\boldsymbol{P}$. From symmetry, $H_{ij}^{DM} = \boldsymbol{D_{ij}} \cdot \left(\boldsymbol{S_i} \times \boldsymbol{S_j}\right)$ which, because S_i and S_j are bound to the $(1\,1\,\bar{2})$ plane and $\boldsymbol{D}_{ij} \| \boldsymbol{P}$, the energy is minimized when $\boldsymbol{S}_{i,j} \parallel [\bar{1}\,1\,0] \perp \boldsymbol{P}$, thus $\boldsymbol{S}_{i,j}$ cants in the $[1\,1\,\bar{2}]$ direction. **b** We observe that when we bind the spins to other crystallographic planes, here $(1\,1\,1)$, this interaction does not form a spin density wave and instead the resultant M forms a cycloid with the same periodicity as the Fe spins. This unmodulated moment is thus compensated and would not be seen with NV microscopy [158], implying that the case in a must be approximately true in our samples. ***c*** As a further control, the same calculation is performed with an imposed centrosymmetry on the BFO unit cell. In this case, there is no canted moment from the simulations, confirming the mechanism of formation from $\boldsymbol{D}_{ij}$ arising due to the ferroelectric polarization. Copyright (2024) Springer Nature. Reproduced from Ref. [2] with permission.

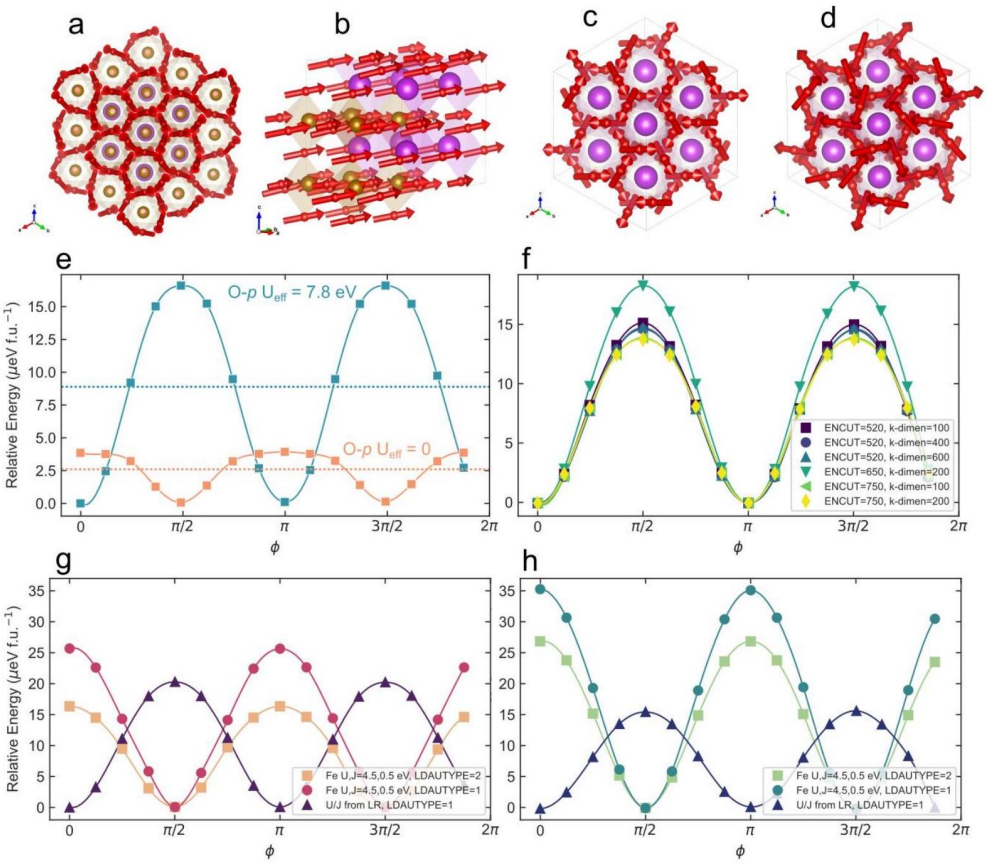

Figure 3.9: DFT methodology. **a-d** Visualized distortions induced from various origins, as well as energy path comparisons over various DFT parameters. To provide a reference chirality of parent AFD distortions, **a**, arrows indicating the displacements of the cubic structure relative to the distorted structure, as reported in Ref. [159]. The relaxed relative distortions under strain is visualized in **b**. Additionally, **c** shows the reduction in antiferrodistortive (AFD) rotations due to the addition of Hund J applied to Fe-d, and **d**, the further reduction in AFD magnitude due to Hubbard corrections to the Bi-p and O-p manifolds. **e** Energies versus rotation angle for $\boldsymbol{k} \parallel [\bar{1}\,1\,0]$, with and without U_{eff} applied to the oxygen $2p$ states. The input structure itself is relaxed with Fe-d: U, J = 5.2, 0.4 eV and O-p: U, J = 9.7, 1.9 eV Hubbard corrections. **f** Anisotropy energy for different energy cutoffs (ENCUT) and k-point densities demonstrating that we have performed a proper convergence test versus the resolution of DFT calculations. **g**, **h** Energy versus rotation angle for different on-site corrections, compared for two different relaxed structures. The linear response Hubbard corrections correspond to Fe-d: U, J = 5.2, 0.4 eV, Bi-p: U, J = 0.8, 0.8 eV, and O-p: U, J = 9.7, 1.9 eV. The structure in **g** is relaxed with these Hubbard parameters, whereas **h** is relaxed with U_{eff} = 4.0 eV applied to Fe-d sites. Copyright (2024) Springer Nature. Reproduced from Ref. [2] with permission.

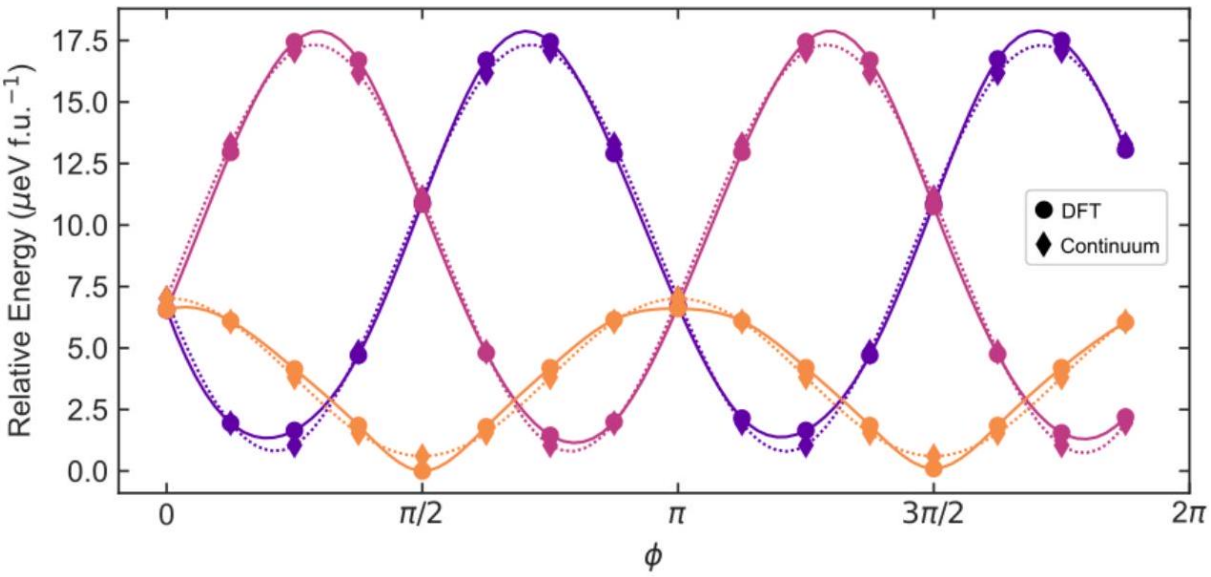

Figure 3.10: Strain dependence of the cycloid propagation. Piecewise DFT calculations for the cycloid in the relaxed supercell, showing the dependence of $\boldsymbol{k}$. In the bulk crystal, the three possible cycloid directions are energetically equivalent, which makes sense given the 3 -fold symmetry of the rhombohedral unit cell. In the epitaxially strained case, this 3-fold symmetry is disrupted by the biaxial strain in the (0 0 1) due to epitaxy, inducing a preferred direction within the (0 0 1). Data overlayed with fits to Equation 3.7 shown as dashed lines.

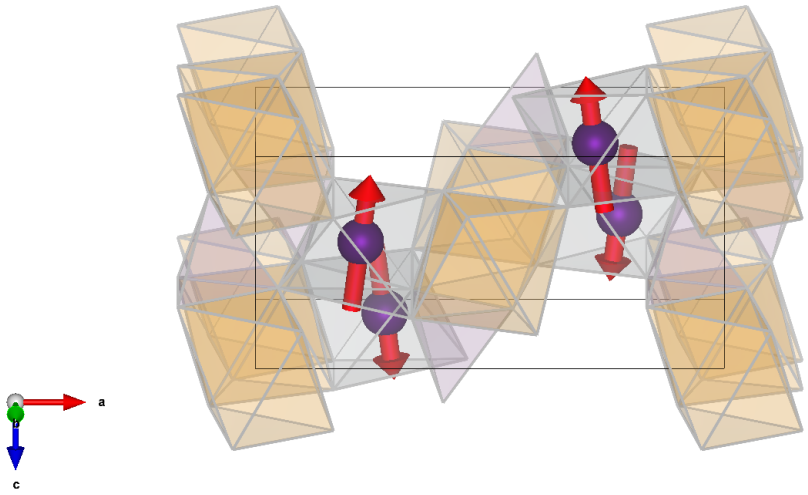

Figure 3.11: Olivine crystal structure of $LiNiPO_4$ with magnetic atoms visible. Taken from [166] via the Bilbao MAGNDATA database [166, 167]. The purple atoms correspond to magnetic nickel atoms. The oxygen octahedra surrounding lithium atoms are indicated in orange, where the grey oxygen octahedra surround nickel sites.

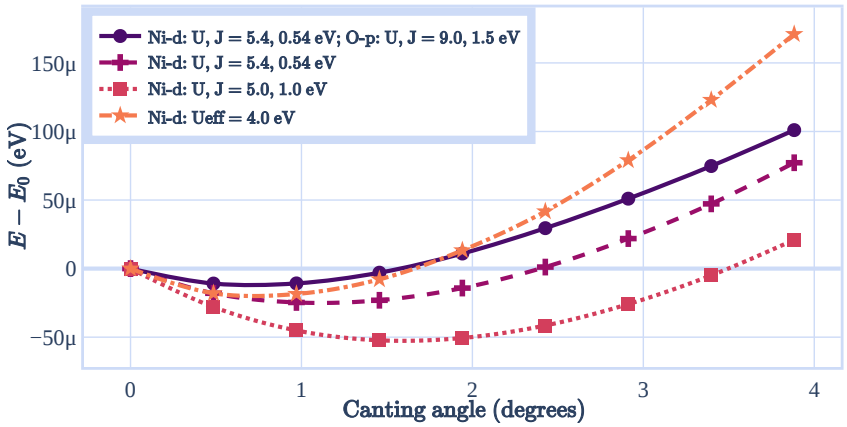

(a) Computed energy versus constraining canting angle

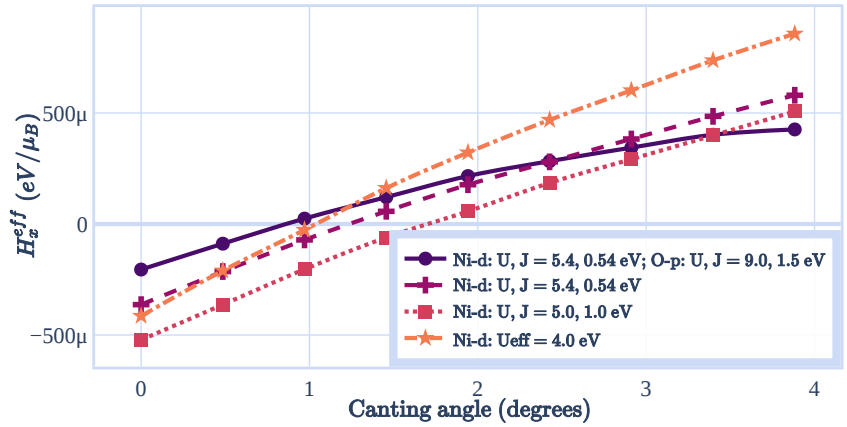

(b) Effective constraining field versus constraining canting angle

Figure 3.12: (a) Computed relative energy and (b) x-component of effective constraining local magnetic field for various Hubbard and Hund on-site corrections applied to the Ni-d and O-p manifolds. Copyright (2024) by the American Physical Society. Reproduced from Ref. [1] with permission.

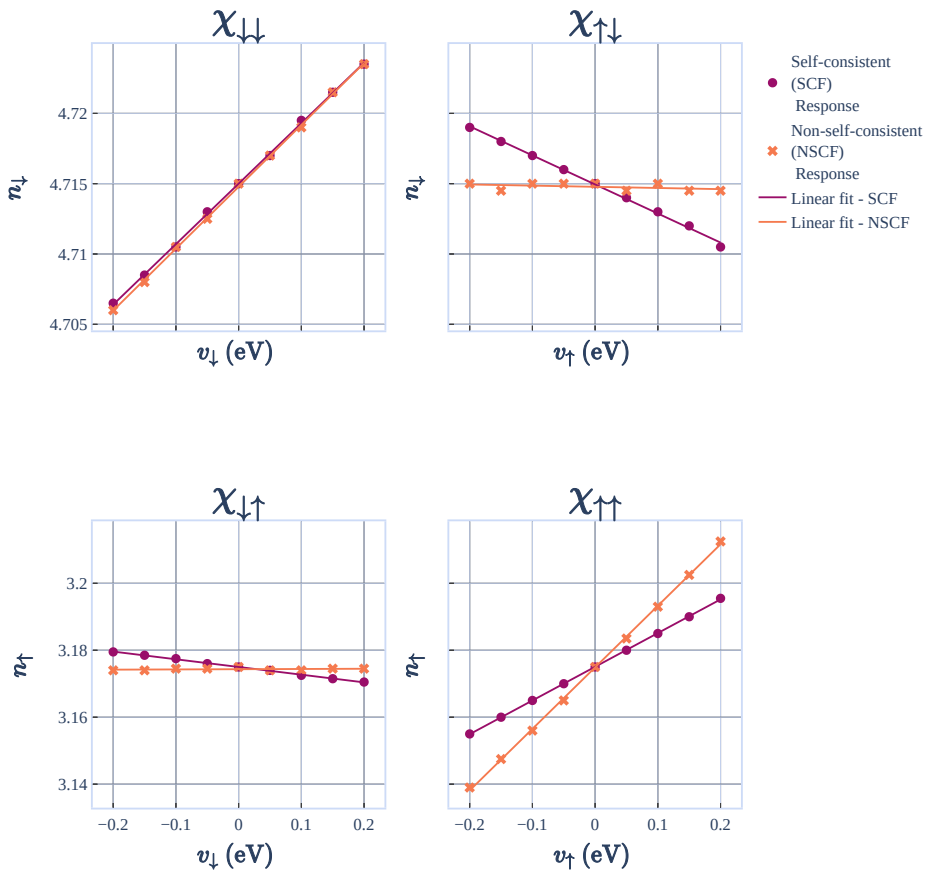

Figure 3.13: Linear response results for Ni-d within $LiNiPO_4$; Response data and linear fit shown in magenta for self-consistent (SCF) and orange for non-self-consistent (NSCF) results; $\chi^{\uparrow\uparrow}$, $\chi^{\uparrow\downarrow}$, $\chi^{\downarrow\uparrow}$, and $\chi^{\downarrow\downarrow}$ responses corresponding to elements of 2×2 response matrix.

Table 3.6: Lattice parameters, cell volume, and mean Ni-O bond length (d) of $LiNiPO_4$ canted structure for different Hubbard U and Hund J corrections. Copyright (2024) by the American Physical Society. Reproduced from Ref. [1] with permission.

method	Ni-d (eV)	O-p (eV)	a (Å)	b (Å)	c (Å)	volume (Å^3)	d (Å)
experiment			10.03	5.85	4.68	274.93	2.086 ± 0.044
PBE			10.09 (+0.6%)	5.92 (+1.1%)	4.72 (+0.9%)	282.09 (+2.6%)	2.099 ± 0.037
PBE+U_{eff}	$U_{\text{eff}} = 4$	$U_{\text{eff}} = 0$	10.14 (+1.1%)	5.92 (+1.1%)	4.73 (+1.0%)	283.71 (+3.2%)	
		$U_{\text{eff}} = 7.5$	10.07 (+0.4%)	5.87 (+0.3%)	4.69 (+0.3%)	277.56 (+1.0%)	
PBE+U+J	$U = 5$	U, $J = 0$	10.15 (+1.2%)	5.92 (+1.1%)	4.73 (+1.0%)	284.19 (+3.4%)	2.108 ± 0.039
	$J = 1$	U, $J = 9$, 1.5	10.07 (+0.4%)	5.88 (+0.4%)	4.69 (+0.3%)	277.86 (+1.1%)	2.095 ± 0.043

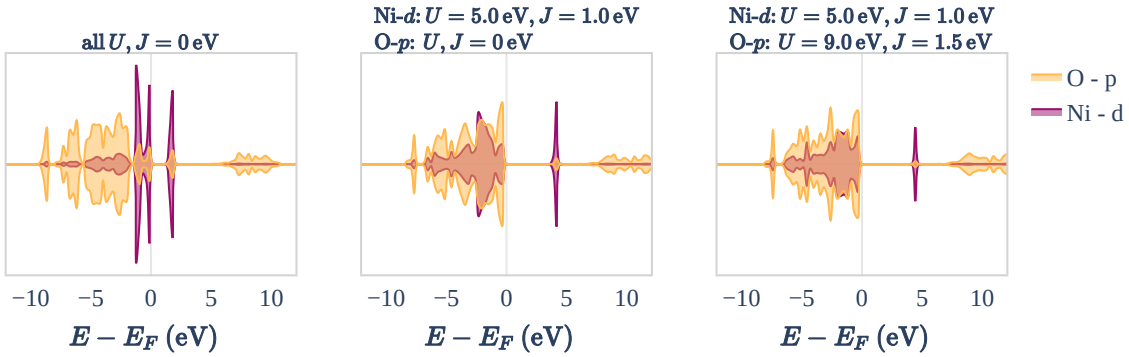

Figure 3.14: Projected electronic density of states for $LiNiPO_4$ (calculated using experimental unit cell [166]) without Hubbard or Hund corrections applied, as well as $+U$ and $+J$ applied to Ni-d channels, and both Ni-d and O-p states, respectively. Copyright (2024) by the American Physical Society. Reproduced from Ref. [1] with permission.

Table 3.7: Ni-d Hubbard U scaled atom-wise (in eV).

Supercell	PAW PBE 52 pseudopotential		
	`Ni_pv`	`Ni`	`Ni_GW`
$1 \times 1 \times 1$	6.10 ± 0.19	5.27 ± 0.12	1.50 ± 0.03
$2 \times 1 \times 1$	5.92 ± 0.17	5.21 ± 0.13	1.58 ± 0.03
$2 \times 2 \times 1$	6.04 ± 0.17	5.24 ± 0.15	1.57 ± 0.03
$2 \times 2 \times 2$	6.15 ± 0.18	5.19 ± 0.14	1.56 ± 0.03
$4 \times 2 \times 2$	6.09 ± 0.16	-	-
$4 \times 4 \times 4$	6.02 ± 0.16	-	-

Table 3.8: Ni-d Hund J scaled atom-wise (in eV).

Supercell	PAW PBE 52 pseudopotential		
	`Ni_pv`	`Ni`	`Ni_GW`
$1 \times 1 \times 1$	0.846 ± 0.032	0.757 ± 0.023	0.315 ± 0.009
$2 \times 1 \times 1$	0.709 ± 0.030	0.668 ± 0.025	0.269 ± 0.008
$2 \times 2 \times 1$	0.733 ± 0.029	0.670 ± 0.025	0.267 ± 0.008
$2 \times 2 \times 2$	0.700 ± 0.029	0.662 ± 0.025	0.261 ± 0.009
$4 \times 2 \times 2$	0.710 ± 0.027	-	-
$4 \times 4 \times 4$	0.707 ± 0.028	-	-

Table 3.9: O-p scaled atom-wise.

Supercell	PAW PBE 52 pseudopotential			
	`O`		`O_GW`	
	U (eV)	J (eV)	U (eV)	J (eV)
$1 \times 1 \times 1$	9.1868 ± 0.1812	1.2290 ± 0.0345	8.61 ± 0.04	1.133 ± 0.013
$2 \times 1 \times 1$	9.7752 ± 0.1838	1.2290 ± 0.0345	8.78 ± 0.04	1.215 ± 0.033
$2 \times 2 \times 1$	9.7364 ± 0.2848	1.3587 ± 0.0410	8.72 ± 0.06	1.321 ± 0.053
$2 \times 2 \times 2$	9.6771 ± 0.1854	1.2681 ± 0.0410	8.52 ± 0.07	1.424 ± 0.065

Table 3.10: Ni-d scaled full (`Ni_pv` PAW PBE 52 pseudopotential)

Supercell	U (eV)	J (eV)
$1 \times 1 \times 1$	4.445 ± 0.134	1.0173 ± 0.0398
$2 \times 1 \times 1$	5.311 ± 0.095	0.9178 ± 0.0240

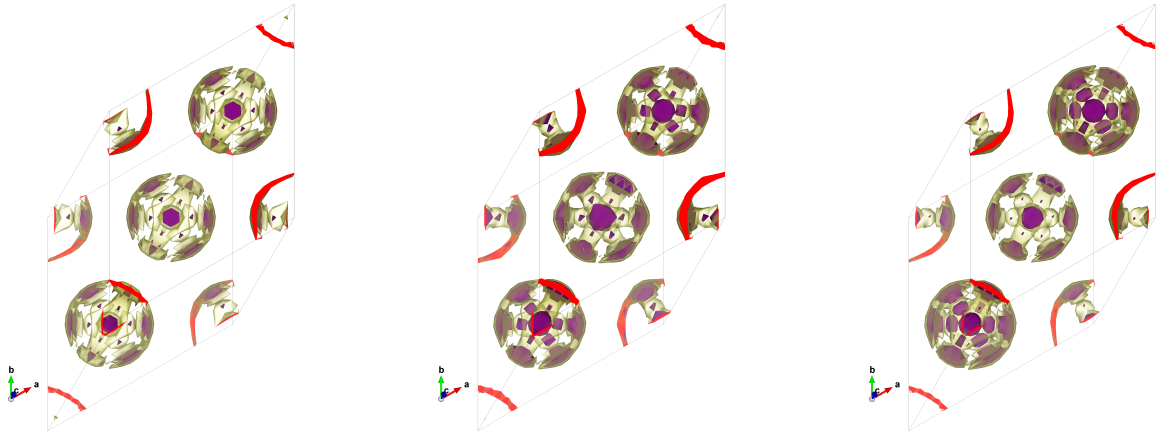

(a) All $U, J = 0.0$ eV

(b) Ni-d: $U, J = 6.3, 0.8$ eV
O-p: $U, J = 0.0$ eV

(c) Ni-d: $U, J = 6.3, 0.8$ eV
O-p: $U, J = 10.0, 1.5$ eV

Figure 3.15: Visualization of electron localization function iso-surfaces in NiO cell (a) without Hubbard or Hund corrections applied, as well as (b) +U and +J applied to Ni-d channels, and (c) both Ni-d and O-p states, respectively. The two nickel atoms are located in the center and corners of the unit cell. The isosurface levels are at 0.142 and 0.146.

Table 3.11: Cell relaxation & linear response iterations.

Iteration	Ni-d: U (eV)	Ni-d: J (eV)	O-p: U (eV)	O-p: J (eV)	Lattice vectors (Å)
1	5.831 ± 0.064	0.422 ± 0.021	10.326 ± 0.068	1.103 ± 0.008	$\boldsymbol{a} = [-2.34, +0.00, +2.37]$ $\boldsymbol{b} = [-2.34, +2.36, +0.00]$ $\boldsymbol{c} = [-4.67, -2.35, -2.36]$
2	5.884 ± 0.070	0.551 ± 0.021	9.755 ± 0.053	1.125 ± 0.007	$\boldsymbol{a} = [-2.23, +0.00, +2.23]$ $\boldsymbol{b} = [-2.23, +2.23, +0.00]$ $\boldsymbol{c} = [-4.45, -2.23, -2.23]$
3	5.881 ± 0.070	0.547 ± 0.021	9.788 ± 0.054	1.124 ± 0.007	$\boldsymbol{a} = [-2.23, +0.00, +2.23]$ $\boldsymbol{b} = [-2.23, +2.23, +0.00]$ $\boldsymbol{c} = [-4.45, -2.23, -2.23]$

Chapter 4

Source-free exchange correlation functional

You spin me right 'round, baby, right 'round
Like a record, baby, right 'round, 'round, 'round

Dead or Alive

Building on the methods and theory introduced in Sections 2.2 and 1.2.1.9, in this chapter we explore the improved convergence properties of the source-free exchange correlation functional over a diverse set of crystalline material test cases [3]. In addition to the correct Hubbard U and Hund J values used [1, 2], we find that this functional correction [3, 37] improves the convergence to the correct symmetric magnetic ground-state. While Hubbard corrections tend to localize moments, the source-free correction tends to delocalize the moments in comparison [37].

4.1 DFT specifications

In all magnetic systems and VASP calculation settings that we tested, we found improved convergence of the SF XC functional using the blocked Davidson (BD) algorithm (`ALGO = Normal`, `IALGO = 38`) compared with the preconditioned conjugated gradient (PCG) algorithm (`ALGO = All`, `IALGO = 58`). Using the PCG algorithm, we found in most instances that the energy decreased up to a threshold, and then increased up to a self-consistency step, after which the absolute energy difference between self-consistency steps decreased very slowly. By comparison, the BD algorithm often required an order of magnitude fewer number of self-consistency steps to converge. Therefore, we strongly recommend that for the SF XC implementation in VASP, users use the BD algorithm (`ALGO = Normal`, `IALGO = 38`). In many instances the source-free constrained PBE calculations took significantly longer to

converge than the conventional PBE counterparts. However, this is not entirely surprising because one would expect the additional constraint on $\boldsymbol{B}_{xc}$ to require a longer convergence trajectory. In a significant number of calculations, on the other hand, we found that the SF calculations converged within a few iterations, similar to their non-SF equivalent. For small enough perturbation from the ground-state, the $\mathrm{PBE_{SF}}$ calculations converged quicker than conventional noncollinear PBE, such as in the case of Mn_3As.

4.2 Results

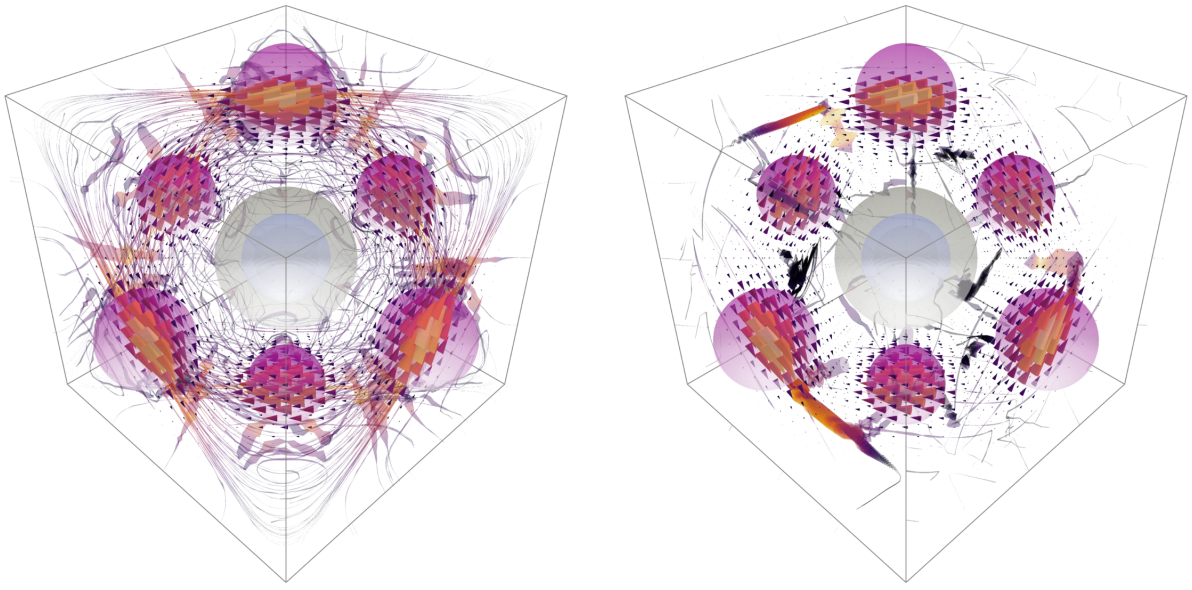

(a) $\mathrm{PBE_{SF}}$ (b) PBE

Figure 4.1: $\mathrm{PBE_{SF}}$ versus PBE comparison plot of ground state magnetization density $\boldsymbol{m}(\boldsymbol{r})$ (vector field) and $\boldsymbol{B}_{xc}(\boldsymbol{r})$ (streamlines) viewed along [111] direction for Mn_3ZnN. Copyright (2023) arXiv. Reproduced from Ref. [3] with permission.

These magnetic structures were obtained from the Bilbao MAGNDATA database [174]. All structures in this study contained less than sixteen atoms in their unit cell. The materials contained in this data set include metallic systems, i.e. Mn_3Pt [176], as well as insulators, i.e. MnF_2 [177]. We take an in-depth focus of Mn_3ZnN [178], because its non-collinear ground state is accomodated by a relatively small unit cell comprised of only three symmetrically disctinct magnetic Mn ions.

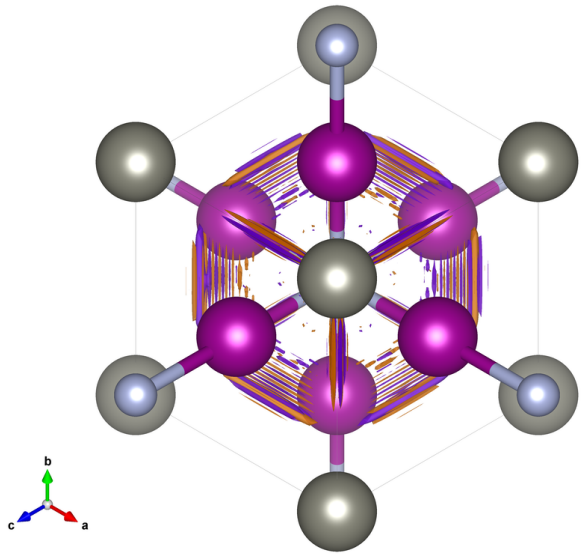

Figure 4.2: Isosurface VESTA plot of PBE ground state $\nabla \cdot \boldsymbol{B}_{xc}(\boldsymbol{r})$ viewed along [111] direction for Mn_3ZnN. Positive isosurface is indicated in violet, and negative counterpart in orange, at a fixed isosurface level. Manganense, zinc, and nitrogen atoms are color-coded in magenta, grey, and light blue, respectively. Copyright (2023) arXiv. Reproduced from Ref. [3] with permission.

Furthermore, for Mn_3ZnN (Figure 4.6) it is clear that the curl of the magnetization, $\nabla \times \boldsymbol{m}$, varies by a much larger relative magnitude than that of Mn_3Pt (Figure 4.7). This can be ascertained by the circulation of spins around the [1 1 1] direction in Mn_3ZnN, which can be seen in Figure 4.1 and Figure 4.6 [178]. We care about a large variance in the spin current for multiple reasons. The first reason has to do with the gauge symmetries of SDFT and CDFT, as explored in Ref. [38]. After all, our goal in this study is to computationally explore these degeneracies. The second reason is that the curl of the magnetization enters into the expression for the net XC torque, as stated in Equation (2.76). Hence, we surmise that the magnetic structure of Mn_3ZnN will test the limits of the ZTT, and to what degree it is, or isn't upheld at the point of self-consistency.

4.2.1 Quantifying the effects of monopoles

We found that for the Mn_3ZnN calculations, the PBE+U+J calculation yielded $|\nabla \cdot \boldsymbol{B}_{xc}(\boldsymbol{r})|_\infty \approx 104$ eV/(μ_B Å^4), and for the source-free PBE+U+J counterpart, $|\nabla \cdot \boldsymbol{B}_{xc}(\boldsymbol{r})|_\infty < 10^{-13}$ eV/(μ_B Å^4), where $|\nabla \cdot \boldsymbol{B}_{xc}(\boldsymbol{r})|_\infty = \max_{\boldsymbol{r}\in\mathbb{R}^3} \left|\nabla \cdot \boldsymbol{B}_{xc}(\boldsymbol{r})\right|$. This numerical comparison confirms that the source-free constraint is working as expected, and draws attention to the large density of magnetic monopoles that form in conventional non-collinear PBE+U+J. A visu-

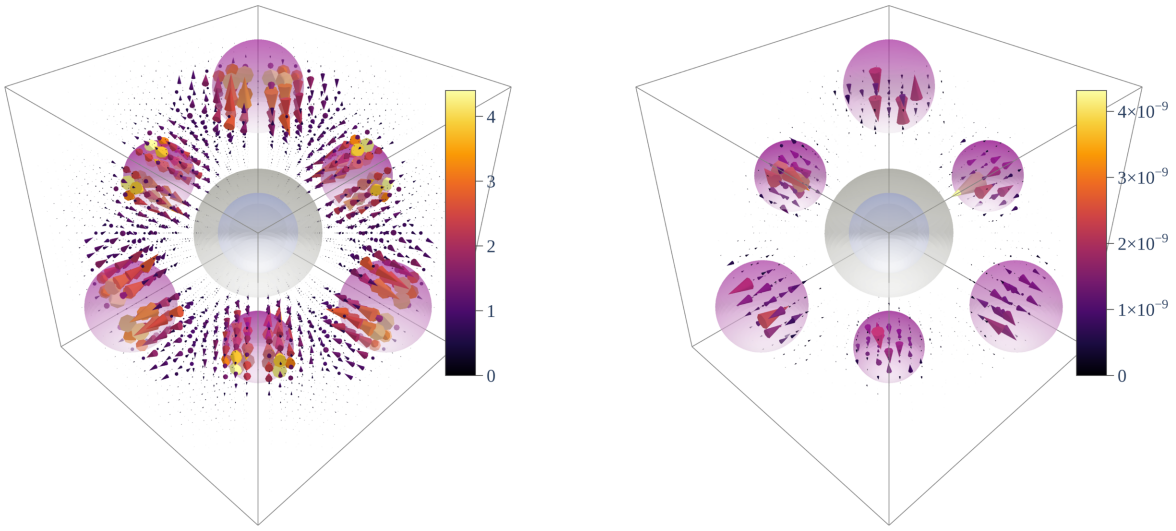

(a) $\mathrm{PBE_{SF}}$ (b) PBE

Figure 4.3: $\mathrm{PBE_{SF}}$ versus PBE comparison plot of ground state magnetic torque vector field $\boldsymbol{\tau}_{xc} = \boldsymbol{m}(\boldsymbol{r}) \times \boldsymbol{B}_{xc}(\boldsymbol{r})$ (vector field) viewed along [111] direction for Mn_3ZnN. The units are in $(\mu_B \text{ eV})/(\mu_B \text{ Å}^3)$. Copyright (2023) arXiv. Reproduced from Ref. [3] with permission.

alization of the monopole density in the Mn_3ZnN test case is provided in Figure 4.2. We hone in on this material for reasons of computational cost and clear visualization. Namely, Mn_3ZnN exhibits a highly non-collinear spin texture, describable with a commensurate unit cell of only three magnetic atoms. Furthermore, this magnetic antiperovskite is known to exhibit exceptionally large and exotic magnetostriction effects [179], which is relevant to magnetostructural phase transitions and therefore magnetocalorics [180].

4.2.2 Local convergence test

In order to compare the convergence of GGA-$\mathrm{PBE_{SF}}$ to conventional non-collinear GGA-PBE, we performed tests on the set of commensurate magnetic structures containing transition metal elements. To test the convergence of all structures, we apply a random perturbation from the experimental structure to all magnetic moments. The rotations of local moments are performed by an implementation of the Rodrigues' rotation formula within a cone angle of 45°.

To compare the performance of the source-free functional versus its SDFT counterpart, we provide a magnetic moment comparison (in Figure 4.4) as well as a symmetry comparison (in Figure 4.5). For the magnetic moment comparison, we plot the mean difference across

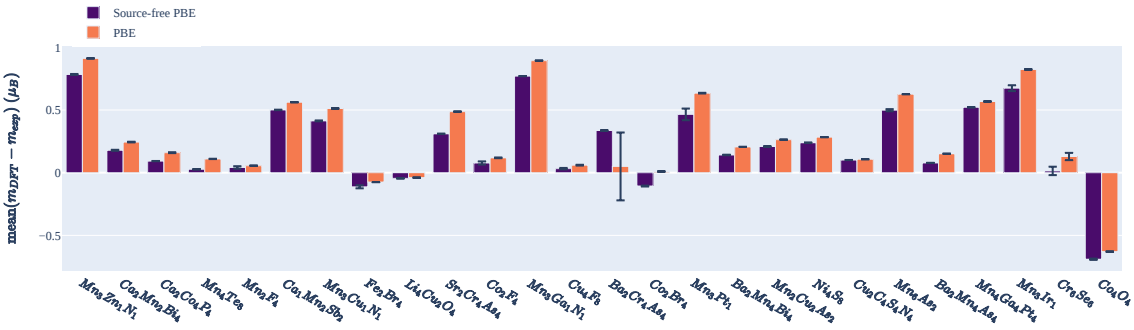

Figure 4.4: Comparison plot of magnetic moment differences with experiment for PBE+U+J and PBE$_{\mathrm{SF}}$+U+J for a selected number of experimental structures from the MAGNDATA Bilbao Crystallographic Server [174]. The y-axis is the difference metric $(1/N)\sum_i(m^i_{\mathrm{DFT}} - m^i_{\mathrm{exp}})$, where m^i_{DFT} and m^i_{exp} are the magnetic moment magnitudes for site "i" from the DFT-computed and experimental magnetic structures, respectfully. Copyright (2023) arXiv. Reproduced from Ref. [3] with permission.

magnetic moments computed using GGA-PBE$_{\mathrm{SF}}$+U+J versus GGA-PBE+U+J. We observe that for all of these magnetic systems, the source-free functional predicts a moment that is slightly smaller than its source-free counterpart, bringing it in closer agreement with experiment, for most systems.

In order to probe the comparison between non-collinear ground states themselves, we show a symmetry metric comparison between converged structures from GGA-PBE$_{\mathrm{SF}}$+U+J and GGA-PBE+U+J in Figure 4.5. For this study, we used the `findsym` program from the ISOTROPY software suite developed by Stokes et al. [175]. We define this symmetry metric to be the minimum tolerance (in μ_{B}), normalized by the absolute maximum magnitude of the individual magnetic moments within the structures, and scaled as a percentage value. Therefore, 0% implies perfect agreement with experimentally resolved magnetic space-group, whereas 100% implies poor agreement. We emphasize that for this study, we use mean U and J values taken from Ref. [1]. In principle, one should calculate these U and J values for each structure, as U and J are very sensitive to local chemical environment, and therefore oxidation and spin states [1]. However, to reduce immediate computational cost, we save this exploration for future studies.

Figures 4.6 and 4.8 show improved agreement with experimentally measured magnetic ground states using PBE$_{\mathrm{SF}}$+U+J compared to PBE+U+J, as well as better consistency of the output computed spin configuration. Improved performance of the SF functional is also achieved in Figures 4.8 and 4.11. In the case of MnF_2 and Mn_3As, we performed structural relaxations, with the spins initialized in the symmetric and/or experimental configuration. We explored the effect of structural optimization in these two materials, because without

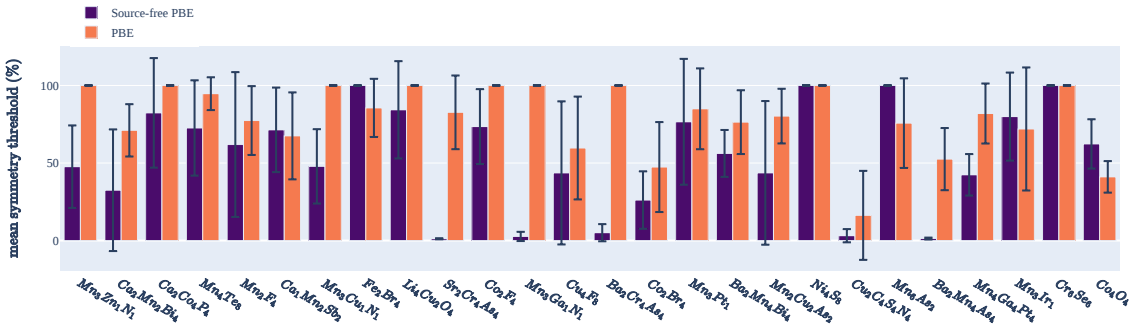

Figure 4.5: Comparison plot of minimum symmetry tolerance agreement with experimentally resolved magnetic space-group PBE+U+J and PBE$_{\mathrm{SF}}$+U+J for a selected number of experimental structures from the MAGNDATA Bilbao Crystallographic Server [174]. The y-axis is the minimum symmetry tolerance (in μ_{B}) at which the experimental magnetic space-group is identified, normalized by $\max_i\{m^i_{\mathrm{exp}}\}$. We use ISOTROPY's `findsym` to identify the magnetic space-group [175]. Copyright (2023) arXiv. Reproduced from Ref. [3] with permission.

allowing for spin-lattice relaxation, a ground state with a strong ferromagnetic component was stabilized, as was the case for MnF_2, which is shown in Figure 4.8.

4.2.3 Convergence case study: $YMnO_3$

To examine whether a tighter energy convergence threshold improves the converged structure for GGA, we imposed a 10^{-8} eV energy cut off to $YMnO_3$, comparing the convergence behavior between GGA and it source-free counterpart. The convergence behavior of GGA compared to GGA$_{\mathrm{SF}}$ is shown in Figure 4.13. In this plot, the absolute relative energy between subsequent self-consistency steps is plotted on a logarithmic scale. For the source-free functional, it is interesting to note that there appears to be a slight energy barrier that the algorithm climbs, only to descend to the symmetric experimentally reported ground state [181], just before 200 self-consistency steps.

To the reader, this may seem to be a long convergence time, however, we direct the attention to the conventional GGA counterpart. While convergence to 1 μeV is achieved rather rapidly, we see that the magnetic spins move very little in the convergence process. Furthermore, with the tighter energy cut off, the DFT calculation does not converge within the 600 electronic self-consistency step limit. At one point, the energy does dip below the tolerance energy threshold, but this is not simultaneously true for the band-structure convergence metric, which stays above the 0.01 μeV energy cut off.

It is worth noting that to improve convergence for this particular calculation, we used

a "sigma" value smearing of 0.2 near to the Fermi level. This is standard practice, and a different smearing can be used by continuing the DFT calculation with a smaller "sigma" value, and a different smearing method. Additionally, we used Gaussian smearing, which is known to be more robust across different material chemistries, such as between insulators and conductors, according to VASP documentation.

4.2.4 Augmented orbital moments in UO_2

Thus far, we have focused on the spin component of the magnetic moment. However, in reality, there is an orbital component to the magnetic moment that supplements the spin contribution [182, 183], especially in materials with strong spin-orbit coupling (SOC). In many $3d$ transition metal oxides, it can be theoretically and experimentally shown that the orbital moment is "quenched" [84, 184], in which case it is fair to neglect the orbital contributions. However, in f-block species, SOC can become much more prevalent. Additionally, we have explored the connections between the orbital moment and the paramagnetic current density, $\boldsymbol{j}_p$ in 2.2.2.8. Therefore, it would behoove us to explore how the source-free functional affects the orbital magnetic moments.

UO_2 has become the archetype of correlated oxides with strong spin-orbit coupling, which gives rise to the strongly non-collinear ground state of UO_2 [185]. Therefore, we apply the source-free functional towards UO_2, which we found to exhibit exceptionally large orbital magnetic moments. Specifically, we report the computed spin and orbital magnetic moments in Table 4.1 using GGA+U+J and GGA_{SF}+U+J. Due to the connection between orbital moments and $\boldsymbol{j}_p$ in Equation (2.72), we plot $\boldsymbol{j}_p(\boldsymbol{r})$ in Figure 4.14. We see that in this visualization, there is strong circulation of $\boldsymbol{j}_p$ around the uranium atoms, shown in grey. It is interesting to note that we achieve this improved agreement with experiment, even without the direct coupling to $\boldsymbol{A}_{xc}$ in the form of Equation (2.50).

4.2.5 Local and global torques arising from the source-free constraint

In Figure 4.3a we observe that it is indeed not the case that $\boldsymbol{\tau}'_{xc} = \boldsymbol{0} \;\forall\; \boldsymbol{r} \in \Omega$. However, for the systems we tested, we found the net (integrated) torque, as stated in Equation (2.76), to be orders of magnitude smaller than the largest local torque, i.e. $\max_{\boldsymbol{r}\in\Omega} \left\{ \left| \boldsymbol{\tau}'_{xc}(\boldsymbol{r}) \right| \right\}$. We found that for our Mn_3ZnN test case, the self-consistent $\boldsymbol{\tau}_{xc}$ obeyed the following inequality $\int_\Omega \boldsymbol{\tau}_{xc}\, d\boldsymbol{r} < 5 \times 10^{-5}$ eV, even though $\max_\Omega \{\boldsymbol{\tau}_{xc}\} \approx 5$ eV. The energy convergence tolerance for this calculation was 1×10^{-6} eV. Therefore, the net torque could simply be an artifact of numerical convergence.

Despite the "small" net torque relative to the energy convergence tolerance, it is nontrivial to determine whether the right-hand side of Equation (2.76) will be "small enough" in general. Additionally, further investigation should examine the effects of enforcing the ZTT at every self-consistency step. In Appendix 2.2.3.1, we propose possible approaches to ensure

that the ZTT is upheld at every self-consistency step. The method in Appendix 2.2.3.1 should be the most general and robust, with added computational cost. We have not implemented these ZTT corrections at this time. However, we imagine that a careful adherence to the ZTT will be important for the calculation of magnetocrystalline anisotropy energy (MAE), which is on the order of μeV, and therefore this additional physical constraint should be considered.

4.2.6 Importance of the constant, $\boldsymbol{q = 0}$, component of $\boldsymbol{B'}_{xc}$

In Figure 4.9, it is clear that when applying the $\overline{\boldsymbol{B'}}_{xc} = \mathbf{0}$ constraint for MnF_2, the SF functional converges to the correct collinear AFM ground state [177]. For $\overline{\boldsymbol{B'}}_{xc} = \overline{\boldsymbol{B}}_{xc}$, the canted FM configuration is erroneously stabilized, which is remedied by structural relaxations, as shown in Figure 4.8. On the other hand, for MnPtGa, if one applies the additional $\overline{\boldsymbol{B'}}_{xc} = \mathbf{0}$ constraint, we see that the ground state is a structure with much stronger AFM character. This differs significantly from the canted ferromagnetic configuration obtained using $\overline{\boldsymbol{B'}}_{xc} = \overline{\boldsymbol{B}}_{xc}$. This canted FM spin configuration is much closer to the magnetic ordering resolved using neutron diffraction [186].

To generalize this behavior, $\overline{\boldsymbol{B'}}_{xc} = \overline{\boldsymbol{B}}_{xc}$ erroneously stabilizes ferromagnetism in antiferromagnetics, and $\overline{\boldsymbol{B'}}_{xc} = \mathbf{0}$ stabilizes antiferromagnetism in ferromagnets, which is equally problematic. Due to the obvious importance of carefully considering $\overline{\boldsymbol{B'}}_{xc}$, we plan to address this in the future. For all other test cases in this study, we simply set $\overline{\boldsymbol{B'}}_{xc} = \overline{\boldsymbol{B}}_{xc}$, in order to maintain consistency with Ref.'s [37] & [76]. As we mention in the introduction, it would be possible to solve for $\overline{\boldsymbol{B'}}_{xc}$ that mitigates the net XC torque, while preserving the XC spin-splitting energy from SDFT, in accordance with Equation (1.24). We plan to explore this rigorously in a follow-up study.

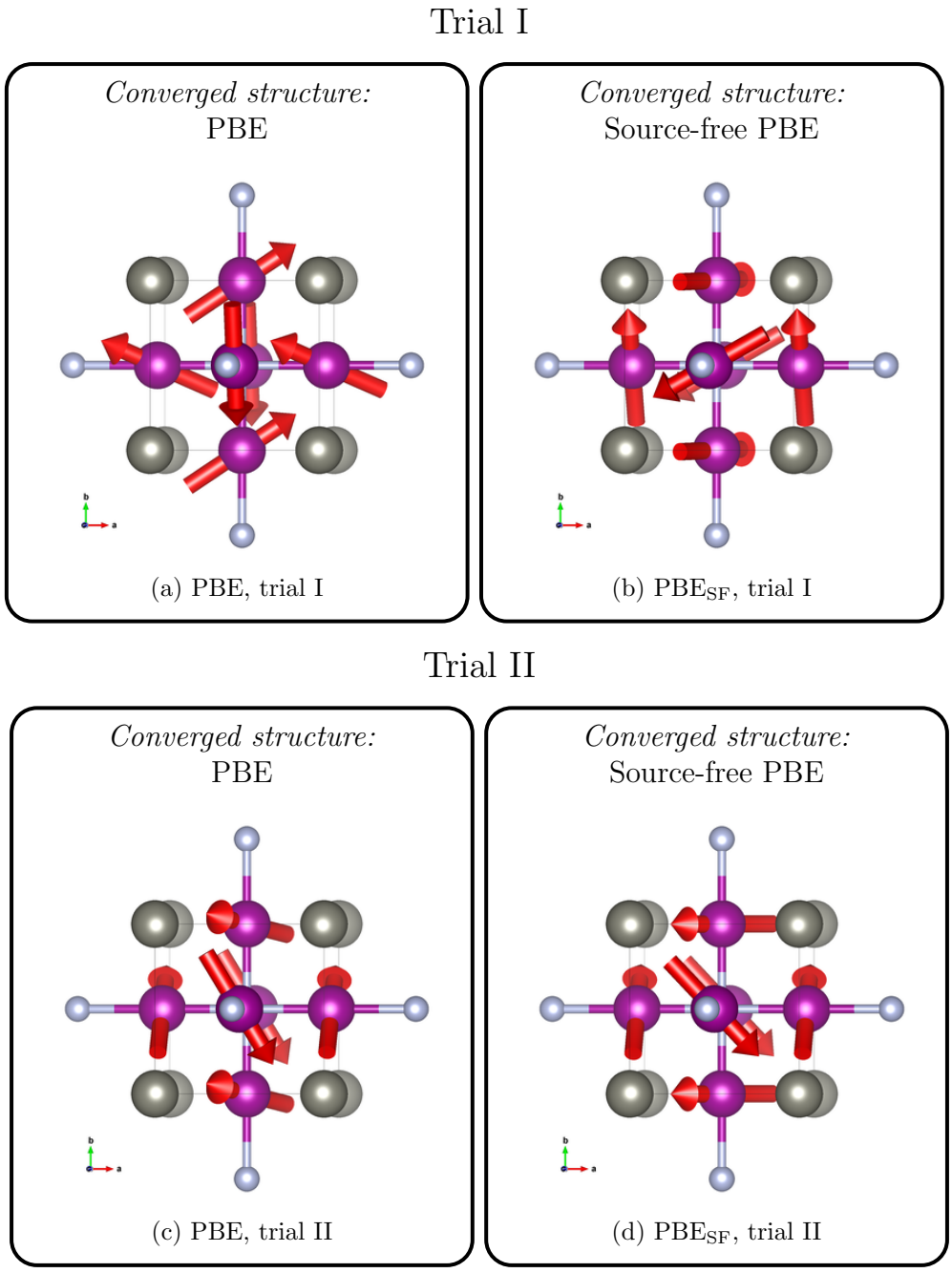

Figure 4.6: Computed ground state magnetic configurations for two input structures (trials A and B) randomly perturbed from the experimentally measured magnetic structure for Mn_3ZnN; Comparisons are provided for the computed structures for PBE$_{SF}$ versus PBE. Copyright (2023) arXiv. Reproduced from Ref. [3] with permission.

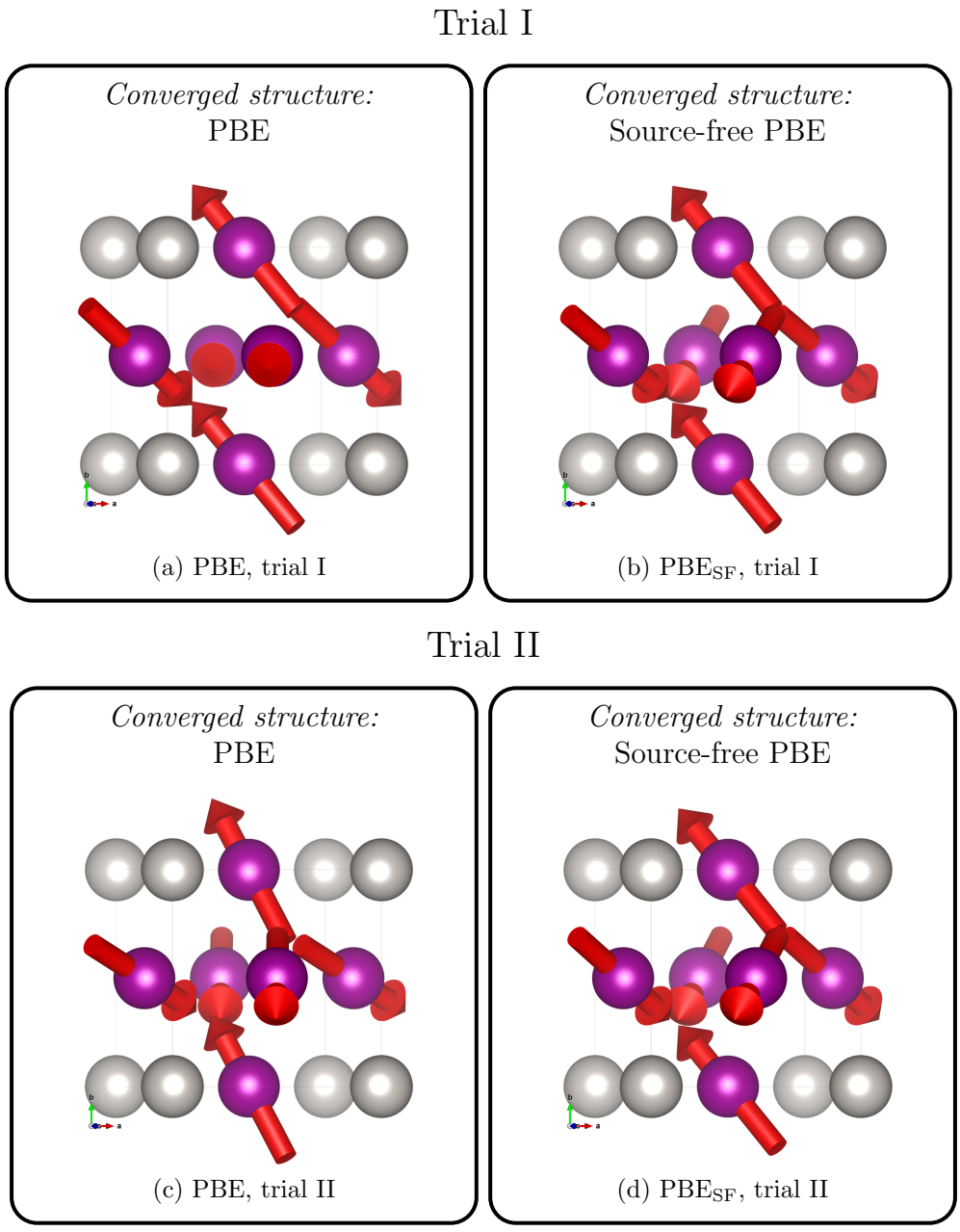

Figure 4.7: Computed ground state magnetic configurations for two input structures (trials A and B) randomly perturbed from the experimentally measured magnetic structure for Mn_3Pt; Comparisons are provided for the computed structures for PBE_{SF} versus PBE. Copyright (2023) arXiv. Reproduced from Ref. [3] with permission.

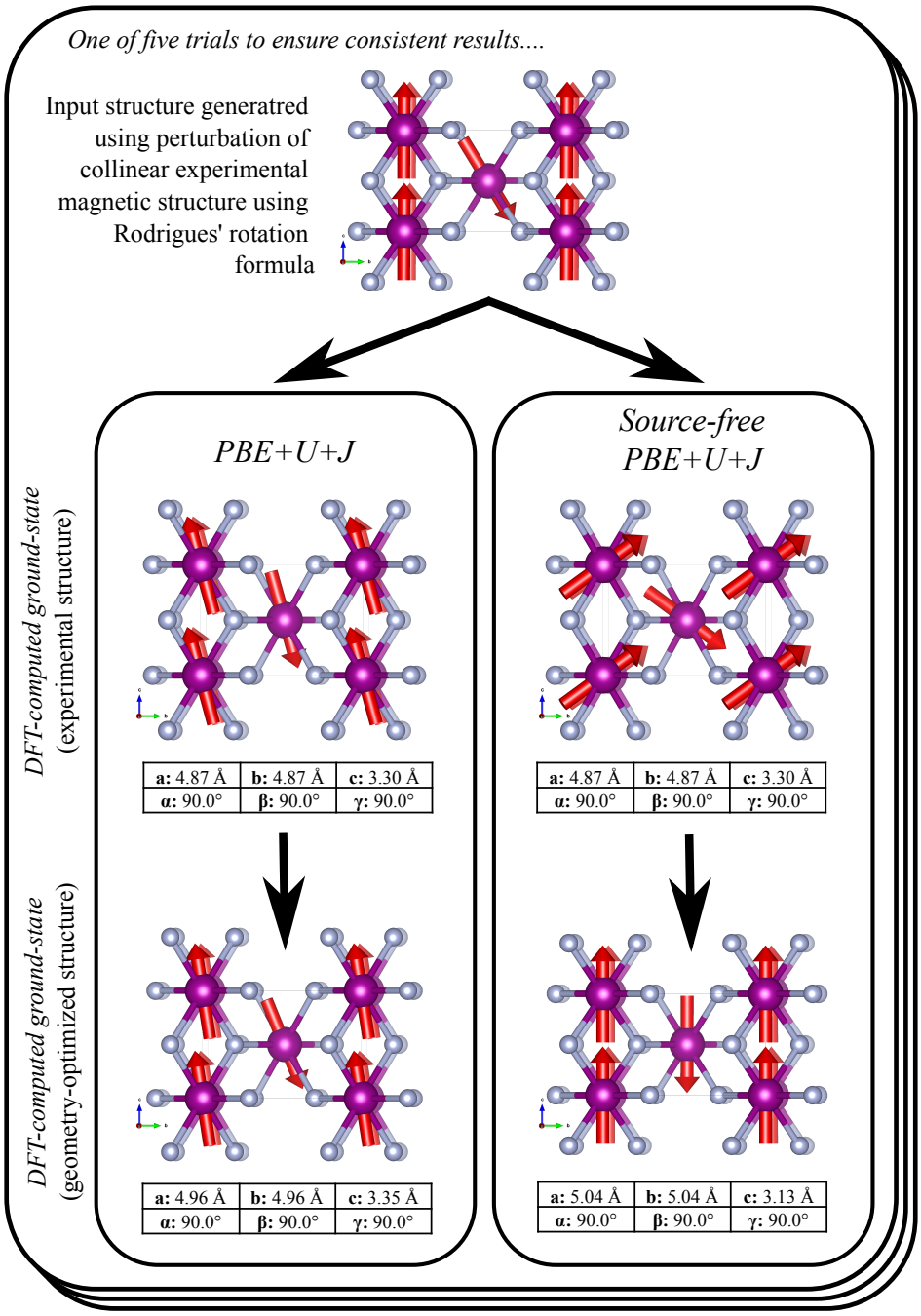

Figure 4.8: Computed ground state magnetic configurations for randomly perturbed input structure from the experimentally measured magnetic structure for MnF_2; Comparisons are provided for the computed structures for PBE_{SF} versus PBE. Copyright (2023) arXiv. Reproduced from Ref. [3] with permission.

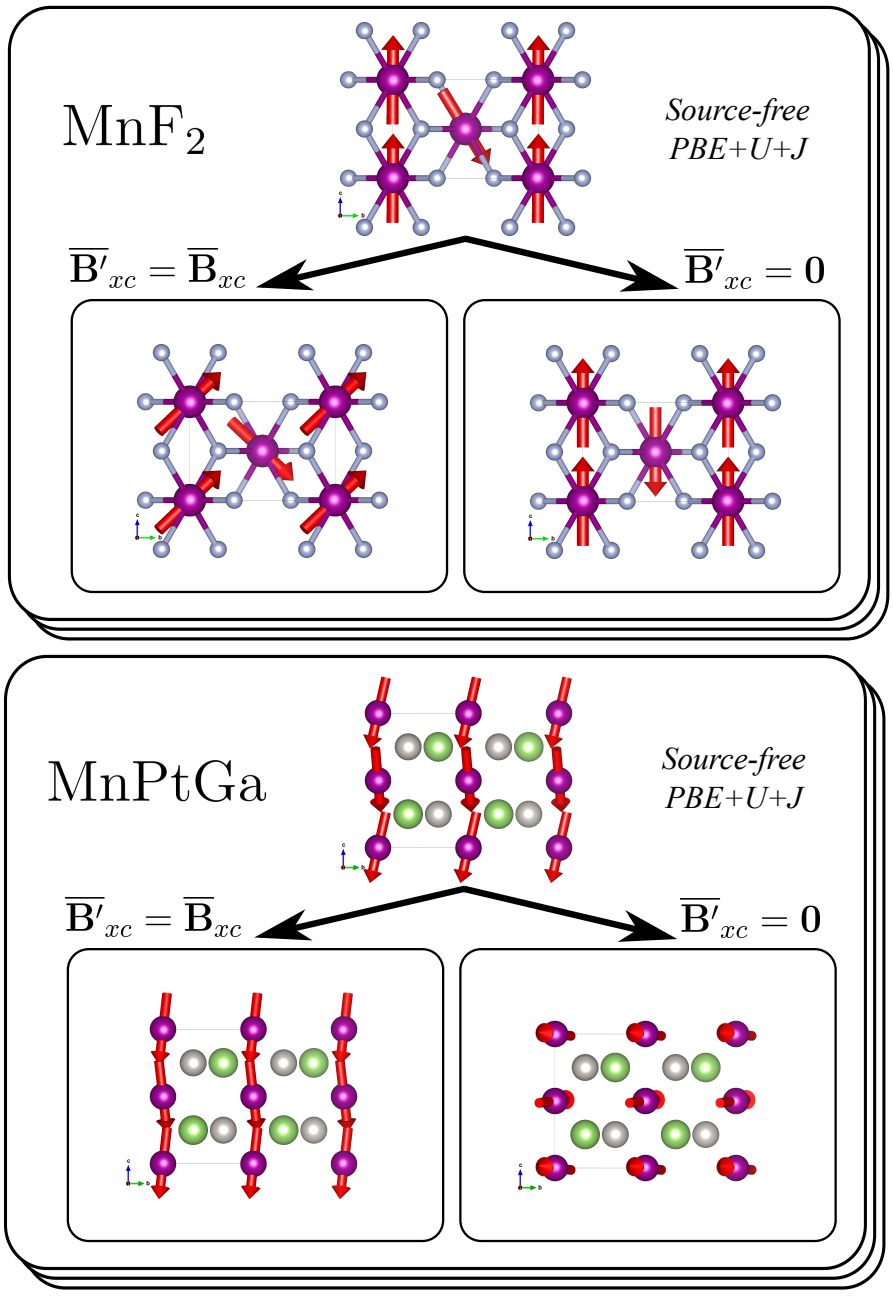

Figure 4.9: Comparison between the different choices of $\overline{\boldsymbol{B}'}_{xc}$ for antiferromagnetic MnF_2 (top) and canted ferromagnetic MnPtGa (bottom). Treatment of $\overline{\boldsymbol{B}'}_{xc}$ alone can dictate the FM or AFM character of spin-polarized systems. As the inclusion of a $q = 0$ component changes the Kohn-Sham effective potential, the absolute energies computed with or without $\overline{\boldsymbol{B}}_{xc}$ are not directly comparable. Copyright (2023) arXiv. Reproduced from Ref. [3] with permission.

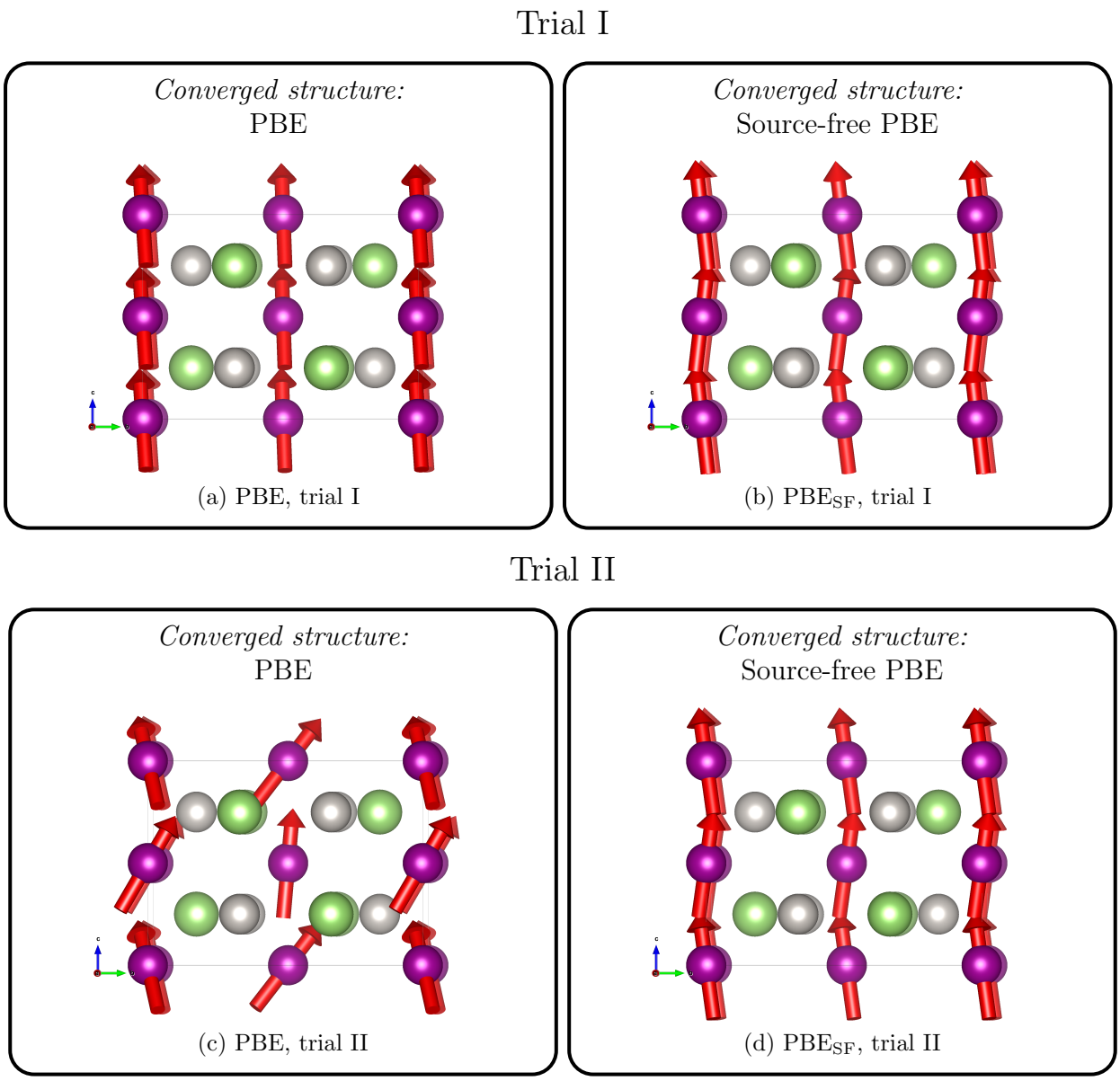

(a) PBE, trial I

(b) PBE_{SF}, trial I

(c) PBE, trial II

(d) PBE_{SF}, trial II

Figure 4.10: Computed ground state magnetic configurations for two input structures (trials A and B) randomly perturbed from the experimentally measured magnetic structure for MnPtGa; Comparisons are provided for the computed structures for PBE_{SF} versus PBE. Copyright (2023) arXiv. Reproduced from Ref. [3] with permission.

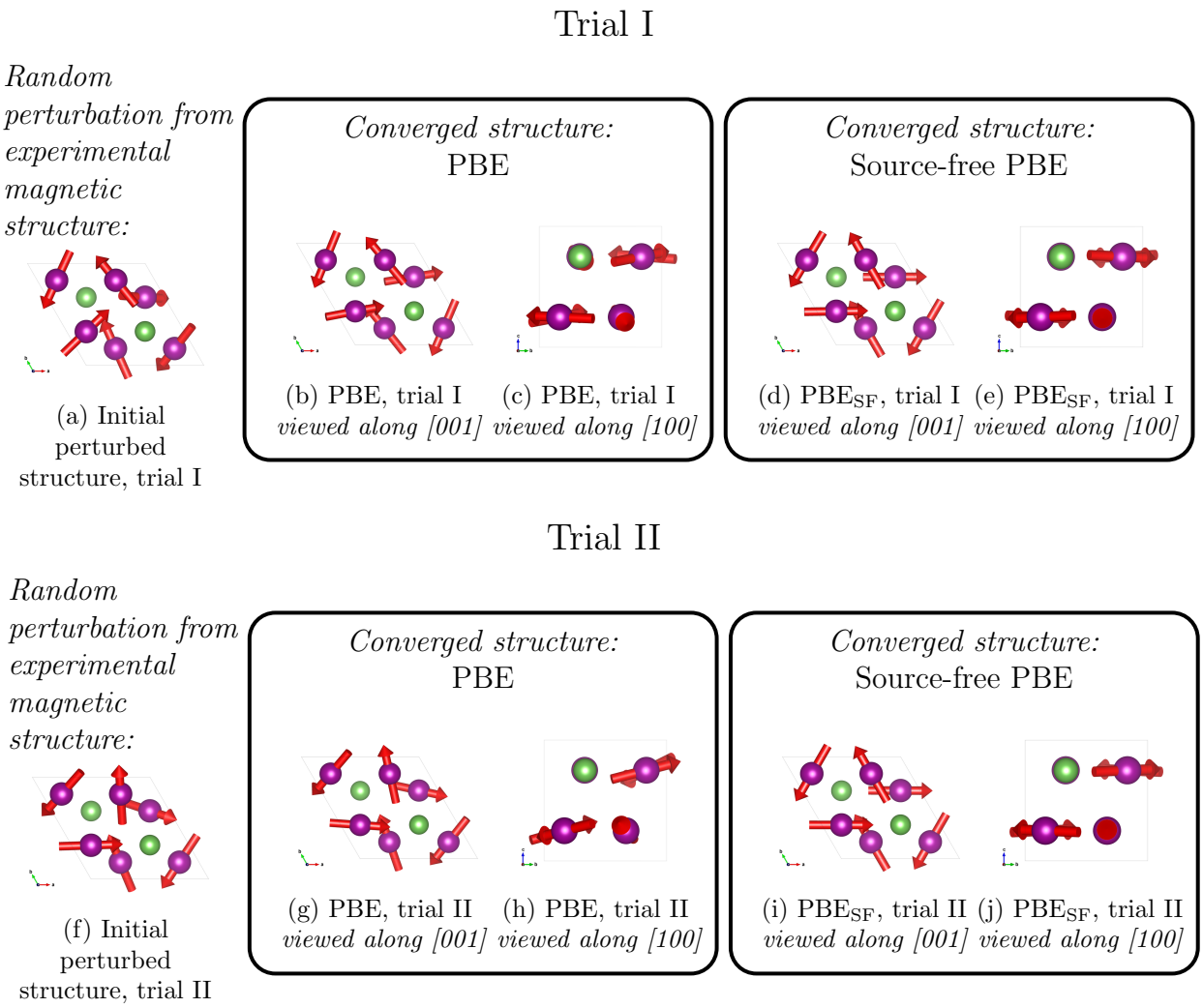

Figure 4.11: Computed ground state magnetic configurations for two input structures (trials A and B) randomly perturbed from the experimentally measured magnetic structure for Mn_3As; Comparisons are provided for the computed structures for PBE_{SF} versus PBE; For PBE_{SF} and PBE runs, input atomic positions and cell shape were first determined by performing structural relaxations, with moments initialized in the symmetric orientation. Copyright (2023) arXiv. Reproduced from Ref. [3] with permission.

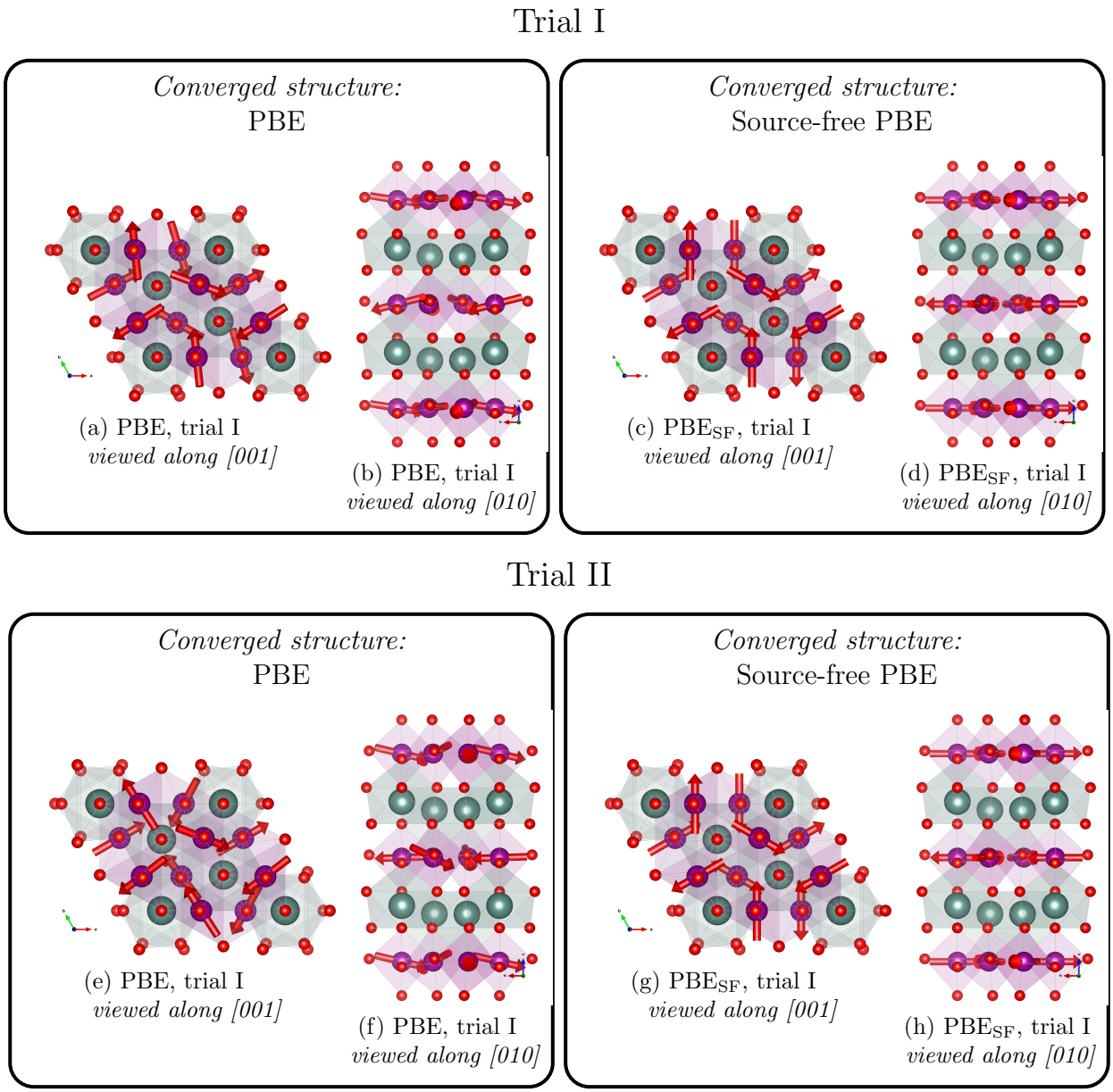

Figure 4.12: Computed ground state magnetic configurations for two input structures (trials A and B) randomly perturbed from the experimentally measured magnetic structure for $YMnO_3$; Comparisons are provided for the computed structures for PBE_{SF} versus PBE; For PBE_{SF} and PBE runs, input atomic positions and cell shape were first determined by performing structural relaxations, with moments initialized in the symmetric orientation. Copyright (2023) arXiv. Reproduced from Ref. [3] with permission.

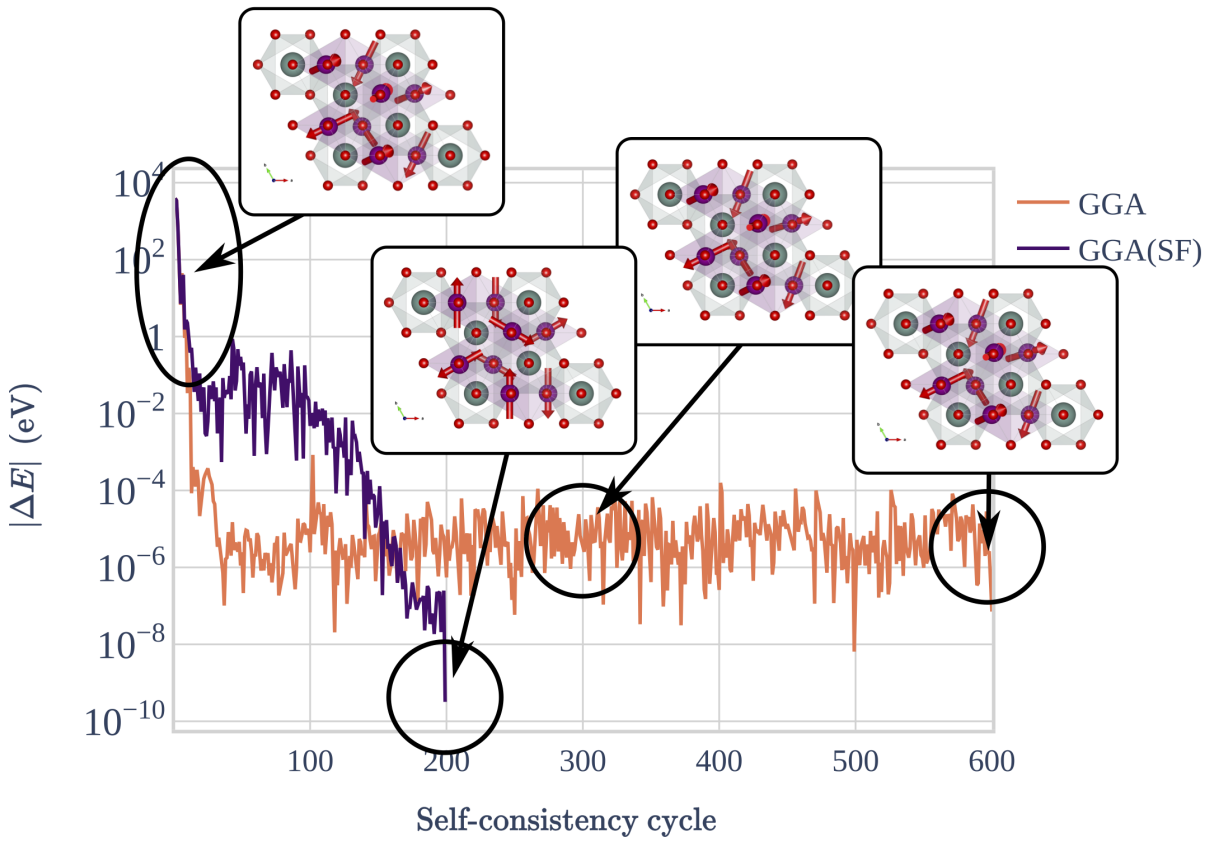

Figure 4.13: Convergence of GGA_{SF} compared against GGA for $YMnO_3$, with moments randomly perturbed from the symmetric ground state structure. Snapshots of the magnetic configuration at each self-consistency step are shown to convey the improved convergence characteristics of the source-free functional. The y-axis is the absolute energy difference between subsequent self-consistency iterations, plotted on a logarithmic scale. Copyright (2023) arXiv. Reproduced from Ref. [3] with permission.

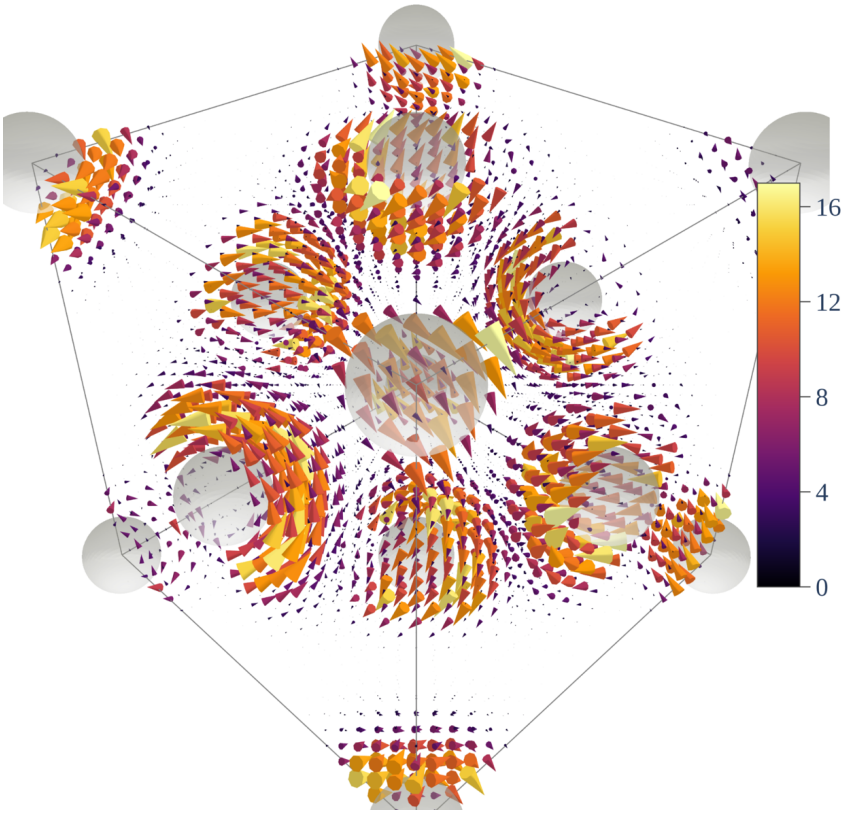

Figure 4.14: Vector field visualization of the probability current density, $\boldsymbol{j}_p$, within UO_2. Strong circulation of $\boldsymbol{j}_p$ is observed surrounding the uranium atoms, in grey. Copyright (2023) arXiv. Reproduced from Ref. [3] with permission.

Table 4.1: Tabulated magnetic moment components of the four uranium atoms in the magnetic unit cell of UO_2. The spin and orbital contributions to the total computed moments by VASP are included below, computed using both PBE$_{SF}$+U+J and PBE+U+J. The on-site corrections of $U, J = 3.46, 0.3$ eV were applied to U-f states to maintain consistency with Ref. [24]. Additionally, we compare to $U, J = 4.5, 1.0$ eV, which is the largest U value reported in Ref. [24], and a "rounded-up" J value of 1.0 eV to examine the effect of a larger Hund J parameter on the spin and orbital uranium magnetic moments. Copyright (2023) arXiv. Reproduced from Ref. [3] with permission.

Functional	Atom	Spin				Orbital				Total			
		m_x	m_y	m_z	$\|\boldsymbol{m}\|$	m_x	m_y	m_z	$\|\boldsymbol{m}\|$	m_x	m_y	m_z	$\|\boldsymbol{m}\|$
PBE+U+J $U, J = 3.46, 0.30$ eV	I	-0.577	-0.583	-0.581	1.01	1.764	1.783	1.778	3.07	1.19	1.20	1.20	2.07
	II	-0.584	0.576	0.581	1.01	1.787	-1.763	-1.776	3.08	1.20	-1.19	-1.20	2.07
	III	0.578	-0.568	0.594	1.00	-1.769	1.739	-1.817	3.07	-1.19	1.17	-1.22	2.07
	IV	0.599	0.571	-0.57	1.00	-1.831	-1.747	1.744	3.07	-1.23	-1.18	1.17	2.07
PBE+U+J $U, J = 4.5, 1.0$ eV	I	-0.19	-0.19	-0.20	0.34	1.41	1.42	1.43	2.46	1.22	1.23	1.23	2.12
	II	-0.20	0.20	0.19	0.34	1.43	-1.43	-1.40	2.46	1.24	-1.23	-1.21	2.12
	III	0.19	-0.19	0.20	0.34	-1.40	1.39	-1.47	2.46	-1.21	1.20	-1.27	2.12
	IV	0.21	0.19	-0.18	0.34	-1.51	-1.40	1.35	2.46	-1.30	-1.21	1.16	2.12
PBE$_{SF}$+U+J $U, J = 3.46, 0.30$ eV	I	0.21	0.17	0.24	0.36	0.73	0.73	0.81	1.31	0.93	0.90	1.04	1.66
	II	0.21	-0.23	-0.19	0.36	0.73	0.73	-0.67	1.23	0.94	0.50	-0.86	1.37
	III	-0.18	0.19	-0.24	0.36	-0.66	-0.66	-0.83	1.25	-0.84	-0.47	-1.07	1.44
	IV	-0.21	-0.21	0.21	0.36	-0.73	-0.73	0.74	1.26	-0.93	-0.93	0.94	1.62
PBE$_{SF}$+U+J $U, J = 4.5, 1.0$ eV	I	0.08	0.08	0.09	0.14	0.95	0.91	1.04	1.68	1.03	0.98	1.13	1.82
	II	0.08	-0.08	-0.08	0.14	0.99	-0.99	-0.92	1.68	1.07	-1.07	-1.00	1.82
	III	-0.08	0.08	-0.09	0.14	-0.96	0.91	-1.03	1.68	-1.04	0.99	-1.12	1.82
	IV	-0.08	-0.08	0.08	0.14	-0.94	-1.01	0.96	1.68	-1.01	-1.09	1.04	1.82

Chapter 5

SpinPSO: Identifying noncollinear magnetic ground-states

From the 31st floor of the
simulation swarm
With the drone of fluorescence
Flicker, fever, fill the form
...

Big Thief

This chapter begins from our physics-informed optimization algorithm, `SpinPSO`, that unifies both the theory of atomistic spin dynamics (ASD) and particle swarm optimization (PSO), which we covered in Sections 2.3 and 1.2.2. From this foundation, we have implemented `SpinPSO` as an automated computational workflow in the `atomate` code framework [46]. The workflow evaluates energies and local fields from DFT, and therefore the DFT+U+J and source-free corrections covered in the previous two chapters provide essential inputs for the optimization workflow, and strongly influence the resulting magnetic ground-state, as we highlight in this chapter.

5.1 Results

In order to test the effectiveness of the `SpinPSO` noncollinear ground state optimizer, we first consider the convergence performance of `SpinPSO` to a Heisenberg model Hamiltonian (Sec. 5.1.1) as well as a representative set of magnetic materials with exotically textured magnetic orderings from the Bilbao MAGNDATA database (Sec. 5.1.2) [167]. These materials are MnPtGa, $YMnO_3$, FeF_3, Mn_3Pt, Mn_3Sn, $Fe_3PO_3O_4$ and Mn_2SiO_4, chosen to exemplify the diverse noncollinear magnetic structures over varying chemistries. This diverse set of materials allows us to test the robustness of the `SpinPSO` optimization algorithm, and the underlying XC functional [3].

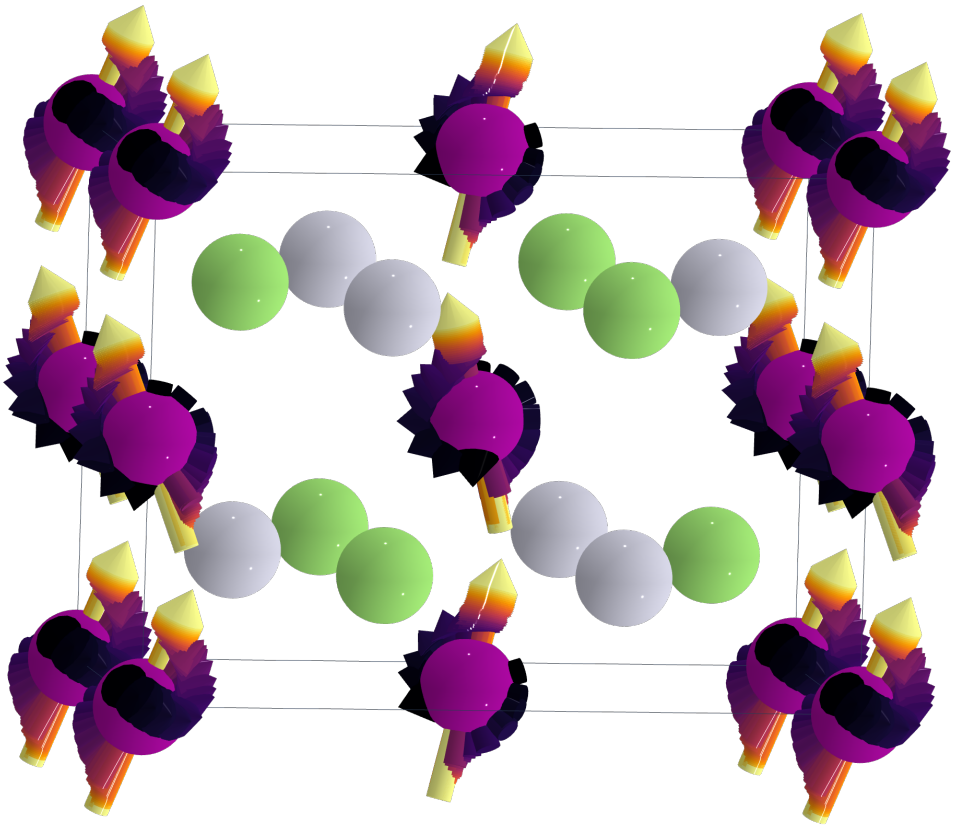

Figure 5.1: The convergence path for one of four agent's trajectory randomly initialized within a single `SpinPSO` optimization, with calls to $\text{PBE}_{\text{SF}}+U+J$. The algorithm converges within fifteen iterations to the experimentally resolved magnetic ground-state [186]. The position along the trajectory is indicated by the length and color of the arrows within the "inferno" color scheme. Copyright (2023) arXiv. Reproduced from Ref. [4] with permission.

5.1.1 Model Hamiltonian

To test the convergence performance of the `SpinPSO` algorithm, we employ the use of the Heisenberg model Hamiltonian in order to robustly quantify the statistics of the stochastic agent-based optimization scheme. We use a model classical Heisenberg Hamiltonian of the form

$$\mathcal{H} = -\sum_{i,j} J_{ij}\ \boldsymbol{s}_i \cdot \boldsymbol{s}_j, \quad \text{where } \boldsymbol{s}_i \in \mathcal{S}^2 \tag{5.1}$$

to evaluate the sensitivity of the `SpinPSO` algorithm to the input random configurations, number of agents, and other hyper-parameters. The improved convergence speed with the inclusion of gradient information is shown in Figure 5.2. Perhaps most importantly, we

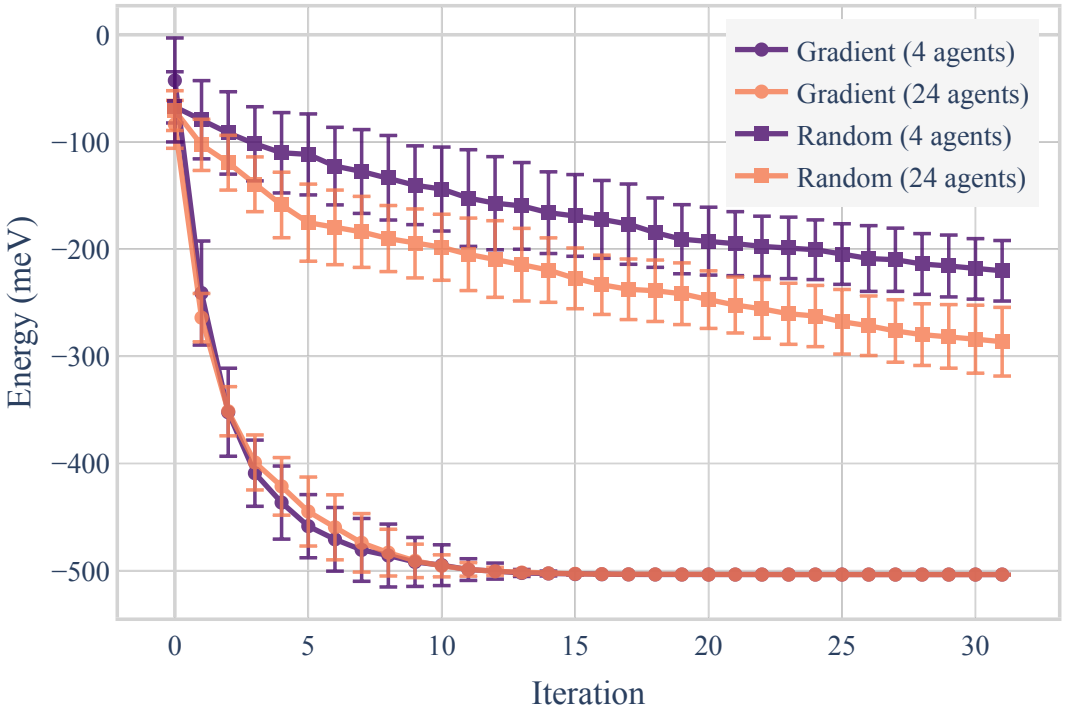

Figure 5.2: The convergence of `SpinPSO` with and without gradient information, as stated in Section 2.3.1.2. For the sake of computational efficiency, energies and local effective fields are evaluated using Equation (5.1) for a Heusler ferrimagnet. Additionally, to explore the sensitivity of each setting to hyperparameters, we compare convergence with 4 versus 24 agents, and averaged over 10 randomly initialized swarms. Copyright (2023) arXiv. Reproduced from Ref. [4] with permission.

quantify the increased local convergence by including gradient contributions to the GCPSO algorithm in Figure 5.2. In this plot, we compare averaged trajectories over 10 swarms initialized with initial spin configurations sampled uniformly over the surface of a unit sphere, with a comparison between 4 and 24 agents. In Figure 5.2 we show the mean and standard deviation of these trajectories visualized using error bars. By incorporating gradient information, the algorithm converges much more rapidly to the expected ferromagnetic or antiferromagnetic ground state compared to the conventional randomly sampled best-agent perturbations used in GCPSO. The latter does not even converge within the limit of thirty iterations.

5.1.2 Material test cases

5.1.2.1 MnPtGa

Hexagonal MnPtGa ($P6_3/mmc$) has been explored as a promising magnetocaloric material as well as a skyrmion host in Cooley et al., Ref. [186]. In addition to resolving the noncollinear magnetic ground-state of MnPtGa using neutron diffraction, the authors of Ref. [186] also performed DFT energy comparisons of different magnetic configurations, confirming that, indeed, the canted ferromagnetic structure was lower in energy compared to the collinear ferromagnetic and antiferromagnetic orderings. We note that, in a similar fashion to Ref. [186], in our calculations we will only consider the $\boldsymbol{q} = 0$ component of the spin-density wave (SDW) identified in the experimental component of Ref. [186]. We will leave a computational investigation of the full spin-spiral incommensurate structure for a future study. Using the `SpinPSO` optimization scheme and a source-free noncollinear exchange correlation functional [3] implemented in VASP [29], we observe rapid convergence to the experimentally resolved magnetic ordering [186]; a symmetric experimentally resolved canted ferromagnetic ordering. Visualizing the global convergence to the ground state, in Figure 5.1, we superimpose the convergence path of one agent in the particle swarm optimization PSO swarm, where the color and magnitude are scaled according to the position along the convergence trajectory [189].

5.1.2.2 $YMnO_3$ and FeF_3

Hexagonal $YMnO_3$ and FeF_3 were chosen as test cases because of their complex magnetic ground-state with a relatively small unit cell. In both cases of $YMnO_3$ and FeF_3, it was observed that the source-free functional, in combination with the `SpinPSO` optimization scheme, resulted in a minimum energy configuration with ferromagnetic orderings of the spins in ab planes, as shown in Figure 5.7a, compared to the experimental ground-state Figure 5.7b. This magnetic ordering has supposedly been experimentally resolved, but only at temperatures above 75 Kelvin in $ScMnO_3$ [181].

Under these assumptions, we observe very good convergence to the experimental ground state. A majority of the runs for $YMnO_3$ converge to the correct state, as shown in Figure 5.6, where the initial states on the left are the `SpinPSO`+GGA converged structures, used as input to GGA_{SF}, which converges to the corresponding orderings on the right hand side. This improved local convergence using the source-free functional is not surprising, based on the analysis and results of past studies [3, 37, 75].

5.1.2.3 Mn_3Pt and Mn_3Sn

Mn_3Pt and Mn_3Sn are also studied using `SpinPSO`, followed by calls to GGA_{SF}. The resulting ground-states are reported in Figure 5.8 and Figure 5.9. We see that compared to the experimentally $R\bar{3}m$ experimentally resolved structure [176], the algorithm `SpinPSO` finds a configuration with circulating spins to be more favorable. This is possibly due to the

fact that the source-free functional imposes a strict dependence on the spin current, which is proportional to the curl of the magnetization $\nabla \times \boldsymbol{m}$ [3, 37]. The role of additional corrections to the source-free functional are explored in Section 5.1.3.

A similar circulation of spins are observed in the case of Mn_3Sn, shown in Figure 5.9. However, it may not be as fair a comparison to experiment, as the neutron diffraction in Ref. [190] was performed around 200 K, and it is ambiguous whether the $Cmc'm'$ or $Cm'cm'$ structures is the preferred ground-state [190].

5.1.2.4 $Fe_3PO_3O_4$ and Mn_2SiO_4

Lastly, trigonal $Fe_3PO_3O_4$ ($R3m$) is explored as a particularly challenging case for its magnetic configuration corresponding to a rich spin spiral ground-state, incommensurate with the underlying lattice, as elucidated by neutron diffraction [9, 188]. Here, we limit the study to the corresponding commensurate ground-state as additional functionality is required to incorporate spin-spiral boundary conditions with the source-free constraint [3]. However, in future studies, we plan to use this material as a test case for optimizing a $\boldsymbol{q}$-spiral ordering over the configuration space of the $\boldsymbol{q}$ wave vector, by incorporating this degree of freedom into the `SpinPSO` framework. The commensurate ordering is of iron arranged within triads, which are antiferromagnetically ordered with respect to one another. We observe that the `SpinPSO`+GGA computed ground-state agrees with the experimentally characterized structure. We also optimized this structure using `SpinPSO`+GGA_{SF}, and found that a slight canting of the triad resulted, which does not agree with the experimentally measured structure.

5.1.3 Discussion on challenges with source-free functional and `SpinPSO`

We found that larger U and J values resulted in stronger ferromagnetic exchange, particularly in the case of in-plane spins in $YMnO_3$. Therefore, for these structures, we ran the `SpinPSO` algorithm with no Hubbard U and Hund J values applied to the transition metal d states. Therefore, it would be worthwhile to assess the effect of these inter-site V values, i.e. DFT+U+J+V, which necessarily affect magnetic exchange the resulting ground state [191–194]. Whether or not these inter-site V values promote FM or AFM exchange is dependent upon the underlying character of the correlated insulator, e.g. whether or not the TMO is a Mott versus charge transfer insulator [193, 194], and warrants further investigation.

However, what's possibly more of note in the context of this study are possible issues with the global energy curvature using the source-free functional. In reference [3], some of the current authors explored the local convergence of the $YMnO_3$ magnetic state starting from random perturbations around the experimentally resolved ground state, and found robust conversions to this experimentally accepted configuration over several sample trials.

Another potential shortcoming of the source-free constrained functional is the neglection of explicit coupling between the probability current and XC magnetic vector potential, which

will arise in spin polarized systems [3, 38]. The question is whether or not these probability (paramagnetic) currents will have a significant effect in the case of quenched orbital moments. The authors also explore the importance of the choice of $\overline{\boldsymbol{B}}_{xc}$, the integral of the source-free XC magnetic field. This will likely have a strong effect on the global energy landscape, based on the results from Ref. [3].

In addition, different couplings could be important to consider. It might be necessary in future studies for us to incorporate optimization over both structure and degrees of freedom using the `SpinPSO` formalism. In reference [3], a stronger dependence of the computed ground-state on structural geometry relaxations were observed for the $\mathrm{GGA}_{\mathrm{SF}}{+}U{+}J$. This more holistic approach may help to resolve some of the issues in the agreement or disagreement between experiment and computed magnetic orderings using `SpinPSO` with $\mathrm{DFT}_{\mathrm{SF}}{+}U{+}J$.

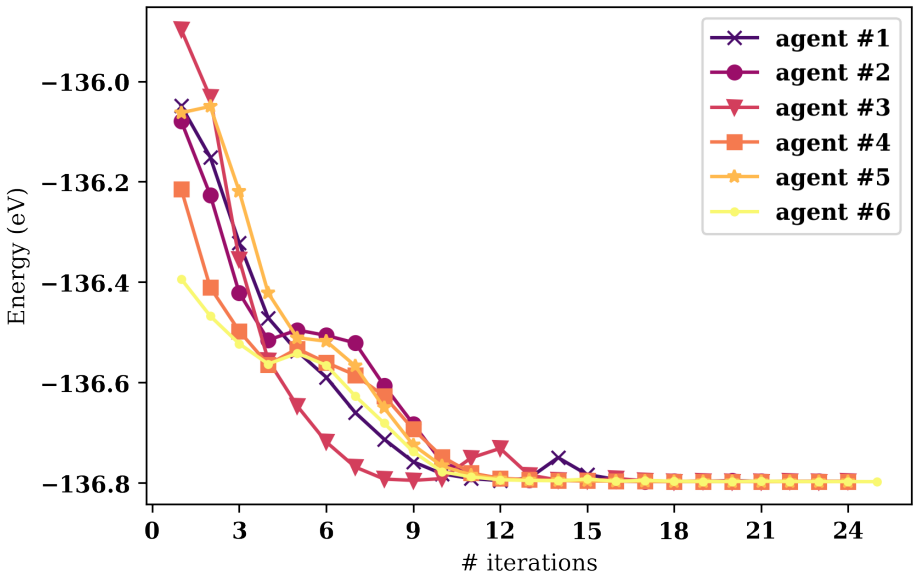

(a) Convergence with 6 agents

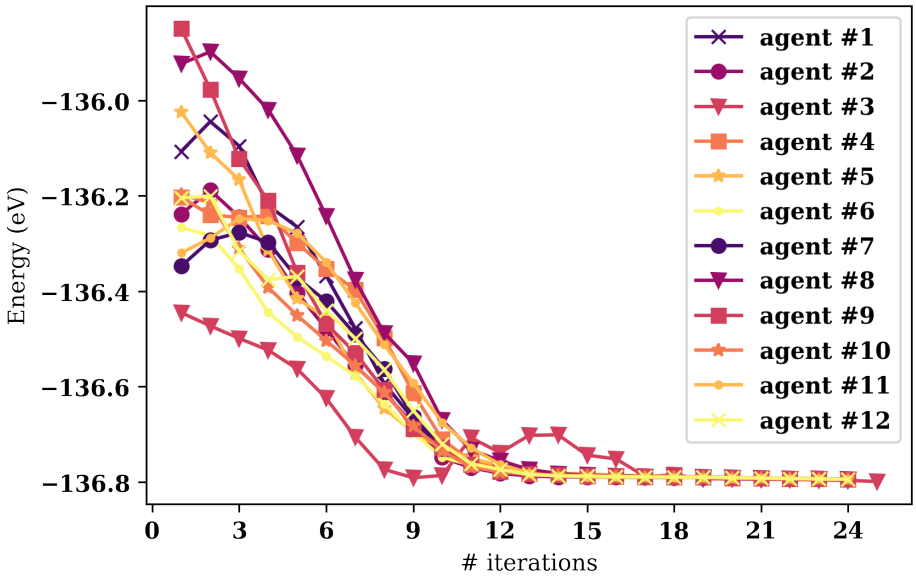

(b) Convergence with 12 agents

Figure 5.3: The robust convergence for two randomly initialized `SpinPSO` trajectories for the FeF_3 magnetic ground-state. This figure provides a convergence comparison for swarm sizes of (a) six agents versus (b) twelve. Figure 5.2 provides a statistically averaged comparison over agent sizes, which is only computationally practical using the model Hamiltonian, Equation (5.1). Copyright (2023) arXiv. Reproduced from Ref. [4] with permission.

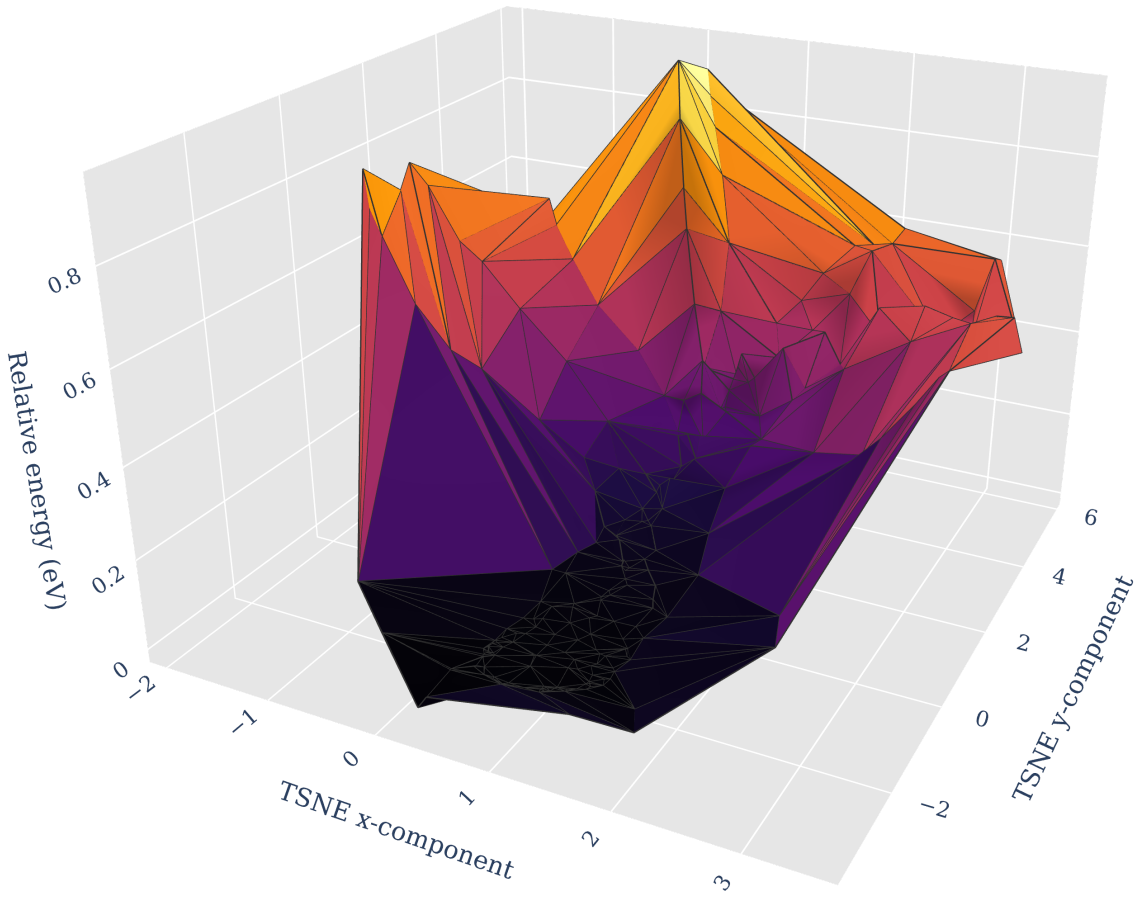

Figure 5.4: The energy landscape for FeF_3 spin configurations, visualized using a t-distributed stochastic neighbor embedding (acronymed TSNE or t-SNE) [187] implemented in `sklearn`. The energy values and positions (spin configurations) are amalgamated from each agent's trajectory within the swarm. Copyright (2023) arXiv. Reproduced from Ref. [4] with permission.

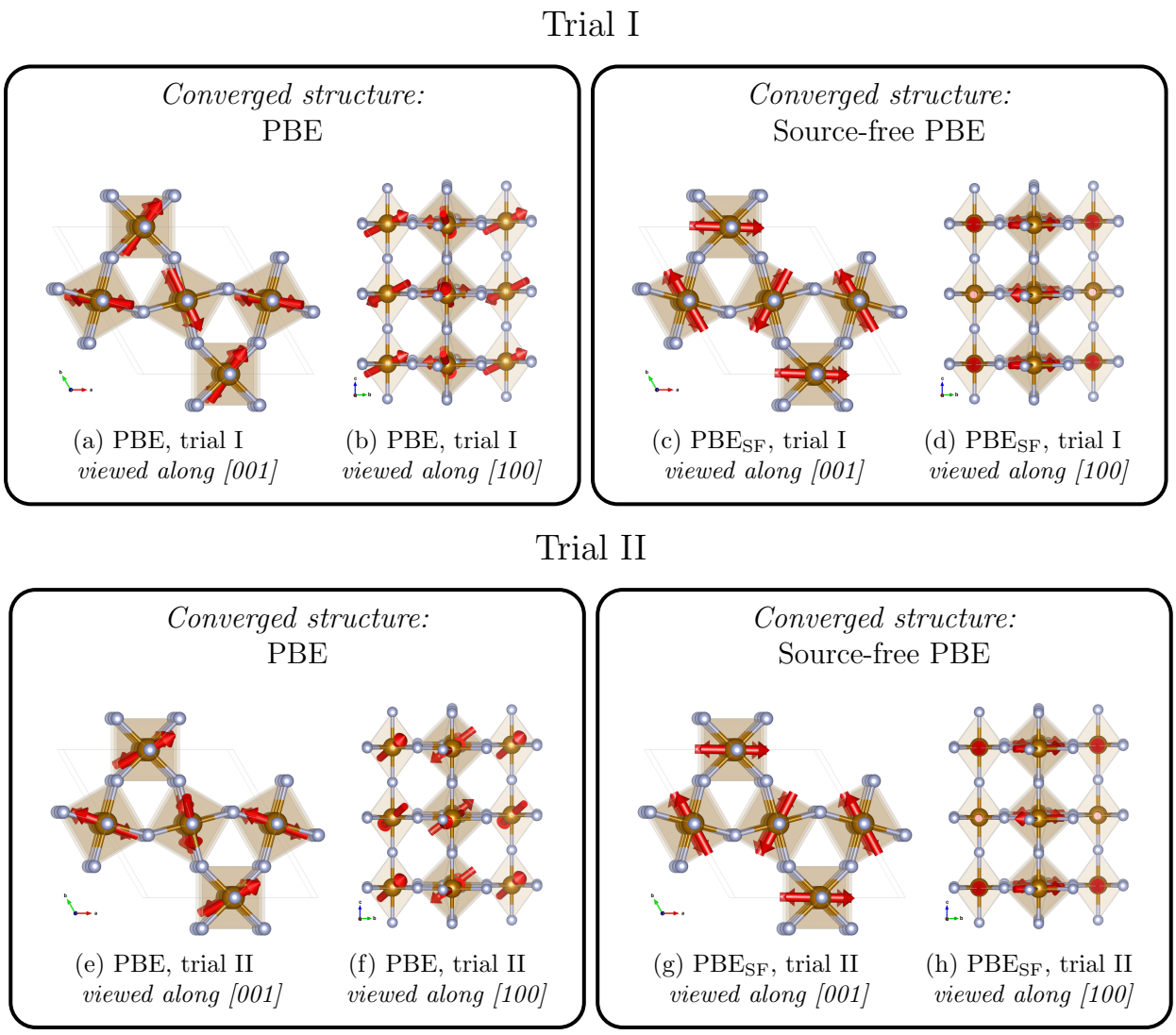

Figure 5.5: Computed ground-state magnetic configurations for FeF_3 obtained from `SpinPSO` with PBE for multiple randomly initialized `SpinPSO` trajectories. On the left are the minimum energy configurations computed from `SpinPSO` with PBE, which are used as input structures for PBE_{SF}, with ground-state structures shown on the right. Copyright (2023) arXiv. Reproduced from Ref. [4] with permission.

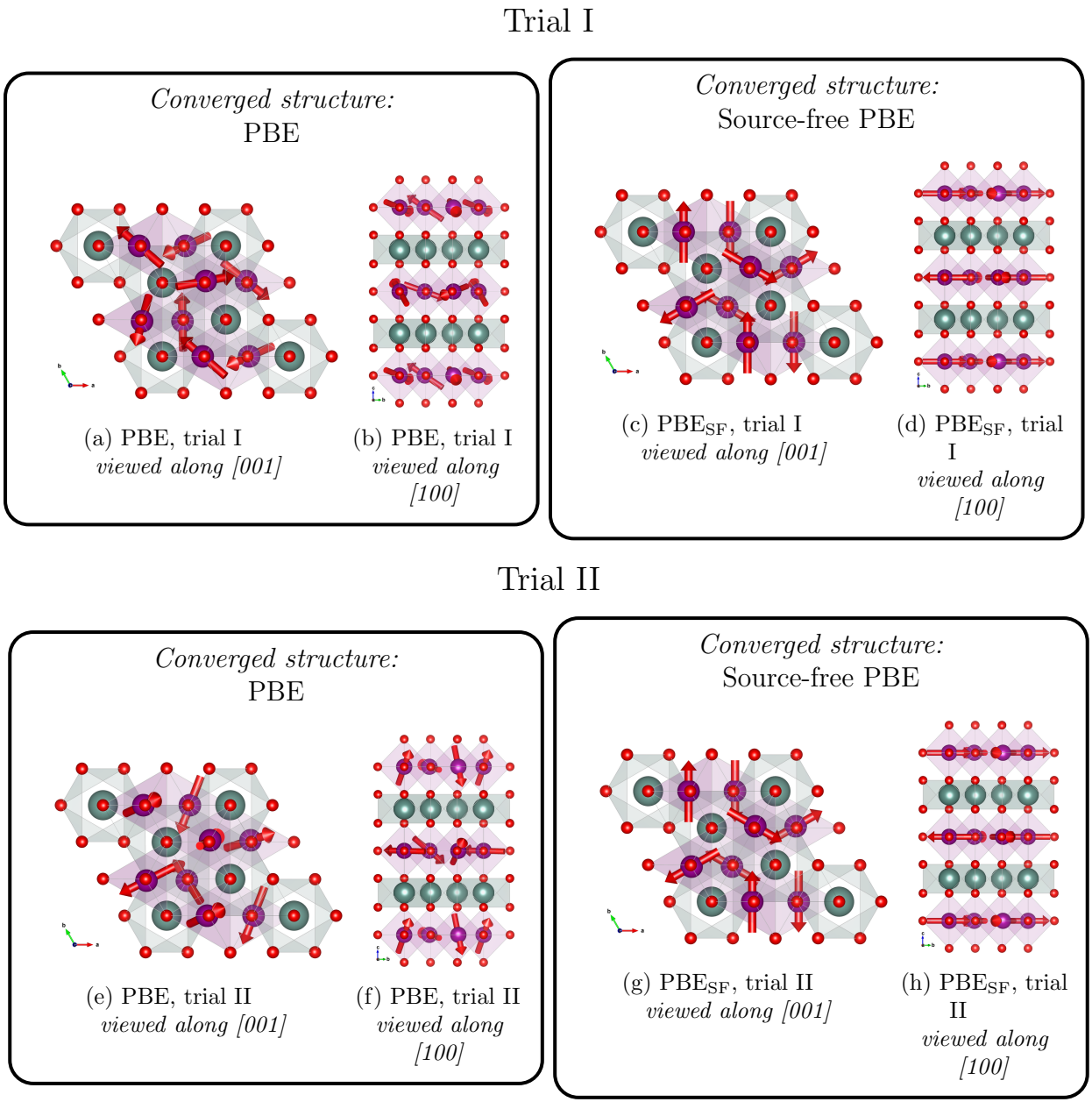

Figure 5.6: Computed ground-state magnetic configurations for $YMnO_3$ obtained from `SpinPSO` with PBE for multiple randomly initialized `SpinPSO` trajectories. On the left are the minimum energy configurations computed from `SpinPSO` with PBE, which are used as input structures for PBE_{SF}, with ground-state structures shown on the right. Copyright (2023) arXiv. Reproduced from Ref. [4] with permission.

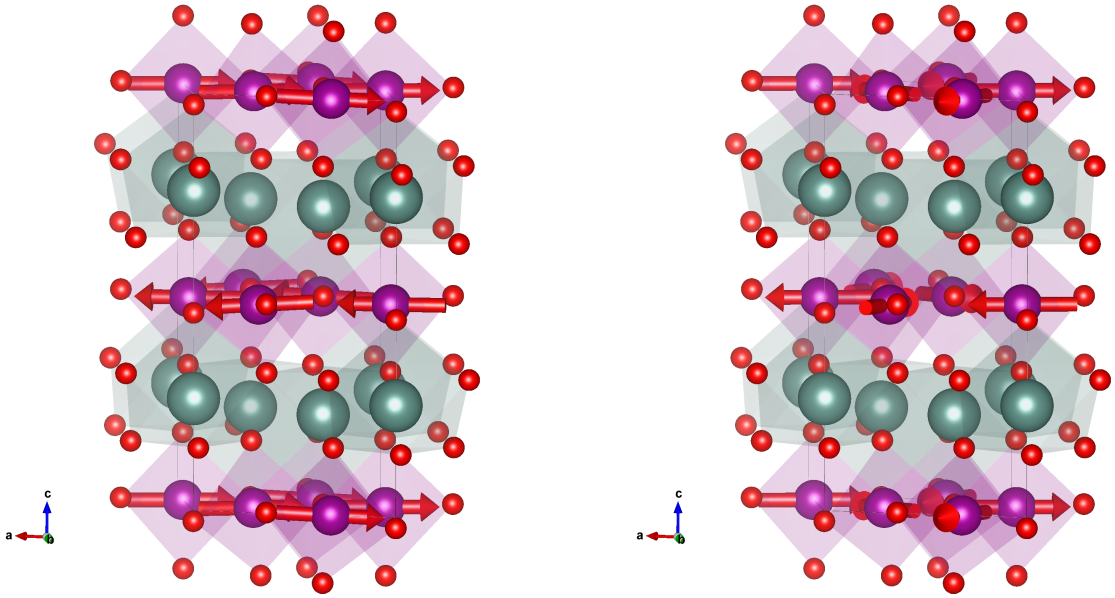

(a) $PBE_{SF}+U+J$ (b) PBE_{SF}

Figure 5.7: (a) The $YMnO_3$ ground state calculated using `SpinPSO` with PBE+U+J, followed by PBE+U+J average Mn-d Hubbard U and Hund J parameters obtained from Ref. [1]. The calculated ground-state in this case contains ferromagnetic ab planes, antiferromagnetically coupled. This structure differs from (b) the experimental structure [181], as well as the ordering obtained from the procedure without U/J parameters, using parameters consistent with Figure 5.6. Copyright (2023) arXiv. Reproduced from Ref. [4] with permission.

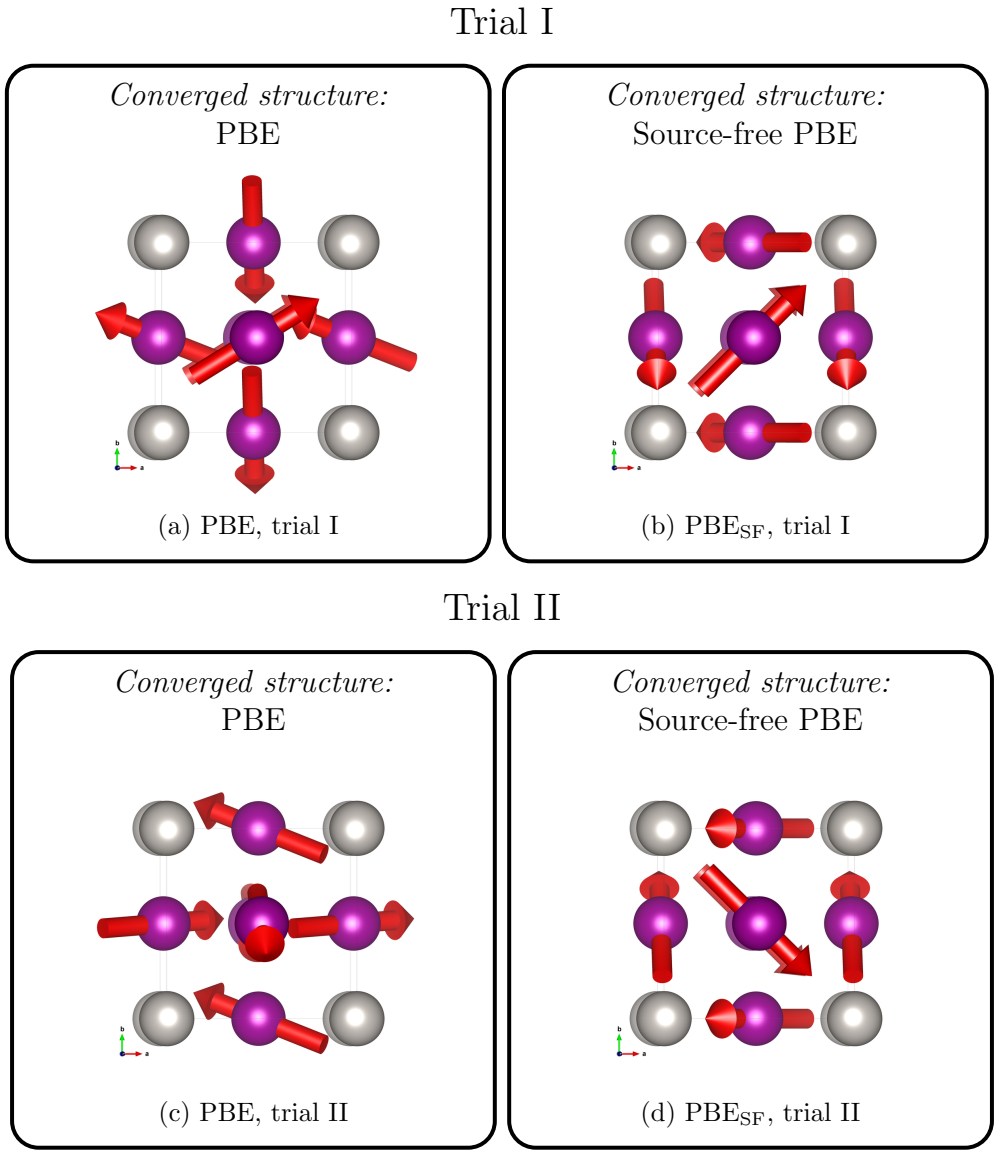

Figure 5.8: Computed ground-state magnetic configurations for Mn_3Pt obtained from `SpinPSO` with PBE for multiple randomly initialized `SpinPSO` trajectories. On the left are the minimum energy configurations computed from `SpinPSO` with PBE, which are used as input structures for PBE_{SF}, with ground-state structures shown on the right. Copyright (2023) arXiv. Reproduced from Ref. [4] with permission.

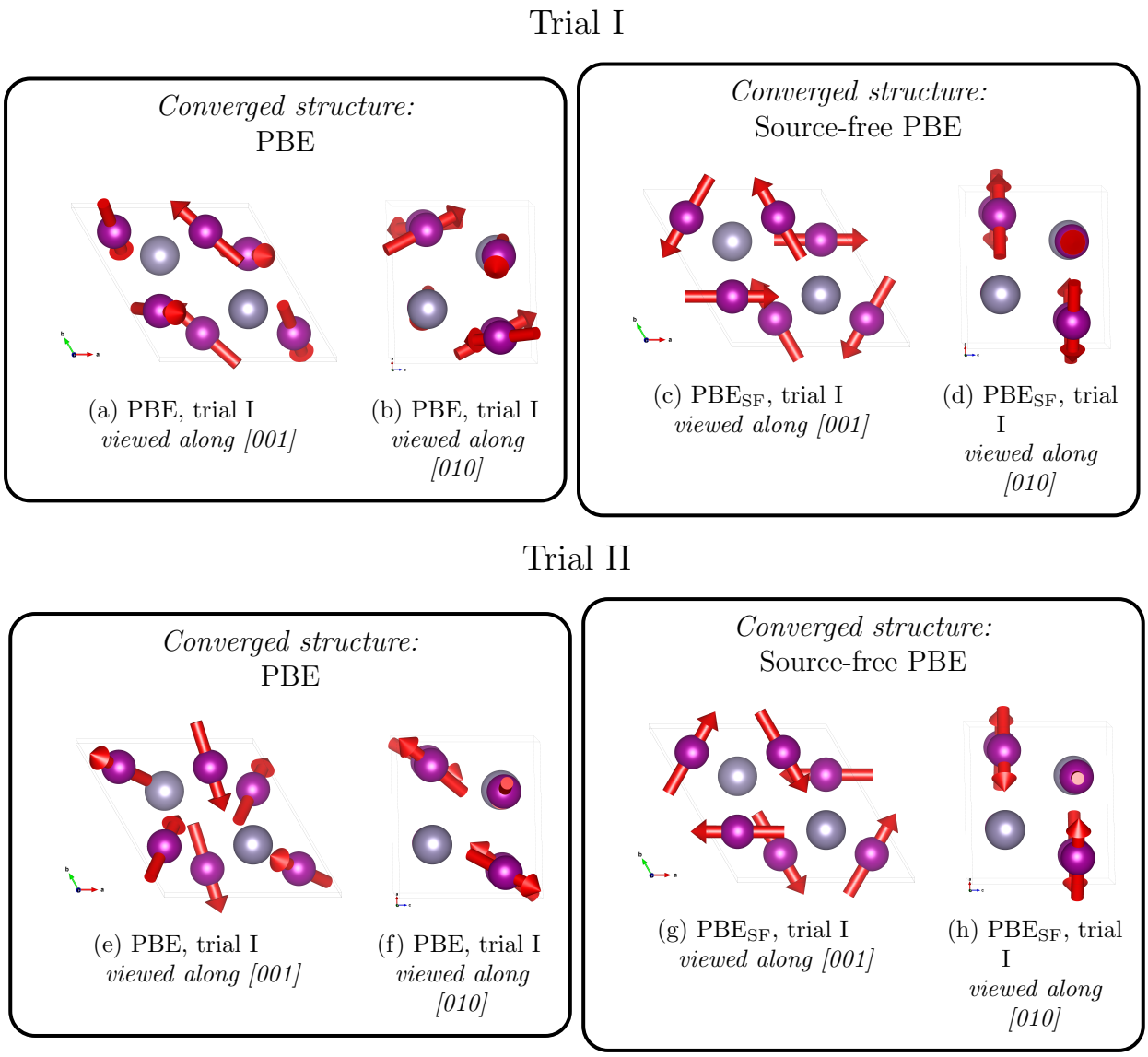

Figure 5.9: Computed ground-state magnetic configurations for Mn_3Sn obtained from `SpinPSO` with PBE for multiple randomly initialized `SpinPSO` trajectories. On the left are the minimum energy configurations computed from `SpinPSO` with PBE, which are used as input structures for PBE_{SF}, with ground-state structures shown on the right. Copyright (2023) arXiv. Reproduced from Ref. [4] with permission.

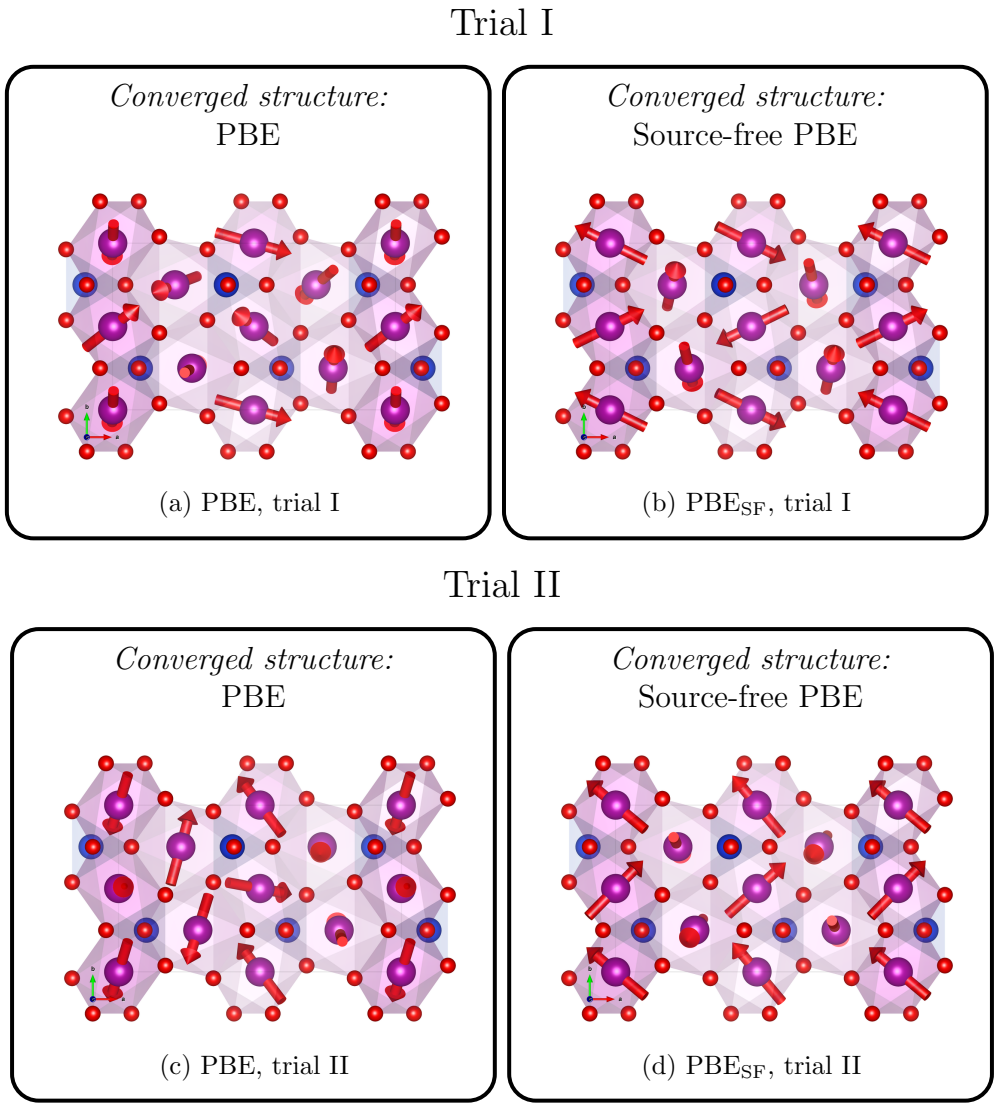

Figure 5.10: Computed ground-state magnetic configurations for Mn_2SiO_4 obtained from `SpinPSO` with PBE for multiple randomly initialized `SpinPSO` trajectories. On the left are the minimum energy configurations computed from `SpinPSO` with PBE, which are used as input structures for PBE_{SF}, with ground-state structures shown on the right. Copyright (2023) arXiv. Reproduced from Ref. [4] with permission.

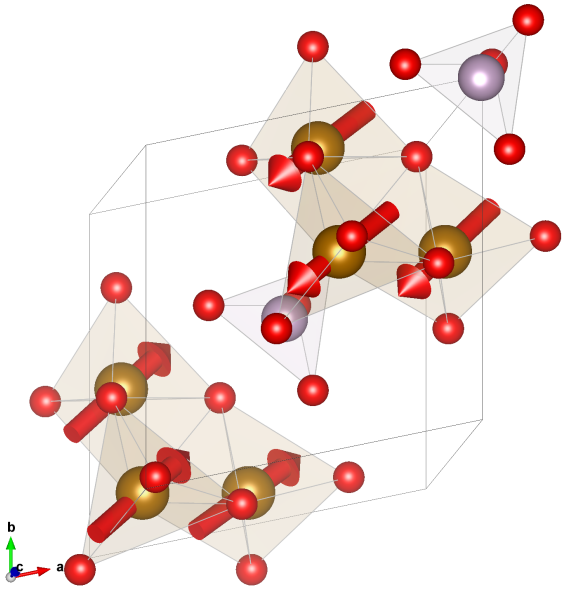

Figure 5.11: Commensurate ($\boldsymbol{q} = \mathbf{0}$) magnetic ground state of $Fe_3PO_3O_4$, obtained using `SpinPSO` with PBE. This magnetic structure agrees with the experimental magnetic ground state obtained from neutron diffraction [9, 188]. Copyright (2023) arXiv. Reproduced from Ref. [4] with permission.

Chapter 6

Conclusions

6.1 Overall Summary

This dissertation presents a comprehensive computational framework for determining and optimizing the magnetic properties of transition metal oxides (TMOs). By sequentially addressing the calculation of Hubbard U and Hund J values, the implementation of a source-free exchange-correlation (XC) functional, and the development of a novel optimization algorithm, we have significantly advanced the methods for identifying noncollinear magnetic ground states. Each section of this dissertation builds upon the previous work, culminating in a robust and unified approach for studying complex magnetic systems.

6.2 High-throughput determination of Hubbard U and Hund J values for transition metal oxides via the linear response formalism

This study provides a high-throughput `atomate` framework for calculating Hubbard U and Hund J values. Using the spin-polarized linear-response methodology [17], we generated a database of U and J values for over one thousand transition-metal-containing materials. This enabled the creation of a "periodic table" of U and J distributions, where for each element we observe a range of Hubbard U and Hund J values. These distributions exhibited clustering depending on the corresponding m_l and n_l values, but these quantities alone do not prove sufficient to predict the Hubbard and Hund parameters.

To investigate inter-site screening effects on the resulting U/J values, we performed a small supercell scaling study for the full screening linear response analysis for NiO, in addition to the conventional, atom-wise, screening. This exploration revealed that the full matrix inversion is much more sensitive to the size of the unit cell compared to the conventional, atom-wise screening. Understanding the theoretical reasons for this phenomenon will be an interesting pursuit for future studies.

To test the validity of the linear response implementation, we explored the spin-canting non-collinear magnetic structure and unit cell shape of $LiNiPO_4$, comparing the results with previous experimental [166] and computational [23, 63] studies. We found that the computed stable canting angle was less than 50% of the experimentally measured canting angle of nickel magnetic moments in olivine $LiNiPO_4$ for all Ni-d Hund J values tested, and that the canting angle was very sensitive to the Hund's J values. Additionally, applying an on-site Hubbard/Hund correction to O-p occupancies greatly improved the agreement of unit cell shape with experiment [166], highlighting the importance of including a $+U+J$ correction to oxygen sites.

6.3 Realistic non-collinear ground states of solids with source-free exchange correlation functional

Significantly improved convergence to the non-collinear magnetic structure has been achieved with the application of the source-free constraint to $\boldsymbol{B}_{xc}$ [37] within the PAW DFT formulation implemented in VASP. Utilizing parallel three-dimensional FFTs for the fast Poisson solver allows this constraint to be applied with minimal additional computational cost and no reduction in the parallel scalability of the DFT code. While this study focused on GGA-$PBE_{SF}+U+J$, the constraint is generalizable to other SDFT functionals in non-collinear implementations, such as meta-GGA.

Future studies will aim to combine the improved local convergence of DFT_{SF} with global optimization algorithms to achieve a robust determination of non-collinear ground states without prior experimental knowledge. The augmented magnetoelectric coupling predicted using the source-free functional lays the groundwork for future investigations into magnetoelectric figures of merit, calculated using this modified functional. The unified theory provides a solid theoretical description of the orbital magnetic moment [182], extending the semiclassical theory discussed in Section 2.2.2.8. Further studies should examine the role of spin and orbital currents in magnetoelectric coupling.

6.4 `SpinPSO`: A computational optimization workflow for identifying noncollinear magnetic ground-states from first-principles

In this study, we developed and implemented a `SpinPSO` workflow within the `atomate` software framework. The improved convergence capabilities were demonstrated by including gradient information in the form of local fields from constrained DFT calculations. For several material systems with varying chemistries, we obtained the correct magnetic ground-state based on neutron diffraction studies. The best results were achieved using `SpinPSO`

with calls to GGA during global convergence, followed by GGA_{SF} calculations to enhance local convergence behavior.

The underlying issues with GGA_{SF} in global convergence remain unclear. Further improvements to the new XC functional, as proposed in Ref. [3], are likely to address these challenges. This work can be extended to optimize over spin-spiral degrees of freedom, including a q-spiral vector and a spin-quantization axis. These boundary conditions are necessary to describe magnetic systems with incommensurate magnetic ground-states and to reduce computational costs. Achieving this will require accurately and efficiently computing the corresponding gradients associated with the q-vector, potentially leveraging the Fourier scaling property.

6.5 Recommended & proposed future work

The identification and study of noncollinear magnetic ground states open up several promising avenues for future research. One critical area is the development and application of mesoscale models of magnetism, particularly using magnetic lattice Hamiltonians and Monte Carlo methods. After obtaining the magnetic ground-state, by the magnetic force theorem, one can derive magnetic exchange constants from tight-binding Hamiltonians based on maximally localized Wannier functions (MLWFs) [195]. These effective magnetic Hamiltonians, which require significantly lower computational cost than DFT, enable the quantification of temperature-dependent material properties.

Another area for future research is the incorporation of magnetostructural coupling in magnetic models. Future work will focus on coupling spin degrees of freedom to structural distortions, further exploring the interaction between magnetic and structural properties. Magnetic exchange constants vary with inter-site spacing, necessitating a description of the coupling between spin and atomic displacements, especially in materials with strong magnetostructural interactions. Various compressible spin models, such as the Bean-Rodbell model and the Baker-Essam model, have been proposed to capture these effects. By investigating these models, we aim to understand and predict metamagnetic phase transitions induced by significant magnetostructural coupling. Building upon the work of this study, it would be worthwhile to examine the role that DFT+U+J and the source-free XC functional have on influencing the calculated exchange and spin-lattice constants. This would include the sensitivity of the requisite perturbation theory to the noncollinear ground-state identified using `SpinPSO`, by the magnetic force theorem [195].

Bibliography

[1] Guy C. Moore et al. "High-Throughput Determination of Hubbard U and Hund J Values for Transition Metal Oxides via the Linear Response Formalism". In: *Physical Review Materials* 8.1 (Jan. 2024), p. 014409. DOI: 10.1103/PhysRevMaterials.8.014409. (Visited on 07/08/2024).

[2] Peter Meisenheimer et al. "Switching the Spin Cycloid in $BiFeO_3$ with an Electric Field". In: *Nature Communications* 15.1 (Apr. 2024), p. 2903. ISSN: 2041-1723. DOI: 10.1038/s41467-024-47232-5. (Visited on 07/09/2024).

[3] Guy C. Moore et al. *Realistic Non-Collinear Ground States of Solids with Source-Free Exchange Correlation Functional*. Sept. 2023. arXiv: 2310.00114 [cond-mat]. (Visited on 10/03/2023).

[4] Guy C. Moore, Matthew K. Horton, and Kristin A. Persson. *SpinPSO: An Agent-Based Optimization Workflow for Identifying Global Noncollinear Magnetic Ground-States from First-Principles*. Oct. 2023. arXiv: 2310.01383. (Visited on 10/03/2023).

[5] Hongbin Zhang. "High-Throughput Design of Magnetic Materials". In: *Electronic Structure* 3.3 (Sept. 2021), p. 033001. ISSN: 2516-1075. DOI: 10.1088/2516-1075/abbb25. (Visited on 07/03/2024).

[6] M. K. Horton et al. "High-throughput prediction of the ground-state collinear magnetic order of inorganic materials using Density Functional Theory". In: *NPG Computational Materials* 5.1 (June 2019). Number: 1 Publisher: Nature Publishing Group, pp. 1–11. ISSN: 2057-3960. DOI: 10.1038/s41524-019-0199-7. URL: http://www.nature.com/articles/s41524-019-0199-7 (visited on 10/27/2020).

[7] Je-Geun Park et al. "Structure and spin dynamics of multiferroic $BiFeO_3$". In: *Journal of Physics: Condensed Matter* 26.43 (Oct. 2014). Publisher: IOP Publishing, p. 433202. ISSN: 0953-8984. DOI: 10.1088/0953-8984/26/43/433202. URL: https://dx.doi.org/10.1088/0953-8984/26/43/433202 (visited on 10/02/2023).

[8] D. H. Lyons and T. A. Kaplan. "Method for Determining Ground-State Spin Configurations". In: *Physical Review* 120.5 (Dec. 1960), pp. 1580–1585. ISSN: 0031-899X. DOI: 10.1103/PhysRev.120.1580. URL: https://link.aps.org/doi/10.1103/PhysRev.120.1580 (visited on 10/02/2023).

[9] K. A. Ross et al. "Nanosized helical magnetic domains in strongly frustrated $Fe_3PO_4O_3$". In: *Physical Review B* 92.13 (Oct. 2015), p. 134419. ISSN: 1098-0121, 1550-235X. DOI: 10.1103/PhysRevB.92.134419. URL: https://link.aps.org/doi/10.1103/PhysRevB.92.134419 (visited on 10/02/2023).

[10] Enya Vermeyen, Carlos A. R. Sá De Melo, and Jacques Tempere. "Exchange Interactions and Itinerant Ferromagnetism in Ultracold Fermi Gases". In: *Physical Review A* 98.2 (Aug. 2018), p. 023635. ISSN: 2469-9926, 2469-9934. DOI: 10.1103/PhysRevA.98.023635. (Visited on 06/28/2024).

[11] Gabriele Giuliani and Giovanni Vignale. *Quantum Theory of the Electron Liquid*. Cambridge: Cambridge University Press, 2005. ISBN: 978-0-521-52796-5. DOI: 10.1017/CBO9780511619915. (Visited on 06/30/2024).

[12] P. Hohenberg and W. Kohn. "Inhomogeneous Electron Gas". In: *Phys. Rev.* 136 (3B 1964), B864–B871. DOI: 10.1103/PhysRev.136.B864. URL: https://link.aps.org/doi/10.1103/PhysRev.136.B864.

[13] W. Kohn and L. J. Sham. "Self-Consistent Equations Including Exchange and Correlation Effects". In: *Phys. Rev.* 140 (4A 1965), A1133–A1138. DOI: 10.1103/PhysRev.140.A1133. URL: https://link.aps.org/doi/10.1103/PhysRev.140.A1133.

[14] D. C. Langreth and M. J. Mehl. "Beyond the local-density approximation in calculations of ground-state electronic properties". In: *Phys. Rev. B* 28 (4 1983), pp. 1809–1834. DOI: 10.1103/PhysRevB.28.1809. URL: https://link.aps.org/doi/10.1103/PhysRevB.28.1809.

[15] Erik Koch, Frithjof Anders, and Mark Jarrell. *Correlated electrons: from models to materials*. Ed. by Eva Pavarini. Vol. 2. Schriften des Forschungszentrums Jülich. Reihe modeling and simulation. Record converted from JUWEL: 18.07.2013. Jülich: Forschungszentrum Jülich GmbH Zenralbibliothek, Verlag, 2012, getr. Paginierung. ISBN: 978-3-89336-796-2. URL: https://juser.fz-juelich.de/record/136393.

[16] M. Cococcioni and S. de Gironcoli. "Linear response approach to the calculation of the effective interaction parameters in the LDA+U method". In: *Phys. Rev. B* 71 (3 2005), p. 035105. DOI: 10.1103/PhysRevB.71.035105. URL: https://link.aps.org/doi/10.1103/PhysRevB.71.035105.

[17] E. B. Linscott et al. "Role of spin in the calculation of Hubbard U and Hund's J parameters from first principles". In: *Phys. Rev. B* 98 (23 2018), p. 235157. DOI: 10.1103/PhysRevB.98.235157. URL: https://link.aps.org/doi/10.1103/PhysRevB.98.235157.

[18] Matteo Cococcioni. "Chapter 4 - The LDA+U Approach: A Simple Hubbard Correction for Correlated Ground States". In: ed. by Eva Pavarini. Vol. 2. Schriften des Forschungszentrums Jülich. Reihe modeling and simulation. Record converted from JUWEL: 18.07.2013. Jülich: Forschungszentrum Jülich GmbH Zenralbibliothek, Ver-

lag, 2012, pp. 4.1–4.40. ISBN: 978-3-89336-796-2. URL: https://juser.fz-juelich.de/record/136393.

[19] A. I. Liechtenstein, V. I. Anisimov, and J. Zaanen. "Density functional theory and strong interactions: Orbital ordering in Mott-Hubbard insulators". In: *Phys. Rev. B* 52 (8 1995), R5467–R5470. DOI: 10.1103/PhysRevB.52.R5467. URL: https://link.aps.org/doi/10.1103/PhysRevB.52.R5467.

[20] B. Himmetoglu et al. "Hubbard-corrected DFT energy functionals: The LDA+U description of correlated systems". In: *International Journal of Quantum Chemistry* 114.1 (2014), pp. 14–49. ISSN: 1097-461X. DOI: 10.1002/qua.24521. URL: https://onlinelibrary.wiley.com/doi/abs/10.1002/qua.24521 (visited on 01/27/2020).

[21] Fredrik Bultmark et al. "Multipole decomposition of LDA+U energy and its application to actinide compounds". In: *Phys. Rev. B* 80 (3 2009), p. 035121. DOI: 10.1103/PhysRevB.80.035121. URL: https://link.aps.org/doi/10.1103/PhysRevB.80.035121.

[22] Luca Binci and Nicola Marzari. *Noncollinear DFT+U and Hubbard parameters with fully-relativistic ultrasoft pseudopotentials*. arXiv:2304.10178 [cond-mat]. Apr. 2023. URL: http://arxiv.org/abs/2304.10178 (visited on 09/18/2023).

[23] E. Bousquet and N. Spaldin. "J dependence in the LSDA+U treatment of noncollinear magnets". In: *Phys. Rev. B* 82 (22 2010), p. 220402. DOI: 10.1103/PhysRevB.82.220402. URL: https://link.aps.org/doi/10.1103/PhysRevB.82.220402.

[24] S. L. Dudarev et al. "Parametrization of LSDA+U for noncollinear magnetic configurations: Multipolar magnetism in UO_2". In: *Phys. Rev. Mater.* 3 (8 2019), p. 083802. DOI: 10.1103/PhysRevMaterials.3.083802. URL: https://link.aps.org/doi/10.1103/PhysRevMaterials.3.083802.

[25] Juan E. Peralta, Gustavo E. Scuseria, and Michael J. Frisch. "Noncollinear magnetism in density functional calculations". In: *Phys. Rev. B* 75 (12 2007), p. 125119. DOI: 10.1103/PhysRevB.75.125119. URL: https://link.aps.org/doi/10.1103/PhysRevB.75.125119.

[26] S. L. Dudarev et al. "Electron-energy-loss spectra and the structural stability of nickel oxide: An LSDA+U study". In: *Phys. Rev. B* 57 (3 1998), pp. 1505–1509. DOI: 10.1103/PhysRevB.57.1505. URL: https://link.aps.org/doi/10.1103/PhysRevB.57.1505.

[27] Burak Himmetoglu, Renata M Wentzcovitch, and Matteo Cococcioni. "First-Principles Study of Electronic and Structural Properties of CuO". In: *Phys. Rev. B* 84.11 (2011), p. 115108.

[28] I. V. Solovyev, P. H. Dederichs, and V. I. Anisimov. "Corrected Atomic Limit in the Local-Density Approximation and the Electronic Structure of d Impurities in Rb". In: *Phys. Rev. B* 50.23 (1994), pp. 16861–16871. ISSN: 0163-1829. DOI: 10.1103/PhysRevB.50.16861.

[29] J. Hafner and G. Kresse. "The Vienna Ab-Initio Simulation Program VASP: An Efficient and Versatile Tool for Studying the Structural, Dynamic, and Electronic Properties of Materials". In: *Properties of Complex Inorganic Solids*. Ed. by Antonios Gonis, Annemarie Meike, and Patrice E. A. Turchi. Boston, MA: Springer US, 1997, pp. 69–82. ISBN: 978-1-4615-5943-6. DOI: 10.1007/978-1-4615-5943-6_10. URL: https://doi.org/10.1007/978-1-4615-5943-6_10 (visited on 03/10/2022).

[30] D. S. Lambert and D. D. O'Regan. "Use of DFT+U+J with linear response parameters to predict non-magnetic oxide band gaps with hybrid-functional accuracy". In: *Phys. Rev. Res.* 5 (1 2023), p. 013160. DOI: 10.1103/PhysRevResearch.5.013160. URL: https://link.aps.org/doi/10.1103/PhysRevResearch.5.013160.

[31] Andrew C. Burgess, Edward Linscott, and David D. O'Regan. "DFT+U-type functional derived to explicitly address the flat plane condition". In: *Phys. Rev. B* 107 (12 2023), p. L121115. DOI: 10.1103/PhysRevB.107.L121115. URL: https://link.aps.org/doi/10.1103/PhysRevB.107.L121115.

[32] Assa Auerbach. *Interacting Electrons and Quantum Magnetism*. Ed. by Joseph L. Birman et al. Graduate Texts in Contemporary Physics. New York, NY: Springer, 1994. ISBN: 978-1-4612-6928-1 978-1-4612-0869-3. DOI: 10.1007/978-1-4612-0869-3. (Visited on 06/19/2024).

[33] S. V. Streltsov and D. I. Khomskii. "Orbital physics in transition metal compounds: new trends". In: *Physics-Uspekhi* 60.11 (Nov. 2017). Publisher: IOP Publishing, p. 1121. ISSN: 1063-7869. DOI: 10.3367/UFNe.2017.08.038196. URL: https://iopscience.iop.org/article/10.3367/UFNe.2017.08.038196/meta (visited on 09/29/2022).

[34] Juan E. Peralta, Gustavo E. Scuseria, and Michael J. Frisch. "Noncollinear Magnetism in Density Functional Calculations". In: *Physical Review B* 75.12 (Mar. 2007), p. 125119. ISSN: 1098-0121, 1550-235X. DOI: 10.1103/PhysRevB.75.125119.

[35] James W. Furness et al. "Current Density Functional Theory Using Meta-Generalized Gradient Exchange-Correlation Functionals". In: *Journal of Chemical Theory and Computation* 11.9 (Sept. 2015), pp. 4169–4181. ISSN: 1549-9618, 1549-9626. DOI: 10.1021/acs.jctc.5b00535.

[36] Mary-Leena M. Tchenkoue et al. "Force Balance Approach for Advanced Approximations in Density Functional Theories". In: *The Journal of Chemical Physics* 151.15 (Oct. 2019), p. 154107. ISSN: 0021-9606. DOI: 10.1063/1.5123608. (Visited on 06/11/2024).

[37] S. Sharma et al. "Source-Free Exchange-Correlation Magnetic Fields in Density Functional Theory". In: *Journal of Chemical Theory and Computation* 14.3 (Mar. 2018), pp. 1247–1253. ISSN: 1549-9618. DOI: 10.1021/acs.jctc.7b01049.

[38] K. Capelle and E. K. U. Gross. "Spin-Density Functionals from Current-Density Functional Theory and Vice Versa:A Road towards New Approximations". In: *Physical Review Letters* 78.10 (Mar. 1997), pp. 1872–1875. ISSN: 0031-9007, 1079-7114. DOI: 10.1103/PhysRevLett.78.1872.

[39] H. Eschrig, G. Seifert, and P. Ziesche. "Current Density Functional Theory of Quantum Electrodynamics". In: *Solid State Communications* 56.9 (Dec. 1985), pp. 777–780. ISSN: 0038-1098. DOI: 10.1016/0038-1098(85)90307-2.

[40] G. Vignale and Mark Rasolt. "Current- and spin-density-functional theory for inhomogeneous electronic systems in strong magnetic fields". In: *Phys. Rev. B* 37 (18 1988), pp. 10685–10696. DOI: 10.1103/PhysRevB.37.10685. URL: https://link.aps.org/doi/10.1103/PhysRevB.37.10685.

[41] G. Vignale, Mark Rasolt, and D. J. W. Geldart. "Magnetic Fields and Density Functional Theory". In: *Advances in Quantum Chemistry*. Ed. by Per-Olov Löwdin. Vol. 21. Density Functional Theory of Many-Fermion Systems. Academic Press, Jan. 1990, pp. 235–253. DOI: 10.1016/S0065-3276(08)60599-7. (Visited on 10/31/2022).

[42] Olle Eriksson et al. *Atomistic spin dynamics: Foundations and applications*. Oxford University Press, Feb. 2017. ISBN: 978-0-19-878866-9. DOI: 10.1093/oso/9780198788669.001.0001. URL: https://doi.org/10.1093/oso/9780198788669.001.0001.

[43] José Luis García-Palacios and Francisco J. Lázaro. "Langevin-Dynamics Study of the Dynamical Properties of Small Magnetic Particles". In: *Physical Review B* 58.22 (Dec. 1998), pp. 14937–14958. ISSN: 0163-1829, 1095-3795. DOI: 10.1103/PhysRevB.58.14937. (Visited on 03/21/2024).

[44] Riccardo Poli, James Kennedy, and Tim Blackwell. "Particle swarm optimization". In: *Swarm intelligence* 1.1 (2007), pp. 33–57.

[45] F. van den Bergh and A.P. Engelbrecht. "A new locally convergent particle swarm optimiser". en. In: *IEEE International Conference on Systems, Man and Cybernetics*. Vol. vol.3. Yasmine Hammamet, Tunisia: IEEE, 2002, p. 6. ISBN: 978-0-7803-7437-9. DOI: 10.1109/ICSMC.2002.1176018. URL: http://ieeexplore.ieee.org/document/1176018/ (visited on 04/01/2020).

[46] K. Mathew et al. "Atomate: A high-level interface to generate, execute, and analyze computational materials science workflows". In: *Computational Materials Science* 139 (2017), pp. 140–152. ISSN: 0927-0256. DOI: https://doi.org/10.1016/j.commatsci.2017.07.030. URL: https://www.sciencedirect.com/science/article/pii/S0927025617303919.

[47] Vladimir I Anisimov, Jan Zaanen, and Ole K Andersen. "Band Theory and Mott Insulators: Hubbard U Instead of Stoner I". In: *Phys. Rev. B* 44.3 (1991), pp. 943–954.

[48] V I Anisimov et al. "Density-Functional Theory and NiO Photoemission Spectra". In: *Phys. Rev. B* 48 (1993), pp. 16929–16934.

[49] Vladimir I Anisimov, F Aryasetiawan, and A I Lichtenstein. "First-Principles Calculations of the Electronic Structure and Spectra of Strongly Correlated Systems: The LDA+U Method". In: *J. Phys. Condens. Matter* 9.4 (1997), p. 767.

[50] W. E. Pickett, S. C. Erwin, and E. C. Ethridge. "Reformulation of the LDA+U Method for a Local-Orbital Basis". In: *Phys. Rev. B* 58.3 (1998), pp. 1201–1209. DOI: 10.1103/PhysRevB.58.1201.

[51] H. J. Kulik et al. "Density Functional Theory in Transition-Metal Chemistry: A Self-Consistent Hubbard U Approach". In: *Physical Review Letters* 97.10 (Sept. 2006), p. 103001. ISSN: 0031-9007, 1079-7114. DOI: 10.1103/PhysRevLett.97.103001. URL: https://link.aps.org/doi/10.1103/PhysRevLett.97.103001 (visited on 08/06/2020).

[52] A. Bajaj, J. P. Janet, and H. J. Kulik. "Communication: Recovering the flat-plane condition in electronic structure theory at semi-local DFT cost". In: *The Journal of Chemical Physics* 147.19 (Nov. 2017). Publisher: American Institute of Physics, p. 191101. ISSN: 0021-9606. DOI: 10.1063/1.5008981. URL: https://aip.scitation.org/doi/full/10.1063/1.5008981 (visited on 12/16/2021).

[53] A. Bajaj and H. J. Kulik. "Molecular DFT+U: A Transferable, Low-Cost Approach to Eliminate Delocalization Error". In: *The Journal of Physical Chemistry Letters* (Apr. 2021). Publisher: American Chemical Society. DOI: 10.1021/acs.jpclett.1c00796. URL: https://pubs.acs.org/doi/pdf/10.1021/acs.jpclett.1c00796 (visited on 12/16/2021).

[54] Vivaldo Leiria Campo and Matteo Cococcioni. "Extended DFT+U+V method with on-site and inter-site electronic interactions". In: *Journal of Physics: Condensed Matter* 22.5 (2010), p. 055602. DOI: 10.1088/0953-8984/22/5/055602. URL: https://dx.doi.org/10.1088/0953-8984/22/5/055602.

[55] Nicolas Tancogne-Dejean and Angel Rubio. "Parameter-free hybridlike functional based on an extended Hubbard model: DFT+U+V". In: *Physical Review B* 102.15 (Oct. 2020), p. 155117. ISSN: 2469-9950, 2469-9969. DOI: 10.1103/PhysRevB.102.155117. URL: https://link.aps.org/doi/10.1103/PhysRevB.102.155117 (visited on 03/06/2022).

[56] Sang-Hoon Lee and Young-Woo Son. "First-principles approach with a pseudohybrid density functional for extended Hubbard interactions". In: *Physical Review Research* 2.4 (Dec. 2020), p. 043410. ISSN: 2643-1564. DOI: 10.1103/PhysRevResearch.2.043410. URL: https://link.aps.org/doi/10.1103/PhysRevResearch.2.043410 (visited on 03/06/2022).

[57] T. A. Mellan et al. "Importance of anisotropic Coulomb interaction in $LaMnO_3$". In: *Phys. Rev. B* 92 (8 2015), p. 085151. DOI: 10.1103/PhysRevB.92.085151. URL: https://link.aps.org/doi/10.1103/PhysRevB.92.085151.

[58] Antoine Georges, Luca de' Medici, and Jernej Mravlje. "Strong Correlations from Hund's Coupling". In: *Annual Review of Condensed Matter Physics* 4.1 (2013), pp. 137–178. DOI: 10.1146/annurev-conmatphys-020911-125045. eprint: https://doi.org/10.1146/annurev-conmatphys-020911-125045. URL: https://doi.org/10.1146/annurev-conmatphys-020911-125045.

[59] H. C. Herper et al. "Combining electronic structure and many-body theory with large databases: A method for predicting the nature of $4f$ states in Ce compounds". In: *Physical Review Materials* 1.3 (Aug. 2017), p. 033802. ISSN: 2475-9953. DOI: 10.1103/PhysRevMaterials.1.033802. URL: https://link.aps.org/doi/10.1103/PhysRevMaterials.1.033802 (visited on 03/06/2022).

[60] A. Jain et al. "Formation enthalpies by mixing GGA and GGA+U calculations". In: *Physical Review B* 84.4 (July 2011). Publisher: American Physical Society, p. 045115. DOI: 10.1103/PhysRevB.84.045115. URL: https://link.aps.org/doi/10.1103/PhysRevB.84.045115 (visited on 05/13/2021).

[61] M. Yu et al. "Machine learning the Hubbard U parameter in DFT+U using Bayesian optimization". In: *npj Computational Materials* 6.1 (Nov. 2020). Number: 1 Publisher: Nature Publishing Group, pp. 1–6. ISSN: 2057-3960. DOI: 10.1038/s41524-020-00446-9. URL: http://www.nature.com/articles/s41524-020-00446-9 (visited on 12/15/2020).

[62] R. C. Albers, N. E. Christensen, and A. Svane. "Hubbard-U band-structure methods". In: *Journal of Physics: Condensed Matter* 21.34 (2009), p. 343201. DOI: 10.1088/0953-8984/21/34/343201. URL: https://doi.org/10.1088/0953-8984/21/34/343201.

[63] F. Zhou et al. "First-principles prediction of redox potentials in transition-metal compounds with LDA+U". In: *Phys. Rev. B* 70 (23 2004), p. 235121. DOI: 10.1103/PhysRevB.70.235121. URL: https://link.aps.org/doi/10.1103/PhysRevB.70.235121.

[64] Yue-Chao Wang, Ze-Hua Chen, and Hong Jiang. "The local projection in the density functional theory plus U approach: A critical assessment". In: *The Journal of Chemical Physics* 144.14 (Apr. 2016), p. 144106. ISSN: 0021-9606, 1089-7690. DOI: 10.1063/1.4945608. URL: http://aip.scitation.org/doi/10.1063/1.4945608 (visited on 03/06/2022).

[65] Xinguo Ren. "Chapter 2 - The Random Phase Approximation and its Applications to Real Materials". In: ed. by Eva Pavarini, Erik Koch, and Schiwei Zhang. Vol. 9. Schriften des Forschungszentrums Jülich. Modeling and Simulation. Jülich: Forschungszentrum Jülich GmbH Zentralbibliothek, Verlag, Sept. 16, 2019, pp. 2.1–

2.27. ISBN: 978-3-95806-400-3. URL: https://juser.fz-juelich.de/record/864818.

[66] Loïg Vaugier, Hong Jiang, and Silke Biermann. "Hubbard U and Hund exchange J in transition metal oxides: Screening versus localization trends from constrained random phase approximation". In: *Phys. Rev. B* 86 (16 2012), p. 165105. DOI: 10.1103/PhysRevB.86.165105. URL: https://link.aps.org/doi/10.1103/PhysRevB.86.165105.

[67] Aron J Cohen, Paula Mori-Sánchez, and Weitao Yang. "Insights into Current Limitations of Density Functional Theory". In: *Science* 321.5890 (2008), pp. 792–794.

[68] Qing Zhao, Efthymios I. Ioannidis, and Heather J. Kulik. "Global and Local Curvature in Density Functional Theory". In: *J. Chem. Phys.* 145.5 (Aug. 2016), p. 054109. ISSN: 0021-9606. DOI: 10.1063/1.4959882. (Visited on 09/08/2016).

[69] John P Perdew, Kieron Burke, and Matthias Ernzerhof. "Generalized Gradient Approximation Made Simple". In: *Phys. Rev. Lett.* 77.18 (1996), pp. 3865–3868.

[70] ***pymatgen*** *code repository*. https://github.com/materialsproject/pymatgen.git. 2023.

[71] Joseph W. Bennett et al. "A systematic determination of Hubbard U using the GBRV ultrasoft pseudopotential set". In: *Computational Materials Science* 170 (Dec. 2019), p. 109137. ISSN: 09270256. DOI: 10.1016/j.commatsci.2019.109137. URL: https://linkinghub.elsevier.com/retrieve/pii/S0927025619304288 (visited on 03/06/2022).

[72] ***atomate*** *code repository*. https://github.com/hackingmaterials/atomate.git. 2023.

[73] C. R. Harris et al. "Array programming with NumPy". In: *Nature* 585.7825 (Sept. 2020), pp. 357–362. DOI: 10.1038/s41586-020-2649-2. URL: https://doi.org/10.1038/s41586-020-2649-2.

[74] B. Ochoa and S. Belongie. *Covariance Propagation for Guided Matching*. 2011.

[75] Jyoti Krishna et al. "Complete description of the magnetic ground state in spinel vanadates". In: *Phys. Rev. B* 100 (8 2019), p. 081102. DOI: 10.1103/PhysRevB.100.081102. URL: https://link.aps.org/doi/10.1103/PhysRevB.100.081102.

[76] Z. Hawkhead et al. *First-principles calculations of magnetic states in pyrochlores using a source-corrected exchange and correlation functional*. 2023. arXiv: 2302.08564 [cond-mat.mtrl-sci].

[77] ***Elk*** *codebase*. https://elk.sourceforge.io. 2023.

[78] J K Dewhurst and S Sharma. "Development of the Elk LAPW Code". In: *Max Planck Institute of Microstructure Physics Theory Department* (). URL: https://www2.mpi-halle.mpg.de/fileadmin/templates/images/articles/elk/article.pdf.

[79] *Source-free $\boldsymbol{B}_{xc}$ code patch repository*. https://github.com/guymoore13/source_free_Bxc_VASP. 2023.

[80] J. J. Sakurai and Jim Napolitano. *Modern Quantum Mechanics*. 2nd ed. Cambridge University Press, 2017. DOI: 10.1017/9781108499996.

[81] G. Vignale and Mark Rasolt. "Density-Functional Theory in Strong Magnetic Fields". In: *Physical Review Letters* 59.20 (Nov. 1987), pp. 2360–2363. ISSN: 0031-9007. DOI: 10.1103/PhysRevLett.59.2360.

[82] Soner Steiner et al. "Calculation of the magnetic anisotropy with projected-augmented-wave methodology and the case study of disordered $Fe_{1-x}Co_x$ alloys". In: *Phys. Rev. B* 93 (22 2016), p. 224425. DOI: 10.1103/PhysRevB.93.224425. URL: https://link.aps.org/doi/10.1103/PhysRevB.93.224425.

[83] K Bencheikh. "Spin–Orbit Coupling in the Spin-Current-Density-Functional Theory". In: *Journal of Physics A: Mathematical and General* 36.48 (Dec. 2003), pp. 11929–11936. ISSN: 0305-4470, 1361-6447. DOI: 10.1088/0305-4470/36/48/002.

[84] Neil W. Ashcroft and David N. Mermin. *Solid state physics*. Australia: Brooks/Cole, 1976 - 1976. ISBN: 0030839939.

[85] Jianmin Tao. "Explicit Inclusion of Paramagnetic Current Density in the Exchange-Correlation Functionals of Current-Density Functional Theory". In: *Physical Review B* 71.20 (May 2005), p. 205107. ISSN: 1098-0121, 1550-235X. DOI: 10.1103/PhysRevB.71.205107.

[86] G. Vignale and Mark Rasolt. "Current- and Spin-Density-Functional Theory for Inhomogeneous Electronic Systems in Strong Magnetic Fields". In: *Physical Review B* 37.18 (June 1988), pp. 10685–10696. ISSN: 0163-1829. DOI: 10.1103/PhysRevB.37.10685.

[87] Elena Braverman et al. "A Fast Spectral Subtractional Solver for Elliptic Equations". In: *Journal of Scientific Computing* 21.1 (Aug. 2004), pp. 91–128. ISSN: 0885-7474. DOI: 10.1023/B:JOMP.0000027957.39059.6b.

[88] Y. Wu et al. "Enhanced orbital magnetic moment on Co atoms in Co/Pd multilayers: A magnetic circular x-ray dichroism study". In: *Phys. Rev. Lett.* 69 (15 1992), pp. 2307–2310. DOI: 10.1103/PhysRevLett.69.2307. URL: https://link.aps.org/doi/10.1103/PhysRevLett.69.2307.

[89] H. Elnaggar et al. "Noncollinear Ordering of the Orbital Magnetic Moments in Magnetite". In: *Phys. Rev. Lett.* 123 (20 2019), p. 207201. DOI: 10.1103/PhysRevLett.123.207201. URL: https://link.aps.org/doi/10.1103/PhysRevLett.123.207201.

[90] S. Sharma et al. "Comparison of exact-exchange calculations for solids in current-spin-density- and spin-density-functional theory". In: *Phys. Rev. B* 76 (10 2007), p. 100401. DOI: 10.1103/PhysRevB.76.100401. URL: https://link.aps.org/doi/10.1103/PhysRevB.76.100401.

[91] Edward A. Pluhar and Carsten A. Ullrich. "Exchange-Correlation Magnetic Fields in Spin-Density-Functional Theory". In: *Physical Review B* 100.12 (Sept. 2019), p. 125135. ISSN: 2469-9950, 2469-9969. DOI: 10.1103/PhysRevB.100.125135.

[92] K. Capelle, G. Vignale, and B. L. Györffy. "Spin Currents and Spin Dynamics in Time-Dependent Density-Functional Theory". In: *Phys. Rev. Lett.* 87 (20 2001), p. 206403. DOI: 10.1103/PhysRevLett.87.206403. URL: https://link.aps.org/doi/10.1103/PhysRevLett.87.206403.

[93] Matthew Kristofer Horton et al. "High-throughput prediction of the ground-state collinear magnetic order of inorganic materials using Density Functional Theory". In: *npj Computational Materials* 5.1 (June 2019). Number: 1 Publisher: Nature Publishing Group, pp. 1–11. ISSN: 2057-3960. DOI: 10.1038/s41524-019-0199-7. URL: https://www.nature.com/articles/s41524-019-0199-7 (visited on 09/28/2023).

[94] Nathan C. Frey et al. "High-throughput search for magnetic and topological order in transition metal oxides". In: *Science Advances* 6.50 (Dec. 2020). Publisher: American Association for the Advancement of Science, eabd1076. DOI: 10.1126/sciadv.abd1076. URL: https://www.science.org/doi/full/10.1126/sciadv.abd1076 (visited on 09/28/2023).

[95] M.-T. Huebsch et al. "Benchmark for *Ab Initio* Prediction of Magnetic Structures Based on Cluster-Multipole Theory". In: *Physical Review X* 11.1 (Feb. 2021), p. 011031. ISSN: 2160-3308. DOI: 10.1103/PhysRevX.11.011031. URL: https://link.aps.org/doi/10.1103/PhysRevX.11.011031 (visited on 06/14/2023).

[96] M.-T. Suzuki et al. "Multipole expansion for magnetic structures: A generation scheme for a symmetry-adapted orthonormal basis set in the crystallographic point group". In: *Physical Review B* 99.17 (May 2019), p. 174407. ISSN: 2469-9950, 2469-9969. DOI: 10.1103/PhysRevB.99.174407. URL: https://link.aps.org/doi/10.1103/PhysRevB.99.174407 (visited on 06/14/2023).

[97] E.S. Peer, F. van den Bergh, and A.P. Engelbrecht. "Using neighbourhoods with the guaranteed convergence PSO". In: *Proceedings of the 2003 IEEE Swarm Intelligence Symposium. SIS'03 (Cat. No.03EX706)*. Apr. 2003, pp. 235–242. DOI: 10.1109/SIS.2003.1202274.

[98] David Cortés-Ortuño et al. "Thermal stability and topological protection of skyrmions in nanotracks". In: *Scientific Reports* 7.1 (June 2017). Number: 1 Publisher: Nature Publishing Group, p. 4060. ISSN: 2045-2322. DOI: 10.1038/s41598-017-03391-8. URL: https://www.nature.com/articles/s41598-017-03391-8 (visited on 10/01/2023).

[99] M. Lakshmanan. "The fascinating world of the Landau–Lifshitz–Gilbert equation: an overview". In: *Philosophical Transactions of the Royal Society A: Mathematical, Physical and Engineering Sciences* 369.1939 (Mar. 2011). Publisher: Royal Society, pp. 1280–1300. DOI: 10.1098/rsta.2010.0319. (Visited on 09/21/2023).

[100] Giorgio Bertotti. "Chapter 3 - Maxwell's Equations in Magnetic Media". In: *Hysteresis in Magnetism*. Ed. by Giorgio Bertotti. Electromagnetism. San Diego: Academic Press, 1998, pp. 73–102. ISBN: 978-0-12-093270-2. DOI: https://doi.org/10.1016/B978-012093270-2/50052-0. URL: https://www.sciencedirect.com/science/article/pii/B9780120932702500520.

[101] Adam Payne et al. "Firefly Algorithm Applied to Noncollinear Magnetic Phase Materials Prediction". In: *Journal of Chemical Theory and Computation* 14.8 (Aug. 2018), pp. 4455–4466. ISSN: 1549-9618, 1549-9626. DOI: 10.1021/acs.jctc.8b00404. URL: https://pubs.acs.org/doi/10.1021/acs.jctc.8b00404 (visited on 06/14/2023).

[102] Saibal K. Pal, C.S Rai, and Amrit Pal Singh. "Comparative Study of Firefly Algorithm and Particle Swarm Optimization for Noisy Non-Linear Optimization Problems". In: *International Journal of Intelligent Systems and Applications* 4.10 (Sept. 2012), pp. 50–57. ISSN: 2074904X, 20749058. DOI: 10.5815/ijisa.2012.10.06. URL: http://www.mecs-press.org/ijisa/ijisa-v4-n10/v4n10-6.html (visited on 10/02/2023).

[103] B. Bhushan and S. S. Pillai. "Particle Swarm Optimization and Firefly Algorithm: Performance analysis". In: *2013 3rd IEEE International Advance Computing Conference (IACC)*. Ghaziabad: IEEE, Feb. 2013, pp. 746–751. ISBN: 978-1-4673-4529-3 978-1-4673-4527-9 978-1-4673-4528-6. DOI: 10.1109/IAdCC.2013.6514320. URL: http://ieeexplore.ieee.org/document/6514320/ (visited on 10/02/2023).

[104] Karl O. Jones and Grégoire Boizanté. "Comparison of Firefly algorithm optimisation, particle swarm optimisation and differential evolution". In: *Proceedings of the 12th International Conference on Computer Systems and Technologies*. CompSysTech '11. New York, NY, USA: Association for Computing Machinery, June 2011, pp. 191–197. ISBN: 978-1-4503-0917-2. DOI: 10.1145/2023607.2023640. URL: https://dl.acm.org/doi/10.1145/2023607.2023640 (visited on 10/02/2023).

[105] Pui-Wai Ma and S. L. Dudarev. "Constrained density functional for noncollinear magnetism". In: *Physical Review B* 91.5 (Feb. 2015), p. 054420. ISSN: 1098-0121, 1550-235X. DOI: 10.1103/PhysRevB.91.054420. URL: https://link.aps.org/doi/10.1103/PhysRevB.91.054420 (visited on 06/14/2023).

[106] E.S. Goh, J.W. Mah, and T.L. Yoon. "Effects of Hubbard term correction on the structural parameters and electronic properties of wurtzite ZnO". In: *Computational Materials Science* 138 (Oct. 2017), pp. 111–116. ISSN: 09270256. DOI: 10.1016/j.commatsci.2017.06.032. URL: https://linkinghub.elsevier.com/retrieve/pii/S0927025617303361 (visited on 03/10/2022).

[107] N. Bondarenko, O. Eriksson, and N. V. Skorodumova. "Polaron mobility in oxygen-deficient and lithium-doped tungsten trioxide". In: *Phys. Rev. B* 92 (16 2015), p. 165119. DOI: 10.1103/PhysRevB.92.165119. URL: https://link.aps.org/doi/10.1103/PhysRevB.92.165119.

[108] J. J. Plata, A. M. Márquez, and J. F. Sanz. "Communication: Improving the density functional theory $+U$ description of CeO_2 by including the contribution of the O $2p$ electrons". In: *The Journal of Chemical Physics* 136.4 (Jan. 2012), p. 041101. ISSN: 0021-9606, 1089-7690. DOI: 10.1063/1.3678309. URL: http://aip.scitation.org/doi/10.1063/1.3678309 (visited on 12/16/2021).

[109] FG Kuang et al. "An ab initio study on the electronic and magnetic properties of MgO with intrinsic defects". In: *RSC Adv.* 4.93 (2014), pp. 51366–51373. ISSN: 2046-2069. DOI: 10.1039/C4RA06340F. URL: http://xlink.rsc.org/?DOI=C4RA06340F (visited on 12/16/2021).

[110] H. A. Kramers. "L'interaction Entre les Atomes Magnétogènes dans un Cristal Paramagnétique". In: *Physica* 1.1 (Jan. 1934), pp. 182–192. ISSN: 0031-8914. DOI: 10.1016/S0031-8914(34)90023-9. URL: https://www.sciencedirect.com/science/article/pii/S0031891434900239 (visited on 12/16/2021).

[111] P. W. Anderson. "Antiferromagnetism. Theory of Superexchange Interaction". In: *Physical Review* 79.2 (July 1950), pp. 350–356. ISSN: 0031-899X. DOI: 10.1103/PhysRev.79.350. URL: https://link.aps.org/doi/10.1103/PhysRev.79.350 (visited on 12/16/2021).

[112] Pauli Virtanen et al. "SciPy 1.0: Fundamental Algorithms for Scientific Computing in Python". In: *Nature Methods* 17 (2020), pp. 261–272. DOI: 10.1038/s41592-019-0686-2.

[113] S. P. Ong. *GGA+U Calculations*. URL: https://docs.materialsproject.org/methodology/gga-plus-u/.

[114] L. Wang, T. Maxisch, and G. Ceder. "Oxidation energies of transition metal oxides within the GGA+U framework". In: *Phys. Rev. B* 73 (19 2006), p. 195107. DOI: 10.1103/PhysRevB.73.195107. URL: https://link.aps.org/doi/10.1103/PhysRevB.73.195107.

[115] A. Wang et al. "A framework for quantifying uncertainty in DFT energy corrections". In: *Scientific Reports* 11.1 (2021), p. 15496. ISSN: 2045-2322. DOI: 10.1038/s41598-021-94550-5. URL: https://doi.org/10.1038/s41598-021-94550-5.

[116] D. van der Marel and G. A. Sawatzky. "Electron-electron interaction and localization in d and f transition metals". In: *Physical Review B* 37.18 (June 1988). Publisher: American Physical Society, pp. 10674–10684. DOI: 10.1103/PhysRevB.37.10674. URL: https://link.aps.org/doi/10.1103/PhysRevB.37.10674 (visited on 04/11/2023).

[117] I. S. Elfimov et al. "Magnetizing Oxides by Substituting Nitrogen for Oxygen". In: *Physical Review Letters* 98.13 (Mar. 2007), p. 137202. ISSN: 0031-9007, 1079-7114. DOI: 10.1103/PhysRevLett.98.137202. URL: https://link.aps.org/doi/10.1103/PhysRevLett.98.137202 (visited on 12/16/2021).

[118] Robert G. Parr and Ralph G. Pearson. "Absolute hardness: companion parameter to absolute electronegativity". In: *Journal of the American Chemical Society* 105.26 (1983), pp. 7512–7516. DOI: 10.1021/ja00364a005. URL: https://doi.org/10.1021/ja00364a005.

[119] Xiao Dong et al. "Electronegativity and chemical hardness of elements under pressure". In: *Proceedings of the National Academy of Sciences* 119.10 (2022), e2117416119. DOI: 10.1073/pnas.2117416119. URL: https://www.pnas.org/doi/abs/10.1073/pnas.2117416119.

[120] D. Guerra et al. "Hardness and softness kernels, and related indices in the spin polarized version of density functional theory". In: *Chemical Physics Letters* 419.1 (2006), pp. 37–43. ISSN: 0009-2614. DOI: https://doi.org/10.1016/j.cplett.2005.11.039. URL: https://www.sciencedirect.com/science/article/pii/S0009261405017574.

[121] C. Ricca et al. "Self-consistent site-dependent DFT+U study of stoichiometric and defective $SrMnO_3$". In: *Phys. Rev. B* 99 (9 2019), p. 094102. DOI: 10.1103/PhysRevB.99.094102. URL: https://link.aps.org/doi/10.1103/PhysRevB.99.094102.

[122] D. Lu and P. Liu. "Rationalization of the Hubbard U parameter in CeO_x from first principles: Unveiling the role of local structure in screening". In: *The Journal of Chemical Physics* 140.8 (2014), p. 084101. DOI: 10.1063/1.4865831. eprint: https://doi.org/10.1063/1.4865831. URL: https://doi.org/10.1063/1.4865831.

[123] I. D. Brown. "Recent Developments in the Methods and Applications of the Bond Valence Model". In: *Chemical Reviews* 109.12 (2009). PMID: 19728716, pp. 6858–6919. DOI: 10.1021/cr900053k. eprint: https://doi.org/10.1021/cr900053k. URL: https://doi.org/10.1021/cr900053k.

[124] John C. Slater. *Quantum theory of atomic structure*. International series in pure and applied physics. New York: McGraw-Hill, 1960. ISBN: 0070580405.

[125] Julia H. Yang et al. "Approaches for handling high-dimensional cluster expansions of ionic systems". In: *npj Computational Materials* 8.1 (June 2022). Number: 1 Publisher: Nature Publishing Group, pp. 1–11. ISSN: 2057-3960. DOI: 10.1038/s41524-022-00818-3. (Visited on 09/19/2022).

[126] John Reed and Gerbrand Ceder. "Role of Electronic Structure in the Susceptibility of Metastable Transition-Metal Oxide Structures to Transformation". In: *Chemical Reviews* 104.10 (Oct. 2004), pp. 4513–4534. ISSN: 0009-2665, 1520-6890. DOI: 10.1021/cr020733x. (Visited on 09/19/2022).

[127] Kisuk Kang et al. "Synthesis and Electrochemical Properties of Layered $Li_{0.9}Ni_{0.45}Ti_{0.55}O_2$". In: *Chemistry of Materials* 15.23 (Nov. 2003), pp. 4503–4507. ISSN: 0897-4756, 1520-5002. DOI: 10.1021/cm034455+. (Visited on 09/19/2022).

[128] Peter Blaha et al. "WIEN2k: An APW+lo program for calculating the properties of solids". In: *The Journal of Chemical Physics* 152.7 (Feb. 2020). Publisher: American Institute of Physics, p. 074101. ISSN: 0021-9606. DOI: 10.1063/1.5143061. URL: https://aip.scitation.org/doi/10.1063/1.5143061 (visited on 04/15/2023).

[129] J. B. Mann. "ATOMIC STRUCTURE CALCULATIONS. II. HARTREE-FOCK WAVEFUNCTIONS AND RADIAL EXPECTATION VALUES: HYDROGEN TO LAWRENCIUM." In: (Jan. 1968). DOI: 10.2172/4553157. URL: https://www.osti.gov/biblio/4553157.

[130] Logan Ward et al. "Matminer: An open source toolkit for materials data mining". In: *Computational Materials Science* 152 (2018), pp. 60–69. ISSN: 0927-0256. DOI: https://doi.org/10.1016/j.commatsci.2018.05.018. URL: https://www.sciencedirect.com/science/article/pii/S0927025618303252.

[131] Tien Lam Pham et al. "Machine Learning Reveals Orbital Interaction in Materials". In: *Science and Technology of Advanced Materials* 18.1 (Dec. 2017), pp. 756–765. ISSN: 1468-6996, 1878-5514. DOI: 10.1080/14686996.2017.1378060.

[132] Mohammadreza Karamad et al. "Orbital Graph Convolutional Neural Network for Material Property Prediction". In: *Physical Review Materials* 4.9 (Sept. 2020), p. 093801. ISSN: 2475-9953. DOI: 10.1103/PhysRevMaterials.4.093801.

[133] G. Moynihan, G. Teobaldi, and D. D. O'Regan. "A self-consistent ground-state formulation of the first-principles Hubbard U parameter validated on one-electron self-interaction error". In: *arXiv:1704.08076 [cond-mat]* (Apr. 2017). arXiv: 1704.08076. URL: http://arxiv.org/abs/1704.08076 (visited on 08/06/2020).

[134] Lane W. Martin et al. "Nanoscale Control of Exchange Bias with BiFeO3 Thin Films". In: *Nano Letters* 8.7 (July 2008), pp. 2050–2055. ISSN: 1530-6984. DOI: 10.1021/nl801391m. (Visited on 07/08/2024).

[135] R. Ramesh and Nicola A. Spaldin. "Multiferroics: Progress and Prospects in Thin Films". In: *Nature Materials* 6.1 (Jan. 2007), pp. 21–29. ISSN: 1476-4660. DOI: 10.1038/nmat1805. (Visited on 07/08/2024).

[136] Manuel Bibes and Agnès Barthélémy. "Towards a Magnetoelectric Memory". In: *Nature Materials* 7.6 (June 2008), pp. 425–426. ISSN: 1476-4660. DOI: 10.1038/nmat2189. (Visited on 07/08/2024).

[137] J. T. Heron, D. G. Schlom, and R. Ramesh. "Electric Field Control of Magnetism Using BiFeO3-based Heterostructures". In: *Applied Physics Reviews* 1.2 (Apr. 2014), p. 021303. ISSN: 1931-9401. DOI: 10.1063/1.4870957. (Visited on 07/08/2024).

[138] Peter B. Meisenheimer et al. "Perspective: Magnetoelectric Switching in Thin Film Multiferroic Heterostructures". In: *Journal of Applied Physics* 123.24 (June 2018), p. 240901. ISSN: 0021-8979. DOI: 10.1063/1.5031446. (Visited on 07/08/2024).

[139] Elzbieta Gradauskaite et al. "Multiferroic Heterostructures for Spintronics". In: *Physical Sciences Reviews* 6.2 (Feb. 2021). ISSN: 2365-659X. DOI: 10.1515/psr-2019-0072. (Visited on 07/08/2024).

[140] Dmitri E. Nikonov and Ian A. Young. "Benchmarking of Beyond-CMOS Exploratory Devices for Logic Integrated Circuits". In: *IEEE Journal on Exploratory Solid-State Computational Devices and Circuits* 1 (Dec. 2015), pp. 3–11. ISSN: 2329-9231. DOI: 10.1109/JXCDC.2015.2418033. (Visited on 07/08/2024).

[141] Dmitri E. Nikonov and Ian A. Young. "Benchmarking Spintronic Logic Devices Based on Magnetoelectric Oxides". In: *Journal of Materials Research* 29.18 (Sept. 2014), pp. 2109–2115. ISSN: 2044-5326. DOI: 10.1557/jmr.2014.243. (Visited on 07/08/2024).

[142] Sasikanth Manipatruni et al. "Scalable Energy-Efficient Magnetoelectric Spin–Orbit Logic". In: *Nature* 565.7737 (Jan. 2019), pp. 35–42. ISSN: 1476-4687. DOI: 10.1038/s41586-018-0770-2. (Visited on 07/08/2024).

[143] Sasikanth Manipatruni, Dmitri E. Nikonov, and Ian A. Young. "Beyond CMOS Computing with Spin and Polarization". In: *Nature Physics* 14.4 (Apr. 2018), pp. 338–343. ISSN: 1745-2481. DOI: 10.1038/s41567-018-0101-4. (Visited on 07/08/2024).

[144] J. T. Heron et al. "Deterministic Switching of Ferromagnetism at Room Temperature Using an Electric Field". In: *Nature* 516.7531 (Dec. 2014), pp. 370–373. ISSN: 1476-4687. DOI: 10.1038/nature14004. (Visited on 07/08/2024).

[145] J. T. Heron et al. "Electric-Field-Induced Magnetization Reversal in a Ferromagnet-Multiferroic Heterostructure". In: *Physical Review Letters* 107.21 (Nov. 2011). DOI: 10.1103/PhysRevLett.107.217202. (Visited on 07/08/2024).

[146] Bhagwati Prasad et al. "Ultralow Voltage Manipulation of Ferromagnetism". In: *Advanced Materials* 32.28 (2020), p. 2001943. ISSN: 1521-4095. DOI: 10.1002/adma.202001943. (Visited on 07/08/2024).

[147] N. Mikuszeit et al. "Magnetostatics and the Rotational Sense of Cycloidal Spin Spirals". In: *Physical Review B* 84.5 (Aug. 2011), p. 054404. DOI: 10.1103/PhysRevB.84.054404. (Visited on 07/08/2024).

[148] D. Lebeugle et al. "Electric-Field-Induced Spin Flop in $BiFeO_3$ Single Crystals at Room Temperature". In: *Physical Review Letters* 100.22 (June 2008), p. 227602. DOI: 10.1103/PhysRevLett.100.227602. (Visited on 07/08/2024).

[149] I. Sosnowska and A. K. Zvezdin. "Origin of the Long Period Magnetic Ordering in BiFeO3". In: *Journal of Magnetism and Magnetic Materials*. International Conference on Magnetism 140–144 (Feb. 1995), pp. 167–168. ISSN: 0304-8853. DOI: 10.1016/0304-8853(94)01120-6. (Visited on 07/08/2024).

[150] X. Ke et al. "Magnetic Structure of Epitaxial Multiferroic $BiFeO_3$ Films with Engineered Ferroelectric Domains". In: *Physical Review B* 82.13 (Oct. 2010), p. 134448. DOI: 10.1103/PhysRevB.82.134448. (Visited on 07/08/2024).

[151] I. Sosnowska, T. P. Neumaier, and E. Steichele. "Spiral Magnetic Ordering in Bismuth Ferrite". In: *Journal of Physics C: Solid State Physics* 15.23 (Aug. 1982), p. 4835. ISSN: 0022-3719. DOI: 10.1088/0022-3719/15/23/020. (Visited on 07/08/2024).

[152] D. Rahmedov et al. "Magnetic Cycloid of ${\mathrm{BiFeO}}_{3}$ from Atomistic Simulations". In: *Physical Review Letters* 109.3 (July 2012), p. 037207. DOI: 10.1103/PhysRevLett.109.037207. (Visited on 07/08/2024).

[153] Satadeep Bhattacharjee et al. "Novel Magnetic Arrangement and Structural Phase Transition Induced by Spin–Lattice Coupling in Multiferroics". In: *MRS Communications* 3.4 (Dec. 2013), pp. 213–218. ISSN: 2159-6867. DOI: 10.1557/mrc.2013.45. (Visited on 07/08/2024).

[154] I. Gross et al. "Real-Space Imaging of Non-Collinear Antiferromagnetic Order with a Single-Spin Magnetometer". In: *Nature* 549.7671 (Sept. 2017), pp. 252–256. ISSN: 1476-4687. DOI: 10.1038/nature23656. (Visited on 07/08/2024).

[155] Aurore Finco et al. "Imaging Topological Defects in a Noncollinear Antiferromagnet". In: *Physical Review Letters* 128.18 (May 2022), p. 187201. DOI: 10.1103/PhysRevLett.128.187201. (Visited on 07/08/2024).

[156] M. Ramazanoglu et al. "Local Weak Ferromagnetism in Single-Crystalline Ferroelectric $BiFeO_3$". In: *Physical Review Letters* 107.20 (Nov. 2011), p. 207206. DOI: 10.1103/PhysRevLett.107.207206. (Visited on 07/08/2024).

[157] A. M. Kadomtseva et al. "Space-Time Parity Violation and Magnetoelectric Interactions in Antiferromagnets". In: *Journal of Experimental and Theoretical Physics Letters* 79.11 (June 2004), pp. 571–581. ISSN: 1090-6487. DOI: 10.1134/1.1787107. (Visited on 07/08/2024).

[158] Hai Zhong et al. "Quantitative Imaging of Exotic Antiferromagnetic Spin Cycloids in $BiFeO_3$ Thin Films". In: *Physical Review Applied* 17.4 (Apr. 2022), p. 044051. DOI: 10.1103/PhysRevApplied.17.044051. (Visited on 07/08/2024).

[159] Jason M. Munro et al. "Discovering Minimum Energy Pathways via Distortion Symmetry Groups". In: *Physical Review B* 98.8 (Aug. 2018), p. 085107. DOI: 10.1103/PhysRevB.98.085107. (Visited on 07/08/2024).

[160] Claude Ederer and Nicola A. Spaldin. "Weak Ferromagnetism and Magnetoelectric Coupling in Bismuth Ferrite". In: *Physical Review B* 71.6 (Feb. 2005), p. 060401. DOI: 10.1103/PhysRevB.71.060401. (Visited on 07/08/2024).

[161] Je-Geun Park et al. "Structure and Spin Dynamics of Multiferroic BiFeO3". In: *Journal of Physics: Condensed Matter* 26.43 (Oct. 2014), p. 433202. ISSN: 0953-8984. DOI: 10.1088/0953-8984/26/43/433202. (Visited on 07/08/2024).

[162] A. I. Liechtenstein, V. I. Anisimov, and J. Zaanen. "Density-functional theory and strong interactions: Orbital ordering in Mott-Hubbard insulators". In: *Physical Review B* 52.8 (Aug. 1995), R5467–R5470. ISSN: 0163-1829, 1095-3795. DOI: 10.1103/PhysRevB.52.R5467. URL: https://link.aps.org/doi/10.1103/PhysRevB.52.R5467 (visited on 03/06/2022).

[163] Leonid V. Poluyanov and Wolfgang Domcke. "Jahn-Teller, Pseudo-Jahn-Teller, and Spin-Orbit Coupling Hamiltonian of a d Electron in an Octahedral Environment". In: *The Journal of Chemical Physics* 137.11 (Sept. 2012), p. 114101. ISSN: 0021-9606. DOI: 10.1063/1.4751439. (Visited on 07/09/2024).

[164] Sergey V. Streltsov and Daniel I. Khomskii. "Jahn-Teller Effect and Spin-Orbit Coupling: Friends or Foes?" In: *Physical Review X* 10.3 (Aug. 2020), p. 031043. DOI: 10.1103/PhysRevX.10.031043. (Visited on 07/09/2024).

[165] D. Sando et al. "Crafting the Magnonic and Spintronic Response of $BiFeO_3$ Films by Epitaxial Strain". In: *Nature Materials* 12.7 (July 2013), pp. 641–646. ISSN: 1476-4660. DOI: 10.1038/nmat3629. (Visited on 07/09/2024).

[166] T. B. S. Jensen et al. "Field-induced magnetic phases and electric polarization in $LiNiPO_4$". In: *Phys. Rev. B* 79 (9 2009), p. 092412. DOI: 10.1103/PhysRevB.79.092412. URL: https://link.aps.org/doi/10.1103/PhysRevB.79.092412.

[167] J. Perez-Mato et al. "Crystallography Online: Bilbao Crystallographic Server". In: *Bulgarian Chemical Communications* 43 (Jan. 2011), pp. 183–197.

[168] Ellen Fogh et al. "Dzyaloshinskii-Moriya interaction and the magnetic ground state in magnetoelectric $LiCoPO_4$". In: *Phys. Rev. B* 99 (10 2019), p. 104421. DOI: 10.1103/PhysRevB.99.104421. URL: https://link.aps.org/doi/10.1103/PhysRevB.99.104421.

[169] P.-W. Ma and S. L. Dudarev. "Constrained density functional for noncollinear magnetism". In: *Phys. Rev. B* 91 (5 2015), p. 054420. DOI: 10.1103/PhysRevB.91.054420. URL: https://link.aps.org/doi/10.1103/PhysRevB.91.054420.

[170] S. K. Panda et al. "High photon energy spectroscopy of NiO: Experiment and theory". In: *Phys. Rev. B* 93 (23 2016), p. 235138. DOI: 10.1103/PhysRevB.93.235138. URL: https://link.aps.org/doi/10.1103/PhysRevB.93.235138.

[171] Hyowon Park, Andrew J. Millis, and Chris A. Marianetti. "Total energy calculations using DFT+DMFT: Computing the pressure phase diagram of the rare earth nickelates". In: *Phys. Rev. B* 89 (24 2014), p. 245133. DOI: 10.1103/PhysRevB.89.245133. URL: https://link.aps.org/doi/10.1103/PhysRevB.89.245133.

[172] B. Silvi and A. Savin. "Classification of chemical bonds based on topological analysis of electron localization functions". In: *Nature* 371.6499 (Oct. 1994), pp. 683–686. ISSN: 0028-0836, 1476-4687. DOI: 10.1038/371683a0. URL: http://www.nature.com/articles/371683a0 (visited on 03/14/2022).

[173] Feng Hao, Rickard Armiento, and Ann E. Mattsson. "Using the electron localization function to correct for confinement physics in semi-local density functional theory". In: *The Journal of Chemical Physics* 140.18 (Apr. 2014). Publisher: American Institute of PhysicsAIP, 18A536. ISSN: 0021-9606. DOI: 10.1063/1.4871738. URL: https://aip.scitation.org/doi/abs/10.1063/1.4871738 (visited on 03/06/2022).

[174] J. Perez-Mato et al. "Crystallography Online: Bilbao Crystallographic Server". In: *Bulgarian Chemical Communications* 43 (Jan. 2011), pp. 183–197.

[175] Harold T. Stokes, Dorian M. Hatch, and Branton J. Campbell. *ISOTROPY Software Suite*. URL: https://iso.byu.edu/iso/isotropy.php (visited on 09/23/2023).

[176] E. Krén et al. "Investigation of the First-Order Magnetic Transformation in Mn_3Pt". In: *Journal of Applied Physics* 38.3 (June 2004), pp. 1265–1266. ISSN: 0021-8979. DOI: 10.1063/1.1709571. URL: https://doi.org/10.1063/1.1709571 (visited on 09/22/2023).

[177] Z. Yamani, Z. Tun, and D. H. Ryan. "Neutron scattering study of the classical antiferromagnet MnF_2: a perfect hands-on neutron scattering teaching issue on Neutron Scattering in Canada." In: *Canadian Journal of Physics* 88.10 (Oct. 2010). Publisher: NRC Research Press, pp. 771–797. ISSN: 0008-4204. DOI: 10.1139/P10-081. URL: https://cdnsciencepub.com/doi/full/10.1139/P10-081 (visited on 09/22/2023).

[178] D. Fruchart et al. "DIFFRACTION NEUTRONIQUE DE Mn_3ZnN". In: *Le Journal de Physique Colloques* 32.C1 (Feb. 1971). Publisher: EDP Sciences, pp. C1–877. ISSN: 0449-1947, 2777-3418. DOI: 10.1051/jphyscol:19711309. URL: http://dx.doi.org/10.1051/jphyscol:19711309 (visited on 09/22/2023).

[179] T. Hamada and K. Takenaka. "Phase instability of magnetic ground state in antiperovskite Mn_3ZnN: Giant magnetovolume effects related to magnetic structure". In: *Journal of Applied Physics* 111.7 (Apr. 2012). Publisher: American Institute of Physics, 07A904. ISSN: 0021-8979. DOI: 10.1063/1.3670052. URL: https://aip.scitation.org/doi/full/10.1063/1.3670052 (visited on 04/16/2023).

[180] Jia Yan Law et al. "A quantitative criterion for determining the order of magnetic phase transitions using the magnetocaloric effect". In: *Nature Communications* 9.1 (July 2018). Number: 1 Publisher: Nature Publishing Group, p. 2680. ISSN: 2041-1723. DOI: 10.1038/s41467-018-05111-w. URL: https://www.nature.com/articles/s41467-018-05111-w (visited on 04/16/2023).

[181] A. Muñoz et al. "Magnetic structure of hexagonal $R\mathrm{MnO_3}$ ($R = \mathrm{Y}, \mathrm{Sc}$) : Thermal evolution from neutron powder diffraction data". In: *Phys. Rev. B* 62 (14 2000), pp. 9498–9510. DOI: 10.1103/PhysRevB.62.9498. URL: https://link.aps.org/doi/10.1103/PhysRevB.62.9498.

[182] Raffaele Resta. "Electrical polarization and orbital magnetization: the modern theories". In: *Journal of Physics: Condensed Matter* 22.12 (Mar. 2010), p. 123201. ISSN: 0953-8984. DOI: 10.1088/0953-8984/22/12/123201. URL: https://dx.doi.org/10.1088/0953-8984/22/12/123201 (visited on 04/07/2023).

[183] Ming-Che Chang and Qian Niu. "Berry curvature, orbital moment, and effective quantum theory of electrons in electromagnetic fields". In: *Journal of Physics: Condensed Matter* 20.19 (Apr. 2008), p. 193202. ISSN: 0953-8984. DOI: 10.1088/0953-8984/20/19/193202. URL: https://dx.doi.org/10.1088/0953-8984/20/19/193202 (visited on 04/07/2023).

[184] S. V. Streltsov and D. I. Khomskii. "Orbital physics in transition metal compounds: new trends". In: *Physics-Uspekhi* 60.11 (Nov. 2017). Publisher: IOP Publishing, p. 1121. ISSN: 1063-7869. DOI: 10.3367/UFNe.2017.08.038196. URL: https://iopscience.iop.org/article/10.3367/UFNe.2017.08.038196/meta (visited on 09/24/2023).

[185] A. S. Borovik-Romanov, H. Grimmer, and M. Kenzelmann. "Chapter 1.5. Magnetic properties". In: *International Tables for Crystallography*. Vol. D. Publisher: International Union of Crystallography. 2013. DOI: 10.1107/97809553602060000904. URL: https://onlinelibrary.wiley.com/iucr/itc/Db/ch1o5v0001/fn/ (visited on 09/22/2023).

[186] Joya A. Cooley et al. "Evolution of noncollinear magnetism in magnetocaloric MnPtGa". In: *Physical Review Materials* 4.4 (Apr. 2020). Publisher: American Physical Society, p. 044405. DOI: 10.1103/PhysRevMaterials.4.044405. URL: https://link.aps.org/doi/10.1103/PhysRevMaterials.4.044405 (visited on 09/22/2023).

[187] Geoffrey E Hinton and Sam Roweis. "Stochastic Neighbor Embedding". In: *Advances in Neural Information Processing Systems*. Vol. 15. MIT Press, 2002. (Visited on 09/28/2023).

[188] M. J. Tarne et al. "Tuning the antiferromagnetic helical pitch length and nanoscale domain size in $Fe_3PO_4O_3$ by magnetic dilution". In: *Physical Review B* 96.21 (Dec. 2017), p. 214431. ISSN: 2469-9950, 2469-9969. DOI: 10.1103/PhysRevB.96.214431. URL: https://link.aps.org/doi/10.1103/PhysRevB.96.214431 (visited on 10/02/2023).

[189] Matthew Horton et al. *Crystal Toolkit: A Web App Framework to Improve Usability and Accessibility of Materials Science Research Algorithms*. arXiv:2302.06147 [cond-mat]. Feb. 2023. DOI: 10.48550/arXiv.2302.06147. URL: http://arxiv.org/abs/2302.06147 (visited on 09/28/2023).

[190] P. J. Brown et al. "Determination of the magnetic structure of Mn_3Sn using generalized neutron polarization analysis". In: (Oct. 2020). Accepted: 2020-10-28T18:19:17Z Publisher: Institute of Physics Publishing. ISSN: 0953-8984. (Visited on 09/22/2023).

[191] Ruchika Mahajan et al. "Importance of intersite Hubbard interactions in $\beta-$ MnO_2 : A first-principles DFT+U+V study". In: *Physical Review Materials* 5.10 (Oct. 2021), p. 104402. ISSN: 2475-9953. DOI: 10.1103/PhysRevMaterials.5.104402. URL: https://link.aps.org/doi/10.1103/PhysRevMaterials.5.104402 (visited on 10/02/2023).

[192] Zahra Mosleh and Mojtaba Alaei. *A Benchmark of Density Functional Theory on the Prediction of Antiferromagnetic Transition Temperature*. arXiv:2308.02026 [physics]. Aug. 2023. URL: http://arxiv.org/abs/2308.02026 (visited on 10/02/2023).

[193] R. Eder, J. Van Den Brink, and G. A. Sawatzky. "Intersite Coulomb interaction and Heisenberg exchange". In: *Physical Review B* 54.2 (July 1996), R732–R735. ISSN: 0163-1829, 1095-3795. DOI: 10.1103/PhysRevB.54.R732. URL: https://link.aps.org/doi/10.1103/PhysRevB.54.R732 (visited on 10/02/2023).

[194] B. Möller and P. Wölfle. "Magnetic order in the periodic Anderson model". In: *Physical Review B* 48.14 (Oct. 1993), pp. 10320–10326. ISSN: 0163-1829, 1095-3795. DOI: 10.1103/PhysRevB.48.10320. URL: https://link.aps.org/doi/10.1103/PhysRevB.48.10320 (visited on 10/02/2023).

[195] Xu He et al. "TB2J: A python package for computing magnetic interaction parameters". In: *Computer Physics Communications* 264 (July 2021), p. 107938. ISSN: 0010-4655. DOI: 10.1016/j.cpc.2021.107938. URL: https://www.sciencedirect.com/science/article/pii/S0010465521000679 (visited on 10/02/2023).